



**University of  
Nottingham**

UK | CHINA | MALAYSIA

**Multidimensional Analysis of Courtyard  
Building Environmental Performance Using  
Computational Fluid Dynamics**

**2024**

**Hao Sun**

**Thesis submitted to the University of Nottingham**

**for the degree of Doctor of Philosophy**

Department of Architecture and Built Environment

Faculty of Engineering

Supervisors: Dr. John Calautit and Professor. Saffa Riffat

## Abstract

Courtyards are important for enhancing natural ventilation and daylight while mitigating extreme heat in urban environments. However, their interaction with courtyards' indoor spaces and the impact of passive technologies such as different roof designs, vegetation, and water sprayers on indoor aerothermal conditions and pollutant transmission has not been studied. To address research gaps, this study explores natural ventilation, temperature control, and pollutant transmission in courtyard buildings using CFD simulations. We validate different courtyard models derived from wind tunnel experiments, comparing various turbulence models—specifically the Reynolds-Averaged Navier-Stokes (RANS) models, including k-epsilon and k-omega—to ensure robust CFD model validation. This study examines ten different roof designs' impact on natural ventilation and passive cooling in courtyard buildings. Results show that dome roofs enhance ventilation, increasing indoor wind speed by 80% and reducing temperatures by up to 2.1°C compared to flat roofs. Integrated vegetation, particularly large trees, significantly improves aero-thermal comfort, with temperature drops up to 6.58°C. Additionally, water sprays in single-sided ventilated courtyards improve indoor thermal conditions, lowering temperatures by 2.06°C and increasing humidity by 4.29%. Pollutant dispersion analysis reveals that structure, orientation, and external wind patterns significantly influence pollutant spread, primarily affecting adjacent rooms on the same floor. This multidimensional analysis focuses on courtyard design features and their impact on indoor environments, evaluating passive technologies like vegetation and water features in improving microclimates. It provides insights into design choices and air quality, promoting sustainable architectural practices to address climate change and create healthier urban living spaces.

## Published Works

1. Hao Sun, Carlos Jimenez-Bescos, Murtaza Mohammadi, Fangliang Zhong, and John Kaiser Calautit. 2021. "Numerical Investigation of the Influence of Vegetation on the Aero-Thermal Performance of Buildings with Courtyards in Hot Climates" *Energies* 14, no. 17: 5388. <https://doi.org/10.3390/en14175388>
2. Hao Sun, Hua Zhong, Abdullah Dik, Kemin Ding, Carlos Jimenez-Bescos, John Kaiser Calautit. 2024. " Numerical investigation of evaporative cooling strategies on the aero-thermal performance of courtyard buildings in hot-dry climates ". *Building and Environment* 258 (2024) 111588. <https://doi.org/10.1016/j.buildenv.2024.111588>
3. Hao Sun, Rafik Bensalem, Abdullah Dik, Zhu Tao, Carlos Jimenez-Bescos, John Kaiser Calautita. 2024. "Are all courtyard shapes created equal? The impact of courtyard geometry on neighboring building ventilation and passive cooling ". *Building and Environment* (Under review)
4. Hao Sun, John S.Owen, Salah Almazmumi, Chong Liu, Murtaza Mohammadi, Abdullah Dik, Carlos Jimenez-Bescos, John Kaiser Calautit. 2024. "Pollutant cross-transmission in courtyard buildings: Wind tunnel experiments and computational fluid dynamics (CFD) evaluation". *Building and Environment* 264 (2024) 111919. <https://doi.org/10.1016/j.buildenv.2024.111919>

## Acknowledgement

Since October 2020, I started my PhD journey at the University of Nottingham. Over the past four years, I have been fortunate to receive support and guidance from many esteemed mentors and friends.

First and foremost, I must express my deepest gratitude to my supervisor, Dr. John Calautit. His meticulous guidance has profoundly impacted my academic career. Arriving in Nottingham with no clue about what my PhD life would entail, it was Dr. John Calautit who guided me every step of the way. I deeply admire his personal integrity and academic excellence. Dr. John Calautit is not only a responsible and patient teacher but also a guiding light on my academic path. I am grateful for his mentorship over these years and aspire to become a researcher like him, treating my future students with the same dedication. Thank you, Dr. John Calautit.

Next, I would like to thank my external supervisor, Dr. Carlos Jimenez-Bescos, who always provided direction and encouragement whenever I felt lost. Our discussions spanned both academic and personal life, and without his support, I would not have reached where I am today. I also owe a debt of gratitude to my co-supervisor, Professor Saffa Riffat, and my collaborator, Dr. John S. Owen, an expert in wind engineering. I cherish the opportunity to have worked with you all. Dr. Abdullah Dik, my dear friend and academic collaborator, whose invaluable support and guidance have greatly contributed to my PhD journey.

I must also extend special thanks to my parents, who have supported me both spiritually and financially. They were always there for me whenever I faced difficulties. Thank you for



your constant presence and support—I love you! Additionally, I am grateful for the companionship of my beloved dog, Snoopy, whose presence brought endless joy to my life.

I would also like to thank all my colleagues and friends. Your support, encouragement, and assistance have been crucial in my progression.

Lastly, I appreciate the continuous support from the University of Nottingham and the Department of Architecture and Built Environment, Faculty of Engineering.

## Nomenclature

### *Abbreviation*

ABL	Atmospheric Boundary Layer
BES	Building Energy Simulation
CFD	Computational Fluid Dynamics
CO <sub>2</sub>	Carbon dioxide
CV	Cross Ventilated
DPM	Discrete Phase Model
FAC2	Factor of Two
FB	Fractional Bias
FVM	Finite Volume Method
GCI	Grid Convergence Index
GHG	Greenhouse Gas
IPCC	Intergovernmental Panel on Climate Change
LES	Large Eddy Simulation
NMSE	Normalized Mean Squared Error
PDD	Percentage of Dissatisfaction Index
PIV	Particle Image Velocimetry
PMV	Predicted Mean Vote
RANS	Reynolds-Averaged Navier-Stokes
RE	Rooms on the eastern side
REF	Room - Eastern - First Floor
REG	Room - Eastern - Ground Floor
RES	Room - Eastern - Second Floor
RET	Room - Eastern - Third Floor

RH	Relative Humidity
RN	Rooms on the northern side
RNF	Room - Northern - First Floor
RNG	Room - Northern - Ground Floor
RNS	Room - Northern - Second Floor
RNT	Room - Northern - Third Floor
RS	Rooms on the southern side
RSF	Room - Southern - First Floor
RSG	Room - Southern - Ground Floor
RSS	Room - Southern - Second Floor
RST	Room - Southern - Third Floor
RW	Rooms on the western side
RWF	Room - Western - First Floor
RWG	Room - Western - Ground Floor
RWS	Room - Western - Second Floor
RWT	Room - Western - Third Floor
SIMPLE	Semi-Implicit Method for Pressure-Linked Equations
SSV	Single-Sided Ventilated
UHI	Urban Heat Island
UTCI	Universal Thermal Climate Index

***Symbols***

A	Area (m <sup>2</sup> )
C	Concentration (mol/m <sup>3</sup> )
C <sub>p</sub>	Specific heat (J/kg·K)
CQ <sub>t</sub>	User-defined dimensionless velocity coefficient

$d$	Diameter (m)
$E$	Energy (J)
$F$	External body force (N)
$g$	Gravitational acceleration ( $\text{m/s}^2$ )
$H$	Height (m)
$J$	Diffusion flux ( $\text{mol/m}^2\cdot\text{s}$ )
$k$	Turbulent kinetic energy ( $\text{m}^2/\text{s}^2$ )
$L$	Length (m)
$N$	Mass transfer rate (kg/s)
$p$	Pressure (Pa)
$R$	Rate of reaction ( $\text{mol/L}\cdot\text{s}$ )
$Re$	Reynolds number
$S$	User-defined source terms ( $\text{kg/m}^3\cdot\text{s}$ , J, $\text{m}^2/\text{s}^2$ , $\text{m}^3/\text{s}^3$ )
$S_c$	Schmidt number
$Sh$	Sherwood number
$t$	Time (s)
$u$	Velocity (m/s)
$W$	Width (m)
$Y$	Mass fraction
$Z$	Height at Z (m)
$\alpha$	Power law exponent
$\varepsilon$	Dissipation rate ( $\text{m}^2/\text{s}^3$ )
$\kappa$	Thermal conductivity ( $\text{W/m}\cdot\text{K}$ )
$\mu$	Molecular viscosity ( $\text{Pa}\cdot\text{s}$ )

$\rho$	Density (kg/m <sup>3</sup> )
$\sigma$	Prandtl numbers
$\tau$	Stress tensor (Pa)

***Subscript***

$d$	Droplet
$\varepsilon$	Dissipation rate
eff	Effective
$h$	Heat
$i$	Species
$k$	Turbulence kinetic energy
$m$	Mass
$\infty$	Free stream
$o$	Opening
ref	Reference

# Table of Contents

Abstract.....	i
Published Works .....	ii
Acknowledgement .....	iii
Nomenclature.....	v
Table of Contents.....	ix
List of Figures .....	xiv
List of Tables .....	xxii
Chapter 1 Introduction .....	1
1.1    Background.....	1
1.2    Aim and objectives .....	5
1.3    Novelty and contribution to knowledge.....	8
1.4    Thesis structure .....	9
Chapter 2 Literature Review .....	15
2.1    Introduction.....	15
2.2    Courtyards.....	16
2.2.1    The definition and historical development of courtyards .....	16
2.2.2    The influence of courtyard geometry and orientation on microclimate and thermal performance: the role of shading .....	18
2.3    Ventilation dynamics in courtyard buildings: modes and strategies .....	23
2.3.1    The influence of courtyard geometry and orientation on microclimate and thermal performance: the role of natural ventilation.....	24
2.3.2    Ventilation strategy for courtyards .....	29
2.4    Impact of roof design on aerothermal performance.....	31
2.5    Impact of evaporative cooling systems on building microclimates.....	34

2.6	Impact of vegetation on building microclimates .....	37
2.7	Pollutant dispersion studies: courtyard building and wind tunnel insights..	41
2.7.1	Pollutant dispersion within courtyard buildings .....	41
2.7.2	Exploring pollutant dispersion: insights from combined wind tunnel experiments and CFD simulations .....	44
2.8	Research gaps.....	52
Chapter 3 Roof Shape Designs for the Courtyard .....		56
3.1	Introduction.....	56
3.2	Method .....	59
3.2.1	CFD theory.....	59
3.2.2	Courtyard geometry, computational domain, and boundary conditions 61	
3.2.3	Boundary conditions for the simulation study .....	65
3.2.4	Grid and sensitivity analysis .....	67
3.3	Results.....	71
3.3.1	Validation of the naturally ventilated courtyard model .....	71
3.3.2	Airflow in the single-sided ventilated courtyards with different shapes of roof.....	80
3.3.2	Temperature distribution for the courtyard with different shapes of roof 89	
3.3.4	Analysis of the relationship between courtyard wind dynamics and indoor airflow enhancement .....	94
3.4	Discussion.....	99
3.4.1	Comparison with other studies.....	99
3.4.2	Limitations and recommendations for future works.....	102

3.5	Conclusion .....	103
Chapter 4 Courtyards with Evaporative Cooling Strategies .....		106
4.1	Introduction.....	106
4.2	Method .....	106
4.1.1	CFD theory.....	107
4.1.2	CFD geometry.....	110
4.1.3	CFD mesh design and verification.....	115
4.1.4	Boundary conditions for the simulation study .....	117
4.3	Result of this chapter .....	121
4.3.1	Validation of the water sprayer model.....	121
4.3.2	Single-sided ventilated courtyard: wind and thermal performance with and without water sprayers .....	124
4.3.3	Cross-ventilated courtyard: wind and thermal performance with and without water sprayers .....	135
4.4	Water flow rate analyse and limitations of this chapter.....	141
4.4.1	Water flow rate analyse .....	141
4.4.2	Limitations .....	144
4.5	Conclusion .....	145
Chapter 5 Courtyards with Vegetation .....		148
5.1	Introduction.....	148
5.2	Method .....	148
5.2.1	CFD theory.....	149
5.2.2	CFD geometry.....	150
5.2.3	CFD mesh design and verification.....	155
5.2.4	Boundary conditions for the simulation study .....	158



5.3	Results.....	158
5.3.1	Validation of the courtyard model .....	158
5.3.2	Validation of the vegetation.....	160
5.3.3	Case 1: Baseline courtyard model.....	163
5.3.4	Case 2: Baseline courtyard model with four small trees.....	166
5.3.5	Case 3: Baseline courtyard model with four large trees .....	172
5.3.6	Ventilation and temperature conditions inside the courtyard .....	180
5.4	Conclusion .....	183
Chapter 6 Pollutant Cross-transmission within Courtyards.....		187
6.1	Introduction.....	187
6.2	Experimental method .....	190
6.2.1	Physical model and wind tunnel experimental setup.....	190
6.2.2	Wind tunnel experimental setup for the pressure measurement .....	195
6.2.3	Wind tunnel experimental setup for the CO <sub>2</sub> measurement.....	195
6.3	CFD Method .....	198
6.3.1	Numerical methods and solver settings .....	198
6.3.2	Courtyard geometry, computational domain, and boundary conditions 201	
6.3.3	Grid and sensitivity analysis .....	203
6.3.4	Validation of the numerical model .....	207
6.4	Results of this chapter .....	213
6.4.1	Airflow movement and pollutant dispersion at 0° wind direction.....	215
6.4.2	Airflow movement and pollutant dispersion at 45° wind direction....	220
6.5	Discussion .....	226
6.5.1	Comparative analysis of optimal and adverse scenarios.....	226

6.5.2 Comparison with other studies.....	231
6.5.3 Limitations and recommendations for future works.....	233
6.6 Conclusion .....	235
Chapter 7 Conclusions and Future works .....	237
7.1 Conclusions.....	237
7.2 Contribution to knowledge .....	242
7.3 Limitations of the thesis.....	243
7.4 Recommendations for further work.....	245
References.....	248

## List of Figures

Figure 1.1 Airflow dynamics in courtyard architecture for wind-driven natural ventilation. ....	3
Figure 1. 2 Layout of the thesis. ....	10
Figure 2. 1 Courtyard forms for enclosed courtyard and semi-enclosed courtyards (Meng et al. 2016). ....	17
Figure 2.2 Early courtyard buildings around the world (Zhu et al. 2023). ....	18
Figure 2.3 Different height/width ratio and sky view factors of courtyards (Martinelli and Matzarakis 2017). ....	20
Figure 2.4 Geometry impact for shading influenced the courtyard, from (Rodríguez-Algeciras et al. 2018) and edited by (Zhu et al. 2023). ....	21
Figure 2.5 Change of courtyard orientation from 0° to 90° (Muhaisen 2006). ....	22
Figure 2. 6 Flow patterns along the courtyard in different length-to-height ratios ((Moonen et al., 2011). ....	25
Figure 2. 7 Three types of flow patterns in courtyards of different depths (Hall et al., 1999a). ....	26
Figure 2. 8 The ventilation and heat exchange within the courtyard (Yang 2012). ....	28
Figure 2. 9 Airflow diagrams of a traditional Malaysian house - Chinese shophouse ((Zakaria et al., 2015). ....	29
Figure 2.10 Leeward roof shapes analysed in (Peren et al. 2015). ....	32
Figure 2.11 Courtyard buildings with different roof shapes and their vertical cross-sectional view (Prakash 2022). ....	33
Figure 2. 12 Evaporative cooling system in the courtyard, air temperature, and vapor mass fraction distribution (H. Montazeri et al. 2017). ....	36

Figure 2.13 CFD analysis of transportational cooling by vegetation (Gromke et al. 2015). .....	39
Figure 2. 14 Skygarden with trees model (Mohammadi et al., 2020). .....	41
Figure 2. 15 Location of airborne pollutant sources and CFD simulation of pollutant dispersion with varying courtyard widths (Leng et al., 2020). .....	42
Figure 2. 16 Pollutant dispersion scenarios and iso-surface contours for different release points using steady and unsteady RANS computations (Tominaga & Stathopoulos 2017). .....	46
Figure 2. 17 Time series showing the evolution of concentration levels within a street canyon, as modelled by LES (Tominaga & Stathopoulos 2011). .....	49
Figure 3.1 Single-sided ventilated courtyard buildings featuring ten different roof styles. .....	57
Figure 3.2 The primary research workflow of the study and the four main research questions are addressed. ....	58
Figure 3. 3 Dimensions of the courtyard building and window opening. ....	62
Figure 3.4 Computational domain dimensions, boundary conditions, top view, and wind tunnel setup for internal flow tests (Bensalem 1991). .....	64
Figure 3.5 Wind velocity simulation, grid sensitivity analysis, and polyhedral mesh around the courtyard building. ....	67
Figure 3.6 Comparison of experimental and CFD numerical models, and deviation analysis between wind tunnel experiments and numerical simulations. ....	72
Figure 3.7 Indoor wind velocity magnitude contour at $Y = 135\text{mm}$ , with arrows representing the observed vectors for baseline flat-roof courtyard model. ....	80
Figure 3.8 Airflow movement patterns for ten different roof styles. ....	83

Figure 3.9 Airflow movement patterns and pressure contours for five different roof styles with specific values.....	87
Figure 3.10 Temperature contours in the cross-section at $Y = 135$ mm for the courtyard with four different roof styles. ....	89
Figure 3.11 Comparison of indoor wind velocity and temperature, and temperature distribution for courtyard buildings with different roof styles.....	91
Figure 3.12 Relationship between courtyard and indoor wind velocities for different roof styles. ....	95
Figure 3.13 Relationship between indoor air flow rate and wind velocity for different roof styles.....	97
Figure 3.14 Airflow movement patterns in the dome courtyard model and the indoor wind velocity magnitude contour at $Y = 135$ mm, with arrows representing the observed vectors.....	99
Figure 4.1 Single-sided ventilated and cross-ventilated courtyards with water sprayers..	111
Figure 4.2 Dimensions and arrangement of SSV and CV courtyards, window openings, and test rooms. ....	113
Figure 4.3 The simulation setup demonstrates the computational domain and the location of water sprayers. ....	115
Figure 4.4 Polyhedral mesh of courtyard building and simulated wind speed results for grid sensitivity analysis.....	117
Figure 4.5 Wind tunnel test setup and comparative analysis of air velocity and temperature profiles between CFD results and experimental data. centre plane lines between CFD results and experimental data). ....	121

Figure 4.6 Comparative visualizations of courtyard ventilation strategies at Y = 14125 mm section.....	125
Figure 4.7 Comparison of indoor wind velocity in the SSV courtyard. ....	126
Figure 4.8 Wind velocity comparison in each test room within the SSV courtyard with and without water sprayers. ....	128
Figure 4.9 Temperature and relative humidity contours at two cross-sections within the SSV courtyard with water sprayers.....	131
Figure 4.10 Temperature and relative humidity contours for each floor in the SSV courtyard with water sprayers (sectioned at the window openings).....	132
Figure 4.11 Comparative plots of indoor temperature (Red) and relative humidity (Purple) levels in each room within the SSV courtyard, with and without water sprayers. ....	133
Figure 4.12 Comparison of indoor wind velocity in the CV courtyard. ....	137
Figure 4.13 Wind velocity comparison in each test room within the CV courtyard with and without water sprayers. ....	138
Figure 4.14 Wind velocity comparison in each test room for the SSV and CV courtyards with water sprayers. ....	139
Figure 4.15 Comparison of indoor average temperature changes for varying water flow rates in the SSV courtyard. ....	141
Figure 4.16 Comparison of indoor average temperature changes for varying water flow rates in the SSV courtyard. ....	143
Figure 5.1 Three scenarios with different vegetation characteristics in this chapter. ....	148
Figure 5.2 Courtyard model and geometry of the central courtyard.....	151
Figure 5.3 The layout of the rooms on each floor (R - Room, N - North, W - West, S-South, E -East, G - Ground floor, F – First floor).....	152

Figure 5.4 The dimensions of each room.....	152
Figure 5.5 The dimensions of each window and schematic showing dimensions.....	153
Figure 5.6 The dimension of the domain and the direction of the wind.....	153
Figure 5.7 The dimension of the vegetation inside the courtyard.....	154
Figure 5.8 Commercial example of cuboidal hedges and relationship of vegetation to occupants.....	154
Figure 5.9 Meshed courtyard and its surrounding microclimate. ....	156
Figure 5.10 Simulated results of temperature along a horizontal center line of the courtyard model with small trees at a height of 0.7 m for the grid sensitivity analysis.....	157
Figure 5.11 Simulation domain and dimensions of the validation model. ....	159
Figure 5.12 Comparison of dimensionless wind velocity along the analysis line. ....	160
Figure 5.13 Simulation field of the validation model, based on the porous vegetation according to the indication of the green square and centred on the x-axis. ....	161
Figure 5.14 Contours of velocity and temperature near the vegetation (black square) based on the validation model.....	162
Figure 5.15 Comparison of wind speed on the analysis line, in addition to the vegetation zone under the in-dictation of the green. ....	162
Figure 5.16 Average wind speed magnitude in each room for the baseline courtyard model.....	165
Figure 5.17 Contours of the wind speed in each room for the baseline courtyard model. .....	165
Figure 5.18 Average air temperature in each room for the baseline courtyard model with four small trees.....	167

Figure 5.19 Simulated results of the air temperature contour with isotherm in each room for the baseline courtyard model with four small trees.....	167
Figure 5.20 Comparison of air temperature for Case 1 and Case 2 in each room. ....	168
Figure 5.21 Average wind speed magnitude in each room for the baseline courtyard model with four small trees.....	170
Figure 5.22 Contours of the wind speed in each room for the baseline courtyard model with four small trees.....	170
Figure 5.23 Comparison of wind speed magnitude for Case 1 and Case 2 in each room. ....	172
Figure 5.24 Average air temperature in each room for the baseline courtyard model with four large trees. ....	174
Figure 5.25 Simulated results of the air temperature contour with isotherm in each room for the baseline courtyard model with four large trees. ....	174
Figure 5.26 Comparison of air temperature for Case 1 and Case 3 in each room. ....	175
Figure 5.27 Comparison of air temperature for Case 2 and Case 3 in each room. ....	176
Figure 5.28 Average wind speed magnitude in each room for the baseline courtyard model with four large trees. ....	177
Figure 5.29 Contours of the wind speed in each room for the baseline courtyard model with four small trees.....	178
Figure 5.30 Comparison of wind speed magnitude for Case 1, Case 2 and Case 3 in each room. ....	180
Figure 5.31 Position of the slice in the courtyard layout diagram. ....	181
Figure 5.32 Contours for the wind speed magnitude and temperature within the courtyard with small trees and large trees (S1: X=7500mm). ....	182



Figure 6.1 Cross-transmission of pollutants between naturally ventilated courtyard units. .....	189
Figure 6.2 Courtyard model in wind tunnel, overall dimensions, pressure tube connections, window dimensions, and pressure measurement points. ....	192
Figure 6.3 Relationship between $Z/Z_{ref}$ , $U/U_{ref}$ and $I/I_{ref}$ .....	193
Figure 6.4 Wind tunnel CO <sub>2</sub> dispersion measurement setup and courtyard model with CO <sub>2</sub> sensors.....	197
Figure 6.5 Courtyard building model for CFD modelling, distribution of monitoring points, and orientation and naming of test rooms. ....	202
Figure 6.6 The dimensions and boundary conditions of the computational domain. ....	203
Figure 6.7 Simulated CO <sub>2</sub> concentration and grid sensitivity analysis with polyhedral mesh around courtyard surfaces.....	204
Figure 6.8 Comparison of pressure coefficient values between the experiment and CFD simulations. ....	210
Figure 6.9 Comparison of CO <sub>2</sub> concentration between the experiment and CFD simulations with three turbulence models.....	213
Figure 6.10 48 CFD simulation scenarios for evaluating the impact of different pollutant sources, wind speeds and directions. ....	214
Figure 6.11 Observed airflow patterns, wind velocity, and pressure distribution around the courtyard building in vertical and horizontal orientations. ....	216
Figure 6.12 Average CO <sub>2</sub> concentrations in different rooms at wind speeds of 5 m/s and 10 m/s, based on different source locations. ....	219
Figure 6.13 CO <sub>2</sub> dispersion pathways and indoor concentration levels from the windward side for Case 1 and Case 13. ....	220

Figure 6.14 Airflow patterns, wind velocity, and pressure distribution around the courtyard building at 45 degrees wind.....	222
Figure 6.15 Average CO <sub>2</sub> concentrations in different rooms at wind speeds of 5 m/s and 10 m/s, based on different source locations..	224
Figure 6.16 CO <sub>2</sub> dispersion pathways and indoor concentration levels from the windward side for Case 25 and Case 43. ....	225

## List of Tables

Table 3.1 Example of discretization error computation employing the GCI method.....	70
Table 3.2 Velocity coefficient $C_{Qt}$ validation results for the courtyard and atriums numerical simulation by using the k-epsilon Standard model. ....	75
Table 3.3 Velocity coefficient $C_{Qt}$ validation results for the courtyard and atriums numerical simulation by using k-epsilon RNG model.....	76
Table 3.4 Velocity coefficient $C_{Qt}$ validation results for the courtyard and atriums numerical simulation by using k-epsilon Realizable model. ....	77
Table 3.5 Velocity coefficient $C_{Qt}$ validation results for the courtyard and atriums numerical simulation by using k-omega Standard model.....	78
Table 3.6 Velocity coefficient $C_{Qt}$ validation results for the courtyard and atriums numerical simulation by using k-omega SST model. ....	79
Table 4. 1 Mesh sensitivity analysis for the CV courtyard with polyhedral mesh. ....	116
Table 4. 2 Summary of the CFD model boundary conditions. ....	120
Table 4.3 Average indoor temperature and relative humidity of the CV courtyard with water sprayers. ....	139
Table 5.1 Three Scenarios for the case study. ....	149
Table 5.2 Mesh setup condition. ....	155
Table 5.3 Mesh setup for sensitivity analysis (courtyard with small trees).....	157
Table 6. 1 Measured average velocity and turbulence intensity of the wind profile for different heights. ....	194
Table 6.2 Sample discretization error calculation using GCI method. ....	206
Table 6.3 Validation metrics for the internal pressure coefficient.....	208
Table 6.4 Comparative analysis of optimal conditions across the first 24 scenarios under a wind direction of 0 degrees. ....	227

Table 6.5 Comparative analysis of adverse conditions across the first 24 scenarios under a wind direction of 0 degrees. ....	228
Table 6.6 Comparative analysis of optimal conditions across the later 24 scenarios under a wind direction of 45 degrees. ....	229
Table 6.7 Comparative analysis of adverse conditions across the later 24 scenarios under a wind direction of 45 degrees. ....	230

# Chapter 1 Introduction

## 1.1 Background

Climate change, global warming, and extreme weather events, coupled with the urban heat island (UHI) phenomenon, are widely recognized as the most significant challenges of the 21st century, having profound impacts on the environment, public health, and the economy (Amaripadath et al., 2023; Santamouris, 2016). The report on climate change released by the Intergovernmental Panel on Climate Change (IPCC) in 2023 emphasizes that human activities, particularly the emission of greenhouse gases (GHG), are continuously driving up global temperatures, which are expected to rise to 1.5°C in the near future (IPCC Core Writing Team, 2023). The building sector consumes a great amount of energy and resources; over 40% of the world's energy consumption comes from buildings and is still increasing (Cao et al., 2016). Especially in hot climates, cooling technologies occupy a major part of the building's energy consumption. Yu et al. (2020) highlighted that active systems and passive design are two main strategies for enhancing energy efficiency. Passive cooling strategy can play an important role in reducing indoor overheating and improving thermal comfort; more and more architects are aware of the importance of developing passive cooling strategies during architectural design (Moghimi et al., 2014). Effective passive cooling technology and the integration of various passive strategies are critical approaches to reducing energy consumption in buildings.

One of the most detrimental consequences of climate change on buildings is overheating, particularly pronounced in hot and dry climate regions (Hamdy et al., 2017). Studies have indicated that such conditions significantly exacerbate the overheating of building interiors.

This not only affects the comfort and health of occupants but also increases the energy consumption of active cooling systems, exacerbating energy crises and environmental pollution issues (Sun et al., 2022; Yilmaz, 2007). Additionally, the UHI phenomenon has significantly contributed to the exacerbated overheating in cities. Predictions suggest that the rise in global average temperatures will lead to increasingly frequent and prolonged heatwaves. However, relying on expanding active cooling systems is not an appropriate solution, especially given the current energy landscape and the fact that resources have not been fully optimized. The growing energy consumption of buildings substantially burdens the energy sector (Diz-Mellado et al., 2023). As a result of an increase in the frequency and intensity of overheating, cooling energy consumption in summer is anticipated to rise by 72% globally by 2100 (Isaac & Van, 2009).

Traditionally, some buildings designed to meet human requirements incorporate an open space at their center, commonly known as a courtyard, serving as an organizational focal point. This design feature, however, varies by region, culture, and historical period. Courtyards have long been regarded as the dynamic social space that nurtures community engagement and enriches the urban landscape (Saadatjoo et al., 2023). These areas, which transcend time and culture, have evolved in terms of architectural style, reflecting the diversity of heritage and the environmental adaptations from ancient to modern times. In addition to their societal advantages, courtyards are also acclaimed for allowing the penetration of natural light and promoting natural ventilation, which makes passive cooling possible in residential settings (Aldawoud, 2008; Yang et al., 2014). Courtyard buildings are one of the common architectural forms in the design process of many traditional buildings, helping to improve the microclimate conditions in surrounding areas and the courtyard, which also creates a more comfortable indoor environment, even if it is passive (Cantón et al.,

2014). Courtyards are a historical architectural element, notably prevalent in China, Middle Eastern countries, the Mediterranean (including Greece, Italy, and Spain), Latin America (especially Mexico and Peru), and North Africa (such as Morocco and Tunisia), reflecting their broad cultural and climatic adaptability. The combination of building and courtyard is widely used to enhance natural ventilation in summer. This is certainly true in some tropical regions; the temperature difference between the courtyard and the indoor area, and between the courtyard's interior and the upper part of it leads to the generation of airflow, creating wind-driven natural ventilation. Air is drawn into the room under the effect of wind and buoyancy (Figure 1.1).

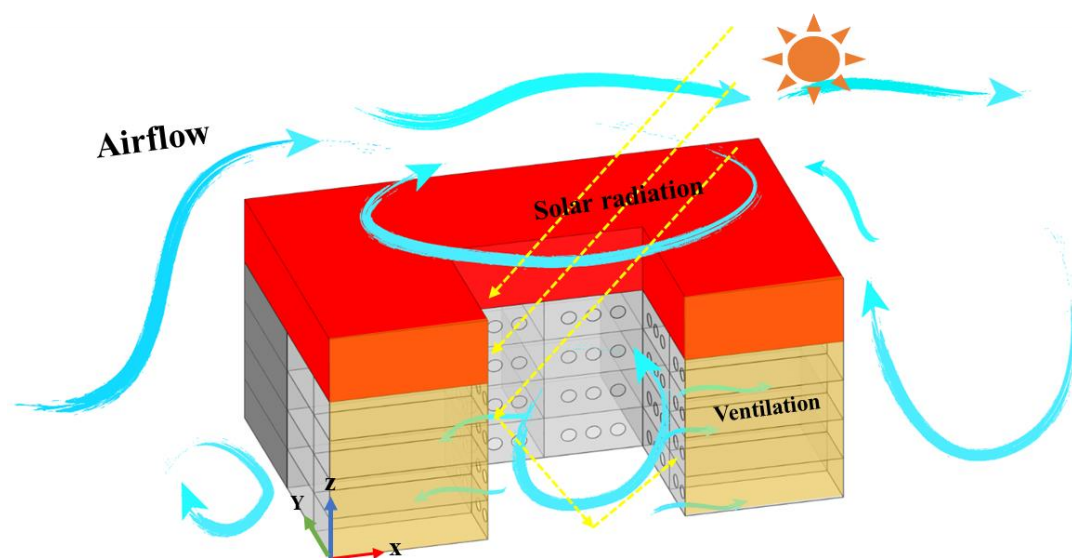


Figure 1.1 Airflow dynamics in courtyard architecture for wind-driven natural ventilation.

Previous research on courtyard architecture primarily focused on exploring the fundamental elements of courtyard design, such as the shape and orientation of courtyards, and how to effectively use natural resources to improve the courtyard environment through

passive design strategies (Al-Hafith et al., 2017; Andreou, 2013, 2014; He et al., 2021; Zhu et al., 2023). Specifically, these studies investigated the importance of vegetation configuration for regulating courtyard temperatures and providing shaded areas (Darvish et al., 2021; Gross, 2012; Sun et al., 2021), analysed how water bodies contribute to a cooler courtyard environment through their evaporative cooling effect (Diz-Mellado, López-Cabeza, et al., 2023a; Katayama et al., 1991; Noordin et al., 2021; Yılmaz, 2007). And also some researchers investigated the effectiveness of shading structures in mitigating the impact of high summer temperatures (Akbari et al., 2021; Asfour, 2020; Teshnehdel et al., 2020). These strategies not only focus on enhancing the comfort of courtyard use but also consider how to reduce energy dependence through natural regulation methods, achieving adaptability and functionality of courtyards under various climatic conditions. However, research on integrating passive technologies such as vegetation and water bodies into courtyards mainly focuses on their effects within the courtyard, with limited consideration of their impact on the indoor environment of surrounding buildings. Existing research on roof styles primarily focuses on individual buildings or urban blocks, examining their effects on the wind environment, airflow patterns, and pollutant dispersion (Abohela et al., 2013; Gough et al., 2020; Peren et al., 2015; Xie & Zhang, 2023). However, there is limited attention to their impact on courtyard buildings, especially regarding indoor thermal performance and temperature distribution. Studies often consider only a few roof styles, resulting in a lack of thorough analysis. Research on different roof styles in courtyard architecture is particularly scarce, with most focusing on flat roofs. Furthermore, comprehensive research on the dispersion of pollutants in courtyard buildings, including the full cycle of pollutants entering indoor spaces via natural ventilation through courtyards, utilizing both wind tunnel experiments and CFD methods, is scarce.



## 1.2 Aim and objectives

Due to the limited studies on courtyards and their impact on surrounding buildings in the existing literature, this research aims to investigate the interactions between courtyards and adjacent buildings, integrating wind tunnel experiments and CFD modelling. Specifically, this study focuses on assessing how the wind and thermal environment of courtyards affects the indoor wind and thermal conditions of surrounding buildings, including how variables such as different courtyard design and the use of passive strategies can influence the courtyard microclimate and, in turn, impact the indoor environment of adjacent buildings. Moreover, this study will also investigate the transmission and distribution patterns of pollutants between courtyards and surrounding buildings to uncover the potential impacts of semi-outdoor space design on the indoor environment. The study encompasses the following objectives and research questions to achieve the above aims.

Analyse and summarize the existing body of research on courtyard buildings. The review focuses on organizing and evaluating studies related to ventilation efficiency, airflow movement, and the aerothermal environment within courtyard architectures. It extends to examining the influence of various courtyard designs and passive technologies—particularly the role of vegetation and water bodies—on the wind-thermal environment, assessing how different design approaches and passive strategies can enhance ventilation, mitigate overheating, and elevate comfort levels in courtyards. Additionally, the review includes an analysis of research findings on pollutant dispersion in courtyard settings, with a particular focus on wind tunnel experiments that investigate the dispersion patterns of pollutants. This foundational review sets the stage for a detailed exploration of how architectural and environmental factors interact in courtyard spaces.

- Develop a detailed CFD model that accurately represents both outdoor and indoor environments of courtyard buildings. The model should incorporate key environmental parameters such as wind speed, pressure coefficient, and CO<sub>2</sub> concentration to simulate the microclimate and pollutant transmission of courtyard buildings. The development of this model is critical for predicting the environmental conditions within courtyard spaces, taking into account the courtyard building features that influence aerothermal performance and air quality.
- Conduct wind tunnel experiments and validate the courtyard: With the CFD model as a theoretical foundation, this objective entails performing wind tunnel experiments specifically designed for courtyard architecture. These experiments aim to gather empirical data on wind flow patterns, pressure distribution, and pollutant dispersion within and around courtyard spaces. Carry out comparisons between the outcomes of the wind tunnel experiments and the predictions made by the CFD model.
- Explore the environmental effects of commonly used passive strategies and diversified design schemes in courtyards. Specifically, the integration of vegetation, water sprayers, and various roof designs affects the wind-thermal environment inside courtyards and the interiors of surrounding buildings. This includes the role of these strategies in temperature regulation and natural ventilation, as well as assessing the differences in airflow movement patterns and their effects between single-sided ventilation and cross ventilation in courtyard architecture.
- Investigate the dynamics of wind-driven pollutant dispersion within courtyard buildings, both indoors and outdoors, by coupling wind tunnel experiments with CFD simulations.

This approach is intended to contribute to improved indoor air quality in living spaces within courtyard buildings.

- 1) How do different roof styles influence the microclimate within courtyard spaces and the adjacent indoor environments? What are the specific effects of various roof designs on airflow patterns and temperature distribution in courtyard buildings?
- 2) What impact do evaporative cooling systems have on the microclimate of courtyard spaces and the thermal performance within adjacent indoor environments? How do different ventilation strategies influence the effectiveness of evaporative cooling devices in courtyard settings?
- 3) What impact does the presence of vegetation in courtyards have on the wind and thermal environments of both the courtyard itself and the interiors of adjacent buildings? How do different sizes of vegetation influence the aerothermal performance of courtyard architecture? What differences in thermal comfort and airflow dynamics are observed when large versus small plants are used within courtyard settings?
- 4) What are the dispersion patterns of pollutants in courtyards with cross ventilation under different wind directions and speeds? How does the position of pollutant sources within different rooms affect the dispersion patterns throughout the courtyard and adjacent indoor spaces? What variations in pollutant concentration levels are observed in courtyards with cross ventilation when subjected to changing wind conditions?

### 1.3 Novelty and contribution to knowledge

Few previous papers related to courtyard architecture primarily focus on external microclimates and overlook the impact on indoor environments. However, the contributions of this study are different and novel in the following ways:

1. To understand how diverse roof styles influence both the courtyard's microclimate and the thermal performance of adjacent indoor spaces. This study aims to bridge this gap by exploring the effect of various roof styles on courtyard microclimates and the indoor environments of adjacent buildings, offering insights to optimize courtyard design for better thermal efficiency and environmental quality.
2. This research investigates the relatively unexplored area of evaporative cooling systems in courtyard buildings, assessing their impact on both the courtyards and the indoor environments of adjacent structures. It further explores how architectural features of courtyards, like cross and single-sided ventilation, enhance indoor aero-thermal comfort. The novelty lies in investigating the synergy between evaporative cooling and courtyard architecture to improve both outdoor and indoor microclimates, offering new insights for designing energy-efficient, comfortable urban living spaces in hot-dry climates.
3. This study investigates the effect of integrating vegetation in courtyards on the aero-thermal comfort of both the courtyard and adjacent indoor spaces in hot climates. By assessing the cooling impact of vegetation through evapotranspiration, this research aims to quantitatively understand its influence on indoor environments. The study evaluates how different types of vegetation affect airflow temperature, velocity, and aero-thermal

comfort, thereby examining the natural ventilation effect on the courtyard and surrounding buildings.

4. Explores how courtyard designs influence pollutant dispersion. Studies often overlook the unique characteristics of courtyards, such as their enclosed nature and interaction with surrounding buildings, which significantly affect air quality and pollutant movement. Additionally, there's a notable gap in employing wind tunnel experiments and CFD simulations to comprehensively study pollutant dispersion within courtyards. This study analysed the dispersion of pollutants in courtyard buildings, using both wind tunnel experiments and CFD simulations to enhance the indoor air quality and analyse the parameters of the courtyard design for urban living spaces.

## 1.4 Thesis structure

The first chapter introduces the background and outlines the aims and objectives while iterating the motivation and contributions of the present work. The subsequent chapters are organised as follows; the layout of the thesis is shown in Figure 1.2.

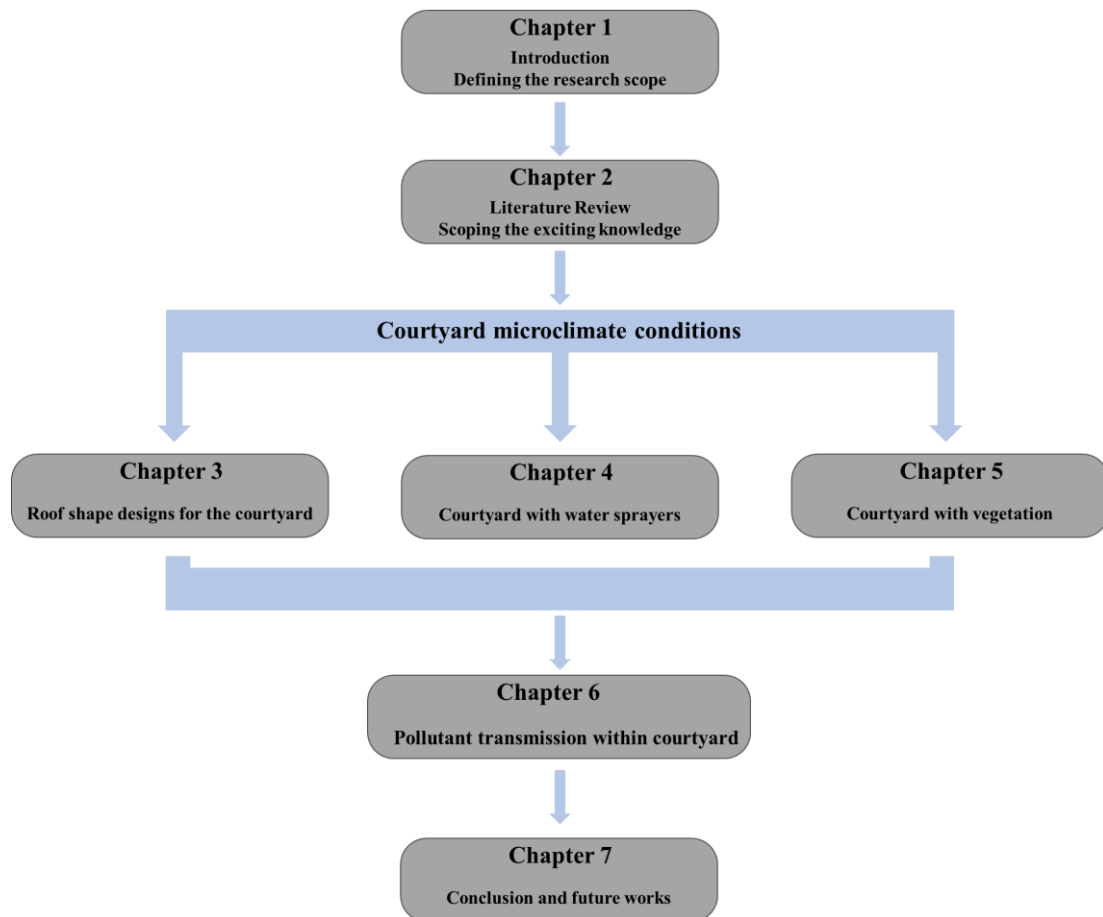


Figure 1. 2 Layout of the thesis.

- **Chapter 2** offers a comprehensive review of courtyard architecture research, focusing on microclimates, aerothermal effects, and various ventilation strategies. It assesses the impact of roof styles on wind environment and ventilation, explores the benefits of evaporative cooling, and discusses the significance of vegetation and water bodies in enhancing courtyard conditions. Additionally, it reviews pollution dispersion studies in courtyards, identifying research gaps and laying the groundwork for future investigations.
- **Chapter 3** analyses the impact of ten different roof styles on the thermal environment of indoor air in courtyard buildings. Section 3.2 introduces the main

methods used in this chapter, primarily based on wind tunnel experiment results of courtyard buildings for validation and modifies different roof styles on the courtyard model used in wind tunnel experiments. For courtyard buildings with different styles, we used CFD to simulate the indoor and outdoor wind and thermal environments, including grid sensitivity analysis and boundary condition settings. Section 3.3 discusses the CFD validation results of wind tunnel experiments and analyses the simulated results of wind and thermal environments for different roof styles. Sections 3.4 and 3.5 provide the discussion and conclusion of this chapter, comparing this study with existing research, proposing modification ideas for courtyard buildings based on simulation results, and discussing the limitations of this study as well as future research directions. This chapter aims to identify which roof design best improves indoor natural ventilation and heat dissipation, and how they affect the wind direction inside and around the building. The study explores the interaction between different roof styles and indoor air flow, laying the foundation for improving indoor ventilation and thermal conditions.

- **Chapter 4** Chapter 4 examines the air and thermal performance of courtyard buildings employing natural ventilation techniques and sprinkler systems. This chapter focuses on the impact of evaporative cooling system on the thermal environment around courtyards in hot and dry climates, assessing the effectiveness of combining cross ventilated and single-sided ventilation strategies with evaporative systems under these conditions. Section 4.2 describes the methodology used in this study, primarily combining wind tunnel experiments and CFD simulation techniques to validate the courtyard building model and water sprayer system used in the wind tunnel experiments. The CFD simulations cover the design

of courtyard buildings with different ventilation strategies, incorporating the water sprayer system, conducting grid sensitivity analysis, and setting boundary conditions. Factors such as wind speed, air temperature, and relative humidity at various locations within the courtyard buildings are considered. Section 4.3 discusses and analyses the study's results, including the CFD validation of sprinklers in wind tunnel experiments and the impact of sprinklers on the indoor wind and thermal environment of single-sided and lateral ventilation courtyard buildings. Sections 4.4 and 4.5 compare this study with previous related research, exploring the limitations and future research directions.

- **Chapter 5** explores the impact of integrating vegetation on the air and thermal comfort conditions of courtyards and surrounding buildings in hot climates. This chapter develops three scenarios based on the size of the vegetation: no vegetation, four small trees in the courtyard, and four large trees in the courtyard. It evaluates the airflow temperature, speed, and aerodynamic thermal comfort in the environment, and analyses the effect of different types of vegetation on the natural ventilation of the courtyard and adjacent buildings. Section 5.2 introduces the methods used in this chapter, including validating wind tunnel experiment results through CFD simulation, which covers the validation of the courtyard building and the vegetation. This section also provides basic information about the CFD simulation model, including dimensions, grid sensitivity analysis, and boundary condition settings. Section 5.3 discusses and analyses the results of this chapter, including the CFD validation of wind tunnel experiments, and the impact of vegetation of different sizes on the indoor and overall wind and thermal



environment of the courtyard buildings. Section 5.4 summarizes the chapter and proposes future research directions and suggestions.

- **Chapter 6** investigates the wind-driven dispersion of pollutants in courtyard buildings and uses wind tunnel data to validate CFD results. Section 6.2 introduces the methodology of the wind tunnel experiments, including the courtyard model and experimental setup, specifically addressing the dimensions of the wind tunnel, the turntable size, and the wind profile measurements. Additionally, this section covers the measurement of pressure coefficients and the monitoring of pollutant dispersion. Section 6.3 describes the CFD simulation methods, including the selection of numerical simulations and solvers, the setup of the fluid domain, grid sensitivity analysis, and boundary condition settings. It also presents the results of the CFD validation against wind tunnel experiments. Section 6.4 analyses the results of 48 scenarios with different wind speeds and directions, thoroughly examining how wind conditions affect pollutant movement and concentration within the courtyard. The study investigates the influence of wind direction, wind speed, and pollutant source location on dispersion patterns and levels, with a particular focus on pollutants such as carbon dioxide. Sections 6.5 and 6.6 provide the discussion and conclusion of this chapter, exploring various scenarios of pollutant dispersion in courtyard buildings. These sections analyse both adverse and optimal scenarios and compare them with related studies. Finally, the limitations of this research and suggestions for future studies are discussed.

- **Chapter 7** provides a summary of the research outcomes and acknowledges the limitations encountered. It outlines potential directions for future research and underscores the contributions made by the current study.

## Chapter 2 Literature Review

### 2.1 Introduction

This chapter aims to summarize and analyse key areas of previous research on courtyards. I begin by discussing the definition of courtyard architecture and its historical development (Section 2.2.1), clarifying the evolution of courtyards across different eras and their sociocultural significance. Considerable research has been conducted on various aspects of microclimates within courtyards. Previous works have discussed the influence of geometry, orientation, wall materials, and landscape elements such as ponds, trees, and grass on courtyard microclimates (Andreou, 2013, 2014; Taleghani et al., 2014; Al-Hafith et al., 2017; He et al., 2021; Sun et al., 2021; Zhu et al., 2023). Numerous factors influence the microclimate and thermal environment of courtyards, among which shading and natural ventilation play particularly significant roles. Numerous studies have demonstrated that the geometry and orientation of courtyards decisively affect the efficiency of shading (Section 2.2.2) and natural ventilation (Section 2.3.1). In strategies for passively improving the microclimate of courtyards, natural ventilation mechanisms play a central role, including unilateral ventilation and cross ventilation, both of which have received corresponding research attention (Section 2.3.2).

Furthermore, altering the geometric shape of courtyard buildings is a common practice for optimizing the microclimate and enhancing thermal comfort. However, studies on changes in roof design are relatively scarce. This section investigates the impact of different roof styles on the wind environment and how these designs can be applied to courtyard buildings to promote more effective aerodynamic characteristics (Section 2.4). Natural landscape elements in courtyards, such as vegetation and water bodies, play a crucial role in

regulating the microclimate. Water bodies can effectively lower temperatures and increase relative humidity (Section 2.5), while vegetation improves the microclimate through shading and enhancing transpiration (Section 2.6).

One major issue that may arise from natural ventilation in courtyards is the diffusion of pollutants within buildings, a challenge that cannot be overlooked. In subsequent sections, we will explore methods of studying the diffusion of pollutants within courtyard buildings using Computational Fluid Dynamics (CFD) and wind tunnel experiments, including pollution distribution from single buildings to blocks and even city scales (Section 2.7). Finally, by summarizing the limitations of existing research, we provide a theoretical foundation and directions for future research in subsequent sections (Section 2.8).

## 2.2 Courtyards

### 2.2.1 The definition and historical development of courtyards

Courtyards are typically bounded open spaces, situated under the sky and surrounded by buildings or walls. This space is both private and connected to the outside, with flat ground shaped by the contours of architecture (Brian et al., 2005). The Cambridge Dictionary's definition of a courtyard aligns with this, describing it as a flat area of ground that is partly or completely surrounded by the walls of a building, highlighting the interplay and integration between man-made structures and the natural environment. Rapoport (2007) notes that the courtyard strategy has been a longstanding element in architectural history and is commonly found as a design feature in many places around the world. Zhu et al. (2023) categorize courtyards into five distinct types, as illustrated in Figure 2.1, encompassing one enclosed courtyards and four semi-enclosed variants (Chatzidimitriou & Yannas, 2017; Meng et al.,

2016; L. Yang et al., 2020). Notably, the parallel courtyard type is commonly referred to as the canyon. This study concentrates primarily on the enclosed courtyards for both CFD analysis and experimental investigations.

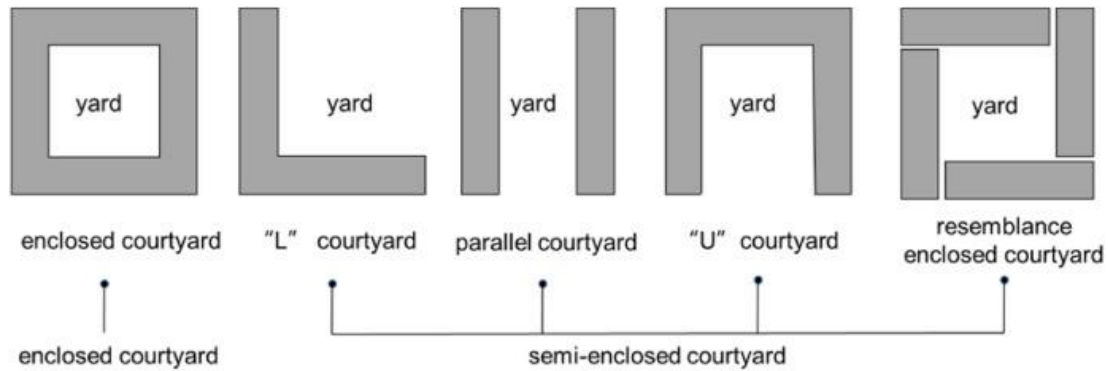


Figure 2. 1 Courtyard forms for enclosed courtyard and semi-enclosed courtyards (Meng et al. 2016).

Residential courtyards have evolved significantly over time, influenced by various cultures and civilizations for their thermal benefits and privacy features. Taleghani et al. (2012) outline several key stages in the evolution of residential courtyards, tracing their origins from ancient civilizations in North Africa to China. Early examples include the troglodyte villages of Matmata in southern Tunisia and underground settlements in Hunan, China, which showcase the initial forms of courtyard architecture. Ancient Greek and Roman civilizations subsequently adopted courtyard designs in their residences, leveraging their thermal benefits to adjust for seasonal sunlight. During the medieval period, courtyard architecture became prevalent in the Mediterranean region, particularly within Islamic culture, where courtyards were appreciated for their thermal advantages and enhanced privacy. Notable examples include Persian four-season houses and Arabic minimalist residences. By the late 19th century, the Spanish Colonial Revival movement in Southern California further

promoted courtyard architecture in North America, a design style that remains popular worldwide today. Figure 2.2 illustrates early courtyard buildings around the world.

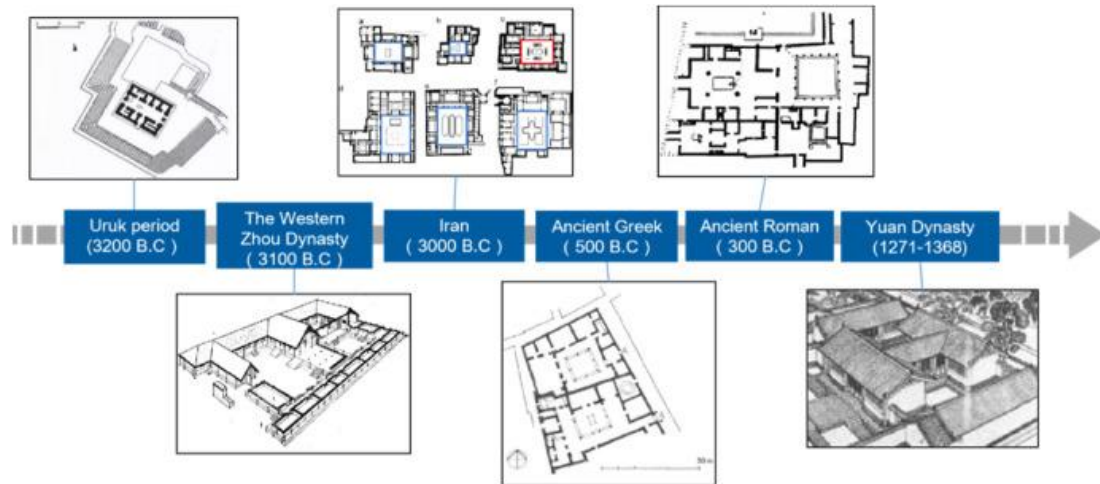


Figure 2.2 Early courtyard buildings around the world (Zhu et al. 2023).

## 2.2.2 The influence of courtyard geometry and orientation on microclimate and thermal performance: the role of shading

The geometry and orientation of courtyards play a critical role in shaping their microclimate and thermal performance, particularly through shading.

Shading in courtyards is crucial for reducing temperatures and influencing buildings' thermal performance and energy consumption, especially in tropical and arid climates. Taleghani et al. (2015) compared three architectural forms (courtyards, pavilions, and ordinary buildings) on the hottest day in the Netherlands by monitoring the outdoor air temperature. They concluded that courtyards provide better microclimate conditions than the other urban forms. During high-temperature periods in summer, solar radiation becomes a

key factor affecting outdoor comfort. Therefore, effective shading measures are essential for mitigating outdoor overheating. Ratti et al. (2003) suggested that courtyard buildings can act as sun protection in some places and serve as solar collectors in other areas. Consequently, designers need to select the appropriate geometry and orientation for buildings and their courtyards to optimize shading (Forouzandeh & Richter, 2019; Manioğlu & Oral, 2015; Yaşa & Ok, 2014).

The height-to-width ratio of courtyards significantly affects their thermal performance and comfort levels. Martinelli & Matzarakis (2017) conducted a comprehensive analysis of how this ratio influences outdoor thermal comfort and the sky view factor in Italian courtyards. They simulated thirty courtyards with varying proportions and found that deeper courtyards significantly enhance thermal comfort. Figure 2.3 illustrates their design factors of different height/width proportions and sky view factors. According to their research, higher H/W ratios (4:5 to 5:5) are suitable for warmer climates, while lower H/W ratios (3:5 to 4:5) are better for cooler climates. The proportions affect the sky view factor and the amount of solar gain in the courtyard.

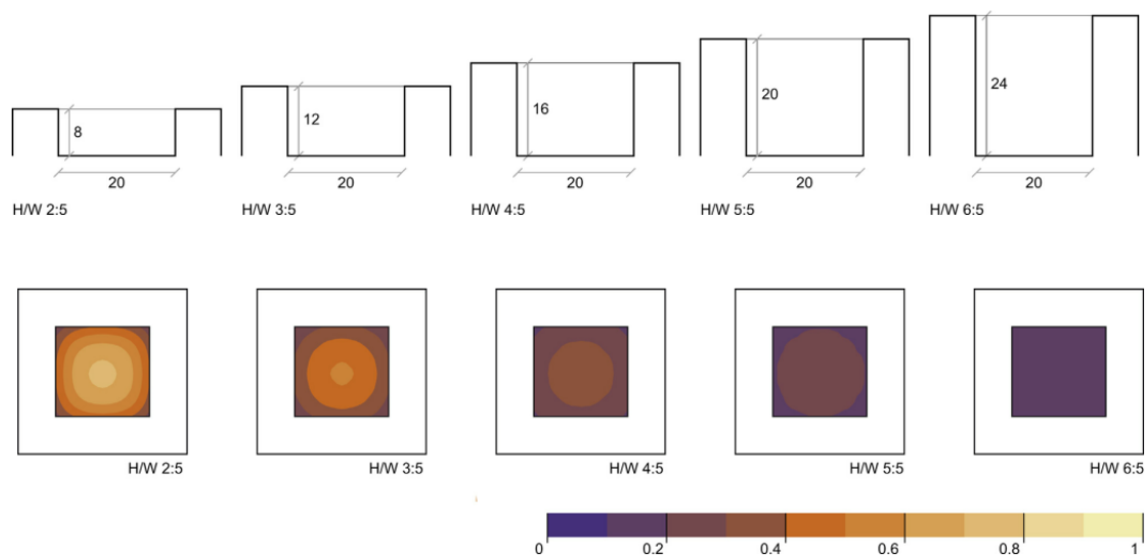


Figure 2.3 Different height/width ratio and sky view factors of courtyards (Martinelli and Matzarakis 2017).

Aspect ratios in courtyards also impact airflow patterns and ventilation efficiency. Rojas et al. (2012) found that in enclosed courtyards, when the aspect ratio is less than 0.3, airflow lines are clear with no vortex formation. However, at a ratio of 0.3, elliptical vortices appear, reducing wind speed and ventilation efficiency, making it suitable for cold climates. Other studies Martins et al. (2016), Xiong et al. (2022) and López-Cabeza et al. (2023) note that although hot air may enter the courtyard, increasing wind speed can reduce overnight overheating, and semi-open courtyards perform better in hot and humid climates. A high aspect ratio, while reducing daylight and ventilation, can also provide wind protection (Oke, 1988). Yang et al. (2020) revealed through CFD simulation that the optimal aspect ratio for ventilation and air quality in courtyards is between 0.5 and 1.

Proportions and courtyard design directly influence thermal and ventilation performance. Salameh & Taleb (2017) employed the IES VE to simulate the thermal and ventilation performance of the courtyard at a range of proportions. Furthermore, three scenarios were selected (i.e., the courtyard widths of 0, 2x and 3x), and one of the rooms was taken as the test room. As revealed from their finding, the courtyard with 2x width outperformed the other two cases in better thermal and ventilation performance.

The integration of shading strategies with courtyard geometry can significantly enhance thermal comfort. Rodríguez-Algeciras et al. (2018) investigated the thermal dynamics of courtyard architecture in Camagüey, Cuba, highlighting how aspect ratios, orientation, and shading strategies collectively influence thermal comfort (shown in Figure 2.4). Simulations



using the RayMan model reveal that courtyards with larger aspect ratios and orientations deviating from the east-west axis substantially mitigate heat, with shading playing a pivotal role in enhancing these effects. The research underscores the critical impact of shading in reducing direct solar exposure, thus significantly improving outdoor thermal conditions. These insights serve as a practical guide for the architectural design and modification of urban courtyards, aiming to optimize thermal comfort in warm-humid climates through strategic use of shading.

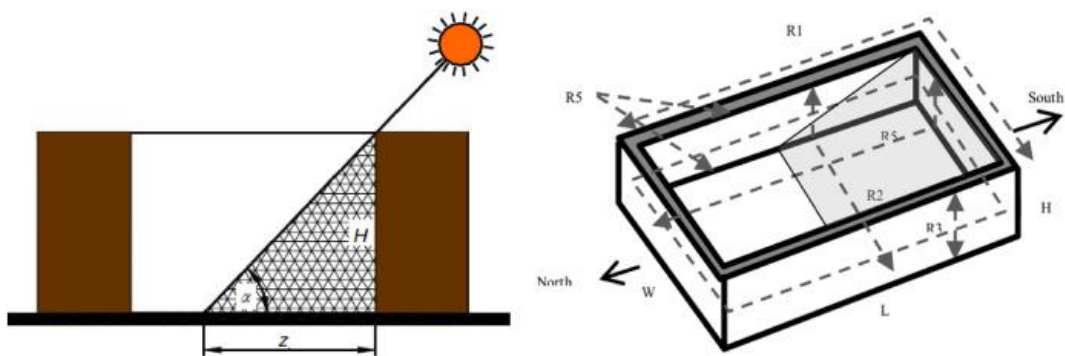


Figure 2.4 Geometry impact for shading influenced the courtyard, from (Rodríguez-Algeciras et al. 2018) and edited by (Zhu et al. 2023).

Orientation plays a crucial role in the thermal performance of courtyards and has been extensively examined in various studies. In hot and dry regions like Iran, optimal orientations such as north-south, northeast-southwest, or northwest-southeast are commonly used to enhance living spaces during both summer and winter (Jamei et al., 2016).

Proper orientation of courtyards can significantly enhance thermal conditions by optimizing sunlight exposure and shading. Research has shown that south- and west-facing courtyards provide better thermal comfort, while incorrect orientations can reduce it (Meir et al., 1995). The impact of courtyard orientation on shading and thermal comfort across diverse climates highlights the importance of strategic orientation. By simulating various orientations,

it has been found that specific configurations enhance thermal efficiency, particularly by maximizing winter sunlight and summer shading (Muhaisen, 2006). Shown in Figure 2.5.

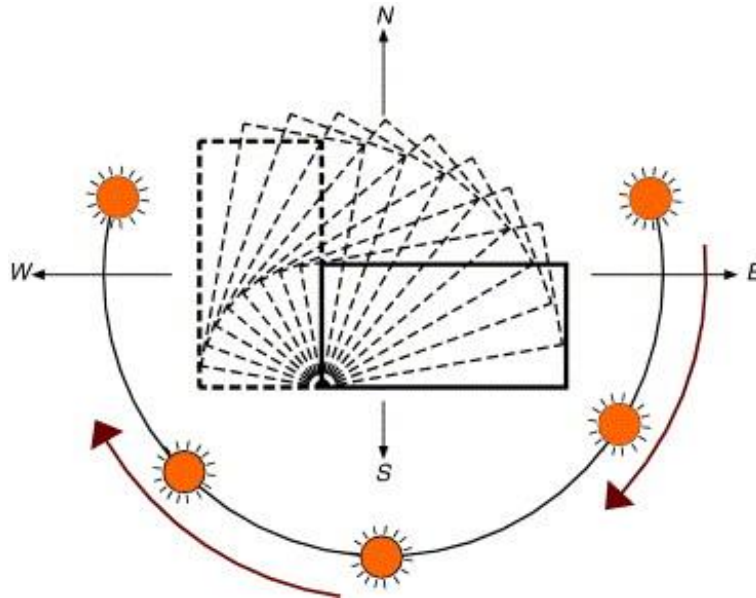


Figure 2.5 Change of courtyard orientation from 0° to 90° (Muhaisen 2006).

Furthermore, material characteristics significantly affect the microclimate of courtyards. Key factors such as thermal mass, material conductivity, surface albedo, and courtyard height influence the thermal environment. Thermal mass absorbs heat when the surrounding temperature exceeds it and releases heat when the temperature drops. Increasing material conductivity improves heat flux into the ground or interior area, while regulating surface albedo impacts solar radiation absorption and air temperature (Yang et al., 2012). Among these factors, the height of the courtyard most noticeably affects the thermal environment, with increased height reducing solar gain and impacting thermal conditions.

Energy efficiency in courtyard buildings can be optimized through strategic design and material selection. Studies have shown that traditional courtyard models can achieve significant reductions in total energy consumption by maintaining original building materials.

Optimized courtyard designs have been found to further enhance energy efficiency, presenting notable reductions in annual energy consumption compared to traditional buildings (Al-Masri & Abu-Hijleh, 2012).

These insights collectively highlight the importance of courtyard orientation, material characteristics, and strategic design in enhancing thermal performance and energy efficiency in courtyard buildings.

### 2.3 Ventilation dynamics in courtyard buildings: modes and strategies

Ventilation systems in courtyard buildings can be categorized into mechanical ventilation and natural ventilation. Mechanical ventilation ensures a stable and controllable air exchange rate using equipment like fans, ducts, and air conditioning systems. This method includes supply ventilation (introducing fresh air), exhaust ventilation (expelling indoor air), and mixed-mode ventilation (balancing air quality and temperature). However, natural ventilation relies on natural forces such as wind pressure differences and thermal buoyancy to exchange indoor and outdoor air, offering higher energy efficiency and lower costs. It includes wind-driven ventilation (using pressure differences), thermal buoyancy ventilation (due to temperature-induced air density changes), and a combination of both.

The efficiency of natural ventilation depends on architectural design, surrounding environment, and indoor-outdoor temperature differences. Effective design can maximize natural ventilation, reducing energy consumption and improving indoor air quality.

Understanding the dynamics of these ventilation modes is essential for optimizing microclimate and thermal comfort in courtyard buildings, ensuring energy efficiency and occupant well-being.

### 2.3.1 The influence of courtyard geometry and orientation on microclimate and thermal performance: the role of natural ventilation

The effectiveness of a courtyard's microclimate and thermal comfort is significantly influenced by its natural ventilation capabilities. This is primarily governed by the stack effect, external wind conditions, and the temperature differential between indoor and outdoor environments. Factors such as the direction of prevailing winds, courtyard design, facade openings, and architectural elements like wind towers play crucial roles (Zhu et al., 2023).

Air movement within courtyards has a considerable impact on their thermodynamic properties, creating distinct microclimatic conditions. The geometric shape of courtyards affects airflow patterns, with variations leading to unique ventilation dynamics. Courtyard buildings, compared to other types, exhibit distinct airflow characteristics due to temperature differences between the interior and exterior, and between the lower and upper parts, which induce a stack effect facilitating vertical air movement (Rajapaksha et al., 2003).

The shape of courtyards is essential for regulating airflow and allowing sunlight, thereby affecting the microclimate and determining heat absorption and release efficiency (Gao et al., 2012). Internal courtyards can enhance natural ventilation efficiency and heat dissipation depending on the building's design (Rojas et al., 2012). Additionally, the orientation of courtyards influences heat dissipation effectiveness.

Courtyard architecture features a dynamic top-to-mid airflow ratio, quantifying the interaction of internal air currents with those passing above. Courtyards with greater length relative to height exhibit a shift from restricted swirling motion to dynamic air exchange, promoting continuous air movement and enhancing environmental air quality. In contrast, smaller length-to-height ratios sustain internal circulation patterns that may hinder effective air exchange (Moonen et al., 2011). As depicted in Figure 2.6.

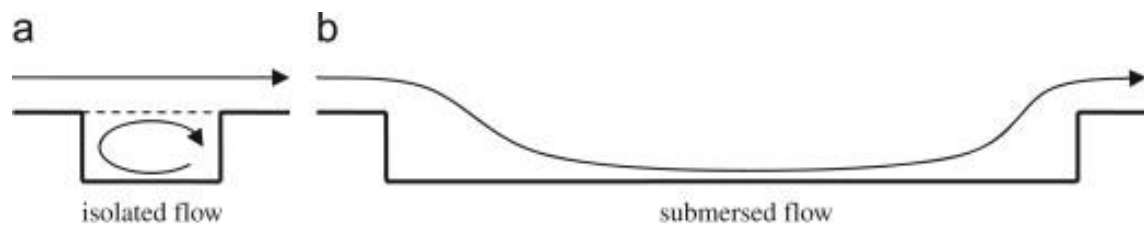


Figure 2. 6 Flow patterns along the courtyard in different length-to-height ratios ((Moonen et al., 2011).

Velocity profiles within courtyards of varying depths are tied to specific wind recirculation patterns. As depicted in Figure 2.7. Shallow courtyards demonstrate minimal recirculation, while moderate-depth courtyards display prominent recirculating eddies that enhance ventilation through continuous vertical velocity gradients. Deep courtyards, however, create stagnant air zones near the ground due to aloft recirculating eddies, resulting in a pattern of negative velocity aligned with the recirculation (Hall et al., 1999a).

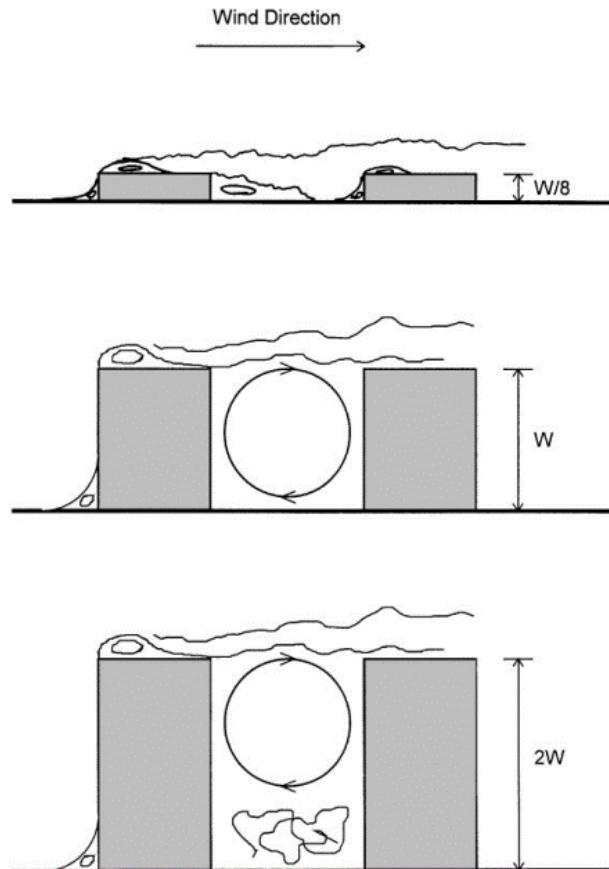


Figure 2. 7 Three types of flow patterns in courtyards of different depths (Hall et al., 1999a).

Understanding and optimizing courtyard designs for effective ventilation and microclimate control involves recognizing the key role of airflow in their thermodynamic behaviour. The geometric form of courtyards induces various airflow patterns, each demonstrating unique ventilation performance under different climatic conditions. Appropriate geometric layout and orientation can significantly reduce thermal loads, while the proper distribution of airflow within courtyards directly enhances overall air quality (Gao et al., 2012).

Courtyard buildings possess unique airflow characteristics that differ from other architectural forms, creating a stack effect influenced by indoor-outdoor temperature differences (Rajapaksha et al., 2003).

Field studies, such as those by Yakubu & Alibaba (2018) in northern Nigeria, have shown that larger courtyards, particularly those centrally located, enhance airflow and natural ventilation. This can reduce the need for cooling and heating equipment in hot and humid climates. Semi-enclosed courtyards, compared to enclosed ones, offer more effective ventilation by enhancing wind circulation, which helps dissipate heat and mitigate nocturnal overheating (López-Cabeza et al., 2023).

Figure 2.8 illustrates natural ventilation and heat exchange in courtyards. During the day, temperature differences between various surfaces of the courtyard building lead to heat exchange, resulting in thermal convection (Yang et al., 2012). Figure 2.8 illustrates natural ventilation and heat exchange in courtyards. During the day, temperature differences between various surfaces of the courtyard building lead to heat exchange, resulting in thermal convection (Yang et al., 2012). Natural ventilation under wind pressure creates a complex temperature distribution in courtyards. Rajapaksha et al. (2003) compared CFD numerical results with monitored temperature data in a Spanish hotel courtyard, showing significant differences in flow patterns between semi-enclosed and enclosed courtyards. Internal courtyards can optimize natural ventilation efficiency to reduce indoor overheating. Zakaria et al. (2015) conducted smoke tests in traditional Malaysian house-Chinese shophouses, revealing three airflow patterns in and around the courtyard (Figure 2.9). During the day, prevailing winds facilitate cross-ventilation from the backyard to the front yard. Increased

wind speed can create vortices, enhancing ventilation. At night, cold air flows downward into the courtyard, driven by nighttime temperature differences (Zakaria et al., 2015).

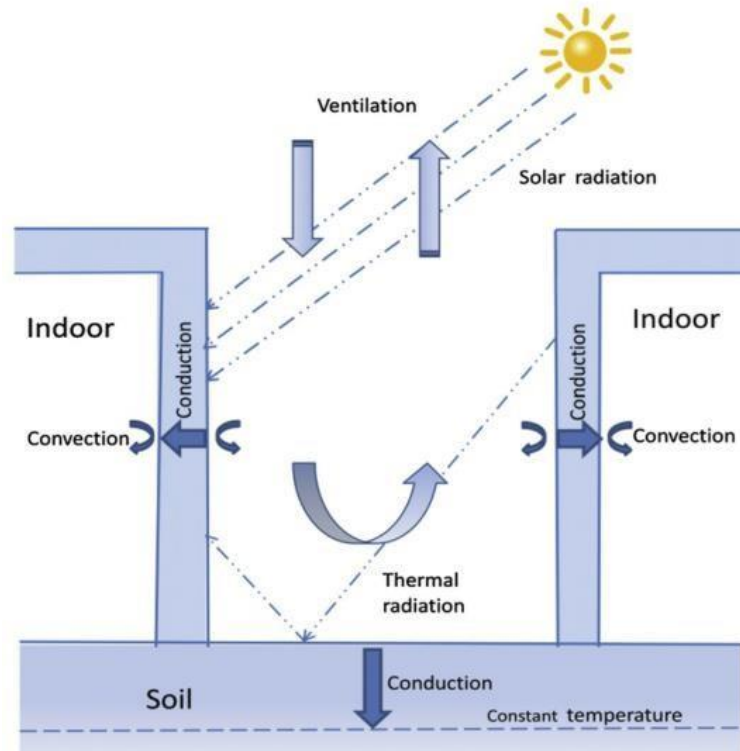


Figure 2. 8 The ventilation and heat exchange within the courtyard (Yang 2012).

These studies collectively highlight the importance of courtyard geometry and orientation in enhancing natural ventilation and thermal performance, underscoring the need for strategic design to optimize microclimatic conditions.



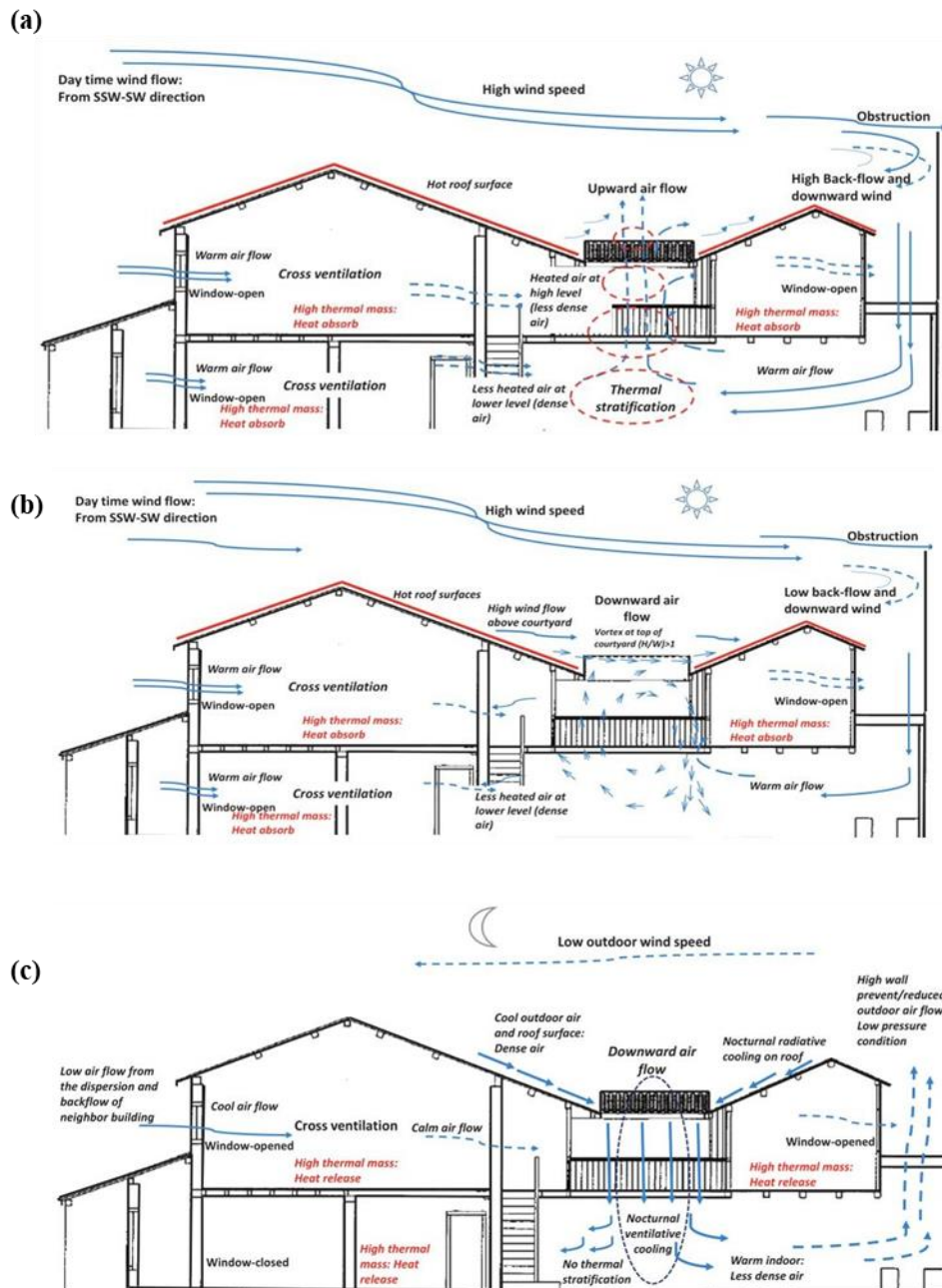


Figure 2. 9 Airflow diagrams of a traditional Malaysian house - Chinese shophouse ((Zakaria et al., 2015).

### 2.3.2 Ventilation strategy for courtyards

Effective ventilation strategies in courtyard architecture primarily include single-sided ventilation and cross ventilation. Single-sided ventilation relies on openings on one side of

the building, utilizing pressure differences to facilitate airflow. This method is effective in narrower spaces where air can move in a straight path. Conversely, cross ventilation uses strategically placed openings on opposite or adjacent walls to create dynamic airflow. Wind pushes air into the courtyard on one side, allowing warmer air to exit from the other, leveraging natural wind patterns and temperature gradients to enhance thermal comfort by removing excess heat and providing fresh air.

Cross ventilation significantly increases the ventilation rate compared to single-sided ventilation. Studies have shown that wind-driven ventilation benefits greatly from the pressure difference between the windward and leeward sides of a structure (Gough et al., 2020; Zhong et al., 2022). Similarly, this fact applies to the efficiency of single-sided ventilation in courtyard buildings, where airflow shows a similar pattern. Tablada et al. (2005) simulated these strategies in courtyard buildings, finding that single-sided ventilation results in lower indoor airflow speed than cross-ventilation. From a thermal perspective, rooms with single-sided ventilation experience less temperature variation, with ground-floor rooms feeling cooler than top-floor rooms. Solar protection is crucial for maintaining stable temperatures in these rooms. In contrast, cross-ventilated rooms achieve higher thermal comfort due to faster airflow, especially on the top floors.

In hot and humid climates, the stack effect in courtyards enhances air movement and heat removal, and strategically positioned openings to the north and south can facilitate cross ventilation (Baboli et al., 2015). Zhang et al. (2020) investigated that both Reynolds-Averaged Navier-Stokes (RANS) and Large Eddy Simulation (LES) models observed significant decreases in ventilation rates when the wind direction shifted from head-on to

lateral. For single-sided ventilation, the reduction was substantial, while for cross-ventilation, the decrease was less severe but still notable.

Optimal courtyard designs for ventilation involve an aspect ratio of 1:2, openings aligned within 0 to 20 degrees of prevailing winds, and an opening area constituting 15-30% of the facade, enhancing natural airflow and occupant comfort (Subhashini & Thirumaran, 2020) However, in hot, dry climates, maintaining continuous natural ventilation through windows may not be as thermally effective as keeping buildings closed to mitigate overheating.

These strategies highlight the importance of careful design in enhancing natural ventilation and improving thermal comfort in courtyard buildings. By understanding the dynamics of single-sided and cross ventilation, architects can optimize airflow and create more comfortable living environments.

## 2.4 Impact of roof design on aerothermal performance

The design of courtyard architecture significantly impacts its microclimate and thermal environment, with roof design playing a pivotal role in influencing airflow within courtyards. The shape of the roof can alter wind patterns, either aiding ventilation or creating zones of higher pressure that restrict air movement. Sloped roofs may channel air down into the courtyard, promoting a refreshing breeze, while certain designs may create stagnant hot air pockets, exacerbating heat within the courtyard.

Research has shown that different roof designs influence ventilation efficiency and indoor climate control in various environments. For example, Mahdavinejad & Javanroodi (2016) found that domed roofs maintain lower indoor temperatures compared to flat, vaulted, or pitched roofs in Tehran's hot and humid climate. This is due to enhanced heat dissipation through convection and thermal radiation facilitated by the curved surfaces of domed roofs, which create higher pressure differences and more efficient airflow.

Studies have shown that roof design affects both airflow patterns and pollutant distribution in urban areas (Asfour & Gadi, 2008). demonstrated that vaulted roofs improve airflow rates and redistribute internal air currents effectively. Similarly, Peren et al. (2015) showed that straight and convex roof geometries significantly enhance wind-driven ventilation by maximizing under-pressure in the building's wake, improving indoor airflow and natural ventilation potential. As illustrated in Figure 2.10. It was revealed that straight or convex roofs can enhance cross-ventilation significantly. The study used the steady SST  $k-\omega$  turbulence model, validated against Particle Image Velocimetry (PIV) measurements from prior research.

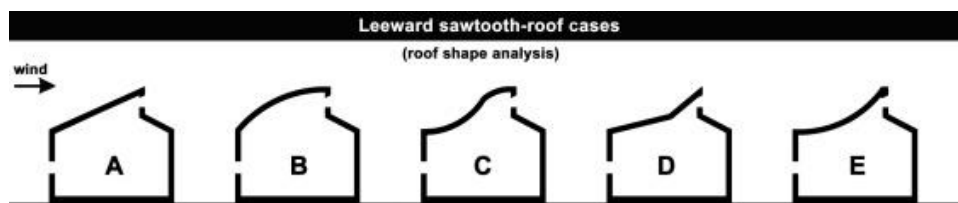


Figure 2.10 Leeward roof shapes analysed in (Peren et al. 2015).

Further studies have highlighted the importance of roof angles and obstacle heights in optimizing airflow. Zobaied et al. (2022) found that steeper roof pitches increase air velocity at openings due to pressure variation, while higher internal obstacles alter airflow direction

and increase internal pressure. This aligns with findings by Moey et al. (2021) and Perén et al. (2015), who concluded that steeper roofs combined with lower obstacles improve ventilation rates. Esfeh et al. (2021) revealed that the efficiency of semi-cylindrical curved roofs is highly sensitive to wind direction, with the highest airflow achieved at a 0° wind angle. Roof height also affects internal air recirculation, indicating that curved roofs can be as effective as wind-catchers for natural ventilation.

The role of roof architecture in airflow dynamics and pollutant distribution is also significant in urban street canyons. Takano & Moonen (2013), alongside the study of Yassin (2011) found that increased roof slope improves airflow and reduces pollution, with lower and angled roofs playing a critical role in reducing vehicular emission pollutants.

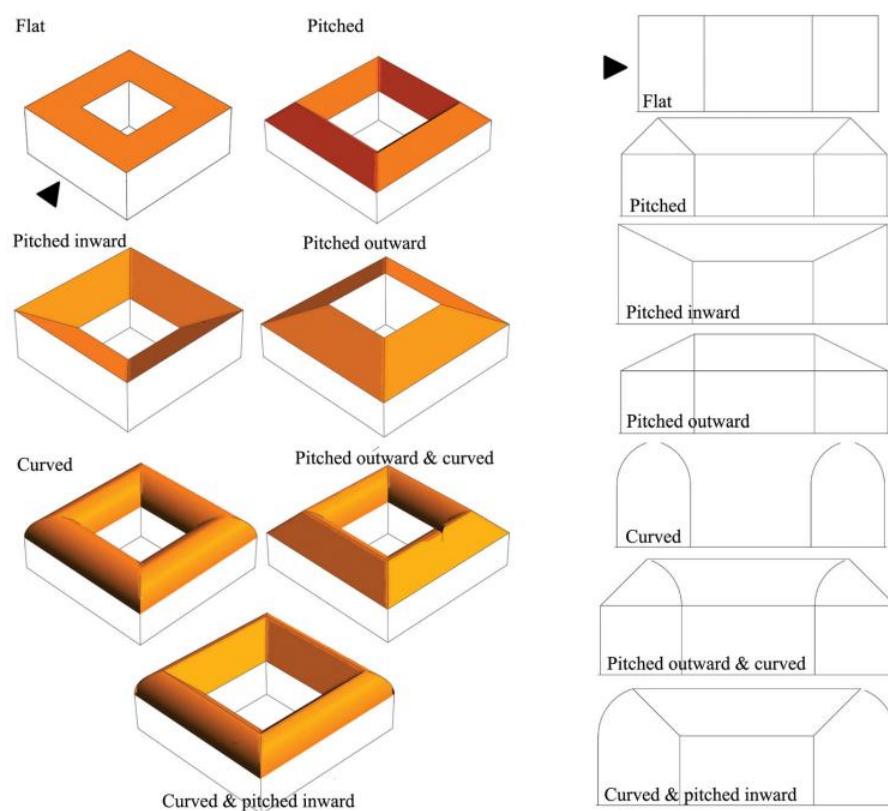


Figure 2.11 Courtyard buildings with different roof shapes and their vertical cross-sectional view (Prakash 2022).

Although much research has focused on isolated buildings, the impact of roof designs on courtyard buildings is less explored. Prakash (2022) examined courtyard design in low-rise buildings, finding that wider courtyards facilitate better air inflow and natural ventilation. The optimal courtyard width should be more than half the building's width to balance ventilation benefits and living space. Roof topology, including flat, pitched, and curved designs, affects airflow, with pitched and inward-curved roofs showing superior performance (Figure 2.11).

## 2.5 Impact of evaporative cooling systems on building microclimates

Evaporative cooling systems offer a significant advantage over vegetation in courtyards due to their pronounced cooling effects. These systems are particularly effective in reducing ambient temperatures in hot and dry regions, where evaporation not only cools but also humidifies the air. The extent of this cooling effect is influenced by factors such as water surface area, air humidity, and water temperature (Sahebzadeh et al., 2018).

In courtyard design, evaporative cooling through water sprayer systems provides a controllable method for reducing overheating and enhancing thermal comfort. Traditional methods, such as planting vegetation or enhancing shortwave reflectance, have year-round effects that can be less controllable. Water spray systems, however, offer precision and efficiency. The study by Sureshkumar et al. (2008) highlights the effectiveness of different nozzle sizes and water flow rates, though field measurements are often complicated by uncontrollable factors like wind. CFD simulations provide a solution, allowing detailed analysis and modelling of spray systems under various conditions.

Optimizing mist spray evaporative cooling systems involves understanding key variables. Research by Montazeri et al. (2017) demonstrates that variables such as inlet air and water temperatures, air humidity, air velocity, and droplet size significantly affect cooling efficiency. Their findings indicate that a temperature difference of 0°C to 8°C between air and water droplets can enhance cooling capacity by over 40%. Furthermore, lower air humidity and water temperatures, combined with higher air velocities and smaller droplets, improve heat and mass transfer, leading to more effective cooling.

In addition to water sprayers, the design of roof cooling systems and air curtain gates plays a crucial role in managing thermal conditions in large spaces like stadiums. Zhong et al. (2021) conducted a detailed study using CFD and Building Energy Simulation (BES) in a simulated environment similar to Qatar World Cup stadiums. Their research identified optimal air supply speeds and temperatures, achieving up to a 15°C reduction on the pitch. Specifically, a roof cooling supply velocity of 25 m/s provided the most comfortable temperature ranges for spectators by effectively blocking hot external air and maintaining lower PMV (Predicted Mean Vote) and PPD (Predicted Percentage of Dissatisfied) indices.

These insights emphasize the importance of precise control and optimization in evaporative cooling systems. By leveraging these systems' capabilities, architects and engineers can create more comfortable and energy-efficient microclimates in buildings and open spaces, tailoring the design to specific environmental conditions and enhancing overall sustainability.

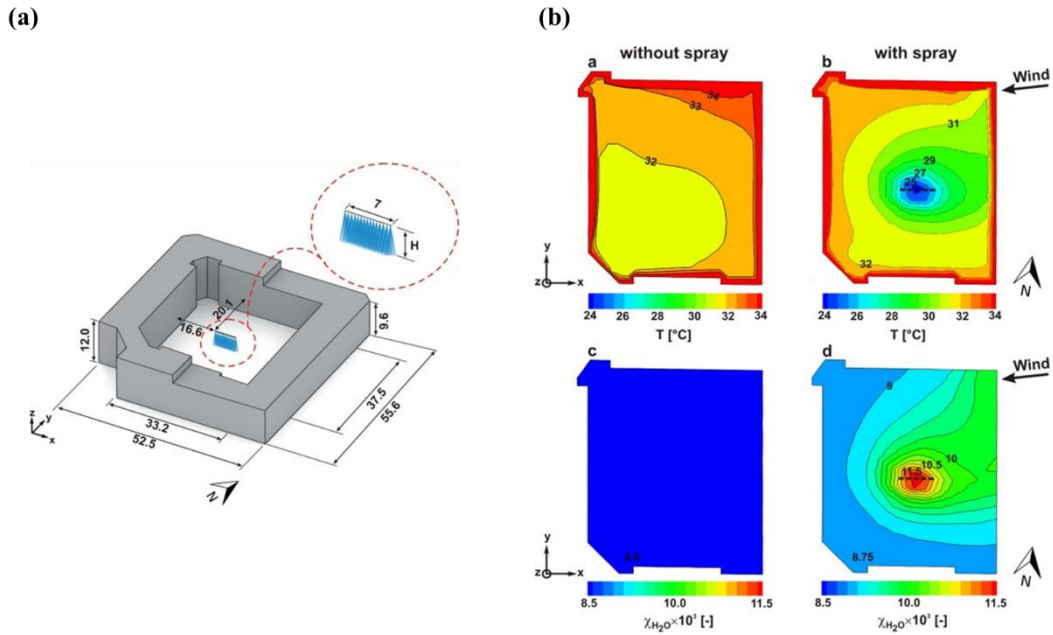


Figure 2. 12 Evaporative cooling system in the courtyard, air temperature, and vapor mass fraction distribution (H. Montazeri et al. 2017).

Evaporative cooling systems, particularly water sprayers, offer significant potential for enhancing thermal comfort in courtyards, though research in this area is limited. As shown in Figure 2.12, Montazeri et al. (2017) conducted a CFD study on the cooling effects of water spray systems in urban courtyards during heat waves. Focusing on a courtyard in Rotterdam, Netherlands, the study used a setup of 15 hollow-cone nozzles and evaluated system performance under varying conditions of water flow rate and system height, validated through wind tunnel experiments.

The study found temperature reductions of up to 7°C at pedestrian height with a water flow rate of 9.0 l/min and a system height of 3 meters. Higher flow rates extended the cooling effects, while increasing the system height from 3 to 5 meters reduced the cooling impact. Additionally, the study incorporated the Universal Thermal Climate Index (UTCI) to assess



heat stress reduction, revealing that well-designed spray systems can significantly mitigate heat stress in urban settings (Montazeri et al., 2017).

These findings highlight the complex interaction between spray characteristics and urban microclimate, providing valuable insights for urban design and the application of sustainable cooling solutions in hot climates. By optimizing these systems, architects and engineers can create more comfortable and energy-efficient microclimates in courtyards and other open spaces.

## 2.6 Impact of vegetation on building microclimates

Numerous studies have explored the impact of vegetation on microclimates, particularly its role in mitigating urban heat island effects. Vegetation influences local climate conditions primarily through shading and transpiration. Shading from trees and plants reduces solar radiation and surface temperatures, creating cooler urban environments. Transpiration, where plants release water vapor into the air, cools the surrounding air by absorbing latent heat. These natural mechanisms highlight the critical role of vegetation in enhancing urban climate resilience, improving thermal comfort, and contributing to sustainable urban development by naturally lowering temperatures in built environments.

The use of CFD to study vegetation's impact on microclimate has provided valuable insights. Mughal et al. (2021) focused on tropical urban environments, using CFD to study a city district in Singapore. They proposed a new numerical model coupling airflow, thermal radiation, heat transfer in porous media, and vegetation modelling. Using OpenFOAM for simulations, they found that vegetation significantly impacts pedestrian thermal comfort. Tall trees with broad crowns were recommended to ensure maximum comfort. Urban parks can

lower local air and surface temperatures, increase relative humidity, and reduce wind speeds. This cooling effect can extend a considerable distance, reducing roof temperatures of nearby buildings. However, the shading effect of trees remains the most significant factor for thermal comfort, mainly benefiting the park area itself (Mughal et al., 2021). Manickathan et al. (2018a) examined the effects of environmental factors and tree properties on the transportation cooling effect of vegetation in urban areas. The study investigates environmental factors such as wind speed, relative humidity, air temperature, solar radiation, and tree properties including stomatal resistance, leaf size, and leaf area density. Additionally, the study examines the impact of vegetation size on the transpiration cooling effect by varying tree height and row spacing. The authors employed a CFD model that modelled vegetation as a porous medium, used a leaf energy balance model to determine heat flux, and studied the cooling effects of single-row trees under various environmental factors and tree properties (Manickathan et al., 2018a). The UTCI was used to estimate the impact of transportation cooling on pedestrian thermal comfort. The study found that pedestrians only perceive the local benefits of transportational cooling at low wind speeds, while vegetation extracts more heat from the airflow at higher wind speeds (Manickathan et al., 2018a).

The effect of green space patch size on urban cooling and humidification was investigated using the ENVI-met urban climate simulation tool. Larger green patches provide better cooling and humidification effects. Specifically, forest patches can lower air temperatures by 0.7-5.7°C and increase relative humidity by 1.3-15.8% compared to surrounding areas. The cooling and humidification effects vary by location and time of day, with larger patches having a greater impact near their centers and during hotter parts of the day. Additionally, larger patches enhance evaporative effects, reducing overall water evaporation in urban environments (Jiao et al., 2017).

The use of vegetation transpiration cooling to mitigate the urban heat island effect in street canyons was modelled in Arnhem, Netherlands. The study found that trees have the greatest cooling effect, reducing temperatures by an average of 0.43°C and up to 1.6°C. Green facades had a smaller effect, reducing temperatures by an average of 0.04°C and up to 0.3°C, while green roofs had no significant effect. The combination of trees and green facades provides the best cooling outcome, as shown in Figure 2.13 (Gromke et al., 2015).

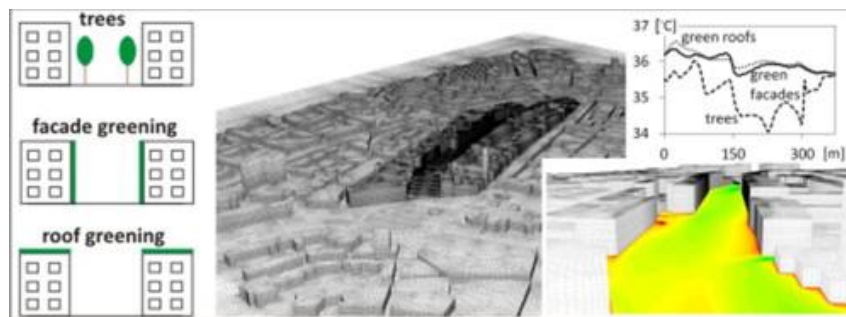


Figure 2.13 CFD analysis of translational cooling by vegetation (Gromke et al. 2015).

These studies underscore the importance of vegetation in urban design. By understanding and optimizing the use of green spaces, urban planners and architects can significantly improve microclimates, enhance thermal comfort, and contribute to more sustainable and resilient urban environments.

Several researchers have studied efficient passive cooling strategies in hot climates by adding vegetation to increase humidity and improve microclimates in courtyards. An appropriate evapotranspiration mechanism can cool the surrounding environment through plant transpiration. Planting large areas with vegetation is an effective approach to improve courtyard microclimates. Utilizing the transpiration effect and shading of different types of vegetation can significantly lower air temperatures in courtyards.

Improving outdoor thermal comfort by increasing vegetation cover in urban courtyards in hot and arid areas has been demonstrated through various studies. Salata et al. (2015) used ENVI-MET software to simulate and validate models with field measurements. Their study, which included five scenarios with different vegetations and materials, compared results on air temperature, mean radiant temperature, relative humidity, and wind speed. They found that vegetation reflects direct shortwave radiation, and its transpiration effect can reduce ambient air and average radiation temperatures, decreasing outdoor PMV by 1.5 in summer. Further research by Zango et al. (2017) examined air temperature differences in a Chinese-shop house in Malacca with varying vegetation percentages (18% and 69%) within the same courtyard area. They observed a 3°C difference between the courtyards, highlighting vegetation's ability to regulate temperature.

Shashua-Bar et al. (2009) analysed outdoor cooling landscape strategies in hot arid regions, using six landscape strategies with different combinations of trees, lawns, and overhead shade mesh in two semi-enclosed courtyards. Their findings showed that courtyards treated with shade trees and grass could reduce daytime temperatures by 2.5 K. More recently, Mohammadi et al. (2020) evaluated the cooling effect of vegetation in sky courtyards. They found that trees located in high-rise courtyards could lower air temperatures by 0.3°C to 1°C, depending on the volume of vegetation. This model is illustrated in Figure 2.14.

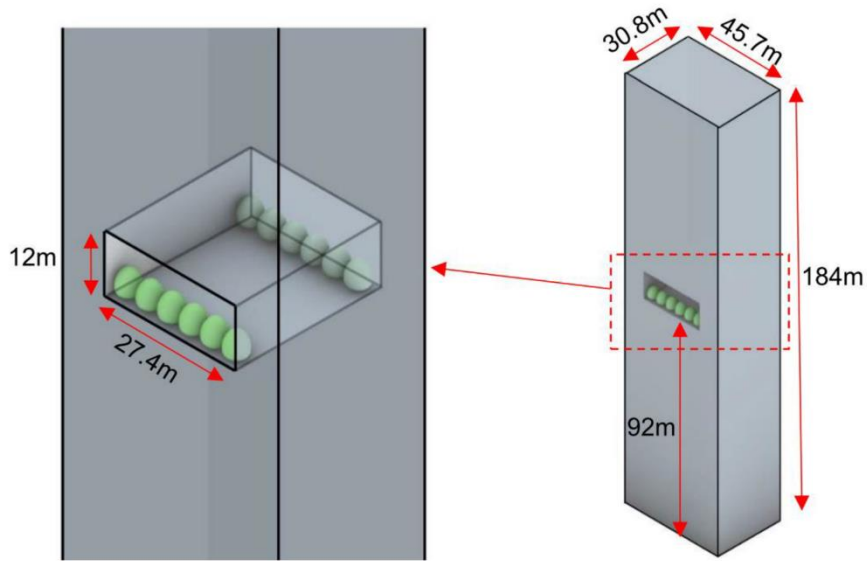


Figure 2. 14 Skygarden with trees model (Mohammadi et al., 2020).

These studies collectively underscore the importance of vegetation in urban design, demonstrating how various planting strategies can significantly enhance thermal comfort and create more sustainable urban environments. By understanding and optimizing the use of vegetation, urban planners and architects can effectively improve microclimates and overall urban resilience.

## 2.7 Pollutant dispersion studies: courtyard building and wind tunnel insights

### 2.7.1 Pollutant dispersion within courtyard buildings

The design of courtyards significantly influences air quality and pollutant dispersion. Geometry and orientation impact internal airflow dynamics, affecting pollutant concentrations and overall air quality.

Effective courtyard design can enhance air quality and control airborne diseases. Leng et al. (2020) demonstrated that increasing courtyard width from 5.8 meters to 11.8 meters can reduce average air pollutant concentration by 80%, though it increases draught sensation by 30%. In static wind conditions, the infection risk in courtyards can be comparable to indoor environments during the COVID-19 crisis, with risk values up to 3%. These findings highlight the importance of wide courtyards in reducing pollution and infection risk, while also suggesting the need for artificial measures like outdoor ventilators or air cleaning devices to ensure a safe environment (Figure 2.15). However, it also suggested that purely passive architectural strategies may not be sufficient to mitigate person-to-person pollutant transmission in varied climate conditions, advocating for the integration of artificial measures like outdoor ventilators or air cleaning devices to ensure a safe and healthy courtyard environment (Leng et al., 2020).

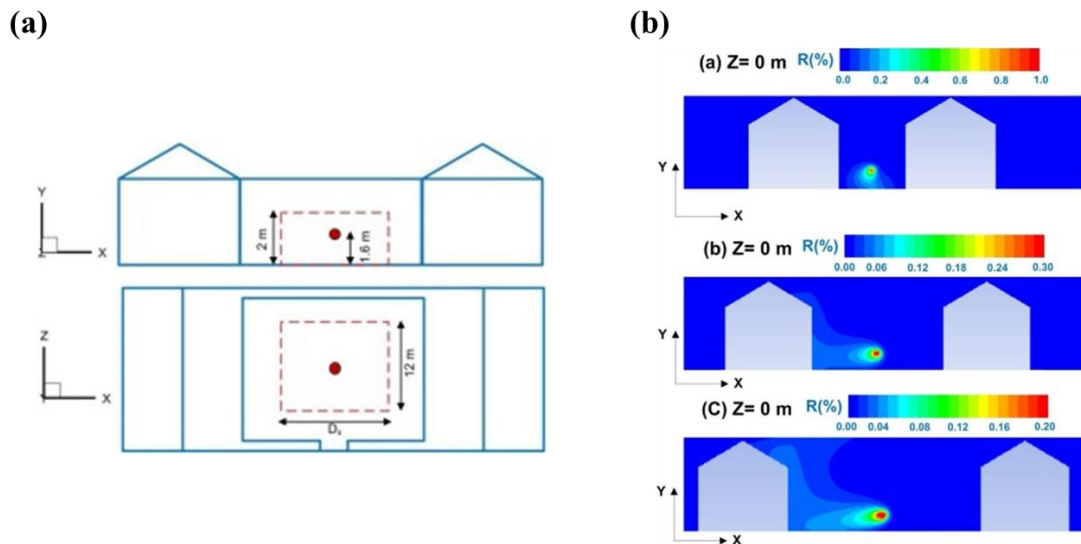


Figure 2. 15 Location of airborne pollutant sources and CFD simulation of pollutant dispersion with varying courtyard widths (Leng et al., 2020).

The configuration of courtyards plays a crucial role in pollutant dispersion. Trindade et al. (2021) emphasized that central and internal courtyards are effective in mitigating pollutant concentrations at pedestrian levels. Various architectural layouts influence pollutant dispersion by modifying airflow, highlighting the importance of courtyard design in managing air quality.

The shape and elevation of courtyards also affect pollutant dispersion. You et al. (2022) found that certain courtyard designs facilitate the upward movement of pollutants, reducing contamination levels. This insight is valuable for optimizing air movement and pollutant control. In enclosed courtyards, pollution issues are exacerbated by vehicular exhaust. Lozhkin et al. (2018) showed higher concentrations of pollutants in enclosed courtyards compared to open ones, especially on low wind speed days. This underscores the necessity of considering ventilation and pollutant dispersion in courtyard design to prevent pollutant accumulation.

Enhancing ventilation effectiveness is critical for managing pollutant distribution. Nosek et al. (2022) and Moonen et al. (2011) studied how courtyard architecture influences street canyon ventilation. They found that courtyards, especially those with pitched roofs, significantly improve ventilation, directly affecting pollutant distribution and cross-transmission. Moonen et al. (2011) further emphasized the role of courtyard dimensions and geometry in facilitating air renewal and pollutant dispersion.

These studies, combining field measurements and numerical simulations, reveal the significant influence of airflow patterns in courtyard architecture on pollutant dispersion. They explore the interplay between pollutant spread and cross-ventilation within courtyards,

considering potential pollutant accumulation. However, the unique characteristics of courtyards as enclosed or semi-enclosed spaces surrounded by buildings or walls are often overlooked. The connectivity of courtyards with surrounding buildings and internal spaces is a critical factor in pollutant dispersion that requires further investigation (Forouzandeh, 2018).

## 2.7.2 Exploring pollutant dispersion: insights from combined wind tunnel experiments and CFD simulations

### 2.7.2.1 Pollutant dispersion in isolated buildings from previous wind tunnel experiments and CFD simulations

Extensive scholarly work has been conducted on pollutant dispersion near single buildings, primarily employing wind tunnel tests and computational fluid dynamics (CFD) simulations. These studies have significantly advanced our understanding of how pollutants disperse around isolated structures.

Early research by Castro & Robins (1977) involved wind tunnel experiments on the flow around a surface-mounted cube within uniform and turbulent streams, laying the foundation for subsequent studies. Their models and results have been widely used to confirm and extend findings in various new research directions. For instance, Li & Meroney (1983) analysed pollutant dispersion around a cubical building with a flush rooftop vent within a wind tunnel's neutral surface boundary layer, documenting average pollutant concentrations at various positions around the building. Numerous computational simulations followed to replicate these findings, focusing on the influence of turbulence model selection on prediction accuracy.



Further investigations have utilized computational simulations to explore air pollutant dispersion around cubic structures. Li & Stathopoulos (1998) employed standard  $k-\epsilon$  turbulence models to examine the impact of the convergence criterion on the computational solution. Blocken et al. (2008) utilized the commercial software Fluent 6.1 to carry out steady RANS CFD simulations. They examined pollutant dispersion within a neutral, stable atmospheric boundary layer under various scenarios.

Tominaga & Stathopoulos (2009, 2010) scrutinized the predictive accuracy of various RANS models for dispersion around buildings. They compared different  $k-\epsilon$  models and found that the LES model had superior predictive accuracy for pollutant dispersion, a finding corroborated by numerous other investigations. Their research included a comparative analysis between Unsteady RANS and Steady State RANS computational outcomes and empirical results. They evaluated pollutant dispersion around the building by considering three distinct emission source locations: upwind, rooftop, and downwind, highlighting the differential effects of source positioning on pollutant distribution (Tominaga & Stathopoulos, 2017).

In comparative analyses of various turbulence models, CFD simulations have been shown to effectively gauge the impact of pollutant dispersion around isolated buildings, aligning with prior wind tunnel experiments (Figure 2.16). Recent studies, such as those by Guo et al. (2021, 2019), have positioned pollutant release sources on the building's surface, often at the top, to understand the impact of source location on dispersion patterns. These studies found notable discrepancies between wind tunnel test outcomes and CFD results, which could not be mitigated solely by selecting an appropriate turbulence model. Tominaga et al. (1997) investigated pollutant dispersion with the gas source positioned on the leeward

side of a solitary building, specifically at  $0.5 H$  (where  $H$  denotes the height of the building). Later studies by Tominaga & Stathopoulos (2018) and Ma et al. (2022) compared the dispersion predictive abilities of the RANS model and LES for tracer gases using CFD, drawing upon wind tunnel experiments. They assessed results for neutral, light, and heavy gases under varying plume buoyancy conditions.

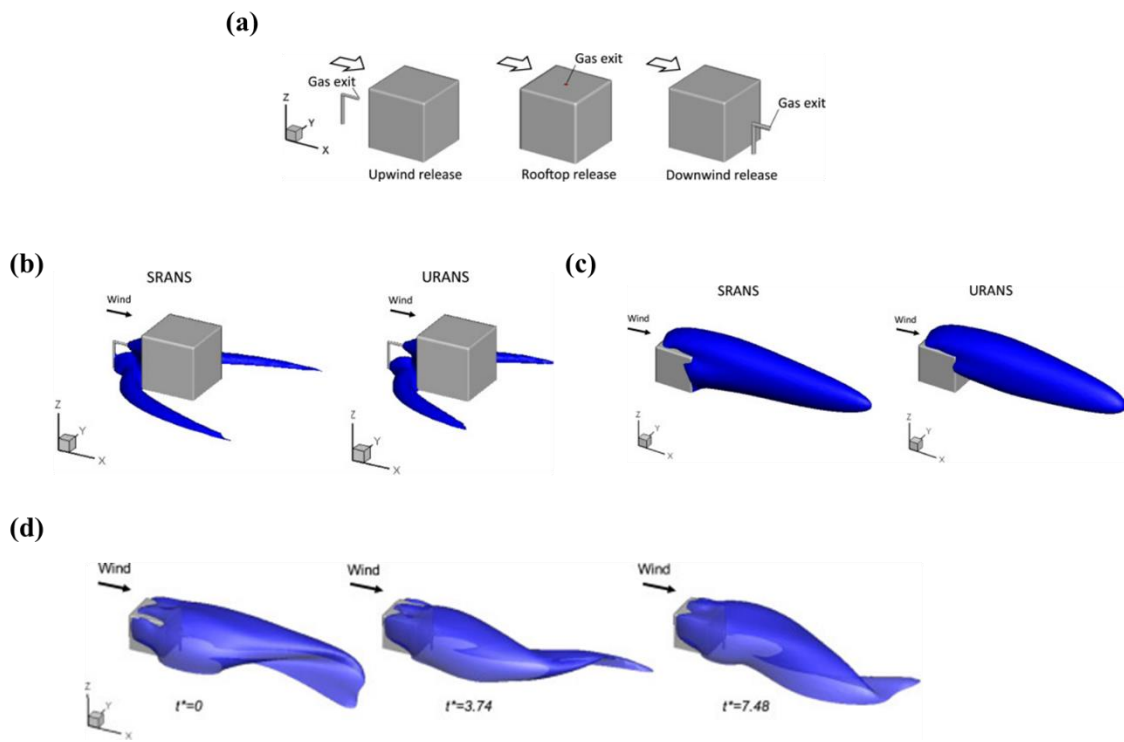


Figure 2.16 Pollutant dispersion scenarios and iso-surface contours for different release points using steady and unsteady RANS computations (Tominaga & Stathopoulos 2017).

These studies collectively highlight the importance of both experimental and computational approaches in understanding pollutant dispersion around isolated buildings. By comparing various turbulence models and considering different emission source locations, researchers can better predict and manage air quality in urban environments.

### 2.7.2.2 Pollutant dispersion in urban buildings from previous wind tunnel experiments and CFD simulations

To mitigate the influence of pollutants on urban environments, accurate simulation and prediction of pollutant dispersion within street canyons have become paramount. Extensive research, primarily through wind tunnel experiments, has been undertaken to model the flow and spread of pollutants from street canyons to building complexes. When investigating structures ranging from a single canyon to building arrays, researchers focus on the interspaces between blocks to examine pollutant dispersion.

Since the 1990s, advancements in CFD technology and computational power have facilitated ongoing comparisons between wind tunnel experiments and CFD simulations. Key studies, such as those by Hunter et al. (1990, 1992), identified the relative Height (H), Width (W), and Length (L) of the canyon as determinants of flow patterns, significantly influencing the vertical mixing of pollutant concentrations. Research has delved into the impacts of pollutant transport models, inflow conditions, canyons, complex structures, and the validation process using diverse turbulence models.

Comparative studies have employed various turbulence models to simulate pollutant dispersion in street canyons. Koutsourakis et al. (2012) compared the  $k-\epsilon$  standard and RNG  $k-\epsilon$  turbulence models for a single street canyon scenario, while Jon et al. (2022) used the standard  $k-\epsilon$  turbulence model to investigate the impact of wind direction on ventilation and pollutant dispersion. Tominaga & Stathopoulos (2011) applied both RANS and LES methodologies in their CFD simulations of pollutant dispersion within a three-dimensional single street canyon, contrasting their results with experimental data (Figure 2.17).

Recent studies have utilized CFD to examine pollutant dispersion around real-life building complexes in urban locales. Trindade Da Silva et al. (2021) explored how diverse urban block configurations influence pollutant dispersion. Using CFD methodologies, they analysed five configurations derived from actual cityscapes: standalone canyons, detached buildings, central courtyards, enclosed courtyards, and linear arrangements. Turbulent effects were simulated via the URANS equation in conjunction with the  $K-\omega$  SST model, validated with wind tunnel experiment data.

Additional research has focused on specific aspects of pollutant dispersion in urban environments. Lateb et al. (2010) implemented RANS models to analyse the spread of pollutants from rooftop chimneys at the weak edges of adjacent towers within a building complex. Carpentieri et al. (2012) quantified mean and turbulent tracer fluxes within authentic street canyon intersection configurations using wind tunnels to investigate turbulent mass exchange processes. Yassin et al. (2022) explored how various roof designs influence wind circulation and pollutant dispersion around buildings, revealing that airflow velocity associated with pitched roofs surpasses that of other forms. They found higher pollutant accumulation on the leeward side of pitched and sloping roofs compared to flat and hip-shaped roofs.

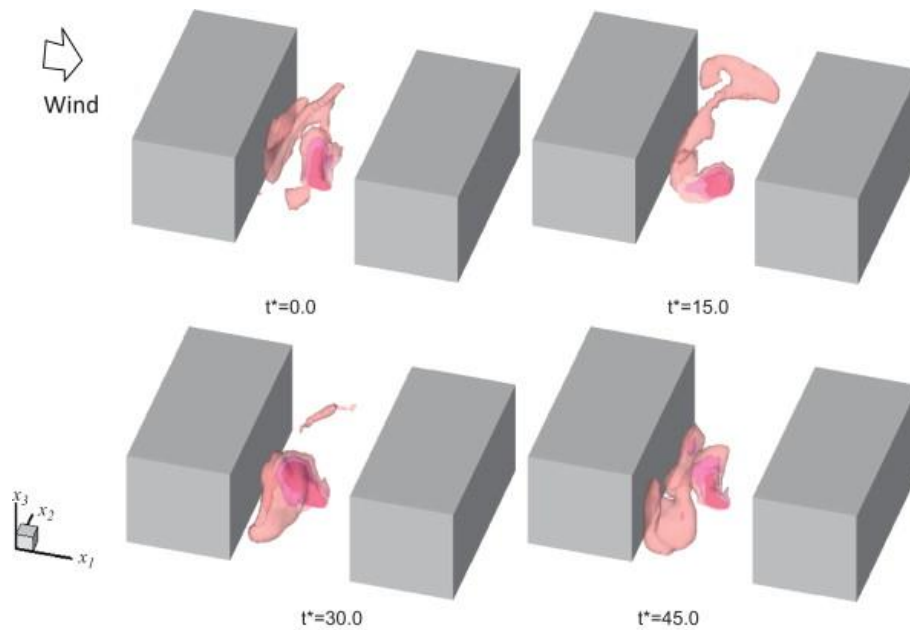


Figure 2. 17 Time series showing the evolution of concentration levels within a street canyon, as modelled by LES (Tominaga & Stathopoulos 2011).

These studies underscore the importance of both experimental and computational approaches in understanding pollutant dispersion in urban environments. By analysing different building configurations and roof designs, researchers can better predict and manage air quality, contributing to healthier urban living conditions.

### 2.7.2.3 Pollutant dynamics for indoor and outdoor dispersion from previous wind tunnel experiments and CFD simulations

Several investigations have leveraged both wind tunnel experiments and CFD simulations to understand the interplay between indoor air quality and natural ventilation, examining pollutant dispersion in both indoor and outdoor contexts. These studies have analysed how external pollution affects indoor air quality, particularly in buildings near street canyons.

Research by Cui et al. (2016) conducted wind tunnel assessments to evaluate the thermal influences on air circulation and pollutant dispersion across diverse scales in urban environments. Pollutants were released from rooftops of windward buildings, with measurements taken inside rooms on the opposite side of the street. Their study revealed a fundamental correlation between temperature and pollution distribution patterns within a street canyon and those within interior spaces, facilitated by cross-ventilation. Additionally, Cui et al. (2021) used smoke visualization experiments under different wind orientations to depict atmospheric pollutant dispersion. Under a  $0^\circ$  wind direction, pollutants clustered in the central street canyon, dispersing downstream and diluting progressively. Conversely, under a  $45^\circ$  wind orientation, the influence expanded significantly, underlining the close association between indoor and outdoor pollutant concentrations.

Further studies have explored the link between street-level pollution and indoor air quality. Santiago et al. (2022) modelled different window opening percentages and locations along with various wind directions. They found that indoor pollutant concentrations declined with ascending floor levels. Similarly, Yang et al. (2015) examined the influence of traffic-generated pollution on air quality within naturally ventilated structures near street canyons, focusing on varying proportions of window openings.

The ingress of outdoor particulate matter into naturally ventilated structures has also been studied. Chu & Yang (2022) employed CFD and Lagrangian particle tracking models to find that the ingress rate of outdoor particulate matter ranged from 7% to 25%, depending on particle size and the distance between the pollution source and the building. Mohammadi & Calautit (2021) explored pollutant transport dynamics from canyon streets to building interiors, considering single-sided and cross-ventilation strategies. For indoor pollutant

generation, several studies using wind tunnel experiments and CFD simulations have investigated the dispersion patterns of indoor-generated pollutants, whether they are disseminated outdoors or transported to other indoor spaces. Tominaga & Blocken (2016) conducted wind tunnel trials focusing on varying opening locations within a structure housing an internal source of pollutants. Their experiments demonstrated that pollutant diffusion is substantially affected by the overall airflow pattern, primarily dictated by the location of the inlet opening.

Van et al. (2017) assessed the validity and applicability of turbulence models, comparing RANS and LES. The study found that LES more effectively replicated parameters such as velocity, turbulent kinetic energy, and volumetric flow velocity. Liu et al. (2010) used wind tunnel tests to study the spread of indoor air pollutants in a high-rise building, focusing on cross-contamination between different units. The results indicated that pollutants could disperse vertically and horizontally, suggesting a risk of cross-contamination in neighbouring units. Chu & Wu (2018) explored factors such as external wind speed, initial pollutant concentration, open area, and interior volume on the transient concentrations and diffusion periods of gaseous pollutants within a two-room building. Bazdidi-Tehrani et al. (2020) examined the impact of different opening shapes on cross-ventilation in a standard isolated building. They found that the effectiveness of cross-ventilation in diminishing pollutant concentration increased with the aspect ratio of the openings.

These studies collectively underscore the complexity of pollutant dynamics in urban environments. By examining the interplay between indoor and outdoor pollutant dispersion, researchers can better understand and mitigate the impacts of pollution on air quality in both contexts.

## 2.8 Research gaps

Previous research on the thermal and wind environment of courtyard architecture has largely focused on the inherent characteristics, such as the geometry and orientation of courtyards, with relatively limited exploration into the integration of passive technologies like evaporative cooling. Even when passive technologies such as vegetation and water bodies are considered, research typically focuses only on their effects within the courtyard, without fully considering their potential impact on the indoor environment of surrounding buildings. Moreover, in studies concerning the geometry of courtyards, discussions on the impact of roof design on the thermal and wind environment within courtyards and their surrounding indoor areas are extremely rare. Previous research on the dispersion of pollutants in courtyard buildings is scarce, particularly the comprehensive application of wind tunnel experiments and CFD methods. Specifically, studies on the entire process of pollutants entering indoors (through courtyards) via natural ventilation are even more scarce. The research gaps are as follows:

1. Previous studies on roof styles primarily examine their effects on wind flow, patterns, and pollution within individual buildings or blocks, with scant regard for indoor thermal efficiency and temperature distribution. This oversight extends to a narrow range of roof styles, leaving a gap in comprehensive analysis and, specifically, the integration of various roof styles in courtyard architecture, where flat roofs are predominantly featured in studies. A notable deficiency exists in investigating the indoor wind and thermal dynamics in courtyard buildings. This study aims to bridge this gap by examining the influence of different roof styles on courtyard microclimates and their subsequent effects on adjacent indoor environments. Concentrating on buildings with single-sided



ventilation, it explores the relationship between roof styles, courtyard configurations, and their indoor impacts. By offering fresh insights and methodologies for designing and improving courtyard architecture, this research seeks to enhance thermal efficiency and overall environmental quality within buildings, thereby addressing the identified research gap.

2. Previous research has limited exploration into the integration of passive technologies like evaporative cooling systems within the courtyards. Furthermore, while the cooling effects of water sprayers in courtyards have been acknowledged, their impact on the indoor thermal and wind environments of surrounding buildings has been scarcely investigated. This oversight extends to a detailed examination of how different ventilation strategies, specifically single-sided versus crossflow ventilation, influence these indoor conditions. This study addresses research gaps by analysing the impact of evaporative cooling systems in courtyard buildings, an area not extensively studied before. It investigates the impact of these systems on both the courtyards themselves and the indoor environments of surrounding buildings. Additionally, it examines the role of courtyard architectural features, such as different ventilation strategies, in improving indoor aero-thermal conditions. These strategies include cross-ventilation (openings on multiple facades) and single-sided ventilation (openings on only one facade). The novelty of this research lies in its examination of how evaporative cooling strategies, combined with specific architectural configurations of courtyard buildings, can improve the microclimate in both outdoor and indoor environments of courtyard buildings. This focus on the interaction between outdoor and indoor spaces and the analysis of ventilation strategies contributes insights for designing urban dwellings that are more comfortable and energy-efficient in hot-dry climates.

3. Some courtyards are decorated with vegetative elements such as trees, flowers, and shrubs, and also embellished with a pond or two, which not only provide beauty and tranquillity, but the combination also provide shade and increase the relative humidity of the court-yard area, acting as a microclimate regulator. The transpiration and the shading of vegetation play an important role in regulating the microclimate of the courtyard. Much research illustrated that the introduction of vegetation in and around buildings positively influences the interior of buildings in terms of thermal comfort. A reasonably arranged vegetation planting pattern can help generate fresh air in the surrounding area. The rational application of vegetation is also one of the directions of passive cooling technology. The vegetation is grown entirely from the external natural environment, but the vegetation can improve the surrounding thermal condition, which meets the requirements of the passive cooling strategy. In many previous studies on courtyard ventilation and thermal environments, researchers have mainly focused on the improvement of the courtyard microclimate conditions by vegetation, however, few studies have concentrated on the influence of incorporating these technologies in the courtyard on the building's indoor thermal and wind environment. Vegetation (via the evapotranspiration process) can help lower air temperature around the surrounding area and the facades. Therefore, a quantitative assessment of the cooling effects of this strategy becomes essential for scientific understanding of its influence on indoor areas of buildings with courtyards.
  
4. Previous studies have shown significant limitations in exploring the relationship between courtyard structures and pollutant dispersion. These studies tend to emphasize the inherent features of courtyards, such as geometric structure and orientation, and their

impact on airflow dynamics and air quality. Although they discuss the interplay of pollutant dispersion, cross-ventilation, and accumulation within courtyards, they often overlook the significant impact of the courtyards' unique enclosed or semi-enclosed nature and their connectivity with surrounding buildings on pollutant dispersion. Simultaneously, these studies have not fully explored complex mechanisms of inter-unit pollutant transmission. Moreover, in the specific context of pollution dispersion in the courtyard, the integration of wind tunnel experiments and CFD simulations is rarely employed to study these complex phenomena. Existing research usually focuses on pollutant dispersion near an isolated cubic building (Castro & Robins, 1977; Blocken et al., 2008; Tominaga & Stathopoulos, 2009, 2010; Guo et al., 2021) or urban blocks (Carpentieri et al., 2012; Hunter et al., 1992; Koutsourakis et al., 2012; Lateb et al., 2010; Tominaga & Stathopoulos, 2011). Studies on indoor and outdoor pollutant distribution also primarily concentrate on external pollution, particularly how pollution near street canyons affects indoor air quality (Bazdidi-Tehrani et al., 2020; Chu & Yang, 2022; Cui et al., 2016, 2021; Liu et al., 2010; Tominaga & Blocken, 2016; Yang et al., 2015). Research on the movement, dispersion, and distribution of pollutants inside and outside enclosed courtyard buildings is still in its early stages, especially lacking studies on the pathways of pollutants spreading from within courtyard structures to the outside and then back indoors. The shortcomings in the literature limit the ability to design courtyard buildings that are both environmentally friendly and ensure the safety and health of residents. My study aims to bridge this gap by analysing pollutant dispersion in courtyard buildings through a combination of wind tunnel experiments and CFD simulations. Through our research, I aim to provide insights into optimizing courtyard design, with the goal of reducing the spread of pollutants and elevating the overall environmental health standards within urban living spaces.

## Chapter 3 Roof Shape Designs for the Courtyard

### 3.1 Introduction

In this chapter, CFD is applied to explore the impact of ten different roof styles on the indoor wind and thermal environment of courtyard buildings. These roof styles are shown in Figure 3.1. The workflow of this study and the key research questions are presented in Figure 3.1. To begin with, the CFD validation of courtyard buildings is conducted by comparing with wind tunnel experiment data to determine the most appropriate turbulence model. Then, the ANSYS CFD Fluent software is used to conduct a simulation analysis of the courtyard buildings with ten different roof styles.

By analysing the simulation results, this study aims to solve four questions. The first theme examines how different roof designs affect wind patterns in courtyards and adjacent buildings. The second assesses which roof style optimizes indoor natural ventilation. The third investigates how various roofs impact natural ventilation's ability to disperse indoor heat, using indoor heat flux settings. The fourth explores the connection between indoor and courtyard wind patterns and their influence on air influx through openings. This offers a basis for enhancing indoor wind conditions.

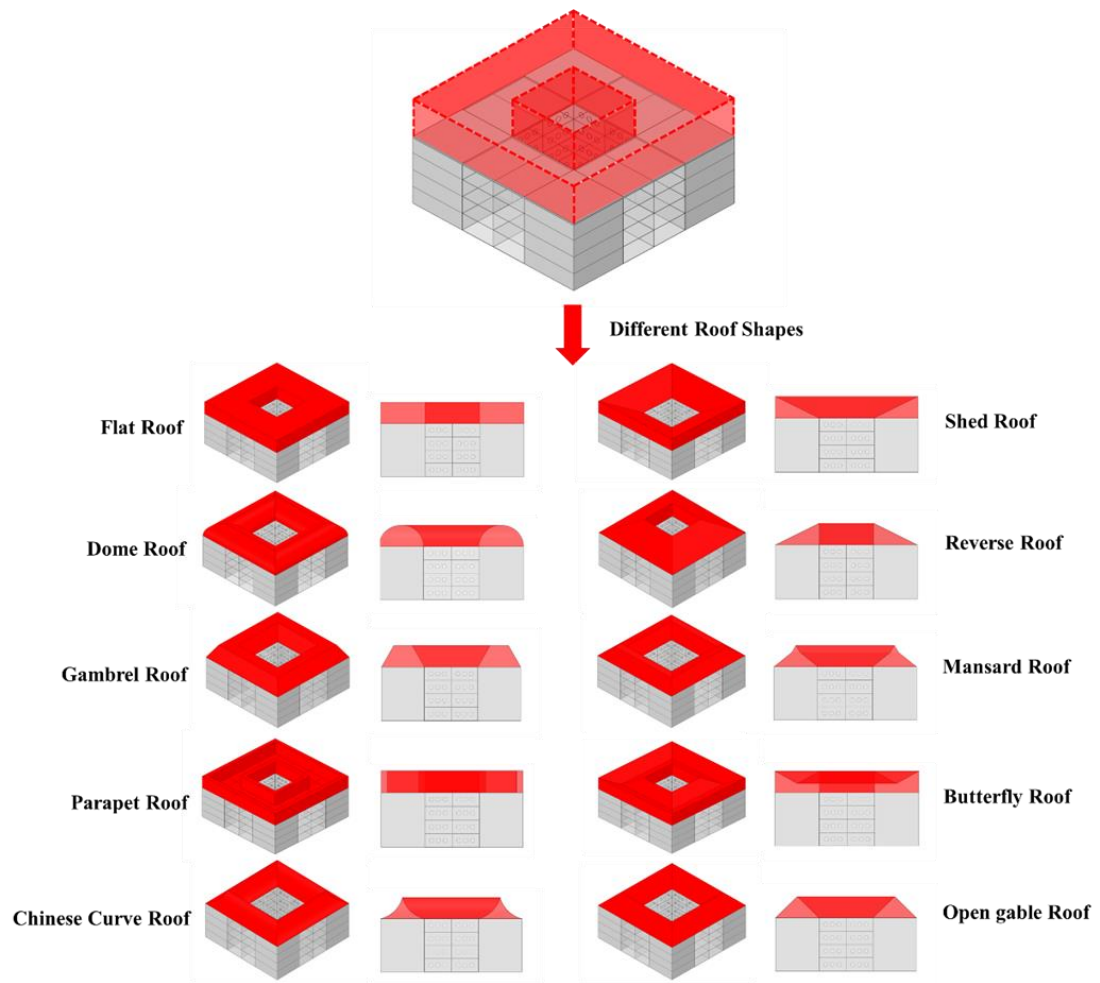


Figure 3.1 Single-sided ventilated courtyard buildings featuring ten different roof styles.

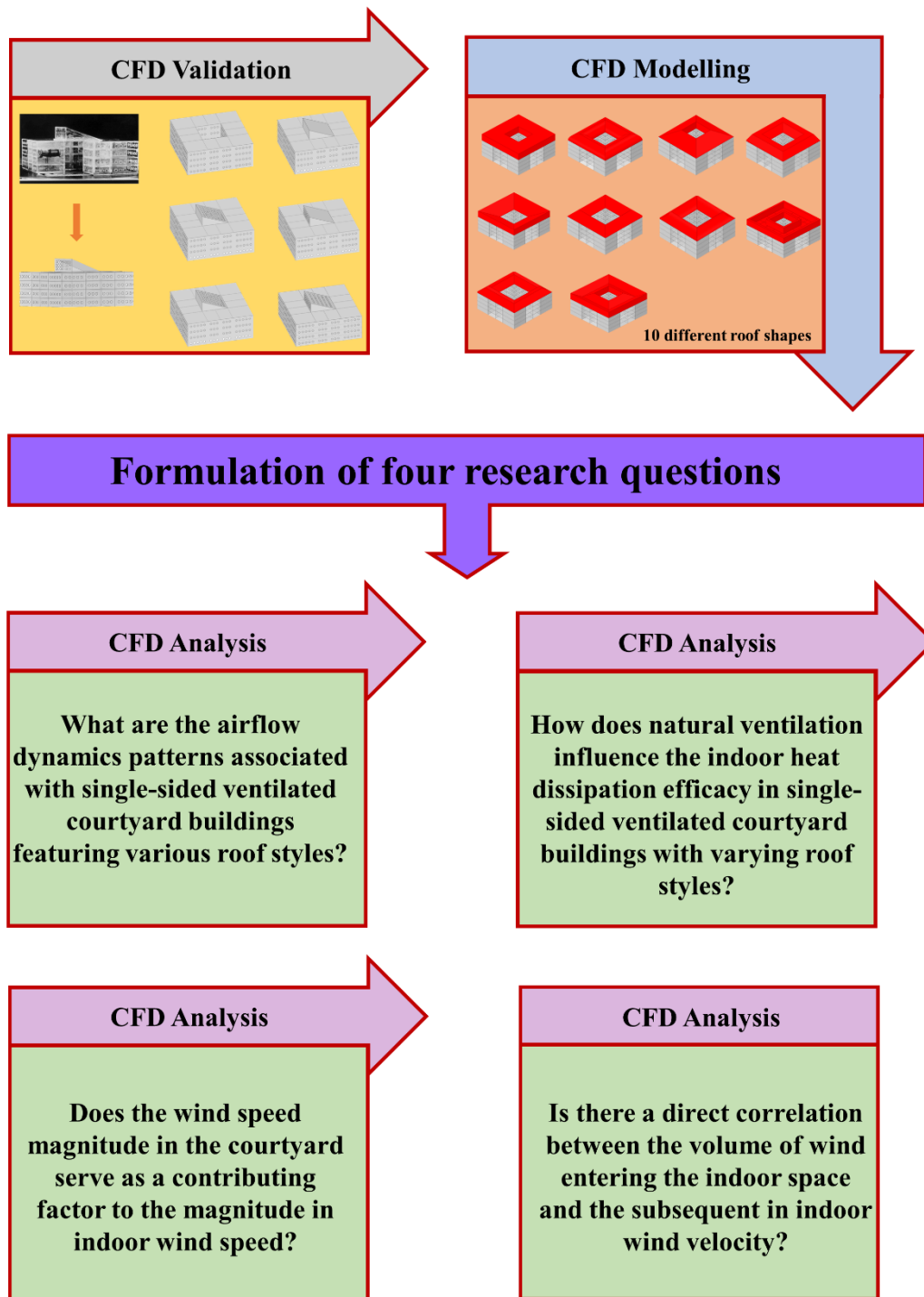


Figure 3.2 The primary research workflow of the study and the four main research questions are addressed.

## 3.2 Method

In this section, an investigation was conducted by analysing the fundamental principles of CFD and defining the solver settings. Then, the courtyard model was elaborated on, including its dimensions, structural composition, and implementation under the simulation framework. The fluid domain setup was then detailed, involving the spatial extent and critical attributes of fluid flow. Besides, the grid design was introduced in detail, focusing on its type, dimensions, and allocation methodology, to capture the intricate phenomena via an optimized grid layout. The reliability and precision of the simulation results were determined through a mesh independence test. Lastly, the boundary conditions were finalized through simulation, covering the fluid inlet and outlet parameters, along with other critical physical boundary specifications.

### 3.2.1 CFD theory

In this study, the control volume approach was adopted, with ANSYS Fluent 2021 software applied to perform steady-state RANS analysis of flow and mass fraction equations. The simulation, conducted in 3D CFD, took into account a fully turbulent and incompressible flow. To close the RANS equations, the *k*- $\omega$  Standard model was applied and guided by the results of validation (detailed in Section 4). The CFD software applied in this study relies on the Finite Volume Method (FVM) and a semi-implicit algorithm to perform velocity-pressure coupling (SIMPLE), for second-order windward discrete pressure correlation equations. The convergence of the solution was achieved when the residuals of mass, momentum, and energy equations fell below  $10^{-6}$ . The governing steady-state equations, as defined by the commercial CFD code ANSYS/FLUENT (Ansys Fluent Theory Guide 2021R2 [Online], 2021), are expressed as follows:

Continuity equation:

$$\nabla \cdot (\rho \vec{v}) = 0 \quad (3.1)$$

where  $\rho$  represents the density, and  $\vec{v}$  refers to the velocity vector.

Momentum equation:

$$\nabla \cdot (\rho \vec{v} \vec{v}) = -\nabla p + \nabla \cdot \tau + \rho \vec{g} \quad (3.2)$$

where  $p$  represents pressure,  $\tau$  indicates the stress tensor, and  $\vec{g}$  denotes the gravitational acceleration vector.

Energy equation:

$$\nabla \cdot \left[ \rho v \left( h_f + \frac{v^2}{2} \right) \right] = \nabla \cdot \left( \kappa_{eff} \nabla T - \sum_j h_j \vec{J}_j + \tau_{eff} \cdot \vec{v} \right) + S_h \quad (3.3)$$

where  $e$  denotes the internal energy;  $h_f$  represents the mass-specific enthalpy, with only dry air considered;  $\kappa_{eff}$  indicates the effective thermal conductivity;  $T$  refers to the temperature of the air;  $h_j$  indicates the sensible heat of species  $j$ , while  $J$  denotes the diffusion flux of species  $j$ , both of which are excluded from this study;  $\tau_{eff}$  indicates the effective stress tensor; and  $S_h$  refers to the volumetric heat source.

In this study, the performance of five commonly used turbulence models is evaluated through wind tunnel experiments, which are the  $k$ -epsilon Standard model (Launder & Spalding, 1974), the  $k$ -epsilon RNG model (Yakhot et al., 1992), the  $k$ -epsilon Realizable model (Shih et al., 1995), the  $k$ -omega Standard model (Wilcox, 2008; Menter, 2009), and the  $k$ -omega SST model (Menter, 1994). Based on the existing results shown from Table 3.2 to



Table 3.6, the  $k$ - $\omega$  Standard model was taken as the primary model for subsequent research. This choice was made by considering the accuracy and efficiency demonstrated by the model in the simulation of wind tunnel experimental data.

The transport equations governing the  $k$ - $\omega$  Standard model are presented in Equ. (3.4) and (3.5):

Turbulence kinetic energy  $k$ :

$$\frac{\partial}{\partial x_i}(\rho k u_i) = \frac{\partial}{\partial x_j} \left( \Gamma_k \frac{\partial k}{\partial x_j} \right) + G_k - Y_k + G_b \quad (3.4)$$

The specific dissipation rate  $\omega$ :

$$\frac{\partial}{\partial x_i}(\rho \omega u_i) = \frac{\partial}{\partial x_j} \left( \Gamma_\omega \frac{\partial \omega}{\partial x_j} \right) + G_\omega - Y_\omega + G_{\omega b} \quad (3.5)$$

In these two equations,  $G_k$  represents the generation of turbulence kinetic energy from mean velocity gradients;  $G_\omega$  refers to the generation term for  $\omega$ ;  $\Gamma_k$  and  $\Gamma_\omega$  denote the effective diffusivity of  $k$  and  $\omega$ , respectively;  $Y_k$  and  $Y_\omega$  represent the dissipation of  $k$  and  $\omega$  due to turbulence; and  $G_b$  and  $G_{\omega b}$  are the terms that take into account buoyancy effects.

### 3.2.2 Courtyard geometry, computational domain, and boundary conditions

Sharpley & Bensalem (2001) conducted a wind tunnel experiment to investigate the changes to airflow rate and air pressure in courtyard and atrium models under the action of urban wind. The courtyard models used in their experiment were scaled down to a 1:100 ratio, focusing on the impact of different window-to-wall ratios and wind directions on the courtyard and atriums. Circular openings were selected for the model because the measurement of indoor airflow rates required the use of a small orifice plate device, necessitating openings with a minimal discharge coefficient (Bensalem, 1991). Further, in

their research, this study adopts the same architectural model of the courtyard but with some improvements to reveal the effects of single-sided ventilation in courtyard buildings. Based on the original courtyard model, the atrium roof style was modified while maintaining the original height, and 10 different roof shapes were chosen for analysis to ensure an equal comparison.

This study employs an idealized model to simulate the geometry and environmental conditions of a courtyard. While this model provides a framework for studying the ventilation and cooling effects of courtyard buildings with different roof styles, it does not encompass all the complexities of real-world scenarios. Nevertheless, this analysis highlights the intricate dynamics of airflow within courtyard buildings and underscores the necessity of such studies for practical applications.

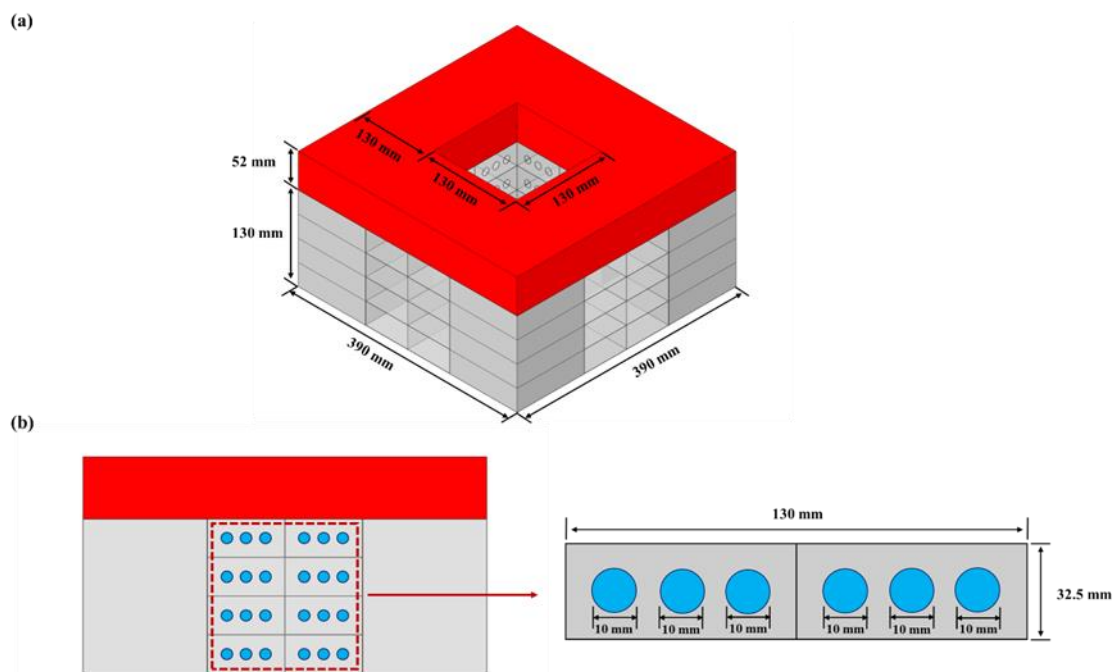


Figure 3. 3 Dimensions of the courtyard building and window opening. Dimensions of the courtyard building and window opening. (a) The dimension of the courtyard building (b)

the cross-section of the building facing the courtyard, and the dimension of the window opening.

As shown in Figure. 3.3 (a), the single-sided ventilation courtyard buildings under study have the same dimensions as the wind tunnel experiment described in (Roache, 1994; Sharples & Bensalem, 2001). In this study, the 'single-sided ventilation courtyard building' refers to a building where only one side of the rooms has windows open for ventilation. To investigate the impact of the courtyard on the aero-thermal conditions of the surrounding buildings, the openings of these buildings face the courtyard. Airflow enters and exits through the same openings on one side of the room or space. With a length and width of 390 mm, they have four stories, each of which is 32.5 mm in height, which means a total height of 130 mm. The roof was uniformly set to 52 mm in height. The courtyard, which measured 130 mm x 130 mm x 130 mm, was located at the centre of the building. Considering single-sided ventilation inside the building, all openings pointed to the courtyard. To quantify the impact of the courtyard on the indoor wind and thermal environment of the surrounding buildings, this study focuses on the rooms facing the courtyard. Each floor had eight rooms facing the courtyard, with two adjacent rooms on each side. As shown in Figure. 3.3 (b), there were three circular openings with a diameter of 10 mm in each room, facing the courtyard.

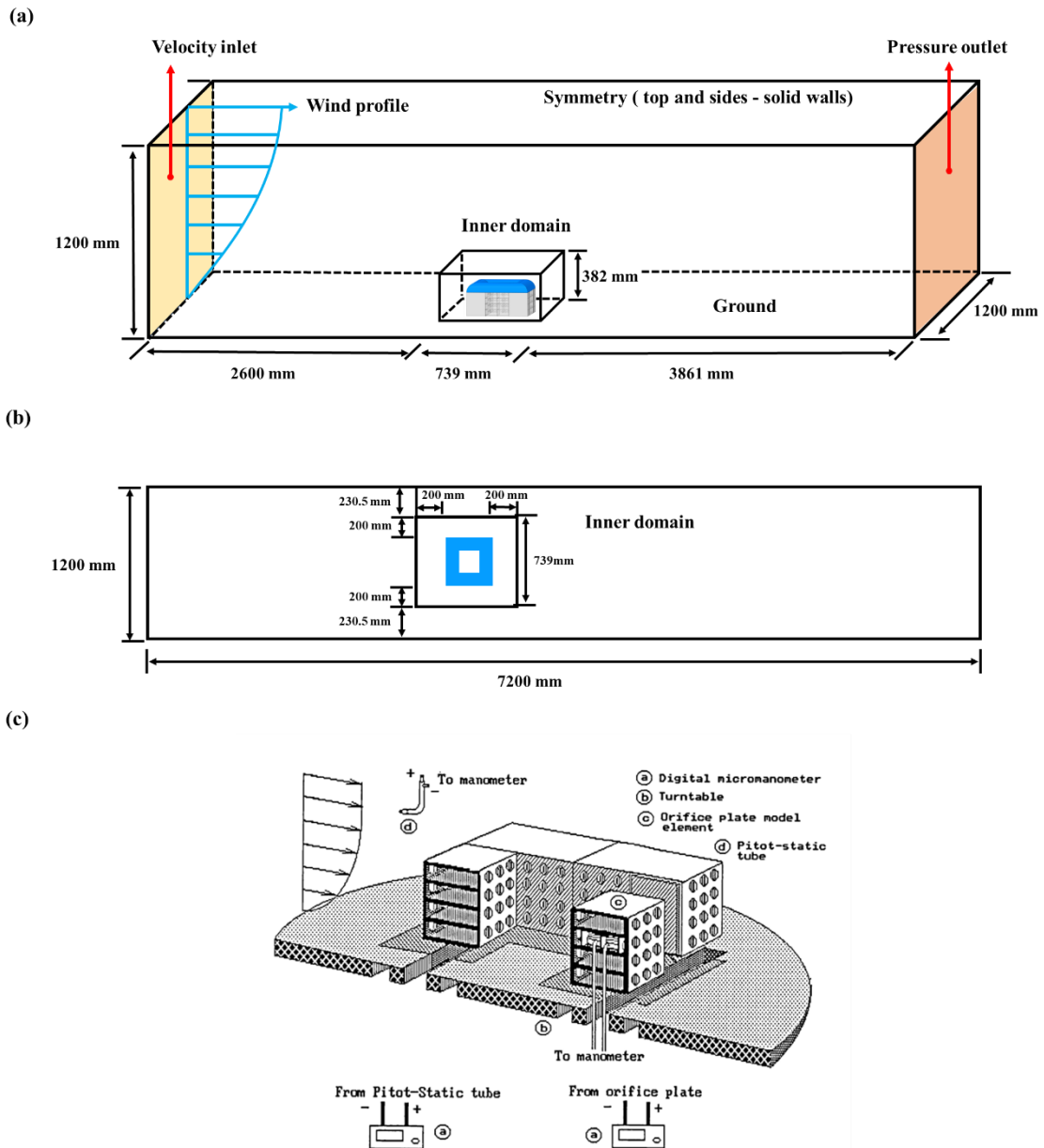


Figure 3.4 Computational domain dimensions, boundary conditions, top view, and wind tunnel setup for internal flow tests. (a) The dimension of the computational domain and the boundary conditions. (b) top view of the computational domain. (c) wind tunnel setup for internal flow tests for the courtyard model from (Bensalem 1991).

Figure. 3.4 (a) shows the dimensions and configuration of the fluid domain, which is consistent with the wind tunnel experiment. To be exact, the length was 7200 mm, and the cross section measured 1200 mm x 1200 mm. The spacing between the courtyard and

symmetrical walls on both sides was set to 430.5 mm. The distance from the courtyard to the velocity inlet and pressure outlet was 2800 mm and 4061 mm, respectively. The distance from the courtyard to the top of the fluid domain was set to 1018 mm. Considering that the volume of the fluid domain in the wind tunnel experiments was relatively larger than in the courtyard building model, an embedded fluid domain was designed within the main fluid domain. Adjacent to the courtyard, as shown in Figure. 3.4 (b), it maintained a distance of 200mm from the courtyard's surfaces and roof. This is purposed to facilitate the effective transition of the grid. It measured 739 mm x 739 mm x 382 mm, whose distance to the velocity inlet and pressure outlet was 2600 mm and 3861 mm, respectively. Thus, simulation precision was balanced with computational efficiency. Figure. 3.4 (c) illustrates the setup for measuring courtyard airflow rates in wind tunnel experiments based on reference (Bensalem, 1991).

### 3.2.3 Boundary conditions for the simulation study

The configuration in Figure. 3.4 (a) requires designating a surface as the velocity inlet, where the wind speed distribution at this inlet is determined by referencing the atmospheric boundary layer (ABL) wind tunnel experiment, to model airflow within the computational domain (Bensalem, 1991; Sharples & Bensalem, 2001). Under all simulation scenarios, the distribution of this inlet wind speed remained constant. The velocity profile, formulated in the power law expression, was obtained through regression fit based on the velocity measurement performed at the centre of the turntable and at different heights. The mean velocity profile is expressed as follows:

$$u(z) = u_{\text{ref}} \left( \frac{z}{z_{\text{ref}}} \right)^\alpha \quad (3.6)$$

In the above equation,  $u(z)$  denotes the mean velocity at height  $z$ , in m/s. The power law exponent  $\alpha$ , determined as 0.245 through wind tunnel experiment, is unique to such environments as suburban areas or urban terrains without significant high-rise structures (Bensalem, 1991). It was derived from the curve fitting of wind tunnel results. The reference height  $z_{\text{ref}}$ , which was set to 800 mm, is aligned with the eaves level. Denoted as  $u_{\text{ref}}$ , the velocity experimentally measured at this reference height was recorded as 16.4 m/s (Sharples & Bensalem, 2001). Then, the specified wind speed distribution was implemented at the inflow boundary within the computational domain. The simulation was performed by following the same wind speed distribution as measured in the experiment. The boundary on the opposite side was treated as a pressure outlet, and was maintained at a static pressure of 0 Pa.

This study was conducted based on the climate of Nottingham, UK (latitude 52.939°N, longitude 1.197°W). Similar to most parts of the UK, Nottingham features a temperate maritime climate, which is characterized by warm and mild summers and cool, mild winters. To conduct this study, the average temperature in Nottingham during a typical summer month in July 2021, which was 22°C (Nottingham, England, United Kingdom Weather Conditions, WeatherUnderground, n.d.), was taken as the initial boundary condition for both the velocity inlet and pressure outlet settings. On this basis, the impact of natural ventilation on indoor air velocity and temperature was examined. The impact of relative humidity was not taken into account in this study for simplification. In the process of CFD simulation, the effect of buoyancy was taken into consideration, and the gravity was fixed at -9.81 m/s<sup>2</sup>. Non-slip boundary conditions were determined for the symmetry of the top, two side walls, and the ground boundary. On this basis, the effectiveness of natural ventilation in removing heat from

the single-sided ventilated courtyard building was explored. For this purpose, a uniform heat flux was created as an internal heat source on the floors of 32 experimental rooms facing the courtyard. Since the courtyard model adopted the same design as used in the wind tunnel experiment without proportional enlargement, the heat flux was set to a value of  $5\text{W/m}^2$ .

### 3.2.4 Grid and sensitivity analysis

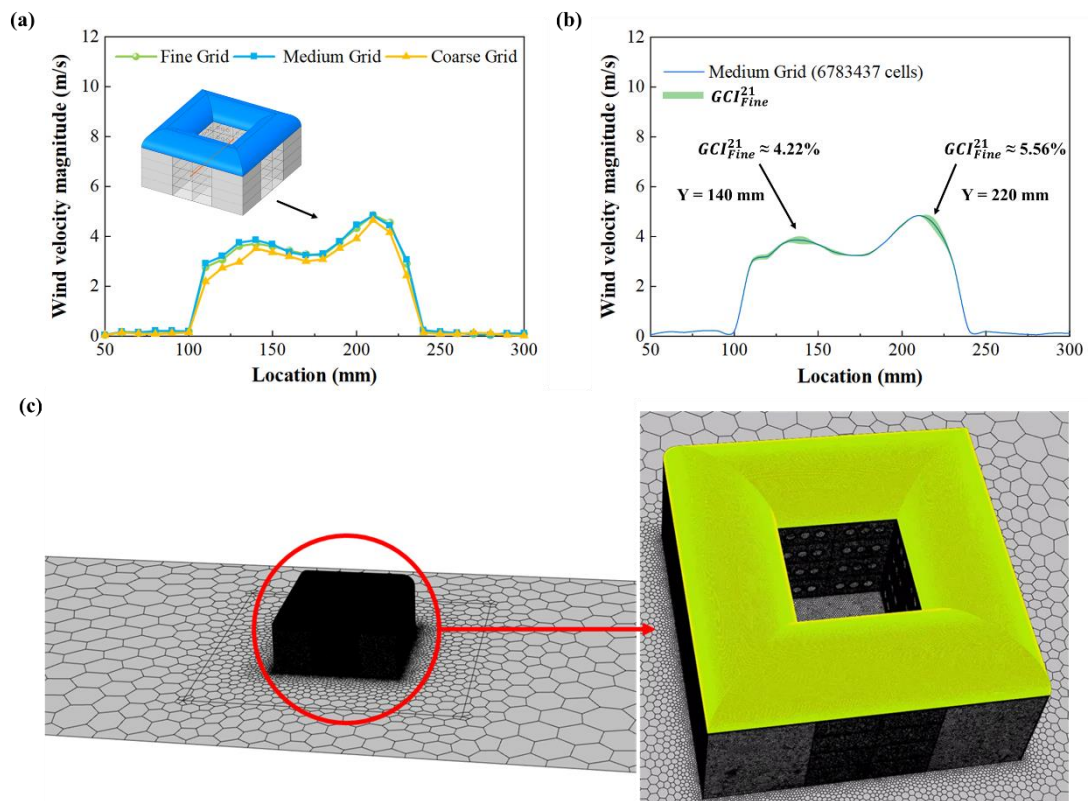


Figure 3.5 Wind velocity simulation, grid sensitivity analysis, and polyhedral mesh around the courtyard building. (a) Simulation results of wind velocity magnitude along a horizontal centre line of the courtyard model at the height of 49 mm for the grid sensitivity analysis. (b) Grid sensitivity analysis was conducted using the GCI method. (c) polyhedral mesh around the courtyard building.

The accuracy of numerical simulation and the duration of computation is affected by mesh quality in the process of modelling. Under the context of ANSYS Meshing, a tetrahedral mesh was created for the fluid domain. To obtain accurate simulation results, two fluid domains were positioned around the courtyard model to optimize grid transition. These domains include an outer domain with a grid size of 100 mm and an inner domain with a grid size of 50 mm. In addition, mesh refinement was performed in the critical areas across the courtyard building. Specifically, the floors with heat flux were set to a grid size of 1.5 mm, while the circular window openings were set to a grid size of 0.8 mm. The roof, which was the focus of this study, was set to a grid size of 0.4 mm. The external surface of the building was set to a grid size of 1mm, while the remaining parts of the courtyard building were set to a grid size of 2 mm. In this way, the accuracy of simulation results was improved. The ratio of expansion for adjacent cells was maintained at a lower level than 1.2. To enhance computational efficiency and accelerate processing, the tetrahedral mesh of the fluid domain was transformed into a more efficient polyhedral mesh in ANSYS Fluent. To verify the accuracy of the numerical model, a mesh sensitivity analysis was performed by examining how the results varied with the change in mesh size. Discretization uncertainty was assessed against the grid convergence index (GCI), as proposed in (Roache, 1994).

For the purpose of calculation, it's necessary to determine the grid size first, which is denoted as  $h$ . Herein,  $\Delta V_i$  represents the volume, and  $N$  refers to the total number of cells used for the computation.

$$h = \left[ \frac{1}{N} \sum_{i=1}^N (\Delta V_i) \right]^{1/3} \quad (3.7)$$



Figure 3.5 and Table 3.1 show the process of choosing three grid sizes — fine, medium, and coarse. They were used in simulation to determine the value of critical variables  $(\phi_1, \phi_2, \phi_3)$  required to achieve the research goals. The grid refinement factor, denoted as  $r = h_{\text{coarse}}/h_{\text{fine}}$ , is supposed to exceed 1.3 (Roache, 1994). When  $h_1 < h_2 < h_3$ , the ratios are expressed as  $r_{21} = h_2/h_1$ , so that  $r_{32} = h_3/h_2$ . Accordingly, the grid sizes were set as N1 (15,889,281), N2 (6,783,437), and N3 (2,391,933), yielding the  $r$  values of 1.328 and 1.415. The effective order of this method, which is denoted as  $p$ , is calculated using Eq. (3.8) to Eq. (3.14), where  $\varepsilon_{32} = \phi_3 - \phi_2$  and  $\varepsilon_{21} = \phi_2 - \phi_1$ .

$$p = \frac{1}{\ln(r_{21})} |\ln |\varepsilon_{32}/\varepsilon_{21}| + q(p)| \quad (3.8)$$

$$q(p) = \ln \left( \frac{r_{21}^p - s}{r_{32}^p - s} \right) \quad (3.9)$$

$$s = 1 \cdot \text{sgn} (\varepsilon_{32}/\varepsilon_{21}) \quad (3.10)$$

The extrapolated values are shown in Eq. (13):

$$\phi_{\text{ext}}^{21} = (r_{21}^p \phi_1 - \phi_2)/(r_{21}^p - 1) \quad (3.11)$$

The estimated relative error, denoted as  $e_a^{21}$ , the extrapolated relative error, denoted as  $e_{\text{ext}}^{21}$ , and the fine grid convergence index, denoted as  $\text{GCI}_{\text{fine}}^{21}$ , can be calculated using Eq. (15) to Eq. (17).

$$e_a^{21} = \left| \frac{\phi_1 - \phi_2}{\phi_1} \right| \quad (3.12)$$

$$e_{\text{ext}}^{21} = \left| \frac{\phi_{\text{ext}}^{12} - \phi_1}{\phi_{\text{ext}}^{12}} \right| \quad (3.13)$$

$$GCI_{\text{fine}}^{21} = \frac{1.25e_a^{21}}{r_{21}^p - 1} \quad (3.14)$$

	<b>Wind velocity magnitude (m/s) at Y = 70 mm</b>	<b>Wind velocity magnitude (m/s) at Y = 140 mm</b>	<b>Wind velocity magnitude (m/s) at Y = 210 mm</b>
N1	15,889,281	15,889,281	15,889,281
N2	6,783,437	6,783,437	6,783,437
N3	2,391,933	2,391,933	2,391,933
$r_{21}$	1.328	1.328	1.328
$r_{32}$	1.415	1.415	1.415
$\phi_1$	0.139	3.710	4.853
$\phi_2$	0.146	3.851	4.836
$\phi_3$	0.103	3.514	4.656
$p$	5.460	2.657	2.516
$\phi_{\text{ext}}^{21}$	0.137	3.585	4.869
$e_a^{21}$	4.883%	3.801%	0.351%
$e_{\text{ext}}^{21}$	1.335%	3.497%	0.336%
$GCI_{\text{fine}}^{21}$	1.646%	4.223%	0.421%

Table 3.1 Example of discretization error computation employing the GCI method.

In this study, comparative analysis was conducted using three grids that varied in size. The outer domain of the most refined grid was set to a grid size of 50 mm, while the floors, facade, and circular openings of the building were set to a grid size of 0.5 mm, 0.5 mm, and 0.4 mm, respectively. The grid size of other parts of the building was adjusted to 1mm, which led to a total of 15,889,281 cells. Moreover, a coarser grid, based on the medium-sized grid,

was developed, which doubled the grid size in the fluid domain and enlarged the details of the courtyard building in a similar way, thus resulting in 2,391,933 cells. Grid sensitivity was assessed by choosing the second floor at coordinates  $X=135$  mm,  $Z=49$  mm, and by increasing  $Y$  from 50 mm to 300 mm.

To observe the magnitude of wind velocity (m/s), a set of 26 points was deployed, whose readings at three different grid sizes are shown in Fig. 3.5 (a). The data shown in Table 3.1 emphasizes points at  $Y = 70$  mm,  $Y = 140$  mm, and  $Y = 210$  mm, with their grid convergence index reaching 1.646%, 4.223%, and 0.421%, respectively. The medium mesh size was used for this study, considering its relatively limited error margin compared to the fine mesh. Meanwhile, computational cost was reduced significantly. Fig. 3.5 (b) shows the convergence index and discretization error bars at all 26 points for the medium grid. The maximum  $GCI_{\text{fine}}^{21}$  was recorded at  $Y = 220$  mm with a value of 5.56%, which is considered acceptable. Additionally, the average  $GCI_{\text{fine}}^{21}$  At all 26 points, was calculated to be 2.37%, confirming that the medium mesh size is appropriate for simulation.

### 3.3 Results

#### 3.3.1 Validation of the naturally ventilated courtyard model

In this study, CFD simulation techniques were applied to thoroughly analyze the courtyard buildings with various roof styles for their performance in natural ventilation. The baseline model was subject to a parametric analysis using the method used in wind tunnel experiments on courtyard buildings, with the aim of refining its design. The process of CFD simulation, ranging from modelling to the final setup, was conducted in the same way as the wind tunnel experiment described in (Bensalem, 1991; Sharples & Bensalem, 2001), as illustrated in Fig.

3.6 (a). According to Sharples & Bensalem (2001) and Bensalem (1991), all model elements consisted of four stories or rooms, each of which was scaled to a ratio of 1:100. Also, the instrumented model was positioned in the centre of the turntable, with a diameter of 1.1 meters inside an ABL wind tunnel. In design, the wind tunnel had a working length of 7.2 m and a cross-sectional area of 1.2 m x 1.2 m. The wind speed reached up to 25 m/s.

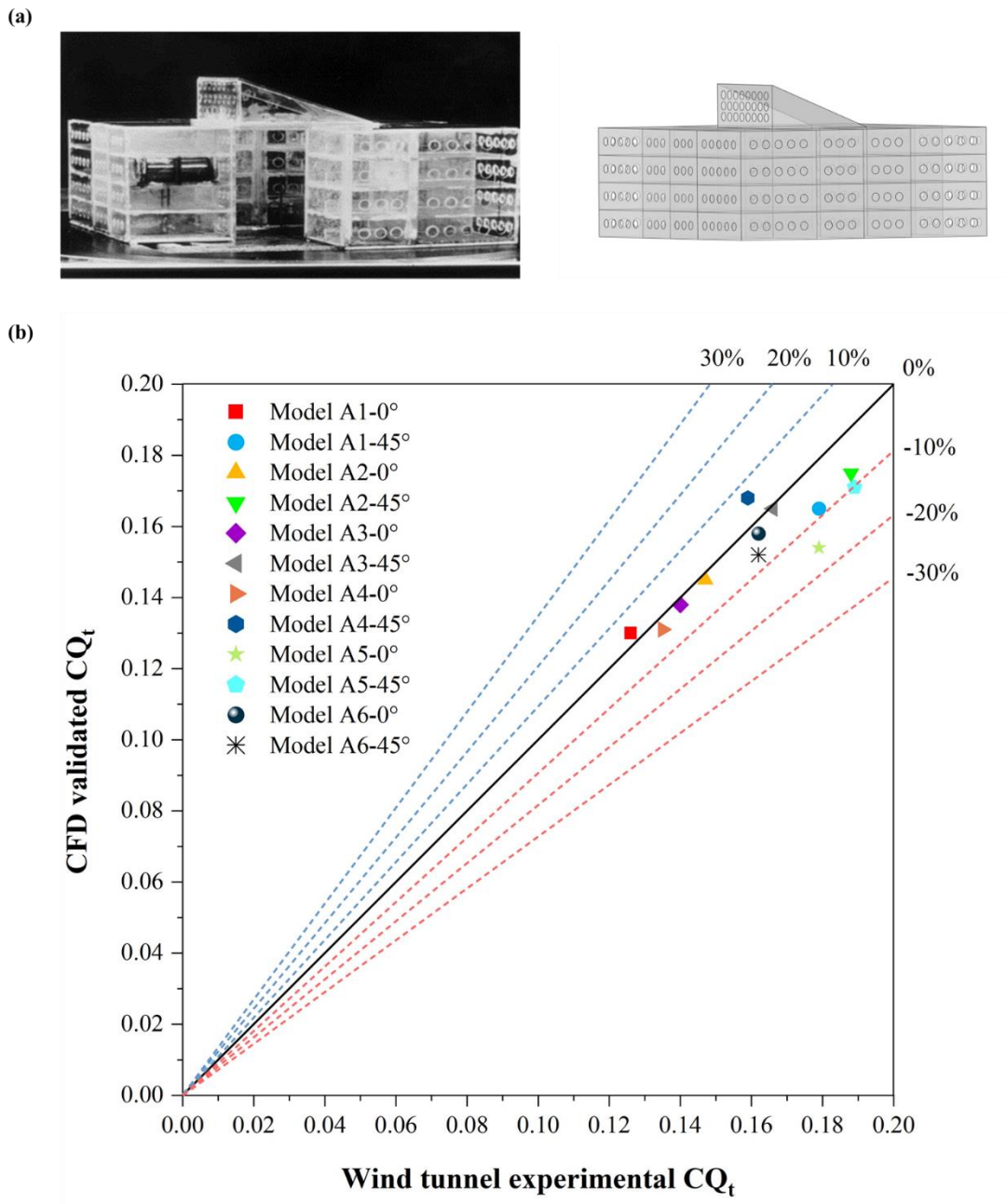


Figure 3.6 Comparison of experimental and CFD numerical models, and deviation analysis between wind tunnel experiments and numerical simulations. (a) Comparison of the

actual experimental model Sharples & Bensalem (2001) and CFD numerical model. (b) Deviation analysis for wind tunnel experiments and numerical simulations was done using the  $k$ - $\omega$  standard model in the courtyard and atriums.

During the experimental process, measurement was performed for various building models, including a courtyard and multiple atrium structures, all of which were 339 mm in length, 339 mm in width, and 130 mm in height. Specifically, the atrium model with a roof at  $22^\circ$  had a height of 52 mm. In this study, six different isolated models were involved in CFD validation: Model A1 that represents a closed courtyard; Model A2 that represents an atrium devoid of roof openings; Models A3 and A5, both of which have roof openings on the windward and leeward sides, with a window-to-wall ratio of 11.4%; and Models A4 and A6, each of which has a window-to-wall ratio of 30.4%. Moreover, five commonly used RANS models were chosen: the  $k$ - $\epsilon$  Standard,  $k$ - $\epsilon$  RNG,  $k$ - $\epsilon$  Realizable,  $k$ - $\omega$  Standard, and  $k$ - $\omega$  SST. Considering courtyard architecture as the focus of this study, the courtyard model used for simulation was constructed by adapting Model A1. Through CFD modelling validation, all four models were assessed in terms of geometry, dimension, the working section of the wind tunnel, the window-to-wall ratio, and the boundary conditions. Each model was subjected to blowing by the wind at  $0^\circ$  and  $45^\circ$  to evaluate their effectiveness. Sharples and Bensalem used an orifice plate to measure the airflow rate in the model and introduced a novel dimensionless coefficient ( $CQ_t$ ) into the experimental process. It was calculated using the following formula.

$$CQ_t = \frac{1}{N} \sum_{i=1}^N \frac{V_0}{V_{800}} \quad (3.15)$$

where  $V_0$  represents the velocity at the opening  $i$ , and  $V_{800}$  refers to the wind speed measured at the height of 800 mm, which was determined as 25 m/s in their experiment (Sharples & Bensalem, 2001). As shown in Table 3.2 to Table 3.6, the RANS models, and especially the  $k$ -omega standard variant, are applicable to predict the pattern of wind distribution for the courtyard and atrium buildings. Figure 3.6 (b) shows that the experimental and validation results (based on the  $k$ -omega standard model) are clearly consistent, with a greater level of similarity than 80%. The errors observed at a 45° wind direction from Table 3.2 to Table 3.6 were larger compared to those at 0°. This discrepancy can be attributed to the increased complexity of the airflow patterns at a 45° angle. Specifically, at 45°, a significant portion of the courtyard building is positioned on the leeward side, where the formation of vortices and intricate flow structures occurs. These conditions are challenging for  $k$ -epsilon and  $k$ -omega turbulence models to predict accurately. The 45° wind direction results in airflow that does not directly enter the indoor environment but instead generates complex secondary flows and recirculation zones. These phenomena are inherently difficult to model with standard turbulence models, leading to higher discrepancies between the CFD simulations and the wind tunnel experiments. However, when the wind direction is 0°, the validation results of Model A1, Model A3, Model A4 and Model A6 are almost consistent with the experimental results. The errors are less than 5%. It illustrates the high efficiency of CFD in accurately predicting the results of wind tunnel experiments and underscores the reliability and accuracy of the following simulation studies.

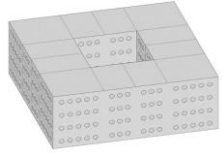
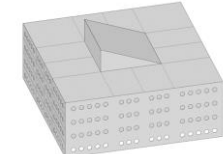
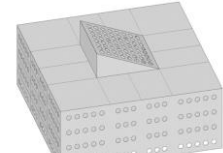
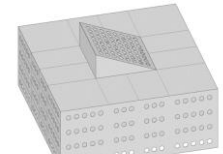
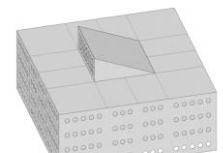
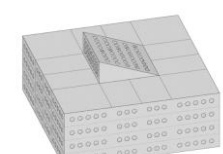
Model	Models	Wind direction (°)	Experimental CQt	k-epsilon Standard CQt	Error (%)
Model A1		0	0.126	0.135	7.18
		45	0.179	0.147	17.87
Model A2		0	0.147	0.140	4.76
		45	0.188	0.164	12.53
Model A3		0	0.140	0.141	1.03
		45	0.166	0.141	15.01
Model A4		0	0.135	0.139	2.96
		45	0.159	0.142	10.69
Model A5		0	0.179	0.148	17.32
		45	0.189	0.167	11.64
Model A6		0	0.162	0.138	14.81
		45	0.162	0.137	15.43

Table 3.2 Velocity coefficient CQt validation results for the courtyard and atriums numerical simulation by using the k-epsilon Standard model.

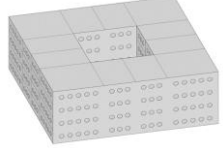
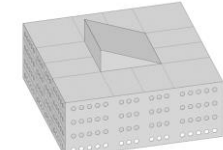
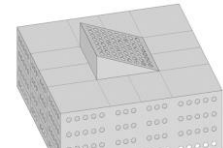
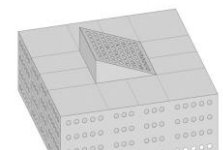
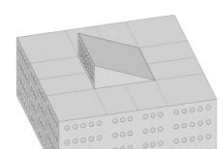
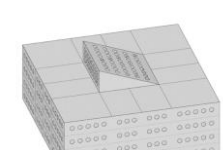
Model	Models	Wind direction (°)	Experimental CQt	<i>k</i> -epsilon RNG CQt	Error (%)
Model A1		0	0.126	0.119	5.28
		45	0.179	0.160	10.61
Model A2		0	0.147	0.145	1.26
		45	0.188	0.172	8.53
Model A3		0	0.140	0.130	7.19
		45	0.166	0.160	3.73
Model A4		0	0.135	0.147	8.89
		45	0.159	0.164	3.14
Model A5		0	0.179	0.141	21.22
		45	0.189	0.171	9.52
Model A6		0	0.162	0.140	13.58
		45	0.162	0.155	4.32

Table 3.3 Velocity coefficient CQt validation results for the courtyard and atriums numerical simulation by using k-epsilon RNG model.



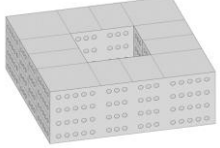
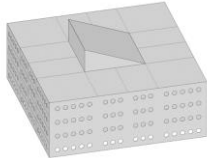
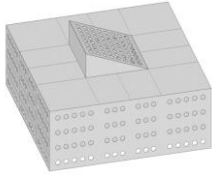
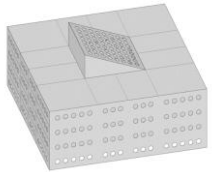
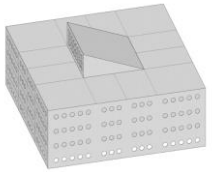
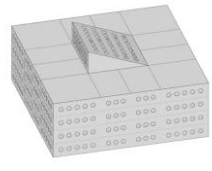
Model	Models	Wind direction (°)	Experimental CQt	k-epsilon Realizable CQt	Error (%)
Model A1		0	0.126	0.129	2.33
		45	0.179	0.161	11.18
Model A2		0	0.147	0.142	3.52
		45	0.188	0.168	11.90
Model A3		0	0.140	0.140	0
		45	0.166	0.145	14.48
Model A4		0	0.135	0.140	3.70
		45	0.159	0.154	3.14
Model A5		0	0.179	0.151	18.54
		45	0.189	0.171	9.52
Model A6		0	0.162	0.138	14.81
		45	0.162	0.137	15.43

Table 3.4 Velocity coefficient CQt validation results for the courtyard and atriums

numerical simulation by using k-epsilon Realizable model.

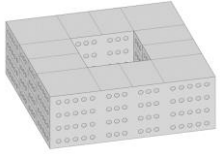
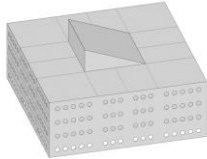
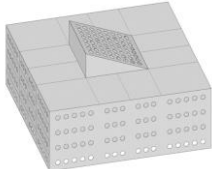
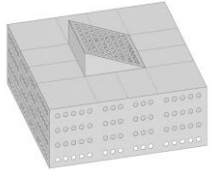
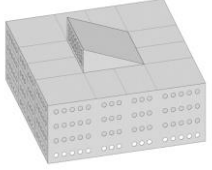
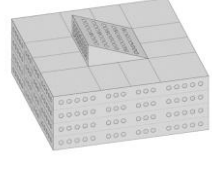
Model	Models	Wind direction (°)	Experimental $CQ_t$	<i>k</i> -omega Standard $CQ_t$	Error (%)
Model A1		0	0.126	0.130	3.36
		45	0.179	0.165	7.82
Model A2		0	0.147	0.145	1.26
		45	0.188	0.175	6.73
Model A3		0	0.140	0.138	1.62
		45	0.166	0.165	0.06
Model A4		0	0.135	0.131	2.96
		45	0.159	0.168	5.66
Model A5		0	0.179	0.154	16.23
		45	0.189	0.171	9.52
Model A6		0	0.162	0.158	2.47
		45	0.162	0.152	6.71

Table 3.5 Velocity coefficient  $CQ_t$  validation results for the courtyard and atriums numerical simulation by using *k*-omega Standard model.

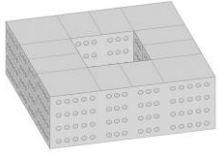
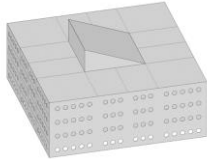
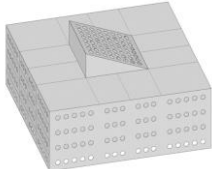
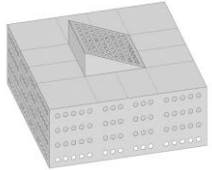
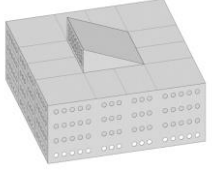
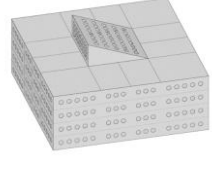
Model	Models	Wind direction (°)	Experimental CQt	<i>k</i> -omega SST CQt	Error (%)
Model A1		0	0.126	0.126	0
		45	0.179	0.162	9.50
Model A2		0	0.147	0.145	1.26
		45	0.188	0.174	7.30
Model A3		0	0.140	0.137	1.62
		45	0.166	0.157	5.65
Model A4		0	0.135	0.142	5.19
		45	0.159	0.173	8.81
Model A5		0	0.179	0.148	17.32
		45	0.189	0.174	7.93
Model A6		0	0.162	0.140	13.58
		45	0.162	0.150	7.50

Table 3.6 Velocity coefficient CQt validation results for the courtyard and atriums numerical simulation by using *k*-omega SST model.

### 3.3.2 Airflow in the single-sided ventilated courtyards with different shapes of roof

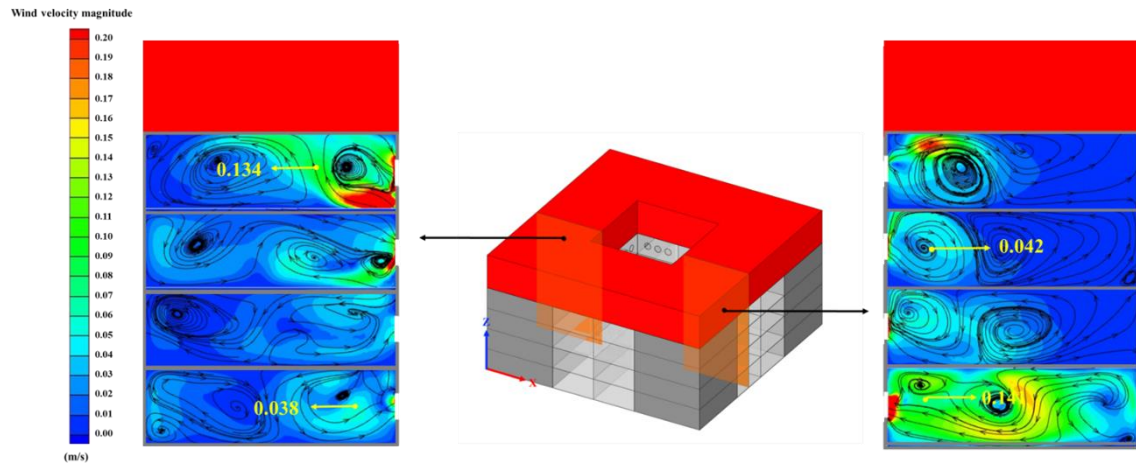
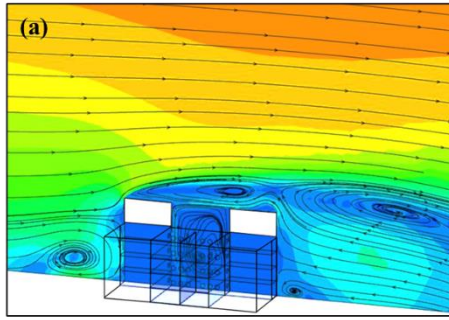


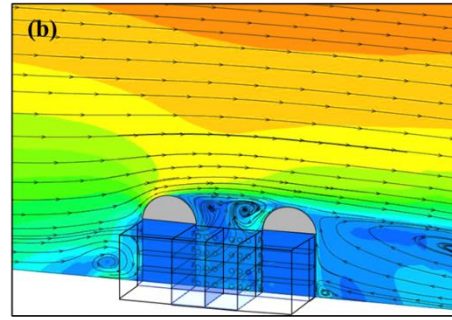
Figure 3.7 Indoor wind velocity magnitude contour at  $Y = 135\text{mm}$ , with arrows representing the observed vectors for baseline flat-roof courtyard model.

Figure 3.7 shows the indoor distribution of wind speed in the cross-section of the baseline model when  $Y = 135\text{ mm}$ . The characteristics of wind speed distribution on the windward and leeward sides are identifiable. In the single-sided ventilated courtyard, the indoor wind speed stays at a relatively low level. However, there is a substantial amount of wind flow into the rooms on the top floor of the windward side, indicating a higher efficiency of air exchange in this area. Meanwhile, indoor wind speeds exceed  $0.1\text{m/s}$  on the leeward side at the bottom floor, although the air movement remains significant. In all the other rooms, the amount of wind flow is lower, but there remains a certain amount of air entering the rooms through the openings. This finding is coherent with the previous descriptions of the direction in which air flows inside the courtyard. Generated above the roof, the vortex creates a counterclockwise vortex within the courtyard when it comes into contact with the left wall of the courtyard. This vortex first affects the top-floor rooms on the windward side, which is

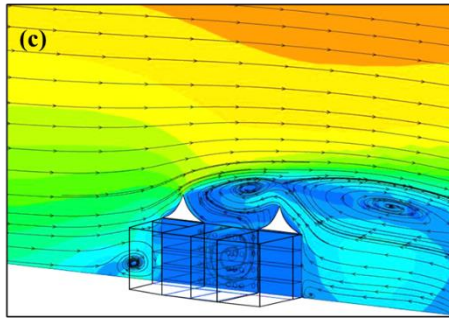
possibly attributed to the concentrated kinetic energy of the vortex at this point. The trajectory of the vortex in the courtyard also indicates that when it meets the right facade of the courtyard, the air partially flows into the rooms on the leeward side at the bottom, with the remaining air still flowing upwards.



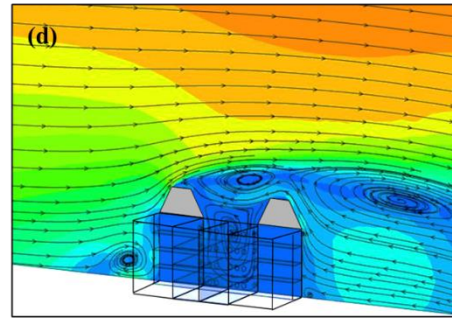
**Flat roof courtyard**



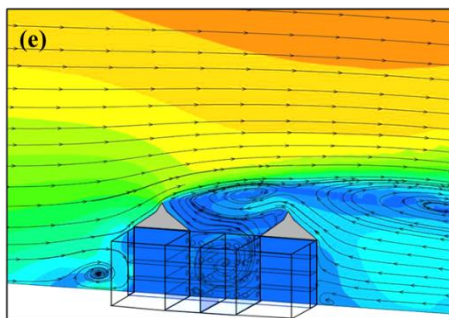
**Dome roof courtyard**



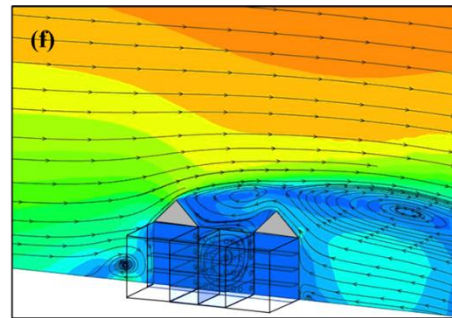
**Chinese curved roof courtyard**



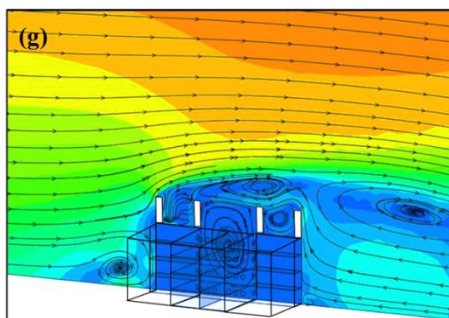
**Gambrel roof courtyard**



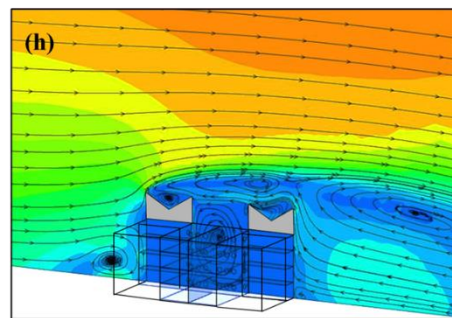
**Mansard roof courtyard**



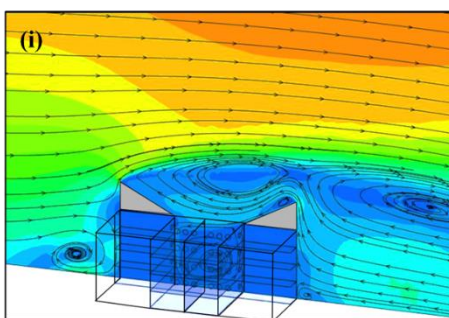
**Open gable roof courtyard**



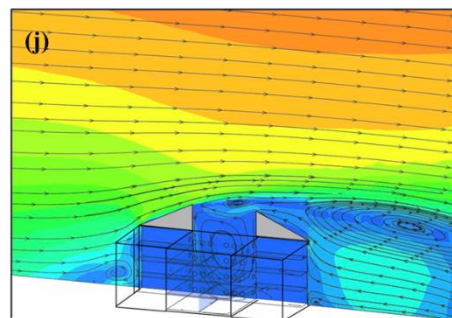
**Parapet roof courtyard**



**Butterfly roof courtyard**



**Shed roof courtyard**



**Reverse shed roof courtyard**

Figure 3.8 Airflow movement patterns for ten different roof styles. (a) Flat roof courtyard. (b) dome roof courtyard. (c) Chinese curved roof courtyard. (d) gambrel roof courtyard. (e) mansard roof courtyard. (f) open gable roof courtyard. (g) parapet roof courtyard. (h) butterfly roof courtyard. (i) shed roof courtyard. (j) reverse shed roof courtyard.

Figure 3.8 shows the patterns of airflow in the courtyards with 10 different roof styles, revealing the significant impact of how the roof is shaped on wind direction and velocity, with the characteristics of airflow above the courtyard in particular. In the single-sided ventilated courtyard buildings with a flat-roof model, as shown in Figure 3.8 (a), the airflow enters the fluid domain in the positive x-direction. This airflow first affects the windward face of the building, leading to the distribution of aerodynamic forces, of which some move upwards along the windward face to the roof. The obstructive effect of the building, combined with the uneven distribution of wind pressure, forces the airflow upwards, thus creating an upward current along the external walls. Meanwhile, the formation of a small local vortex can be observed below the windward face, which results from the occurrence of boundary layer separation in fluid dynamics. As the air reaches the flat roof, it partially crosses the roof edge and flows downwards. On the leeward side of the building, a significant clockwise vortex is generated. Part of the airflow in this large vortex returns to the roof area due to the change in height of the building and wind pressure gradients. Consequently, another clockwise vortex is generated above the roof. Part of this large vortex changes in direction upon contact with the left facade of the courtyard, directing the flow into the courtyard. Inside the courtyard, a counterclockwise vortex develops under the constraint of the surrounding walls, which promotes the influx of fresh air and thus improves the outcome of ventilation indoors.

Compared to the flat roof baseline model (Figure 3.8 (a)), the impact of other roof styles on airflow is evident mainly in the area above the roof, and especially the leeward side of the roof. For example, in the courtyard with a gambrel roof (Figure 3.8 (d)), the wind speed is reduced after the airflow encounters the windward slope due to the lower slope, and it gradually rises along the slope. When the steeper lower slope is reached, the airflow forms tight streamlines on the roof surface and accelerates upwards, especially at the roof edges where a turbulent boundary layer develops due to the significant changes in wind pressure and velocity. As the airflow crosses the roof apex and reaches the leeward side of the building, significant vortices are generated by the roof shape-induced fluid separation rise along the right side of the roof. Consequently, a clockwise vortex develops above the courtyard.

As can be seen from the dome roof in Figure 3.8 (b), the streamlined design of the roof ensures smooth airflow with minimal resistance along the surface of the dome at the windward side. The continuous curvature of the dome optimizes airflow adherence, which is effective in reducing airflow separation. This results in stable streamlines at the top. Compared to the roofs with sharp edges, the changes in airflow over the dome roof are less significant, thereby minimizing the generation of large vortices. As the airflow crosses the highest point of the dome and reaches the leeward side, a low-pressure area may develop afterwards, which results from fluid separation. Consequently, noticeable vortices are induced at the base of the roof. These vortices develop along the right edge of the dome and shift horizontally, causing the airflow to enter the space above the courtyard as it crosses the roof boundary. Due to the symmetrical nature of the dome, it is ensured that the vortices on the leeward side are evenly distributed around the dome, which has a significant effect on the airflow above the courtyard.



Figure 3.8 (c), Figure 3.8 (e), and Figure 3.8 (f) show the Chinese curved roof, mansard roof, and open gable roof, respectively. Despite their distinctive designs, these roofs exhibit a consistent pattern of airflow. The wind first encounters the roof at the windward point of contact, generating an upward force. Thus, continuous streamlines are generated along the roof surface before rising to the roof's apex. In this context, the shape of the roof and wind speed contribute jointly to the generation of vortex on the leeward side. These vortices elevate the airflow on the leeward side of the roof, developing swirls at the top right of the roof or above the courtyard. The mansard roof is characterized by the varied slope on the upper and lower surfaces, increasing the complexity of vortex dynamics at the roof's fold. In contrast, the smooth curves of the Chinese curved roof reduce airflow separation, which improves the smoothness of vortices at the roof's edges. The open gable roof, due to its sharp gable shape, leads to more concentrated airflow separation at the roof's apex, thus causing concentrated vortex formation. Although each roof leads to slight variations in the shape of the airflow and vortices entering or hovering above the courtyard, they maintain a consistent pattern of airflow, which is characterized by the rising of the wind, the formation of vortices, and the direction of airflow.

As shown in Figure 3.8 (g) and Figure 3.8 (h), both the parapet roof and butterfly roof exhibit significant roof indentations, which are the active zones where the vortex develops. On the parapet roof, its wall edges are extended beyond the roof surface to create a broad space of indentation. This leads to a strong resistance encountered by the wind flow at the top of the wall on the windward side. Consequently, vortex is generated. In this case, the airflow accelerates and generates strong vortices. Then, it flows along the top of the wall to the leeward side, where new vortices are generated. Regarding the butterfly roof, its unique V-

shaped indentation structure plays a role in guiding the windward airflow towards the central low point, which increases the wind speed at this point and promotes concentrated vortex formation. These vortices may show a greater strength in the indentation area. Subsequently, the airflow rises along the slopes and crosses over to the leeward side at the roof apex, thus generating new vortices.

Figure 3.8 (i) and Figure 3.8 (j) show the design of the shed roof and reverse shed roof, highlighting the significant role of roof design in the wind environment of courtyards. For the shed roof, the windward facade forces the upward airflow to the roof's edge, where the slope accelerates the airflow and creates a significant vortex at the roof's top. This vortex covers the entire roof. In contrast, the reverse shed roof, due to its sloped design on both windward and leeward sides, causes the airflow to climb these slopes. Because of the vertical roof above the courtyard, vortices are generated primarily in the space above the roof, rather than in the courtyard. After being generated on the windward slope of the airflow, the vortices rise to the roof's apex, which generates another vortex on the vertical leeward side.

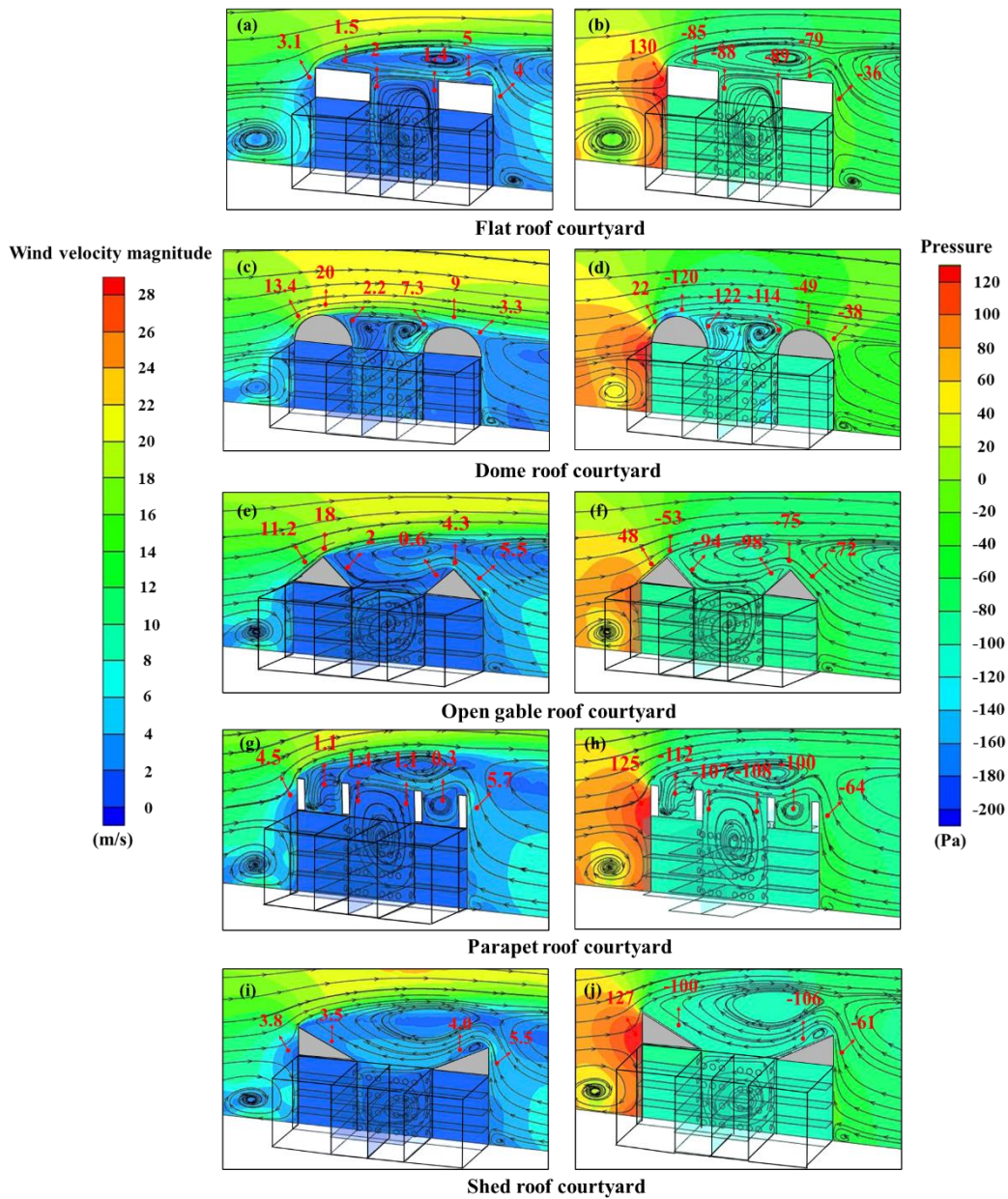


Figure 3.9 Airflow movement patterns and pressure contours for five different roof styles with specific values. (a) Wind flow contour for the flat roof courtyard. (b) pressure contour for the flat roof courtyard. (c) wind flow contour for the dome roof courtyard. (d) pressure contour for the dome roof courtyard. (e) wind flow contour for the open gable roof courtyard. (f) pressure contour for the open gable roof courtyard. (g) wind flow contour for the parapet roof courtyard. (h) pressure contour for the parapet roof courtyard. (i) wind flow contour for the shed roof courtyard. (j) pressure contour for the shed roof courtyard.

Figure 3.9 illustrates five representative roof structures: flat roof, dome roof, parapet roof, shed roof, and open gable roof. An analysis was conducted using velocity and pressure contour maps to draw a comparison between wind speed and pressure distribution around each roof. According to the analytical results, a positive pressure of over 120 Pa is exerted when the airflow shows the impact on the windward side of vertically oriented roof structures, such as the flat roof (Figure 3.9 (a) and Figure 3.9 (b)), parapet roof (Figure 3.9 (g) and Figure 3.9 (h)) and shed roof (Figure 3.9 (i) and Figure 3.9 (j)). Accordingly, the wind speed is 3.1 m/s, 4.5 m/s, and 3.8 m/s, respectively. The inclined roof structures, like the open gable roof (Figure 3.9 (e) and Figure 3.9 (f)), apply a positive pressure of 48 Pa on the windward side, demonstrating an upward flow along the roof slope to the peak. The dome roof, with its streamlined geometry, has the least significant resistance but the highest wind speed observed at the same location, reaching 13.4 m/s. The geometric characteristics of roof shapes exert a significant impact on the aerodynamic characteristics of the airflow, particularly when the air flows over the roof apex and reaches the leeward side. As a result, there is a change occurring in the direction of flow due to structural variations. For instance, different negative pressures (-85 Pa, -120 Pa, and -53 Pa) were recorded at the top left of the flat roof, dome roof, and open gable roof, respectively. At these positions, two different wind speeds (20 m/s and 18 m/s) were observed for the dome and open gable roofs, respectively, indicating a significant acceleration of airflow. The unique design of the parapet roof gives rise to a pronounced low-pressure area in its indented region, with the pressure falling below -100 Pa. This leads to vortex formation. In contrast, there is little difference in wind speed inside the other four roofs. Specifically, the respective wind speed reaches 2 m/s and 1.4 m/s on the flat roof, while it reaches 1.4 m/s and 1.1 m/s on the parapet roof. Notably, the wind speed reaches up to 7.3 m/s inside the dome roof, particularly on the right side. This indicates a significant

increase in wind velocity in that direction, which is likely due to the symmetry that causes a non-uniform distribution of airflow.

### 3.3.2 Temperature distribution for the courtyard with different shapes of roof

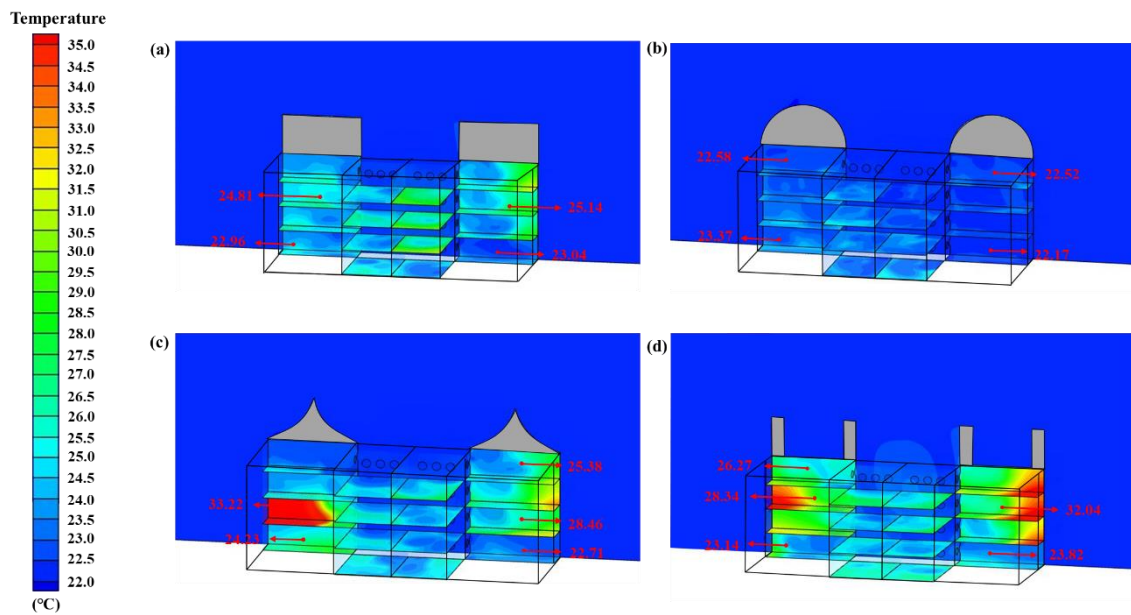


Figure 3.10 Temperature contours in the cross-section at  $Y = 135$  mm for the courtyard with four different roof styles. (a) Flat roof shape courtyard. (b) dome roof shaped courtyard. (c) Chinese curved roof shaped courtyard. (d) parapet roof shape courtyard.

To fully reveal the impact of natural ventilation on indoor temperature control within the courtyard with various roof styles, the outdoor temperature was maintained at  $22$  °C in the CFD simulation, with the heat flux set to  $5$  W/m<sup>2</sup> for all indoor floors. Figure 3.10 illustrates the temperature contour at a section of  $Y = 135$  mm in the courtyard with four different roof styles. According to the results, the significant variation in the cooling effects is attributable to the variation in roof design. Notably, the courtyard with a dome roof, as shown in Figure 3.10 (b), performs the best in cooling, with the temperature across the room maintained

below 24 °C. This is particularly evident on the ground floor and first floor on the right side, where temperature rise is almost negligible, indicating that the courtyard with a dome roof is more effective in indoor heat dissipation through natural ventilation. For the courtyard with a flat roof and that with a Chinese curved roof as shown in Figure 3.10 (a) and Figure 3.10 (c), the difference in temperature across most rooms is minimal, with a better outcome of heat dissipation shown on the leeward ground floor. However, there is an overall uneven distribution of temperature observed, especially in the courtyard with a Chinese curved roof, on the windward side of which the accumulation of heat occurs in the first-floor rooms. It is suggested that ventilation is inadequate in this room, which hinders the wind from entry and suppresses heat dissipation. Among all the roof styles examined, the courtyard with a parapet roof as shown in Figure 3.10 (d) performs worst in terms of temperature regulation. The four rooms within this courtyard accumulate heat, especially on the inner sides, indicating that ventilation is insufficient to remove heat from the deeper areas of the rooms despite the presence of airflow.

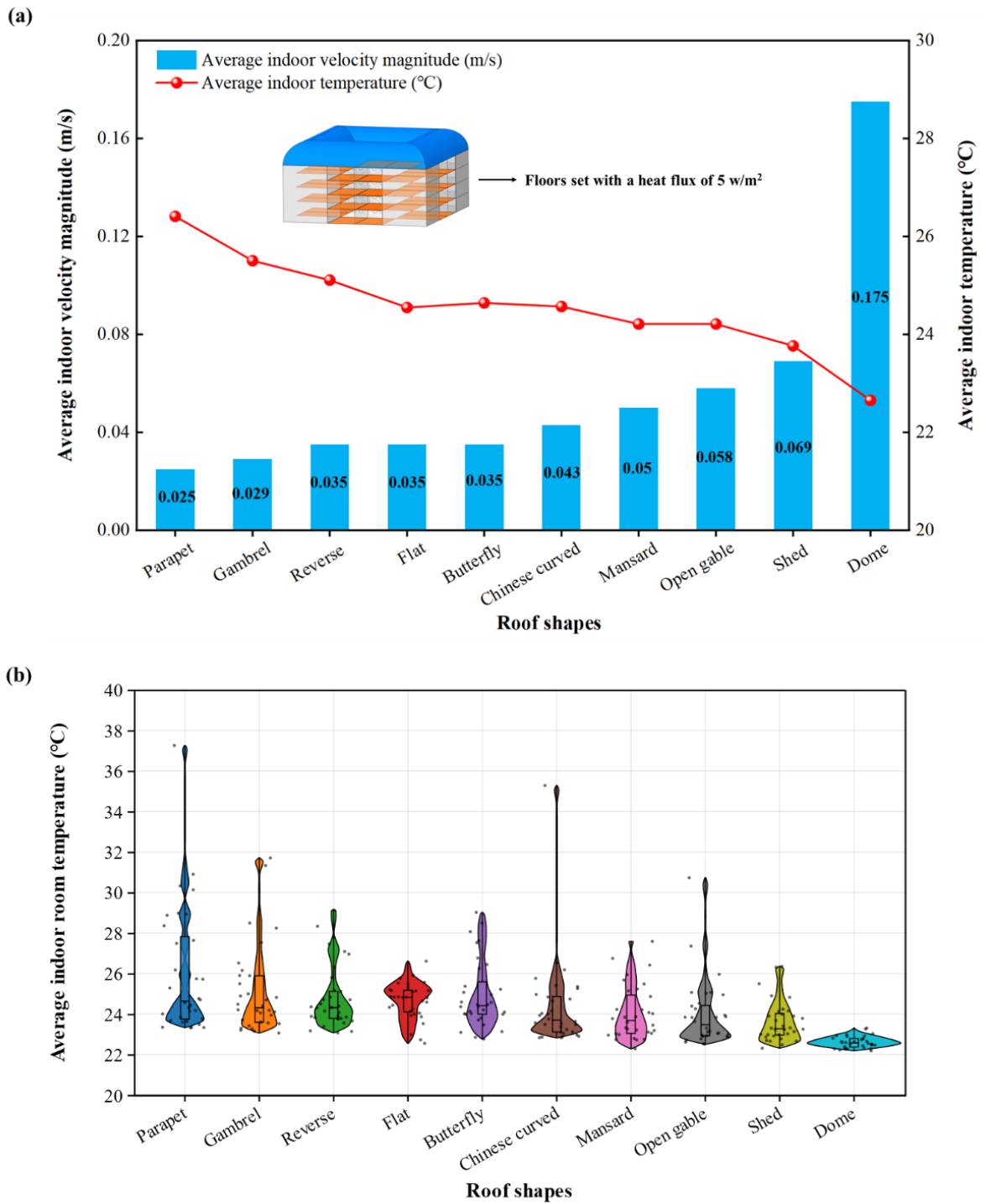


Figure 3.11 Comparison of indoor wind velocity and temperature, and temperature distribution for courtyard buildings with different roof styles. (a) Comparison of average indoor wind velocity magnitude and average temperature for courtyard buildings with ten different roof styles. (b) distribution of average temperatures across 32 test rooms in courtyard buildings with ten roof styles.

Figure 3.11 (a) shows the impact of 10 different roof styles on the average temperature and wind speed within the single-sided ventilated courtyard. According to the results, the dome roof performs best in enhancing the outcome of natural ventilation and regulating indoor temperature, with the maximum average wind speed and the lowest average indoor temperatures reaching 0.175 m/s and 22.65 °C, respectively. In contrast, the lowest average wind speed of 0.025 m/s and the highest average indoor temperature of 26.41°C is reached on the parapet roof, indicating its unsatisfactory performance in ventilation and heat dissipation. Notably, the wind speed on the dome roof is approximately seven times that on the parapet roof, and its average indoor temperature is 14.23% lower, highlighting its significant cooling effect. The shed roof, as the second-best option, has an average indoor temperature of 2.65 °C, which is lower compared to the parapet roof. This evidences its enhanced cooling performance. Compared to the baseline courtyard with a flat roof, the courtyard with a dome roof shows a reduction of the temperature by 2.10 °C and an increase in wind speed by about 0.140 m/s, which confirms its better performance in indoor environmental regulation. Meanwhile, the temperature is 1.66 °C higher in the courtyard with a parapet roof than in that with a flat roof, with a lower wind speed of 0.010 m/s. Among the roofs with indentation in design, the butterfly roof outperforms the parapet roof in cooling, with an average indoor temperature of 1.77 °C lower, suggesting a better outcome of heat dissipation. On roofs with a similar pattern of airflow, such as the courtyard with mansard roof, Chinese curved roof, or open gable roof, the open gable roof stands out with an indoor temperature of 24.21 °C and a wind speed of 0.058 m/s. When an opposite-style shed roof is compared with a reverse shed roof, the shed roof produces a more pronounced effect in terms of ventilation and cooling. Additionally, Figure 3.11 (a) reveals a significant negative correlation between average indoor wind speed and temperature. Specifically, a higher wind speed is typically associated with



lower indoor temperatures, underscoring the effectiveness of strong ventilation for indoor heat dissipation. Evidently, different roof styles vary significantly in the effectiveness of ventilation and indoor temperature reduction.

Figure 3.11 (b) shows the average indoor temperature across 32 rooms with 10 different roof shapes under test. The analytical results demonstrate the unique characteristics and performance of the courtyard with various roof shapes in terms of temperature control, consistency, and stability. Obviously, the shape of the roof has a significant impact on the distribution and regulation of indoor temperatures. Take the dome roof as an example, where the distribution of temperature shows a high degree of concentration, with an average temperature of as low as 22.61 °C and a minimal fluctuation of temperature (standard deviation of only 0.30). This demonstrates its improved performance in indoor temperature control. Both its average and median temperatures are lower compared to all other types of roofs, reaching 22.61 °C and 22.57 °C, respectively. This performance in maintaining the stability of indoor temperature. In contrast, the courtyard with a parapet roof has an average temperature of 26.01 °C, with a wider range of fluctuation (standard deviation of 3.14) from 23.33 °C to 37.26 °C. It is suggested that this is possibly not the ideal choice in hot weather. Differently, the Chinese curve roof still produces a decent performance in temperature control at its average and median temperatures (24.37 °C and 23.70 °C respectively), despite a high frequency of extremely high temperatures (peaking at 35.28 °C and with a skewness of 3.88). Moreover, the courtyard with a flat roof and that with an open gable roof vary in temperature distribution, although their average and median temperatures are relatively comparable (24.65 °C and 24.83 °C vs. 24.83 °C and 23.47 °C). It is indicated that these roof shapes create an environment with stable temperatures under general conditions. The results also illustrate that the "Shed," "Reverse Shed," "Butterfly," "Gambrel," and "Mansard" roof

styles have moderate effects on temperature control. For instance, the "Shed" roof has an average temperature of 23.62 °C with a standard deviation of 1.02, demonstrating high temperature stability. By contrast, the "Reverse Shed" and "Mansard" roofs show a stable, moderate effect in controlling their average and median temperatures, with a standard deviation of 1.54 and 1.34, respectively. It is suggested that these roof styles ensure a relatively stable temperature under normal conditions. Differently, the "Butterfly" and "Gambrel" roofs, despite being slightly higher in average temperature, maintain a controllable range of temperature fluctuation (standard deviations of 1.68 and 2.21 respectively).

### 3.3.4 Analysis of the relationship between courtyard wind dynamics and indoor airflow enhancement

As shown in Figure 3.12, there is a significant negative correlation present between the average indoor wind speed and temperature across different roof styles. That is to say, when indoor wind speed is higher, natural ventilation is promoted, which is equivalent to better heat dissipation, thus lowering the average indoor temperature. In this section, the impact of courtyard wind conditions on indoor average wind speed is explored. Specifically, an investigation is conducted into not only the relationship between the magnitude of the average wind speed in the courtyard and that within indoor environments, but also the connection between the outcome of ventilation and the average indoor wind speed.

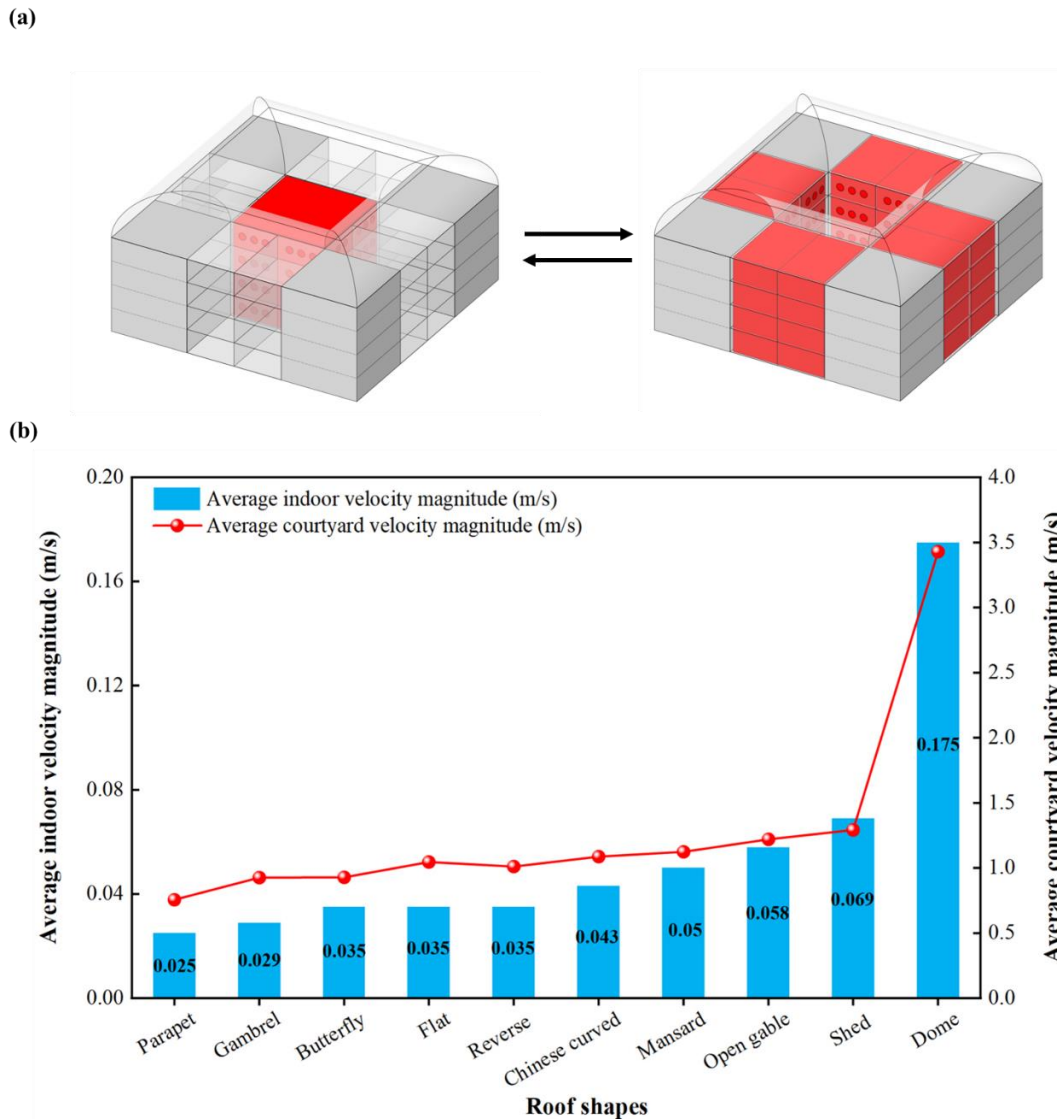


Figure 3.12 Relationship between courtyard and indoor wind velocities for different roof styles. (a) Investigation of the relationship between average wind velocity magnitudes in the courtyard and indoors. (b) comparison of average courtyard wind velocity magnitudes with indoor average wind velocities for courtyard buildings with 10 different roof styles.

Figure 3.12 illustrates the complex relationship between roof shape and the impact of courtyard wind speed on indoor wind speed. The courtyard with a dome roof has an average indoor wind speed of 0.175 m/s. Accordingly, the wind speed in the courtyard is 3.429 m/s, which is significantly higher than other types of roofs. This demonstrates the better

performance of dome roofs in directing courtyard airflow into indoor spaces. In contrast, the courtyard with a parapet roof has the lowest recorded indoor wind speed of just 0.0249 m/s, and the lowest wind speed of 0.756 m/s, reflecting its inadequate outcome of ventilation and heat dissipation. The courtyard with an open gable roof shows moderate wind speed both indoors and, in the courtyard, reaching 1.219 m/s and 0.0577 m/s respectively, which indicates a satisfactory outcome of ventilation. The shed roof achieves an enhanced performance in indoor ventilation with an average wind speed of 0.0695 m/s and a courtyard wind speed of 1.291 m/s. The courtyards with butterfly, flat, and reverse roofs have relatively similar indoor wind speeds, suggesting that these types of roofs maintain a certain level in terms of indoor ventilation performance at comparable courtyard wind speeds. Despite the variation in courtyard wind speed, the differences are insignificant, suggesting a similar efficiency in regulating wind speed. It is necessary to carefully consider these slight variations in courtyard wind speed for architectural design and the assessment of indoor ventilation efficacy, given a significant impact on the indoor thermal environment. Except for the dome, the other nine types of roofs have a lower courtyard wind speed than 1.3 m/s, and the courtyard with shed roof has the courtyard wind speed that is the closest to this threshold. However, there remains a substantial gap compared to the wind speed reached in the case of the dome roof. The indoor wind speed of the dome roof is approximately 2.5 times that of the shed roof, highlighting a clear advantage in enhancing the outcome of indoor ventilation. This is likely attributable to the optimization of its structure for airflow direction and ventilation efficiency. Furthermore, the graph shows a significant positive correlation between courtyard and indoor wind speeds, with the correlation coefficient close to indicating a perfect linear relationship (approximately 0.99). This underscores the significant role of courtyard design in regulating inward natural ventilation.

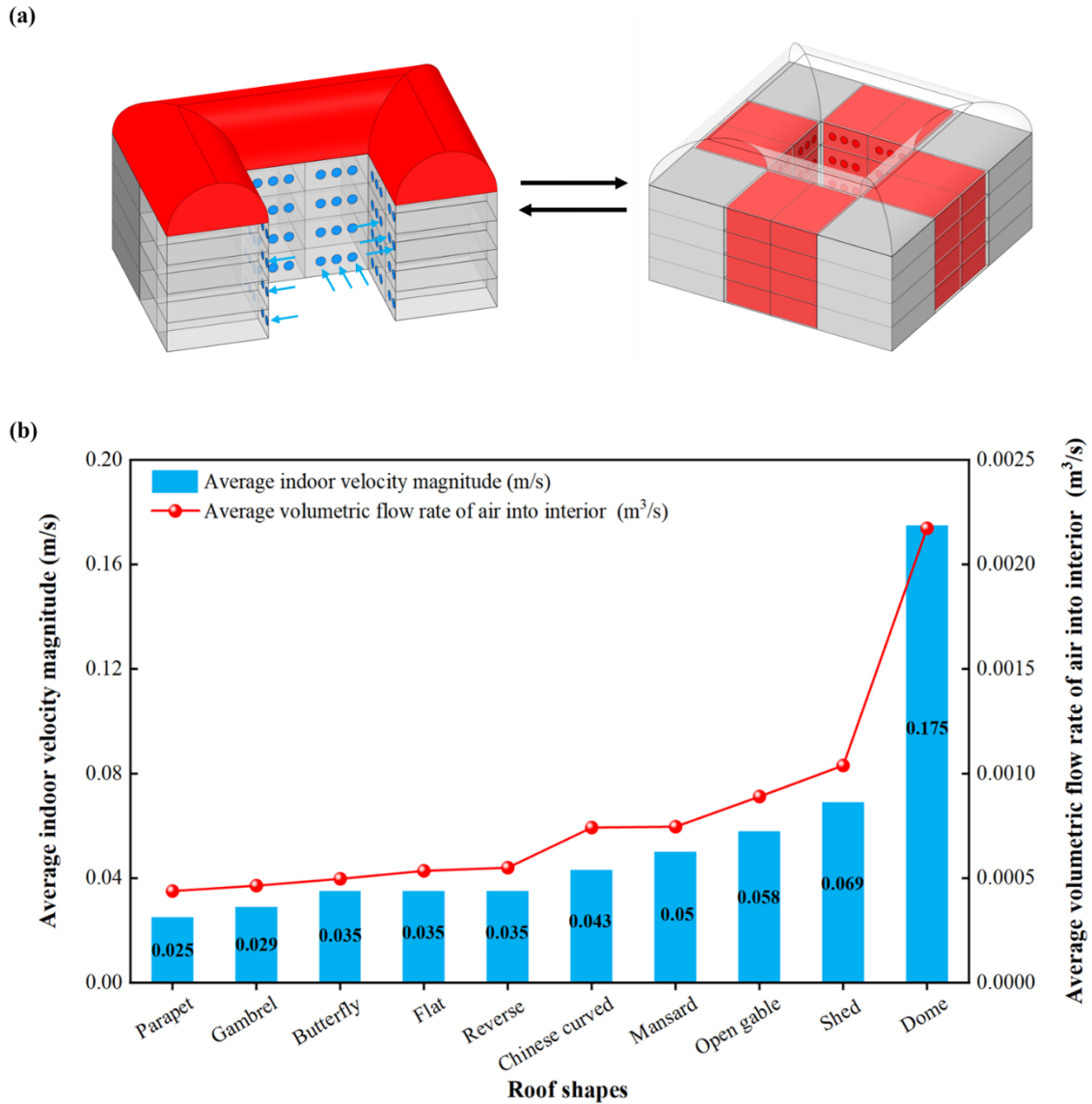


Figure 3.13 Relationship between indoor air flow rate and wind velocity for different roof styles. (a) Exploration of the relationship between the volumetric flow rate of air entering indoors and average indoor wind velocity magnitude. (b) Comparison of indoor average wind velocity magnitudes and the volumetric flow rate of air entering indoors for courtyard buildings with 10 different roof styles.

Figure 3.13 shows a thorough examination of the significant differences in how various roof structures regulate indoor wind speed and airflow volume. The focus of the study is to explore the correlation between the wind speed in the courtyard and the average volumetric

flow rate as well as the average speed of wind entering the room through the openings. Statistically, the courtyard with a parapet roof performs poorly in ventilative cooling efficiency, with an indoor wind speed of merely 0.0249 m/s and a volumetric flow rate of  $4.38 \times 10^{-4} \text{ m}^3/\text{s}$  accordingly. Moderate wind speeds and flow rates are observed mainly in the courtyard with butterfly and reverse roofs, with velocities ranging from 0.0349 m/s to 0.0353 m/s and volumetric flow rates approaching  $5 \times 10^{-4} \text{ m}^3/\text{s}$ . This indicates the moderate effectiveness of these structures in stabilizing airflow. The performance of the courtyard with the open gable roof shape especially that with the shed roof is more effective, with a wind speed of 0.0695 m/s and a volumetric flow rate of  $1.04 \times 10^{-4} \text{ m}^3/\text{s}$  reached. This demonstrates the significant role of the design in indoor air circulation. The courtyard with dome roof stands out with the highest indoor wind speed and volumetric flow rate, reaching up to 0.175 m/s and  $2.17 \times 10^{-4} \text{ m}^3/\text{s}$  respectively. It highlights the clear advantage of the dome roof in enhancing indoor aerodynamics (as shown in Figure 3.14). Specifically, the volumetric flow rate of the dome roof is 2.09 times that of the shed roof, and its indoor wind speed is 2.5 times higher, underlining its significantly better performance in natural ventilation. The courtyards with Butterfly, Flat, and Reverse roofs exhibit the least significant variation in indoor wind speeds, suggesting that these structures achieve comparable ventilation efficiency under similar wind conditions. However, the courtyard with Flat and Reverse roofs is slightly advantageous in volumetric flow rate, which may be attributed to their better structural design that promotes airflow. The high correlation coefficient of nearly 0.995 between average volumetric flow rate and wind speed underscores a significant positive correlation between the amount of air entering indoors and the indoor wind speed, which means a significant impact of courtyard design on inward natural ventilation.

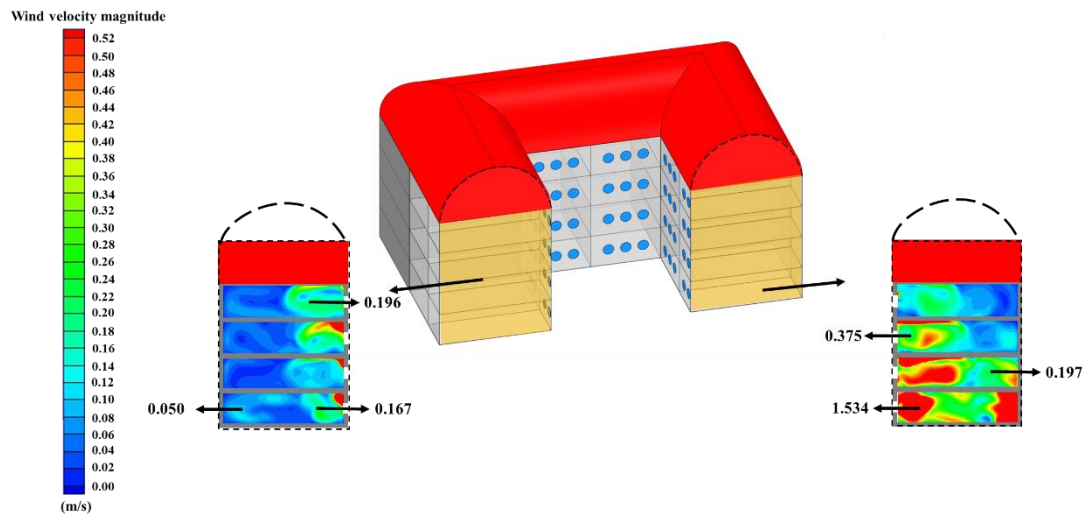


Figure 3.14 Airflow movement patterns in the dome courtyard model and the indoor wind velocity magnitude contour at  $Y = 135\text{mm}$ , with arrows representing the observed vectors.

### 3.4 Discussion

In this section, the results of the CFD simulations are compared with the previous relevant studies. Based on these results, suggestions are made for the improved indoor thermal and airflow conditions of courtyard buildings by modifying the roof design. Additionally, the potential areas of improvement are identified in this research.

#### 3.4.1 Comparison with other studies

By analyzing the impacts of 10 different roof styles on airflow patterns and wind environments in courtyard buildings, it is discovered in this study that the shape of the roof has a significant impact on the recirculation zones above the roof, the reattachment length of the wind, and the position of the shear layer. Consequently, the airflow within the courtyard space is affected. This conclusion is consistent with Prakash (2023), who observed similar

phenomena when analysing the effect of seven different roof styles on courtyard buildings. Additionally, it is observed in this study that the geometry of the roof can make a difference to the negative pressure in the building, thus enhancing wind-driven ventilation. Since the vortices formed on the leeward side of buildings with different roof styles vary in size, change occurs in the flow of air from the exterior to the courtyard and indoor areas. In the study of Peren et al. (2015), it was highlighted that straight or convex roofs can maximize the negative pressure in the building, thereby improving the efficiency of wind-driven cross-ventilation. In this research, a broader range of roof styles is analysed to reveal that the patterns of airflow in courtyard buildings are more complex than in standalone structures. Nonetheless, both studies underscore the significant impact of roof geometry on the wind environment around the buildings.

Through an analysis of various roof styles used in courtyard buildings, it is revealed in my study that dome-shaped roofs, with their unique curvature, can significantly enhance the outcome of natural ventilation both inside and outside the building, which makes it advantageous over other roof styles. This finding is coherent with Esfeh et al. (2021), where the effects of semi-cylindrical curved roofs on natural ventilation are explored by conducting experiments and numerical simulations at different wind direction angles ( $\alpha$ ). According to their results, the ventilation efficiency of curved roofs is largely determined by the wind direction, with the outcome of ventilation achieved at  $0^\circ$ . This effect is attributed primarily to the changes in pressure difference at the openings, as driven by the airflow acceleration and separation essential for ventilation. Moreover, the height of the curved roof plays a crucial role in enhancing the effectiveness of internal airflow circulation. In the study of Esfeh et al. (2021), it is further demonstrated that semi-cylindrical curved roofs can improve indoor natural ventilation compared to wind-catchers, with greater cost-effectiveness achieved in



terms of structural expenses. Similarly, the study by Asfour & Gadi (2008) used CFD technology to support these findings, examining the effectiveness of dome and vaulted roofs in improving wind-driven natural ventilation, while taking into account various climatic and geometric factors. According to their research results, these roof styles can increase the inflow rate in the building and effectively improve ventilation in its upstream and central areas by redirecting airflow from roof openings rather than wall openings. Additionally, it is indicated in their study that there are many similarities between dome and vaulted roofs in the efficiency of ventilation. In Prakash (2023), an investigation is conducted into the impact of various roof styles on airflow above the courtyard buildings, including flat, pitched, pitched inward, pitched outward, curved, pitched outward with a curve, and the curve with pitched inward roof shapes. As revealed by the research, among all the roof shapes analysed, the pitched roof and curve with pitched inward roof performed relatively better in terms of airflow within the courtyard space, while flat roofs performed worst (Prakash, 2023). Consistent with our findings, it was also indicated that roof style has a significant impact on the wind environment of courtyard buildings. Differently, this research went further to demonstrate that dome-shaped roofs produce a better outcome of natural ventilation, with parapet roofs being the most ineffective. This variation may arise from the differences in courtyard design between the two studies. The finding from Prakash (2023), hybrid roof structures were studied. In our study, a broader range of roof styles are examined. Moreover, it is indicated in our research that changing roof styles can not only optimize the outcome of natural ventilation within courtyard buildings but also enhance indoor heat dissipation. This argument is confirmed in Prakash (2023), where it was found that the changes in roof structure could lead to a significant improvement in the level of indoor thermal performance.

### 3.4.2 Limitations and recommendations for future works

This study focuses primarily on investigating the impact of different roof styles on the indoor and outdoor wind and thermal environment in single-sided ventilated courtyard buildings. However, the specific effects of roof height and slope on airflow are ignored. In the study of Zobaied et al. (2022), it was suggested that an increase in roof slope could improve wind speed at the windows and roof openings, with airflow behaviour and characteristics largely affected by the roof slope. These findings indicate an important direction for future research. Moreover, the wind direction was set to  $0^\circ$  in this study, and the impact of other wind directions was not considered. Different wind directions could result in varying airflow patterns and thermal performance, potentially leading to different outcomes for the effectiveness of various roof styles. This is another area for improvement and should be addressed in future studies to provide a more understanding of roof performance under diverse wind conditions. The courtyard model used in this study is based on a wind tunnel experiment, which presents some differences compared to actual buildings and boundary conditions. Due to the single-sided ventilation model, the indoor wind speed and ventilation rate are very low. Additionally, being a scaled-down model, certain boundary conditions, including wind speed and heat flux settings, differ from real-life scenarios. However, this model serves as a hypothetical scenario. Future research can explore real-scale conditions to provide more accurate and applicable results. Also, it is worth considering in future research to simulate actual buildings and conduct field tests on the effects of different roof styles. Lastly, for the verification and simulation of CFD, the widely used RANS model is applied for comparative research. This is because of their applicability to predict airflow in courtyard buildings and the relatively low computational costs to incur. In this study, the *k*- $\omega$  standard model is selected considering the validation from wind tunnel experiment data.

Allowing for computational resources and time efficiency, the large eddy simulation (LES) model is discarded from this study. Nevertheless, given the high accuracy of the LES model in describing complex flows, it can be applied for future research. Further studies will be conducted to explore the application of curved solar panels in courtyard buildings, as discussed in Section 3.4.2.

### 3.5 Conclusion

This study presents an analysis of how different roof styles affect the aerothermal environment inside and around single-sided ventilated courtyard buildings. In the previous research on natural ventilation in courtyards, the focus is placed primarily on buildings with flat roofs, with relatively little attention paid to the effects of different roof designs. Additionally, prior studies overlook the indoor environment surrounding the courtyard. Despite the prior research in which a significant impact of roof shape on airflow movement patterns is demonstrated, these investigations are mostly limited to individual buildings or urban street settings, with limited attention paid to discussing the application of different roof styles in courtyard architecture. Therefore, this research aims to fill this gap by conducting thorough CFD validation on courtyard and atrium buildings based on wind tunnel experiments and by comparing the performance of various commonly used turbulence models in model validation. It was found that the k-omega standard model performed well in validating wind tunnel experiment models, with a higher accuracy than 80% reached. Based on the wind tunnel experiment design, the courtyard model incorporates some innovative changes made to its roof styles, involving ten common roof styles: the baseline flat roof shape, dome roof shape, butterfly roof shape, parapet roof shape, Chinese curved roof shape, mansard roof shape, open gable roof shape, gambrel roof shape, shed roof shape, and reverse

shed roof shape. This provides a new perspective on optimizing the wind and thermal environment in courtyard architecture.

Through the CFD simulation analysis of ten different roof styles, it is discovered in this study that:

1. Roof shape has a significant impact on the recirculation above the roof, the length of wind attachment, and the position of shear layers, which in turn affects the distribution of airflow within the courtyard. Moreover, the geometric design of the roof can affect the negative pressure areas in the building, thereby enhancing the effectiveness of wind-driven ventilation. Specifically, the dome roof, with its streamlined design, makes the airflow closer to the surface. As a result, the outcome of natural ventilation is significantly better than other roof styles, with an indoor average wind speed that is 0.14m/s higher than the baseline model (flat roof). Among all the roof styles under study, the parapet roof shape performs worst, as its unique recessed design causes the accumulation of much airflow in the recessed area, with an indoor average wind speed of only 0.025 m/s. Although some roof styles lead to similar indoor wind speeds, their efficiency may differ in guiding and maintaining wind speed within the courtyard. Such slight differences in wind speed in the courtyard can have a significant impact on the indoor wind and thermal environment during the architectural design and evaluation of indoor ventilation performance.
2. To investigate the impact of roof styles on the efficiency of natural ventilation for single-sided ventilated courtyard buildings and their performance in the dissipation of indoor heat, a heat flux is created inside the building. The results show a linear relationship

between the indoor wind speed and the effect of cooling. That is to say, the higher the indoor wind speed, the more heat is dissipated. Among them, the lowest indoor temperature is reached in the courtyard with a dome roof shape, that is, 22.61°C. In contrast, the courtyard with a parapet roof shape records the highest indoor temperature.

3. Compared to the courtyard buildings with cross ventilation, those with single-sided ventilation better reflect the impact of the courtyard on the indoor wind and thermal environment, thus reducing external disturbances. According to the simulation results, there is a linear relationship present between indoor wind speed and both the wind speed in the courtyard and the volumetric flow rate of air entering the building from the courtyard. That is to say, the outcome of ventilation can be achieved by increasing the wind speed in the courtyard and the volumetric flow rate of inward air.

This study provides a novel perspective on improving future courtyard architectural design, with recommendations made for the modification to non-domed roofs. Also, it highlights the potential of "Shed" and "Dome" roof styles in significantly improving the efficiency of natural ventilation, which makes them particularly suited to environments requiring enhanced airflow. For the roof shapes that generate lower wind speeds, additional ventilation strategies may be required to ensure a sufficient comfort level. Furthermore, these recommendations are worth considering for architects to integrate natural ventilation mechanisms during the design process for a more energy-efficient and environmentally friendly building environment. It also reflects the importance of paying closer attention to the impact of roof shapes on the dynamics of indoor and outdoor airflow in the design of courtyard buildings.

## Chapter 4 Courtyards with Evaporative Cooling Strategies

### 4.1 Introduction

This chapter focuses on evaluating the wind and thermal efficiency of courtyard buildings that incorporate natural ventilation methods and water spraying systems through CFD modelling with ANSYS Fluent. It aims to assess how water sprayers affect the aerothermal environment of courtyards in arid climates and to evaluate the effectiveness of cross-ventilation and unilateral ventilation strategies in such buildings, especially when paired with evaporative cooling techniques. The validity of the CFD simulations will be compared with data from wind tunnel experiments, taking into account variables like wind velocity, air temperature, and humidity across different locations within the courtyard buildings. It's important to mention the study's limitations: there is an inherent margin of error between the wind tunnel experiments and CFD simulations due to the model's complexity and external environmental influences, making some discrepancies unavoidable. Furthermore, the research relies on CFD simulations derived from a simplified wind tunnel model rather than actual field experiments, which may not fully represent the myriad of complex factors present in real-world settings.

### 4.2 Method

In the methodology section, I initiated my exploration with an analysis of the theoretical foundations of CFD and the definition of the solver settings. Subsequently, I described the courtyard model, including its dimensions, structural layout, and configuration in the simulation environment. Next, I presented the fluid domain setup, including the

determination of the spatial range and key characteristics of fluid flow. These chosen settings ensured the simulation environment's accurate capture of key phenomena in fluid dynamics. Additionally, I showcased specific details of the grid design, including the type, size, and distribution strategy of the grid, aimed at capturing complex phenomena. The accuracy and stability of the simulation results were assessed through mesh independence verification. Finally, this section explains the simulation's boundary conditions, including fluid inlet and outlet conditions, wall conditions, and other boundary conditions.

#### 4.1.1 CFD theory

The steady-state, three-dimensional simulations were performed using the ANSYS Fluent 2021R2 CFD tool and the Reynolds-Averaged Navier-Stokes (RANS) equations. The *k*-epsilon realizable model (Shih et al., 1995) was utilized to simulate turbulence, with both continuous and discrete phases of the flow being solved on a fully coupled technique. The following sections will detail the justification for selecting this particular turbulence model. Additionally, the droplet momentum, heat, and mass transport equations are addressed in a fully coupled manner within the discrete phase. A SIMPLE algorithm is used for pressure-velocity coupling. Second-order interpolation is applied for pressure calculations, and both convective and viscous elements within the equations are solved by a second-order discrete technique. The governing equations, as defined by the commercial CFD code ANSYS/Fluent (Ansys Fluent Theory Guide 2021R2 [Online], 2021). The continuity, momentum, energy, and turbulent kinetic energy equations are presented from Eq. (3.1) to Eq. (3.4). The equation for turbulent dissipation rate ( $\epsilon$ ) is shown in Eq. (4.1), and the species equation is given in Eq. (4.2).

$\epsilon$  Equation (Turbulent dissipation rate):

$$\nabla \cdot (\rho \vec{u} \epsilon) = \nabla \cdot \left[ \left( \mu + \frac{\mu_t}{\sigma_\epsilon} \right) \nabla \epsilon \right] + C_{1\epsilon} \frac{\epsilon}{k} P_k - C_{2\epsilon} \rho \frac{\epsilon^2}{k} \quad (4.1)$$

Where  $\mu$  is molecular viscosity,  $\mu_t$  is turbulent viscosity,  $\sigma_k$  and  $\sigma_\epsilon$  are Prandtl numbers,  $C_{1\epsilon}$  and  $C_{2\epsilon}$  are constants, which are 1.44 and 1.9. And  $P_k$  is the production of turbulent kinetic energy.

Species Transport Equation:

$$\nabla \cdot (\rho \vec{u} Y_i) = -\nabla \cdot J_i + R_i \quad (4.2)$$

Where  $Y_i$  is the mass fraction of the species  $i$ ,  $J_i$  is the diffusion flux, and  $R_i$  is the rate of reaction.

The Discrete Phase Model (DPM) is particularly pertinent for this study involving water sprayers, as it enables a detailed analysis of droplet dynamics. This model is essential for accurately simulating the behaviour of water droplets, including their dispersion, evaporation, and interaction with the surrounding air, which are critical factors in evaluating the effectiveness of the sprayers in modifying the courtyard's microclimate. Eq.4.3 to Eq.4.8 Montazeri et al. (2015a) show the DPM equations used in this research.

Droplet Motion Equation:

$$\frac{d\vec{U}_d}{dt} = \vec{F}_{\text{drag}} + \vec{F}_{\text{gravity}} + \vec{F}_{\text{buoyancy}} + \vec{F}_{\text{Saffman}} + \vec{F}_{\text{Magnus}} \quad (4.3)$$

$$\vec{F}_{\text{drag}} = \frac{1}{2} \rho C_d A_d \cdot (\vec{U}_d - \vec{U}_f) \cdot (\vec{U}_d - \vec{U}_f) \quad (4.4)$$



$$\vec{F}_{\text{gravity}} = m_d \cdot g \quad (4.5)$$

$$\vec{F}_{\text{buoyancy}} = -\rho V_d \cdot g \quad (4.6)$$

$$\vec{F}_{\text{Saffman}} = C_s \mu \sqrt{\frac{\rho}{\mu}} (\vec{U}_d - \vec{U}_f) \quad (4.7)$$

$$\vec{F}_{\text{Magnus}} = C_m \mu \vec{U}_f \omega \quad (4.8)$$

Where  $\vec{F}_{\text{drag}}$ ,  $\vec{F}_{\text{gravity}}$ ,  $\vec{F}_{\text{buoyancy}}$ ,  $\vec{F}_{\text{Saffman}}$ ,  $\vec{F}_{\text{Magnus}}$  represent forces due to drag, gravity, buoyancy, saffman, and magnus effects, respectively.  $\vec{U}_d$  is the droplet velocity,  $\vec{U}_f$  is the fluid velocity,  $C_d$  is the drag coefficient,  $A_d$  is the surface area of the droplet,  $m_d$  is the droplet mass,  $g$  is the gravitational acceleration.  $V_d$  is the droplet volume,  $C_s$  is the Saffman lift coefficient and  $\mu$  is the fluid dynamic viscosity.  $C_m$  is the Magnus force coefficient and  $\omega$  is the droplet angular velocity.

Droplet Evaporation and Heat Exchange Equation:

$$\frac{dm}{dt} = -A_d \sum N_i \quad (4.9)$$

$$\frac{dQ}{dt} = hA_d(T_f - T_d) - \lambda \frac{dm}{dt} \quad (4.10)$$

Where  $\frac{dm}{dt}$  is the mass transfer rate of the droplet,  $\frac{dQ}{dt}$  is the heat transfer rate of the droplet.  $m$  is the mass of the droplet,  $A_d$  is the surface area of the droplet, and  $N_i$  is the mass transfer rate of species  $i$ .  $Q$  is the heat energy,  $h$  is the convective heat transfer coefficient,  $T_f$  is the fluid temperature,  $T_d$  is the droplet temperature, and  $\lambda$  is the latent heat of evaporation.

Mass Transfer Rate Equation:

$$N_i = k_c(C_{i,s} - C_{i,\infty}) \quad (4.11)$$

Where  $k_c$  is the mass transfer coefficient,  $C_{i,s}$  is the concentration of species  $i$  at the droplet surface, and  $C_{i,\infty}$  is the concentration in the free stream.

Sherwood Number Equation:

$$\text{Sh} = \frac{k_c d_p}{D_{i,m}} = 2.0 + 0.6 \text{Re}_d^{0.5} S_c^{0.33} \quad (4.12)$$

Sh is the Sherwood number,  $d_p$  is the droplet diameter,  $D_{i,m}$  is the molecular diffusivity of species  $i$ ,  $\text{Re}_d$  is the droplet Reynolds number (Montazeri et al., 2015a), and  $S_c = 0.7$  is the Schmidt number.

## 4.1.2 CFD geometry

### 4.2.2.1 Courtyard and computational domain

The courtyard building models presented in this work were based on the wind tunnel experiments on scaled courtyards and atriums models carried out by Sharples & Bensalem (2001), who monitored airflow and air pressure in the courtyard and atriums exposed to the urban wind flow, evaluating various window-to-wall ratios and wind directions. In this study, I utilized courtyard architectural models featuring two distinct ventilation methods, as derived from previous wind tunnel experiments (as shown in Figure 4.1). The courtyard models used in these wind tunnel experiments were scaled down to a ratio of 1:100. However, for my CFD simulations, I scaled up the wind tunnel models to their original, actual sizes. This approach ensured that the simulation results more accurately reflected the real courtyard architectural environment.

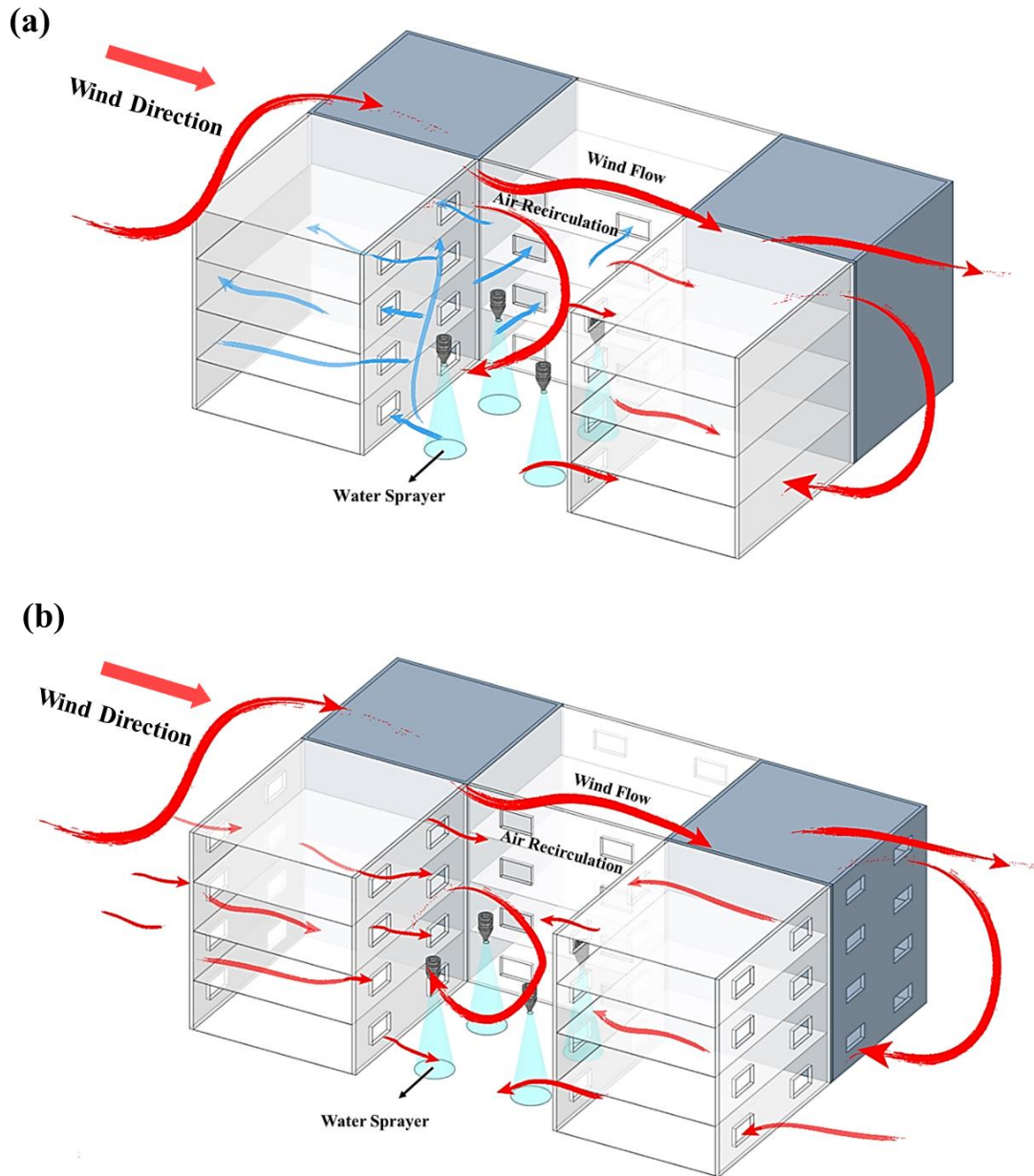


Figure 4.1 Single-sided ventilated and cross-ventilated courtyards with water sprayers. (a) Single-sided ventilated (SSV) and (b) cross-ventilated (CV) courtyard with water sprayers.

For both cross-ventilated (CV) and single-sided ventilated (SSV) courtyards, the full-scale sizes ( $L \times W \times H$ ) were  $33.9 \text{ m} \times 33.9 \text{ m} \times 13 \text{ m}$ , as shown in Figure 4.2 (a) and Figure 4.2 (b). Each courtyard building consisted of four stories, with each floor measuring  $3.25 \text{ m}$  in height. As depicted in Figure 4.2 (d), the courtyard was situated in the centre of the structure, spanning  $12.62 \text{ m} \times 12.62 \text{ m}$ . In the SSV courtyard, all 32 windows faced the

courtyard. In contrast, a specific number of windows were allocated on the facade of the CV courtyard building to simulate cross ventilation. The distribution and size of all windows ( $2\text{ m} \times 1.047\text{ m}$ ) were retained and consistent with the previous research Sharples & Bensalem (2001), presenting an 11.4% window-to-wall ratio, and the window opening ratio was set to 20% for a more accurate reproduction of the actual scenario as illustrated in Figure 4.2 (c). The exact distribution of rooms was applied to the CV courtyard and the SSV courtyard, with each test room measuring 12.62 m in width and 10.64 m in depth. Each floor included four test rooms positioned in east, west, north, and south. All rooms near the courtyard were separately labelled according to the floor and room orientation to analyse the wind and temperature variables in the different rooms as presented in Figure 4.2 (e).

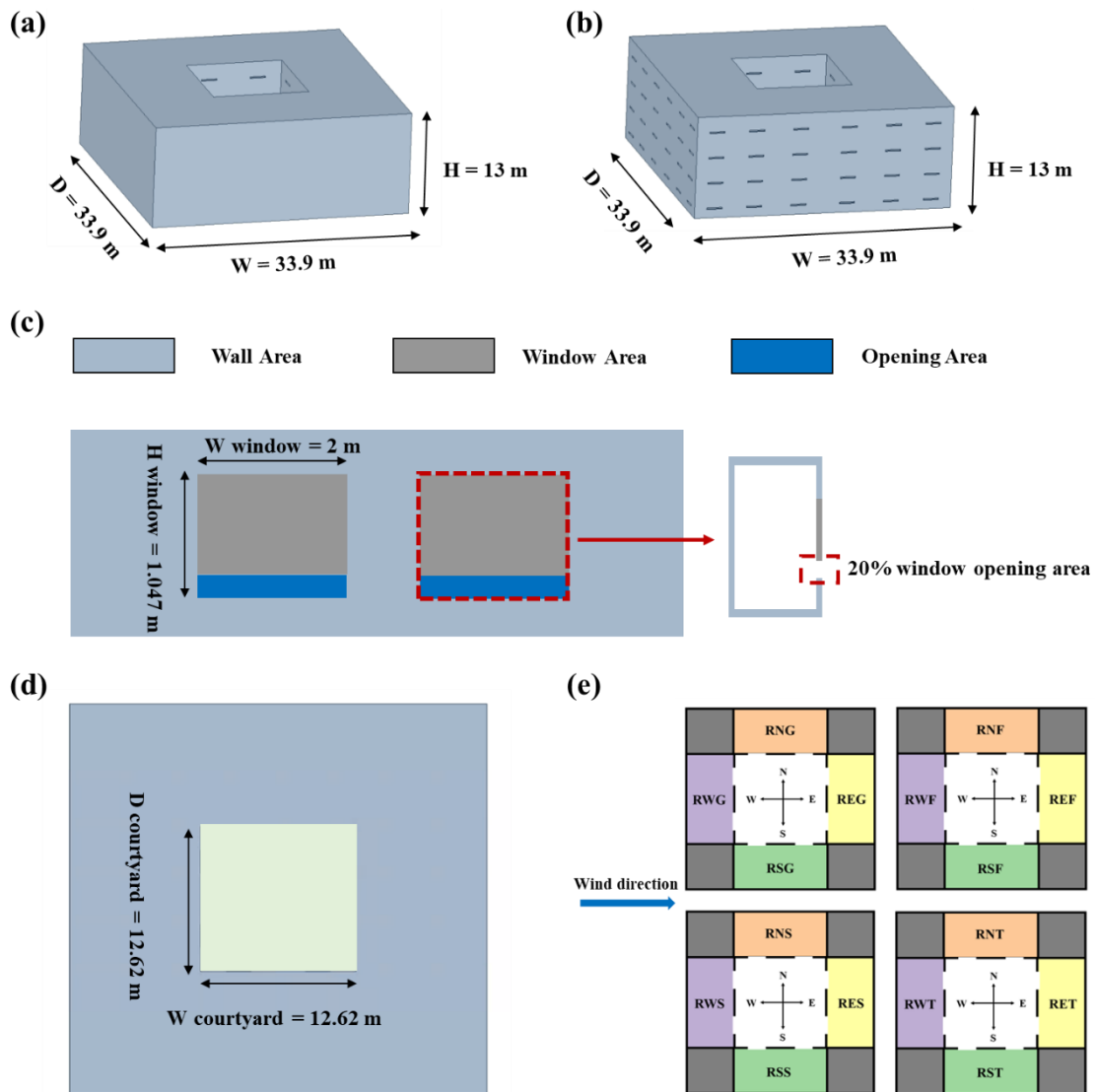


Figure 4.2 Dimensions and arrangement of SSV and CV courtyards, window openings, and test rooms. (a) The dimension of the SSV courtyard. (b) The dimension of the CV courtyard. (c) The dimension of each window and the size of the opening area. (d) The location and the size of the courtyard area. (e) The arrangement of each test room (R—Room, N—North, W—West, S—South, E—East, G—Ground floor, F—First floor, S—Second floor, T—Third floor. The second letter on the label represents the orientation and the third represents the floor).

This research simulated indoor and outdoor airflow within a single computational domain, as demonstrated in Figure 4.3 (a). The domain size generally accords with best practice recommendations for wind flow simulations, as detailed in (Abu-Zidan et al., 2021; Blocken, 2015; Franke, J & A. Hellsten, K. Schlünzen, B. Carissimo, 2007; Tominaga et al., 2008). In the computational domain, both side walls and the top wall were defined as symmetry walls. The distance from the courtyard to the two side symmetry walls was set at 5 H, where H is the height of the courtyard building. The distances from the courtyard to the inlet and outlet were set at 8 H and 20 H, respectively. Additionally, the distance from the courtyard to the top wall of the domain was established at 5 H. As can be seen in Figure 4.3 (b), in both SSV and CV courtyards, four identical evaporative spray injectors were set, positioned at a height of 6.5 meters above the ground and uniformly distributed in the central area of the courtyard. To ensure uniform distances between the injectors, as well as between the injectors and the courtyard walls, the spacing was set at 4.2 m both between each injector and from the injector to the walls. The injectors were directed vertically downward. Detailed boundary conditions are provided in the following sections.

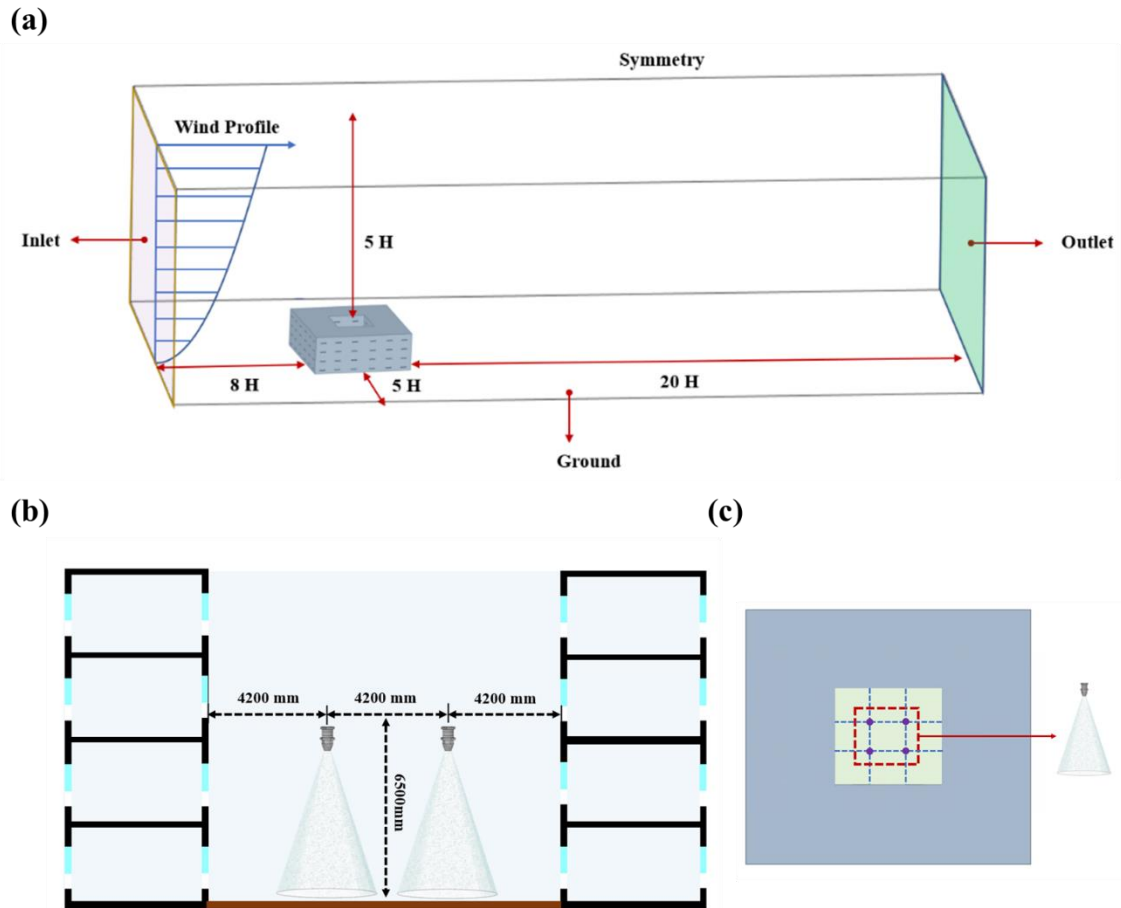


Figure 4.3 The simulation setup demonstrates the computational domain and the location of water sprayers. (a) The dimension of the computational domain and the boundary conditions. (b) The dimension, and (c) the placement of 4 water sprayers inside the courtyard.

### 4.1.3 CFD mesh design and verification

The ANSYS 2022 Meshing tool was used to generate the computational domain grid, forming a tetrahedral grid, and the results were imported into Fluent to generate polyhedral meshes, as shown in Figure 4.4 (a). In the simulation, to accurately capture the wind-thermal environment within the courtyard and its surrounding buildings, the grid of the entire simulation area was refined to a granularity of 0.2 m. Specifically, for a more precise simulation of the flow characteristics near windows, the grid in these key areas was further

refined to a mesh size of 0.05 m. Such grid settings were conducive to capturing flow variations within the indoor environment with greater detail. To reduce the calculation time and to ensure the quality of the mesh, the other areas utilized a coarse grid size of 3.5 m. The mesh settings for both the SSV and CV courtyard were identical.

Sensitivity analysis requires using the same model with different mesh sizes to confirm that the mesh size has a minimal effect on the simulation results. The CV courtyard was selected for grid independence analysis, as detailed in Table 1. In addition to the baseline grid consisting of 1,790,681 cells, classified as a medium-sized grid, two additional grid sizes were generated. A coarse mesh containing 941,223 cells and a fine mesh comprising 6,998,825 cells were generated by adjusting the mesh size for the CV courtyard building.

Mesh Size	Mesh Setup	Number of		Average error relative to fine mesh size (%)
	Courtyard building surface size (mm)	Elements	Nodes	
Coarse	300	941,223	4,962,961	3.69
Medium A	200	1,790,681	9,878,792	1.24
Medium B	160	2,793,534	15,517,712	1.02
Medium C	120	5,001,735	28,032,923	0.87
Fine	100	6,998,825	39,334,552	-

Table 4. 1 Mesh sensitivity analysis for the CV courtyard with polyhedral mesh.

On the first floor, a horizontal line was drawn, traversing the room and the courtyard. Figure 4.4 (b) compares the horizontal wind speed magnitude between five distinct grid sizes. According to the results, the average error between the Medium A and the Coarse mesh was 2.45%, while the error between the Medium A and Fine mesh was 1.24%. This confirms that the different mesh sizes have minimal impact on the simulation outcomes. Therefore, this study chose the medium A-sized grid to reduce computing power requirements. In subsequent simulation studies, the SSV courtyard model utilized a total of 1,266,979



polyhedral mesh elements (comprising 7,126,317 nodes), while the CV courtyard model employed 1,790,681 polyhedral mesh elements (comprising 9,878,792 nodes).

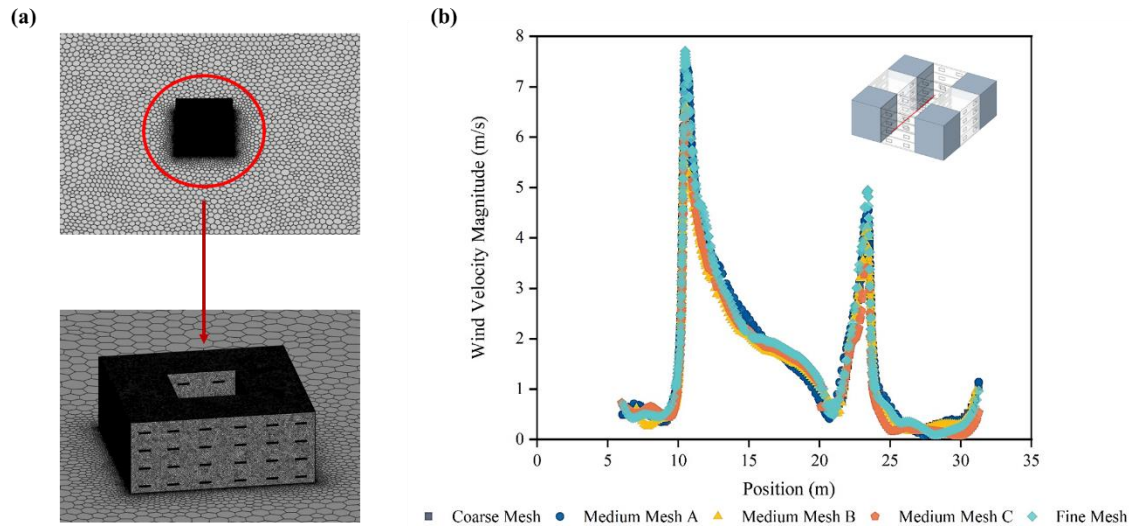


Figure 4.4 Polyhedral mesh of courtyard building and simulated wind speed results for grid sensitivity analysis. (a) The courtyard building and outdoor environment surfaces meshed with a polyhedral mesh. (b) Simulated wind speed results along a horizontal centre line of the courtyard model at the height of 4.45 m for the grid sensitivity analysis.

#### 4.1.4 Boundary conditions for the simulation study

In the setup shown in Figure 4.3 (a), a surface was selected as the velocity inlet, and the wind speed distribution at the inlet was determined by referring to atmospheric boundary layer (ABL) wind tunnel experiments to simulate airflow within the computational domain (Sharples & Bensalem, 2001). In all simulated scenarios, the inlet wind speed distribution was maintained consistently. The calculation of the average wind speed was based on a power law formula that was calibrated with wind tunnel measurement data. The formula is defined as follows:

$$u(z) = u_{\text{ref}} \left( \frac{z}{z_{\text{ref}}} \right)^{\alpha} \quad (4.13)$$

where  $u(z)$  is the mean velocity at height  $z$  (m/s),  $\alpha = 0.245$  is the power law exponent found by curve fitting the wind tunnel result,  $z_{\text{ref}} = 800$  mm is the reference height, which is the height at the eaves level,  $u_{\text{ref}}$  is the velocity measured at the reference height in the experiment, which is 16.4m/s (Sharples & Bensalem, 2001). Subsequently, this wind speed distribution was applied to the inlet boundary within the computational domain. In this way, the simulation was able to accurately reproduce the wind speed distribution observed in experiments. The opposite side was set as a pressure outlet at 0 Pa.

The study location was based in Seville, Spain (coordinates 37°22'58" N, 5°58'23" W, elevation 16 m), chosen primarily due to the region's unique climatic conditions and the abundance of traditional courtyard buildings. Particularly during the hot seasons, Seville frequently experiences heatwaves, prompting a thorough analysis of the courtyards' regulatory functions and thermal environment (Diz-Mellado, López-Cabeza, et al., 2023a, 2023b). Given the focus of this study on hot and dry climatic conditions, the temperature (40°C) and relative humidity (15%) of the region on July 17, 2023, at 6 PM were chosen as the inlet boundary conditions for the CFD simulation, maintaining these conditions constant (Seville, Spain Weather History, Weather Underground, n.d.). The purpose of this approach was to analyse the cooling and humidifying effects of water spraying devices in the courtyard environment. The simulation in the CFD included the influence of buoyancy, and the gravity was set to  $-9.81 \text{ m/s}^2$ . The top and two side walls were defined as non-slip boundary conditions. For the material settings of the model, ash solid and brick were utilized for the ground and courtyard structure, respectively.

According to previous works, the evaporative cooling spray system, equipped with four injections, was modelled based on the injection model available in Fluent 2022 (Montazeri et al., 2015b, 2017). The settings for the spray and droplet characteristics are detailed in Table 2. The volume flow rate, temperature, and velocity of water spray were set to 3 l/min, 30 °C and 15 m/s, respectively (Montazeri et al., 2017). The number of droplet streams for the spray was defined as 300, and the Rosin-Rammler model was adopted to establish the diameter distribution of droplets in the simulations (Vesilind, 1980). According to the settings of the Rosin-Rammler model (Montazeri et al., 2015b), the minimum and maximum diameters of droplets taken into account in the simulations were 74 µm and 518 µm, respectively, with the mean diameter established at 369 µm and the spread parameter set at 3.67. In addition, the number of diameters per stream assumed to be introduced into the courtyard space was 20. Additionally, the drag coefficients for the drag force exerted on droplets were estimated by the spherical drag law with the assumption that the droplets remain undeformed.

Time	Steady state
Velocity inlet	ABL (m/s) from (Sharples & Bensalem, 2001)
Temperature inlet	40°C
Relative humidity inlet	15%
Pressure outlet	Atmospheric
Gravity	-9.81 m/s <sup>2</sup>
Building – Brick (ASTM C67 Standard, 2014)	Density: 1900 kg/m <sup>3</sup> , C <sub>p</sub> : 840 J/kgK, Thermal Conductivity: 0.72 W/mK
Ground – Ash solid ( <i>Ansys Fluent Theory Guide 2021R2 [Online]</i> , 2021)	Density: 600 kg/m <sup>3</sup> , C <sub>p</sub> : 7950 J/kgK, Thermal Conductivity: 0.071 W/mK

<b>Spray settings</b> (Montazeri et al., 2015b, 2017)	
Mass flow rate of water spray streams	3 L/min
Temperature of water spray streams	30 °C
Water flow velocity	15 m/s
Direction of water spray streams	Downward
<b>Droplet settings</b> (Montazeri et al., 2015b, 2017)	
Number of droplet streams	300
Droplet diameter distribution model	Rosin-Rammler model
Number of diameters per droplet stream	20
Maximum diameter	518 $\mu\text{m}$
Minimum diameter	74 $\mu\text{m}$
Mean diameter	369 $\mu\text{m}$
Spread parameter	3.67

Table 4. 2 Summary of the CFD model boundary conditions.

## 4.3 Result of this chapter

### 4.3.1 Validation of the water sprayer model

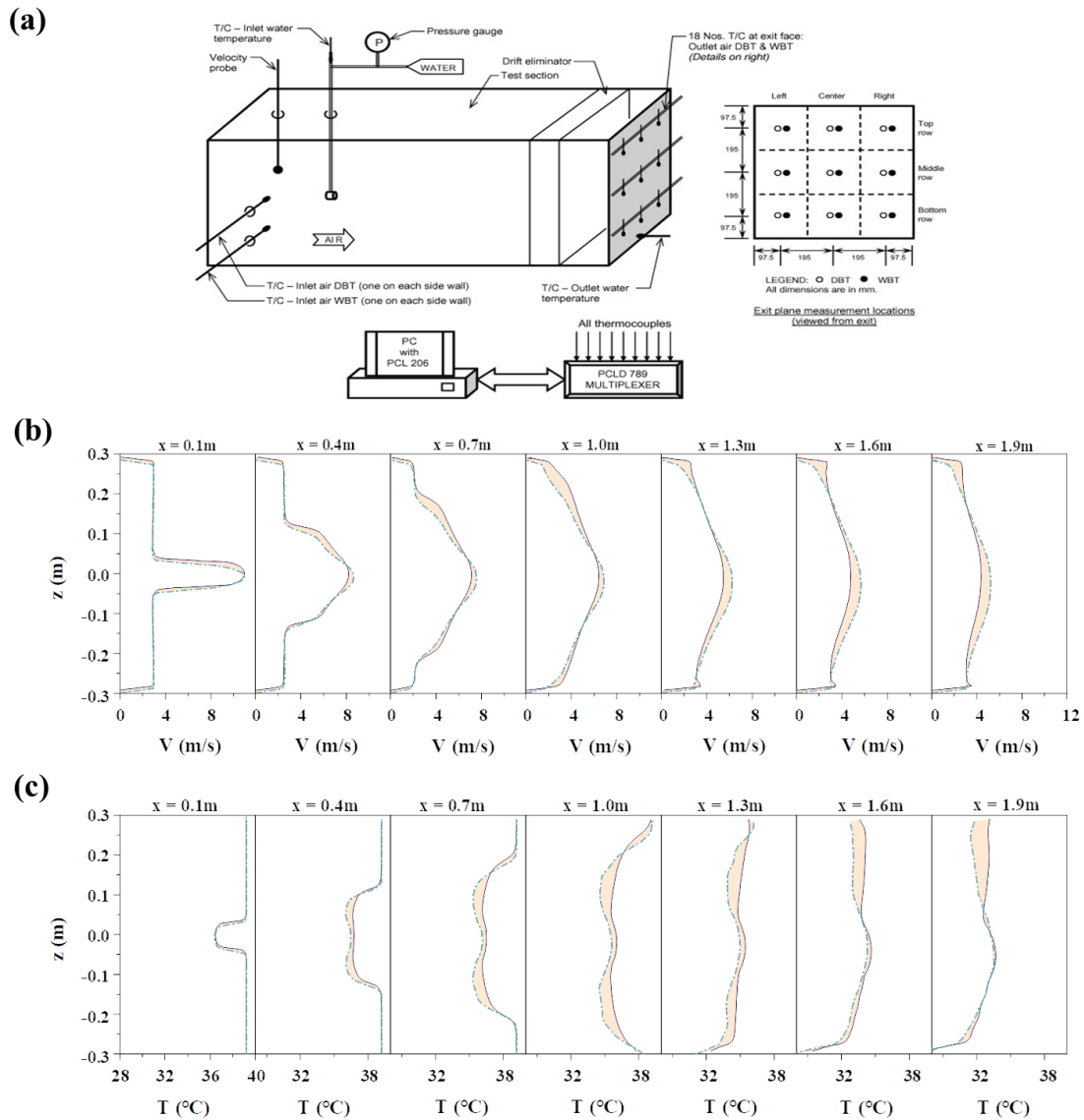


Figure 4.5 Wind tunnel test setup and comparative analysis of air velocity and temperature profiles between CFD results and experimental data. (a) Wind tunnel test setup for the evaporative cooling water sprayer (Sureshkumar et al., 2008). Comparative analysis of (b) air velocity and (c) temperature profile along a vertical centre plane lines between CFD results and experimental data from (Montazeri et al., 2015b). Representation key: dashed line for current validation results; solid black line for previous findings.

The validation of the evaporative cooling spray, based on earlier works by Montazeri et al. (2015b) and Sureshkumar et al. (2008), sought to assess the cooling jet characteristics in CFD. This study conducted a comprehensive evaluation of the Lagrangian-Eulerian approach for evaporative cooling using a water spraying system equipped with a hollow cone nozzle. The validation was conducted in a computational domain measuring  $0.585\text{ m} \times 0.585\text{ m} \times 1.9\text{ m}$ , with a scaled-down hollow cone nozzle of 4 mm diameter, as depicted in Figure 4.5 (a), which illustrates the wind tunnel test setup (Sureshkumar et al., 2008). The CFD validation encompassed boundary conditions, spray jet properties, droplet characteristics, and solver settings in line with (Montazeri et al., 2015b). Figure 4.5 (b) and Figure 4.5 (c) compare the current CFD results with previous data, with a focus on wind velocity and temperature along a central cross-section vertical line. For the comparison of wind speeds, the experimental results and CFD simulation results indicate that from  $x = 0.1\text{ m}$  to  $x = 1.9\text{ m}$ , the peak wind speed gradually decreases, and the distribution becomes smoother as the distance from the nozzle increases. The error between the CFD validation data and the experimental data becomes more significant at positions farther from the nozzle, particularly in high wind speed regions. At position  $x = 0.1\text{ m}$  near the nozzle, the overall average error between the experimental and CFD simulated wind speed results is 3.21%, with the maximum error reaching 8.47% when the wind speed exceeds 4 m/s. At  $x = 0.4\text{ m}$ , the overall average error is 5.89%, while at  $x = 0.7\text{ m}$ , the error is 7.64%. When the distance exceeds 1m, the error between the wind speed results from experiments and simulations gradually increases, with the maximum error occurring at  $x = 1.6\text{ m}$  at 5 m/s, reaching 10.71%. While, from the temperature readings, from  $x = 0.1\text{ m}$  to  $x = 1.9\text{ m}$ , as the distance from the nozzle increases, the peak temperature gradually decreases, and the distribution becomes smoother. In the region close to the nozzle ( $x = 0.1\text{ m}$ ), the experimental results and CFD simulation results are

very close, with almost no error. In the intermediate regions ( $x = 0.4$  m,  $x = 0.7$  m,  $x = 1.0$  m), the temperature distribution gradually smoothens, and the error between the experimental results and CFD simulation results begins to appear, especially in higher temperature regions. In the regions farther from the nozzle ( $x = 1.3$  m,  $x = 1.6$  m,  $x = 1.9$  m), the temperature distribution becomes more uniform, and the overall temperature decreases. The error between the CFD simulation results and experimental results significantly increases, particularly in the regions where  $z$  higher than 0 m and temperature is higher. Near the nozzle at  $x = 0.1$  m, the overall average error between the experimental and CFD simulation temperature results is 1.49%. At  $x = 0.4$  m, the overall average error is 3.47%, while at  $x = 0.7$  m, the error is 7.86%. When the distance exceeds 1 m, the error between the temperature results from experiments and simulations gradually increases, with the maximum error occurring at  $x = 1.9$  m and  $z$  higher than 0 m, reaching 15.64%. The increase in error for both wind speed and temperature may be due to the increased complexity of the flow field with distance from the nozzle, where turbulence and boundary layer effects have a more significant impact on the simulation results, leading to increased errors. Additionally, at positions farther from the nozzle, the attenuation of the flow may cause the CFD model to be less sensitive to subtle velocity and temperature changes, resulting in increased errors. Overall, the CFD simulation results tend to be larger than the experimental results, possibly because the turbulence models and boundary conditions in the CFD model overestimate the flow velocity and temperature, especially in high wind speed and high-temperature regions. Furthermore, the mesh resolution and time step used in the simulation may not be sufficient to capture all the details present in the experiments, leading to larger simulation results. These trends were in complete agreement with past findings, with minor variations potentially attributed to differences in boundary condition settings and grid processing between the current and previous studies, affirming the high consistency between the two datasets.

### 4.3.2 Single-sided ventilated courtyard: wind and thermal performance with and without water sprayers

The airflow patterns around the single-sided ventilated courtyard building, as illustrated in Figure 4.1 (a) and Figure 4.6, demonstrate the wind approaching from the inlet boundary on the left-hand side (the west side). A portion of the air ascends along the windward facade to the top of the building. The flow then splits, with some of the air entering the courtyard and some passing over, and then exiting to the pressure outlet on the right-hand side. A large recirculation region can be observed on the leeward side of the building. Within the single-sided ventilated courtyard, the behaviour of the upper-level airflow can be described in terms of two primary directions. The predominant portion of the flow, known as the skimming flow, occurs at the windward edge and creates a negative pressure region above the courtyard with a magnitude of approximately -85 Pa, preventing this airflow segment from penetrating the courtyard, as shown in Fig. A.3 (a). This phenomenon is attributed to the interaction between the building's height and the wind pressure differential at the upper level. Consequently, this skimming flow does not return to the courtyard but instead continues along the roof's edge, contributing to the creation of negative pressure. The remaining airflow, affected by the courtyard's aspect ratio and the negative pressure induced by the skimming flow, is diverted downwards into the courtyard itself. This stream of air is guided along the courtyard's walls, leading to a complex pattern of circulation that includes upward motion and the formation of a vortex within the courtyard space. This vortex plays a crucial role in enhancing ventilation effectiveness by drawing fresh outdoor air into the interior spaces, as indicated by the courtyard's internal pressure, which measures around -70 Pa.



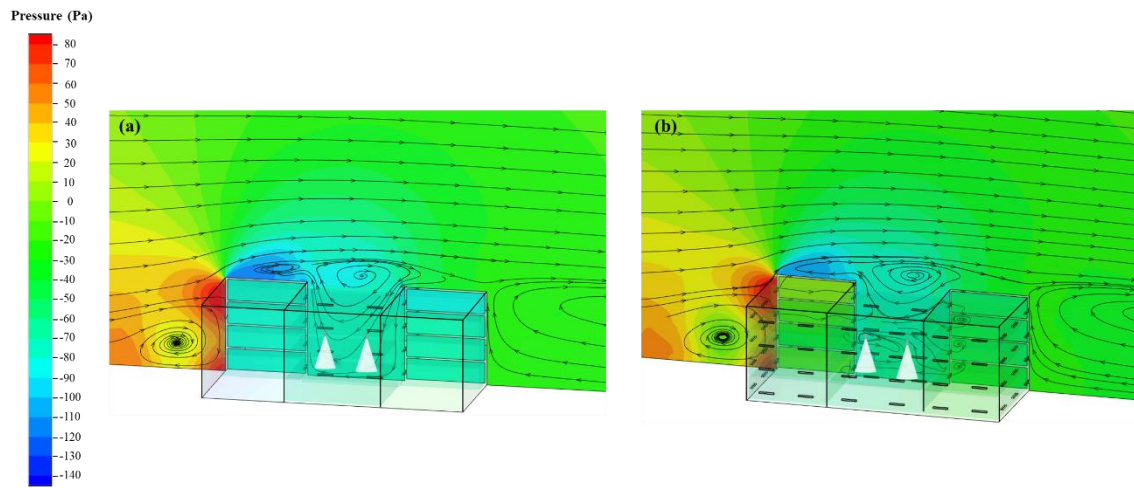
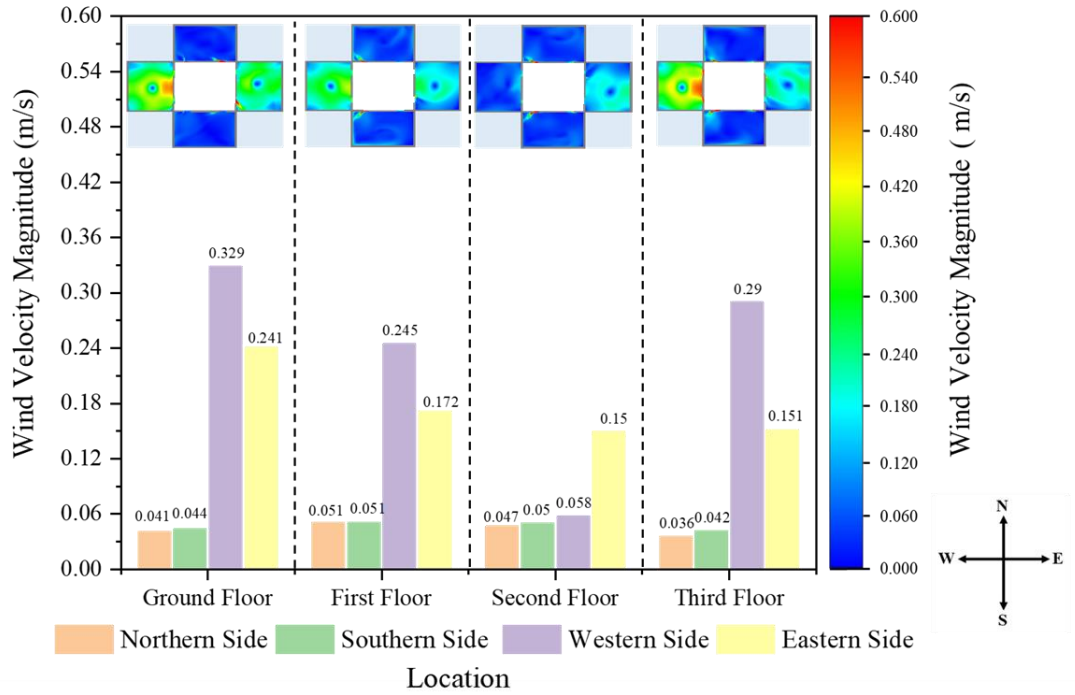


Figure 4.6 Comparative visualizations of courtyard ventilation strategies at  $Y = 14125$  mm section: (a) SSV courtyard with water sprayers, (b) CV courtyard with water sprayers.

(a)



(b)

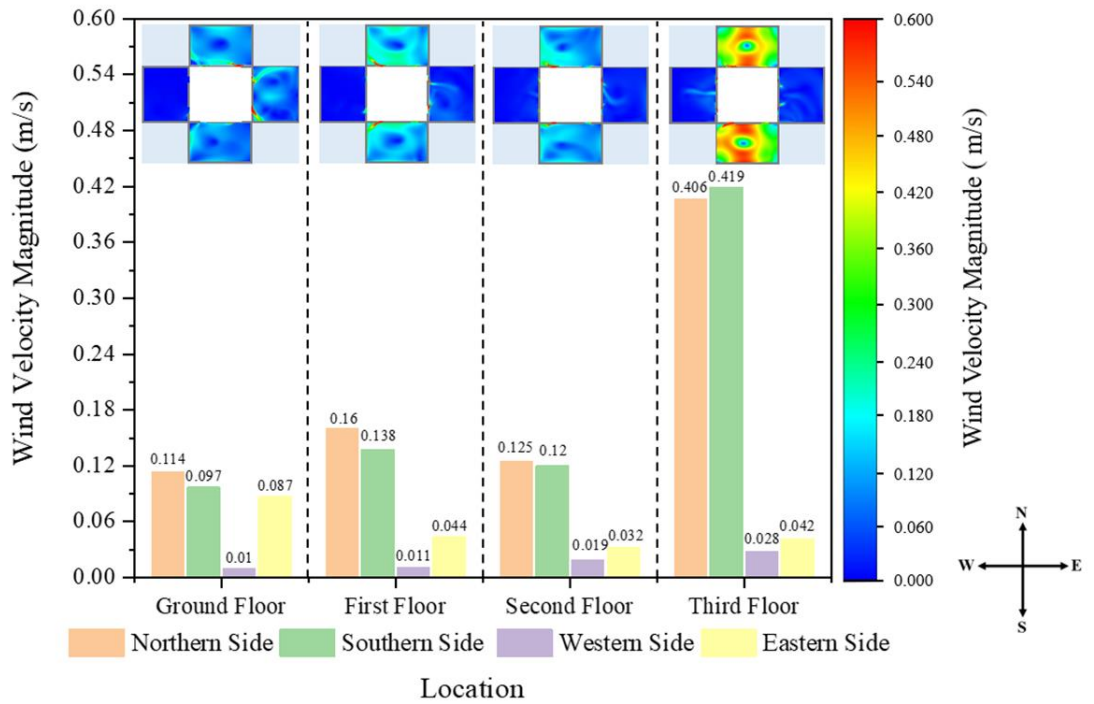


Figure 4.7 Comparison of indoor wind velocity in the SSV courtyard. (a) Without and (b) with water sprayers, including cross-sectional velocity contours for each room.

Figure 4.7 (a) presents the average indoor wind velocity for 16 monitored rooms in the absence of water spraying devices. Notably, rooms on the west side exhibit the highest

average wind velocity at 0.231 m/s. Specifically, the ground floor's RWG room experiences the highest wind velocity at 0.329 m/s. This is followed by rooms on the east side, which have an average velocity of 0.179 m/s as the incoming airflow encounters the opposite east side wall, leading to a change in the wind's direction due to the wall's resistance. This change generates a clockwise-rotating vortex within the centre of the courtyard. As this vortex impacts the west side rooms, the resulting dynamic pressure difference due to the collision and redirection contributes to the entry of part of the airflow into the RWG room, thereby increasing its wind velocity. The vortex then ascends along the wall of the west side rooms and eventually exits over the top of the courtyard. Consequently, this vortex facilitates the entry of a portion of the wind into the rooms on both the east and west sides, enhancing the indoor wind velocity of these rooms.

However, the rooms on the south and north sides experience lower wind velocities, as exemplified by the RSG and RNG rooms, with velocities of only 0.044 m/s and 0.041 m/s, respectively. The observation is based on the fact that when the entering wind collides with the east side wall, it generates a vortex. The primary dynamic force of the airflow concentrates along the direction of the vortex's formation, i.e., the east-west direction. The motion of the vortex intensifies airflow along its axial direction, whereas in directions perpendicular to the vortex's axis (south-north direction), the airflow disperses, which reduces wind velocities. Furthermore, since the vortex predominantly moves in the east-west direction, the south and north side rooms, which do not directly face the main wind entrance, receive less dynamic airflow. Compared to the direct ventilative effect observed in the east and west side rooms, the south and north side rooms rely primarily on the secondary distribution of airflow for ventilation.

Variations in wind velocity across different orientations have been observed within the courtyard building with water sprayers. As illustrated in Figure 4.7 (b) rooms on the northern side demonstrate the highest average wind velocity, recorded at 0.201 m/s, with the third-floor RST room reaching a wind speed of 0.419 m/s. This indicates a significant influence of the water sprayers on the upper-level rooms facing north. Similarly, rooms on the southern side exhibit relatively high wind velocities, with an average speed of 0.194 m/s, while the third-floor RNT room achieves a wind speed of 0.406 m/s. In contrast, rooms on the western side present the lowest average wind velocity at a mere 0.017 m/s, and the ground-floor RWG room has the minimal recorded wind velocities of 0.010 m/s. The eastern side rooms have slightly higher wind velocities, averaging 0.051 m/s, with the third-floor RET room having a wind speed of 0.042 m/s.

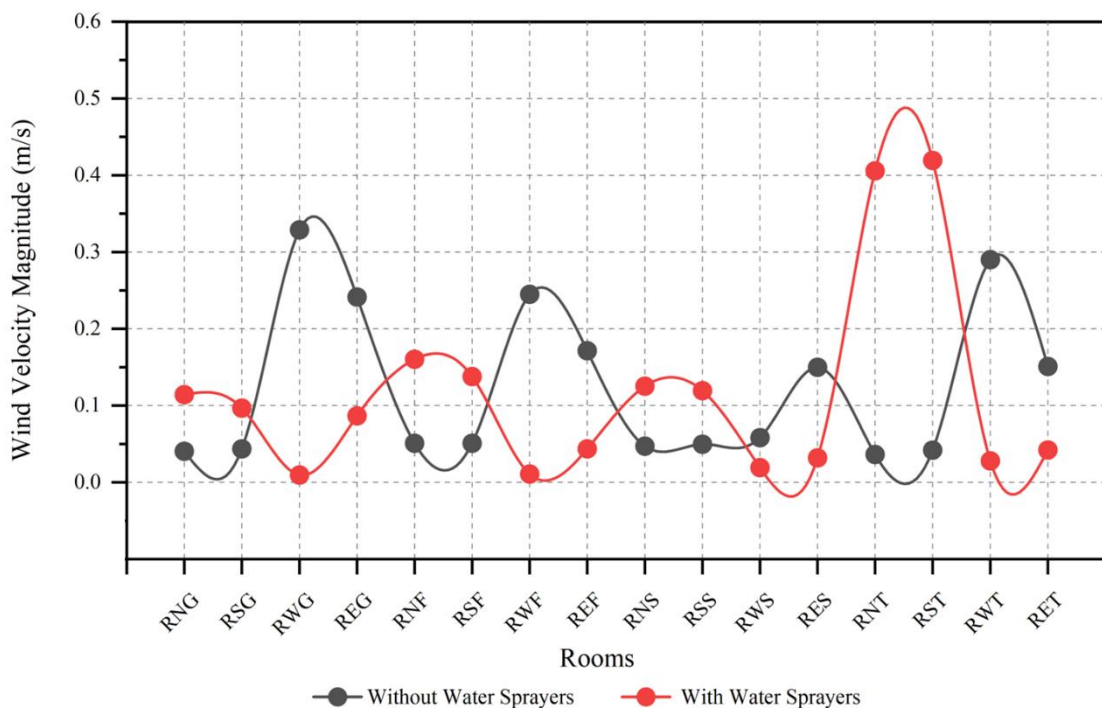


Figure 4.8 Wind velocity comparison in each test room within the SSV courtyard with and without water sprayers.

A comparative analysis of wind speed contour maps for each room, as shown in Figures 4.7 (a) and 4.7 (b), along with the wind speed comparison in Figure 4.8 following the installation of water sprayers, reveals substantial changes in ventilation within the courtyard building. Out of the 16 monitored rooms, 8 exhibited increased wind speeds, all located on the southern and northern sides. The average wind speed in the northern rooms rose from 0.043 m/s without sprayers to 0.201 m/s with sprayers, with a surgeon the third floor RNT room from 0.036 m/s to 0.406 m/s. Conversely, 8 rooms, predominantly within the east and west-facing rooms, experienced a decrease in wind speed. The western rooms, particularly the ground-floor RWG room, witnessed a drastic drop from 0.329 m/s to 0.010 m/s. The average wind speed in these western rooms decreased by approximately 0.214 m/s, while the eastern rooms, less drastically affected, saw an average decrease of 0.127 m/s. Moreover, the second floor exhibited the most notable change in wind velocity after the water sprayer installation, with an increase of approximately 0.094 m/s.

A series of notable changes were observed in a detailed comparative analysis of ventilation effects before and after the water sprayer installation in the courtyard building. Before the installation, rooms on the east and west sides, positioned along the primary movement path of the courtyard's vortex, exhibited higher average wind speeds compared to the north and south sides, which depend on secondary airflow distribution. However, post-installation, there was a marked increase with increased wind speeds on the north and south-facing rooms and a decrease in the east and west sides. Two key factors contributed to this change:

(i) While the fundamental motion pattern of the courtyard's vortex remained unchanged, the introduction of water spraying devices and the resultant mist created obstructions and

diversions in the main airflow pathways. For instance, the RWG room, initially characterized by the highest wind speed, underwent a substantial impact, likely due to the obstruction caused by the water sprayers. Consequently, the vortex within the courtyard, disrupted by the water sprayers, redirected a greater airflow towards the north and south sides, increasing wind speeds in these directions.

(ii) The evaporative cooling effect induced by the water sprayers led to a reduction in air temperature and increased humidity, consequently increasing air density. This denser, cooler air tended to move downwards, altering the natural airflow patterns within the courtyard. This mechanism explains the observed increase in wind speeds in the north and south rooms during the operation of the water sprayers, as they likely directed airflow towards these areas. The introduction of cooler air through evaporative spraying created local pressure differentials within the courtyard, influencing the direction and speed of the airflow. Natural wind patterns might dominate in configurations without water sprayers, leading to higher airflow in the east and west rooms. In contrast, the water spraying configuration could generate new pressure gradients and redirect the airflow towards the north and south rooms.

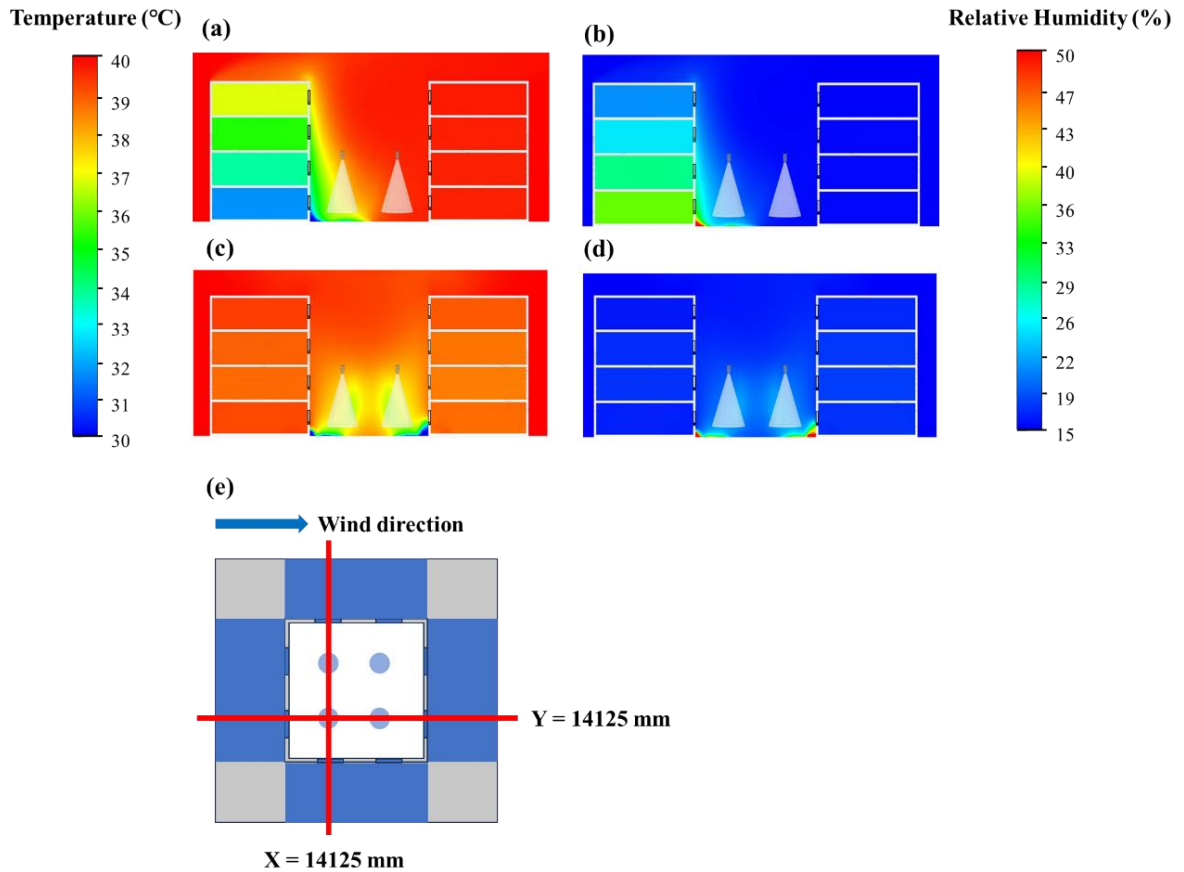


Figure 4.9 Temperature and relative humidity contours at two cross-sections within the SSV courtyard with water sprayers. (a) Temperature at cross-section  $Y = 14125$  mm and (b) Relative humidity at cross-section  $Y = 14125$  mm. (c) Temperature at cross-section  $X = 14125$  mm and (d) Relative humidity at cross-section  $X = 14125$  mm. (e) Location of the cross-sections.

To investigate the impact of water spraying on the indoor temperature and humidity of courtyard buildings, the inlet conditions were set to  $40^{\circ}\text{C}$  and 15% humidity without water spraying. The provided images display the variations in temperature and humidity at different sections after the installation of water spraying devices. Figure 4.9 (a) and Figure 4.9 (b) show changes at the  $Y=14125$  mm cross-section, which corresponds to the west and east sides of the building, as well as the respective parts of the courtyard. Observations indicate a general decrease in temperatures in rooms on the west side, and this cooling effect gradually

weakened with the increase in floor height. Notably, a concentration of cold air was observed outside the RWG room. However, temperature changes in rooms on the east side were minimal. The trend in humidity changes was similar to that of temperature, with the highest humidity observed in the RWG room. Furthermore, humidity in the rooms on the west side decreased with increasing height. Figures 4.9 (c) and 4.9 (d) present the temperature and humidity changes at the X=14125 mm section, corresponding to the rooms on the north and south sides. Analysis of the figures reveals insignificant changes in indoor temperature and humidity in the north and south rooms, indicating limited cooling and humidifying effects of the water spraying devices in these directions. It is also noticeable that the main areas of temperature decrease, and humidity increase are concentrated around the water spraying devices and have not significantly propagated into the indoor areas, which implies that the influence of the water spraying devices is primarily confined to their immediate vicinity, with limited regulation exerted on the wider indoor environment of the courtyard building (Figure 4.10).

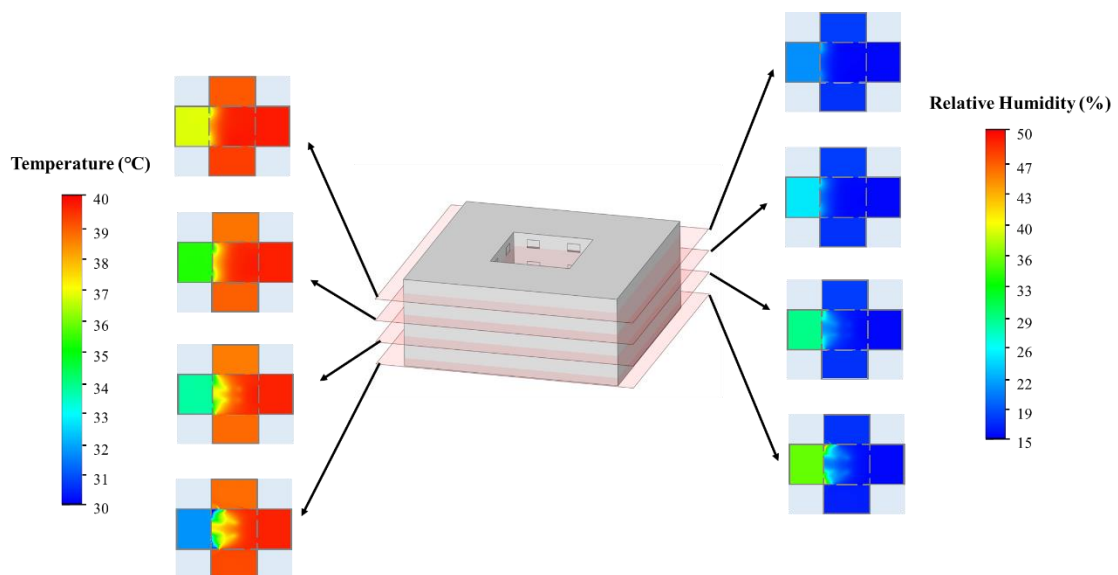


Figure 4.10 Temperature and relative humidity contours for each floor in the SSV courtyard with water sprayers (sectioned at the window openings).



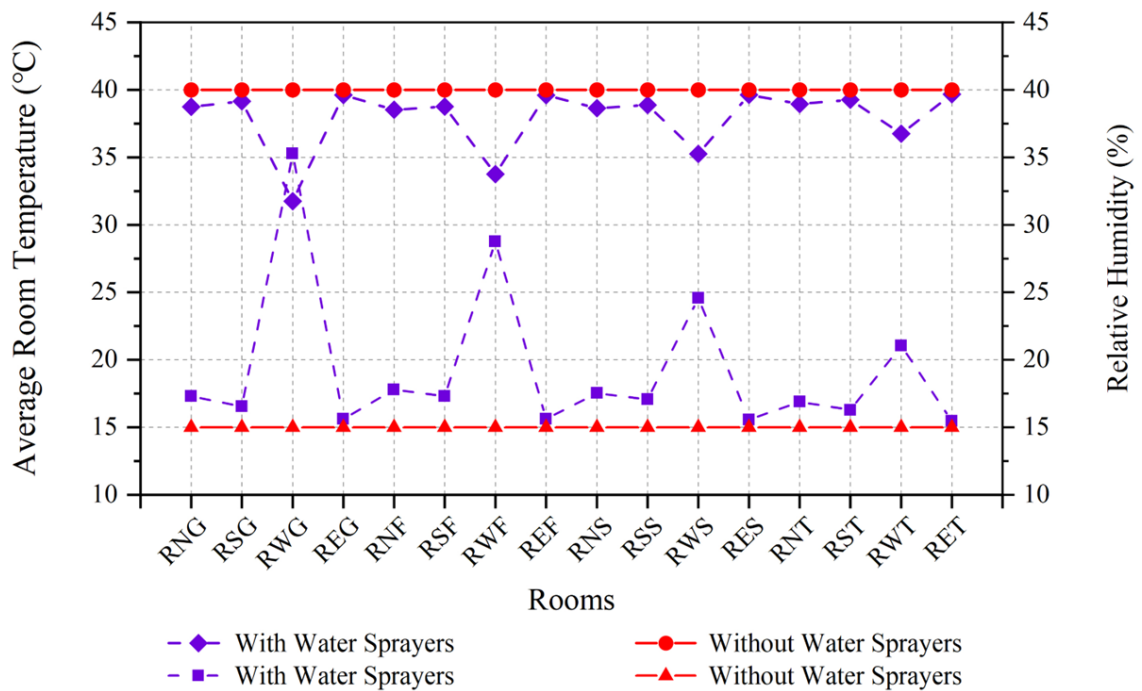


Figure 4.11 Comparative plots of indoor temperature (Red) and relative humidity (Purple) levels in each room within the SSV courtyard, with and without water sprayers.

Figure 4.11 reveals the variations in temperature and humidity across different rooms before and after the installation of water spraying devices, indicating a correlation between indoor temperature and humidity. The data suggests that a decrease in temperature is often accompanied by an increase in humidity, with minor temperature changes corresponding to smaller shifts in humidity. Rooms on the west side, which experienced the most significant cooling, exhibited a substantial increase in humidity. The average temperature drop from 40°C to 34.38 °C was accompanied by a rise in humidity to 27.42%. Specifically, the ground-floor RWG room saw a temperature drop of 8.25 °C and a humidity increase of 20.27%. In contrast, the east side, particularly the RET room, displayed a marginal temperature decrease of 0.32 °C, indicating a relatively weaker cooling and humidifying effect. Combined with the temperature and humidity contour maps in Figure 4.11, it is observable that the cooling and humidifying effects are not pronounced in the rooms on the east, south, and north sides.

Moreover, the height of the floors also influenced the effectiveness of the water spraying devices.

An examination of the cooling and humidifying effects revealed a significant increase in temperature and humidity around the devices, consistent with the physical principles of evaporative cooling. As water evaporation requires heat absorption, the surrounding air temperature decreases, and the addition of water vapor also raises relative humidity. When the airflow enters the courtyard and comes into contact with the water-spraying devices, the warm air passing through the mist undergoes a cooling effect, albeit with a reduction in flow velocity. The main airflow in the courtyard follows a vortex structure. When the vortex-driven airflow directly hits the eastern rooms without any contact with the water sprayers, the cooling and humidifying effect in these rooms is weaker. Additionally, as the vortex-direction airflow strikes the eastern wall, it partially redistributes towards the south and north sides. However, due to the obstruction caused by the water sprayers, most of the airflow bypasses and enters the south and north rooms. This diversion results in an increase in wind speed without a significant reduction in temperature. In rooms with higher wind speeds, the cooler and more humid air may dissipate quickly, reducing the overall effects of cooling and humidification. Conversely, rooms on the west side, positioned in the main wind direction of the vortex core and directly exposed to the airflow from the water sprayers, experience the most notable cooling effect, particularly the RWG room, where a significant influx of cooled airflow achieves a temperature reduction of up to 8.25 °C. The lower wind speed inside the RWG room allows the cold air to linger for a longer period, which enhances the cooling effect. As the vortex ascends and departs the courtyard near the west side rooms, the cooling and humidifying effects gradually diminish with the increase in floor height, likely due to the

tendency of cold air to sink and warm air to rise, leading to a relative weakening of the cooling effect in the upper rooms.

#### 4.3.3 Cross-ventilated courtyard: wind and thermal performance with and without water sprayers

Compared to single-sided ventilation, the cross ventilation in the courtyard building presents significantly different airflow characteristics. The pattern of ventilation in courtyard buildings is shown in Figure 4.1 (b). The wind approaches from the inlet boundary on the left-hand side, initially impacting the western windward side, which results in substantial airflow into the rooms facing west. Subsequently, some of this airflow moves directly into the centre of the courtyard. Above the courtyard, the airflow diverges into two principal directions, a phenomenon referred to as skimming flow. This flow, characterized by its passage along the building's upper edges, establishes a distinct aerodynamic behaviour. The negative pressure above the courtyard is somewhat lower, measuring around  $-75$  Pa, with the internal courtyard pressure being approximately  $-55$  Pa, as illustrated in Figure 4.6 (b). One air stream initiates a downward motion, creating a vortex that extends deep into the courtyard—this is indicative of the skimming flow's influence as it redirects air vertically. Concurrently, another portion of the airflow, adhering to the path of the skimming flow, crosses the courtyard's centre and veers towards the eastern side. This action precipitates a considerable vortex formation on the leeward side of the building, a direct result of the skimming flow as it moves across the building's surface. The ensuing vortex creates a unique circulation pattern, where a segment of the air bypasses the eastern structure, infiltrates the indoor spaces, and subsequently re-enters the courtyard. This interaction between the skimming flow and the courtyard's architectural features significantly enhances the complex internal airflow dynamics. Meanwhile, the courtyard building acts as a wind boundary,

guiding part of the airflow along the north and south sides, with only a small amount entering the rooms on the north and south. In such a ventilation configuration, the airflow from inside to the courtyard is no longer the main channel for indoor air intake compared to the vortex within the courtyard.

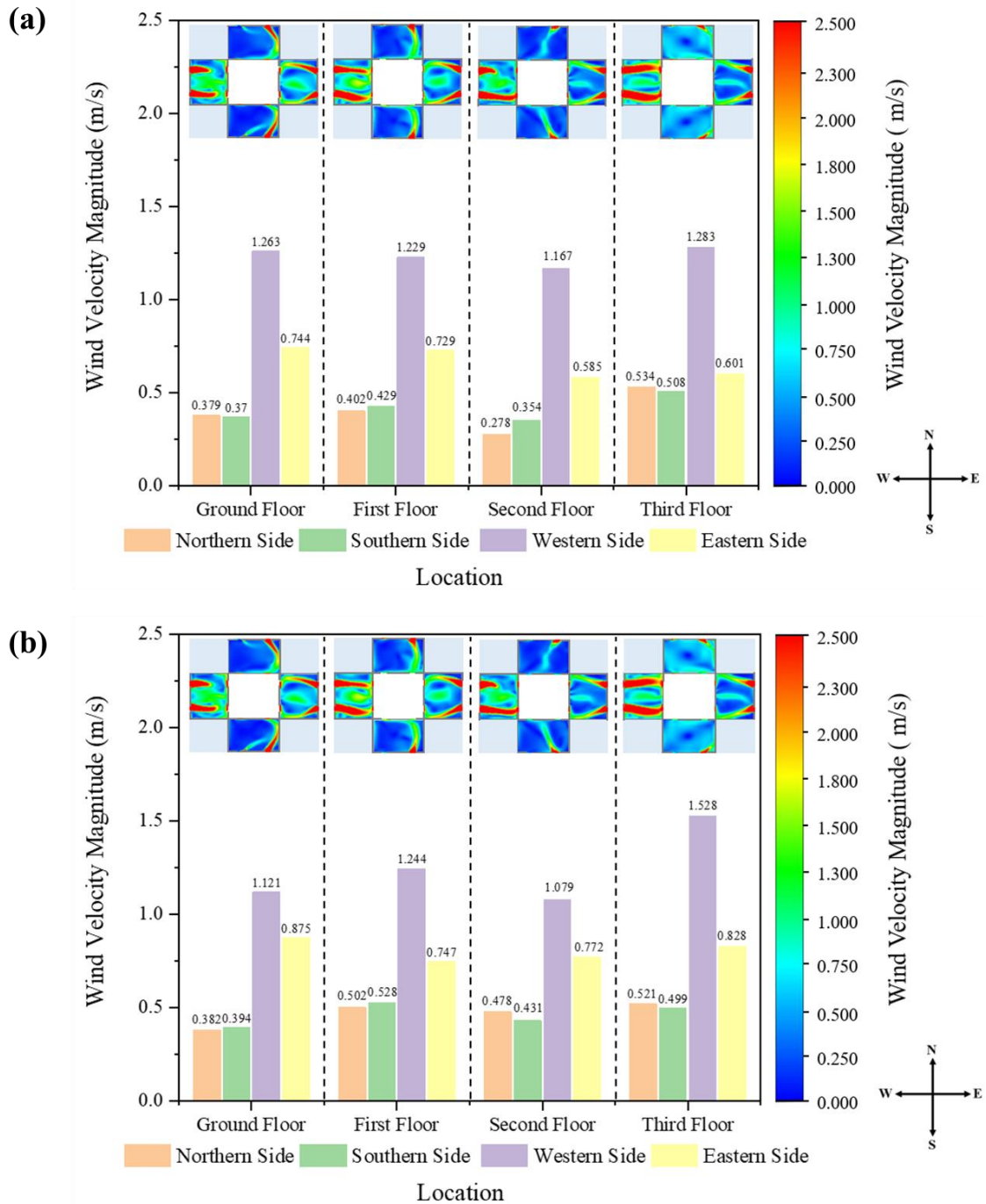


Figure 4.12 Comparison of indoor wind velocity in the CV courtyard. (a) Without and with (b) water sprayers, including cross-sectional velocity contours for each room.

Figure 4.12 (a) displays the velocity magnitude and contour diagram of the indoor wind speed on various floors in the CV courtyard without water sprayers. The highest wind speeds are concentrated in the rooms on the west side, with an average wind speed of 1.236 m/s.

Particularly, the RWT room on the third floor exhibits the highest wind speed of up to 1.283 m/s. The rooms on the east side, positioned on the leeward side, have an average wind speed of about 0.665 m/s, approximately half that of the west side. The average wind speeds of the rooms on the north and south sides are quite similar, both around 0.4m/s. Upon the operation of the water sprayers, as shown in Figure 4.12 (b), there is no significant change in the overall trend of wind speed distribution. The average wind speed in the rooms on the west side remains the highest at 1.243 m/s, followed by the four rooms on the east side with an average wind speed of about 0.806 m/s. The comparison of indoor wind speeds before and after the introduction of water sprayers clearly shows that under cross flow ventilation, the impact of water sprayers in the courtyard on the indoor wind environment is negligible. This phenomenon indicates that under this ventilation mode, the main source of indoor airflow comes from the wind from outside the courtyard.

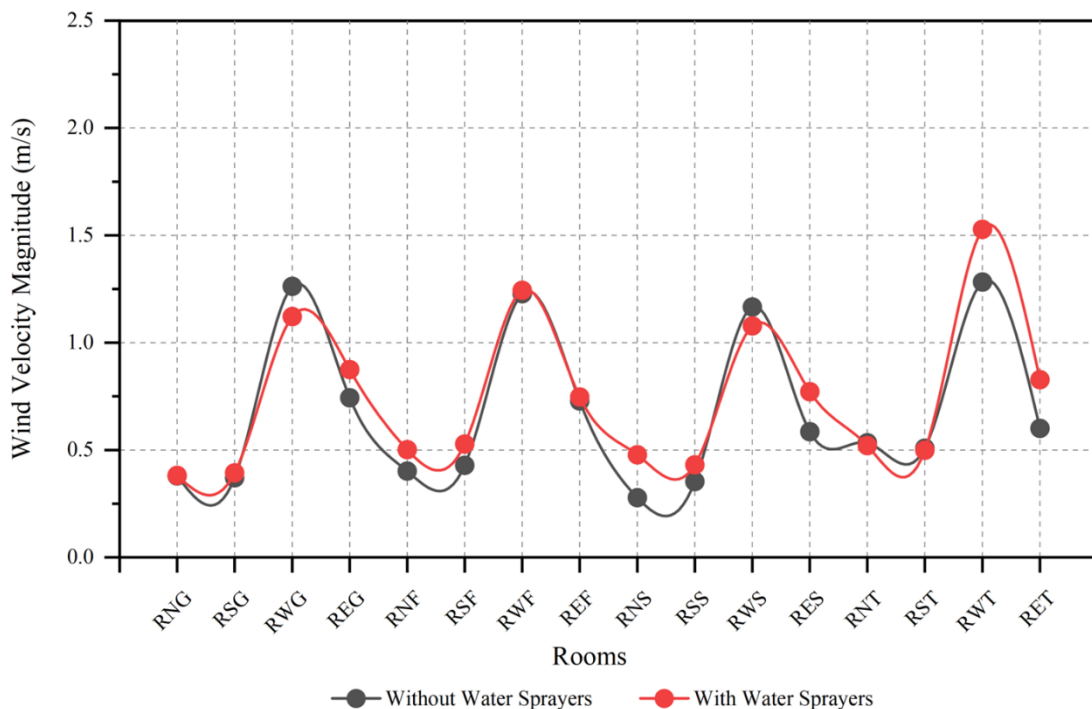


Figure 4.13 Wind velocity comparison in each test room within the CV courtyard with and without water sprayers.

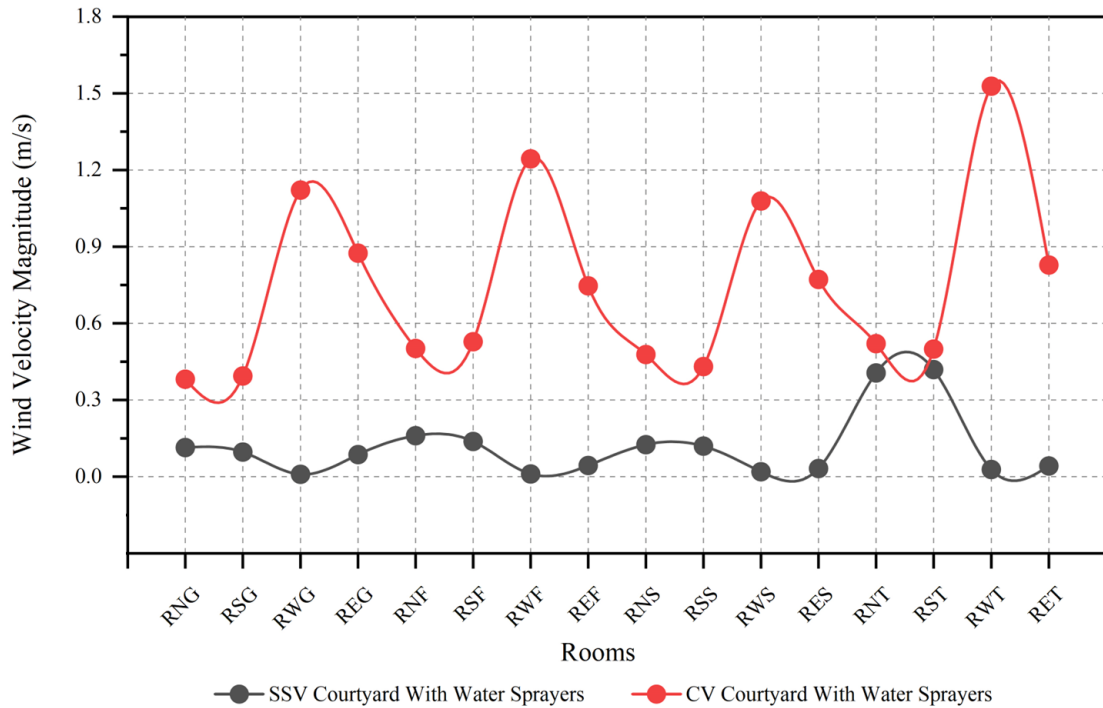


Figure 4.14 Wind velocity comparison in each test room for the SSV and CV courtyards with water sprayers.

Rooms	Temperature (°C) With water sprayers	RH (%) With water sprayers
RNG	40.00	15.00
RSG	40.00	15.00
RWG	40.00	15.01
REG	39.99	15.03
RNF	40.00	15.00
RSF	40.00	15.00
RWF	40.00	15.00
REF	39.99	15.03
RNS	40.00	15.00
RSS	40.00	15.00
RWS	40.00	15.01
RES	39.99	15.03
RNT	40.00	15.00
RST	40.00	15.00
RWT	40.00	15.01

Table 4.3 Average indoor temperature and relative humidity of the CV courtyard with water sprayers.

After the installation of water spraying devices in the courtyard building with cross ventilation design, data showed no changes in indoor temperature and humidity. The initial

indoor conditions were set at 40 °C, with a relative humidity of 15%. This phenomenon revealed that under such a ventilation strategy, indoor air is primarily drawn from the outside of the courtyard and then flows through the indoor space before it recirculated back to the courtyard, see Figure 4.1 (b). Consequently, the water spraying devices in the courtyard have a limited role in the heat exchange process as they fail to effectively cool and humidify the hot air. It can be inferred that in courtyard buildings with a cross flow ventilation mode, the installation of water spraying devices contributes minimally to improving the indoor thermal and humidity environment (as shown in Figure 4.13 and Table 4.3). The wind velocity comparison in each test room for the SSV and CV courtyards with water sprayers is shown in Figure 4.14.



## 4.4 Water flow rate analyse and limitations of this chapter

### 4.4.1 Water flow rate analyse

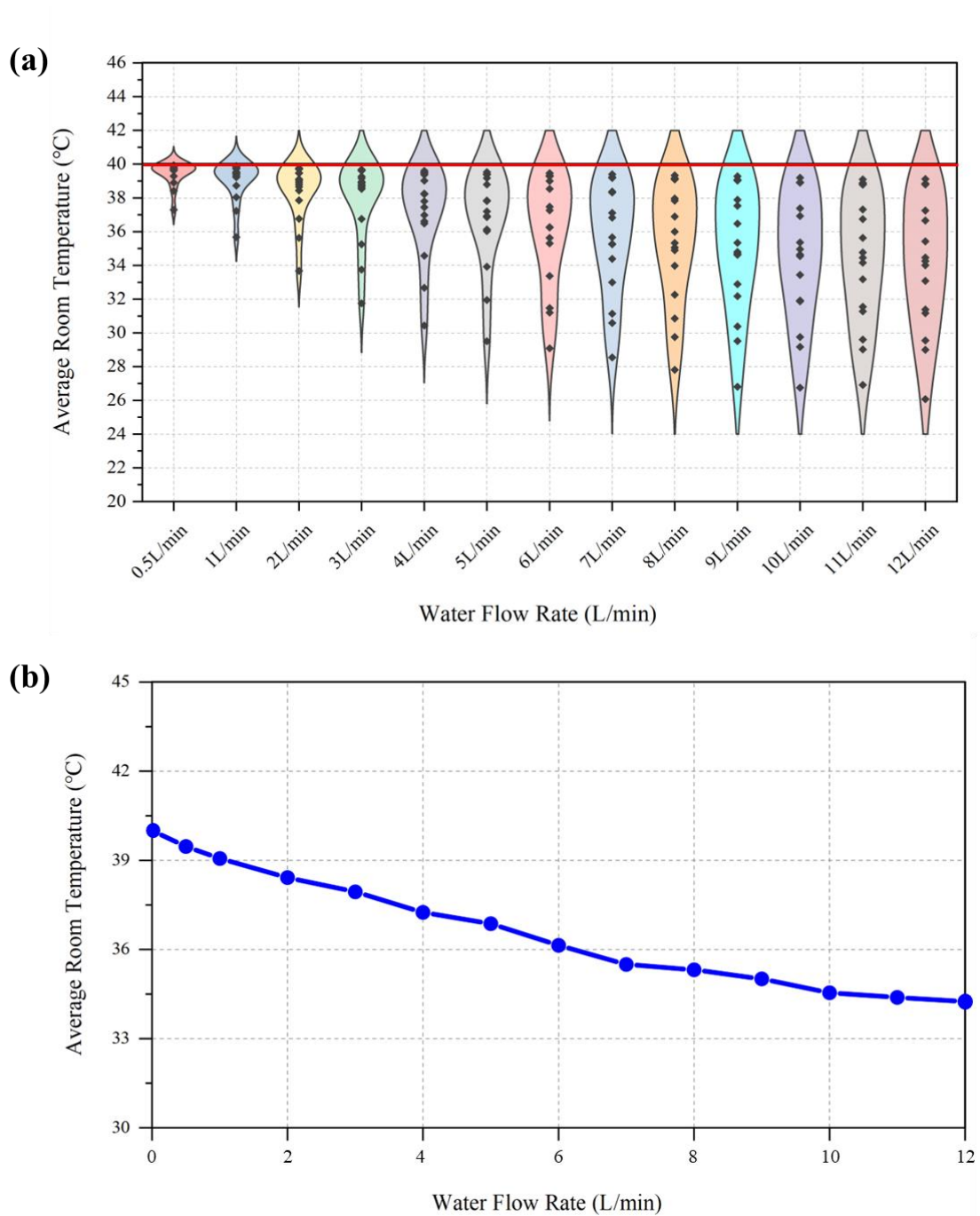


Figure 4.15 Comparison of indoor average temperature changes for varying water flow rates in the SSV courtyard. (a) Variations of indoor temperature across the rooms, the red line represents the outdoor temperature and (b) overall average room temperature.

To investigate the impact of varying evaporative cooling system water flow rates on indoor thermal control in single-sided ventilated courtyard buildings, this study systematically analysed 13 different flow rates ranging from 0.5 l/min to 12 l/min. Maintaining constant water temperature and velocity, the study focused on single-sided ventilated courtyards, which demonstrated a more significant cooling effect compared to courtyards with cross flow ventilation. There is a clear trend shown in Fig. 14 (a), as the water flow rate increases, the distribution of average temperatures within buildings surrounding the courtyard gradually expands. This finding indicates that increasing the water flow rate has a significant cooling effect on certain rooms, while for others, this cooling effect is less pronounced. In other words, increasing the water flow rate can effectively improve the temperature conditions in certain spaces, but the effect is not uniform, reflecting the differences in how various rooms respond to cooling measures. The results presented in Figure 4.16 show the effectiveness of water sprayers in reducing the room air temperature. Notably, the cooling effect progressively intensifies as the water flow rate increases.

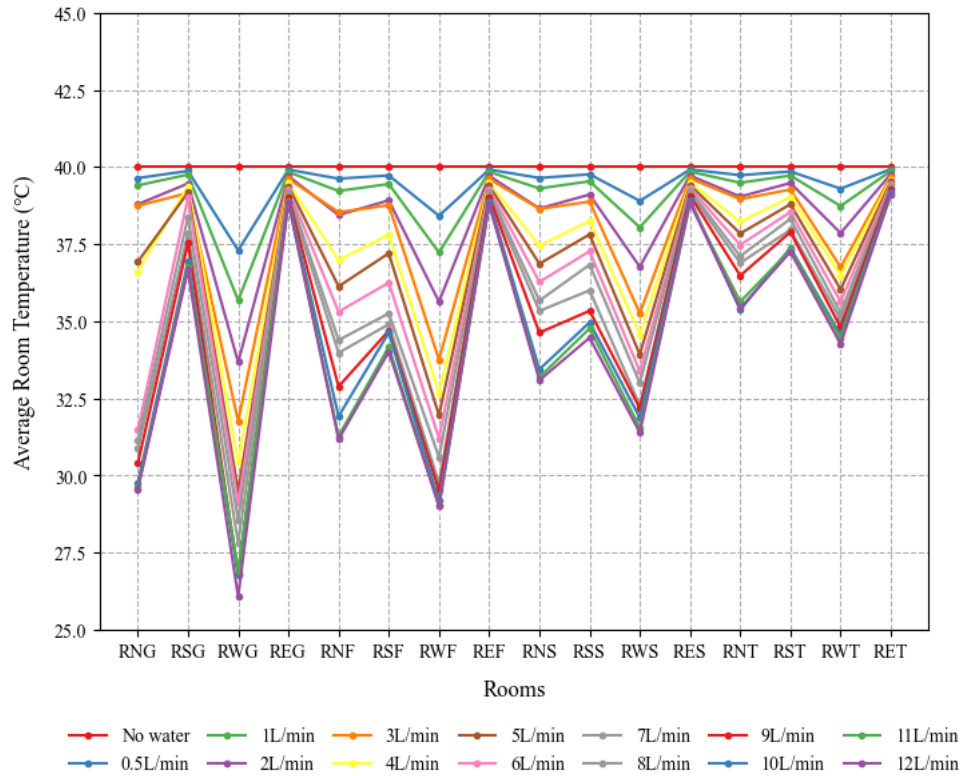


Figure 4.16 Comparison of indoor average temperature changes for varying water flow rates in the SSV courtyard.

Detailed observation of temperature reductions across different rooms revealed the most significant change in the RWG room on the ground floor, where the temperature dropped by 2.70 °C at a flow rate of 0.5 l/min and 13.93 °C at 12 l/min. This finding highlights the enhanced cooling capacity of water sprayers with increasing flow rates, particularly in the RWG room. Overall, the west-facing rooms experienced the most notable cooling effects, while the east-facing rooms exhibited minimal change even with increased flow rates. Additionally, the cooling effects in the north and south-facing rooms varied with the flow rates. For instance, in the RNG room, the temperature decrease ranged from 1.26 °C to 3.39 °C when the flow rate increased from 3 l/min to 4 l/min. A further increase from 5 l/min to 6 l/min raised the cooling effect from 3.08 °C to 8.53 °C, suggesting that higher water flow

rates might alter the wind field within the courtyard, benefiting both the west and north-facing rooms simultaneously.

However, irrespective of water flow rate changes, east-facing rooms showed no cooling, indicating that the indoor airflow in single-sided ventilated courtyard buildings is mainly influenced by the large courtyard vortex. The diminishing cooling effect with increased floor height also corresponds to the physical property of cold air being denser and accumulating at lower levels. As displayed in Figure 4.15 (b), the average temperature across all rooms shows a trend of gradual decrease with increasing water flow rates, this trend stabilizes beyond the flow rates of 10 l/min, 11 l/min, and 12 l/min. This stabilization of temperature reduction corresponds to the physical limit of evaporative cooling efficiency. Beyond a certain water flow rate, the air reaches a moisture content at which it cannot effectively absorb more water vapor, leading to a state of saturation. Thus, while increasing the flow rate initially improves cooling due to enhanced evaporation, the effect becomes less pronounced as the air's capacity for vapor absorption nears its limit.

#### 4.4.2 Limitations

In this study, I conducted an analysis of the impact of water sprayers in courtyard buildings under different ventilation strategies using CFD simulations. Despite the key findings obtained, it is crucial to acknowledge the limitations of the research process. The operation and positioning of water sprayers in this study may not accurately represent the diverse configurations found in real-world settings. One of the limitations of this study is that it only varied the water spray rate while keeping other factors such as nozzle distribution, position, height, and the speed and temperature of the sprayed water constant. This limits the analysis, as these variables could impact the results. Future research should explore varying

these additional parameters to provide a more thorough understanding of their effects on the performance of the courtyard building's cooling system. Additionally, the ventilation strategies explored here may not encompass the range of approaches applied in actual environments. The occurrence of errors between wind tunnel experiments and CFD simulations is inevitable, primarily attributed to the complex nature of the model and external factors. Moreover, our study exclusively utilizes simplified wind tunnel models for CFD simulations, which may overlook critical complex factors present in real-world environments.

## 4.5 Conclusion

This study investigates the impact of evaporative cooling from water sprayers in courtyard buildings under different ventilation strategies on the indoor thermal environment and microclimate. Although the influence of passive techniques on courtyards has been widely studied, their specific impact on the indoor thermal environment of courtyard buildings remains relatively unexplored, which constitutes the innovative focus of this study. With CFD analysis and validation through wind tunnel experiments, the study focused on courtyard buildings with two different ventilation strategies, each featuring uniformly distributed water sprayers.

In courtyard buildings with single-side ventilation, the introduction of water sprayers induced significant changes in the indoor wind environment, primarily due to the obstruction of incoming wind by sprayers and alterations in air movement direction caused by changes in temperature and humidity. The most significant cooling effect of up to 8.25 °C and a humidity increase of 20.27% were observed in the ground-floor rooms on the west side. On average, the temperature in the 16 test rooms decreased by 2.06 °C, and the relative humidity increased by 4.29%. The cooling effect was predominantly observed in the west-facing rooms

and gradually diminished with rising floor levels. In contrast, in courtyard buildings with cross-ventilation, the impact of water sprayers on the indoor thermal environment was relatively modest, with minimal changes in the indoor wind environment and cooling-humidifying effects.

This study analysed the impact of different water flow rates, ranging from 0.5 l/min to 12 l/min, on indoor thermal control in a single-sided ventilated courtyard building. A notable temperature reduction in certain rooms was observed when the water flow rate increased from 5 l/min to 6 l/min. However, further increases in water flow rate led to a saturation of the indoor cooling effect. Overall, the study emphasizes the potential of evaporative cooling strategies in improving thermal conditions in courtyard buildings, especially in hot and dry climates, while also underscoring the need for tailored solutions based on specific building features and environmental conditions. This study lays a solid foundation for further research under varying ventilation strategies and water flow rates.

Future works, based on the identified limitations in the current study, will expand and adjust our existing model, which involves adjustments to the position, height, and water temperature of the water sprayers to investigate deeper into their impact on the indoor thermal environment of the courtyard buildings. Additionally, our previous research revealed that evaporative cooling techniques in single-sided ventilated courtyard buildings significantly affect only specific areas. Conversely, cross-ventilated courtyard buildings did not improve the indoor thermal and humidity environment across all rooms. Future studies aim to extend these cooling and humidifying effects to a broader range of rooms. For instance, I could adopt a similar approach to that referenced in (Bagasi & Calautit, 2020), which employed evaporative cooling strategies directly at the inlet of the building. This could

potentially remedy the limitations observed in cross flow ventilation configurations, where indoor air is predominantly drawn from outside the building.

Another critical aspect of future research will entail transitioning from wind tunnel-based courtyard models to simulations based on real-life courtyard buildings. This will involve integrating actual weather data into the simulations, thereby enhancing realism and applicability. By simulating scenarios based on real-world conditions, I can better capture the complexities of air-thermal interactions within courtyard environments, thus increasing the accuracy and relevance of our findings.

Finally, in this study, the RANS turbulence model (specifically the k-epsilon realizable model) was primarily selected for its adequacy in meeting basic requirements for validating courtyard and water spray simulations, coupled with its cost-effectiveness in computational resources. However, future research will undertake a comparative analysis of the accuracy of transient large eddy simulation (LES) models to determine if they offer a more precise understanding of the microclimatic conditions within courtyard environments. This comparison is anticipated to provide valuable insights into the selection of appropriate simulation models for different research objectives.

# Chapter 5 Courtyards with Vegetation

## 5.1 Introduction

This chapter investigates the influence of vegetation integration on enhancing aerothermal comfort within courtyards and adjacent buildings situated in warm climates. By developing three distinct scenarios that vary according to vegetation size, illustrated in Figure 5.1, the study evaluates the effects on air temperature, flow velocity, and overall aerothermal and thermal comfort for indoor areas. Utilizing ANSYS Fluent v18.1 for detailed simulations, and grounding its findings in experimental data, the investigation sheds light on how different size of vegetation can alter airflow patterns, either by obstructing airflow or changing its direction due to temperature variations around the vegetation.

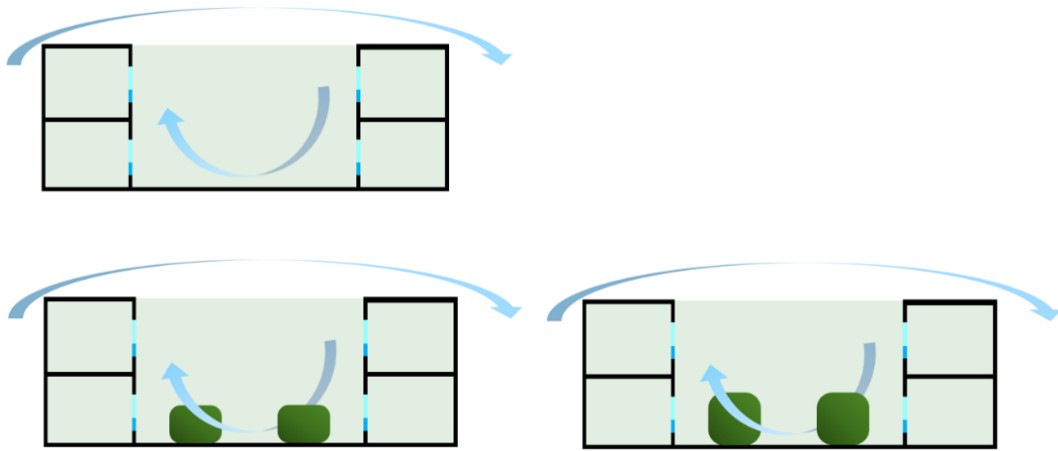


Figure 5.1 Three scenarios with different vegetation characteristics in this chapter.

## 5.2 Method

For investigating the influence of different passive cooling technologies installed in courtyards on the thermal and wind environment inside buildings, the simulation study is divided into three cases (Table 5.1), Case 1 forms the reference for this study, which is an



enclosed courtyard model with no passive cooling strategies. For Cases 2-3, vegetation with different heights is arranged in the baseline courtyard. In the last case, one water jet is set in the centre of the courtyard. In this study, two passive cooling elements are selected to investigate their effectiveness in the indoor environment.

Case 1	Baseline enclosed courtyard model with no vegetation
Case 2	Four small trees inside the courtyard
Case 3	Four large trees inside the courtyard

Table 5.1 Three Scenarios for the case study.

### 5.2.1 CFD theory

For simulating the baseline courtyard model in the Fluent, the viscous model was set to the standard k-epsilon model, which is used to show the natural ventilation flow pattern, the energy model was set to simulate the change of the temperature inside the courtyard.

The vegetation setup in this study involves assumptions and differs from real vegetation, as it only simulates certain properties of the vegetation. Vegetation such as trees and hedges act as momentum sink, slowing down the airflow in them. Many studies have modelled vegetation as a porous body, accounting for pressure loss across the domain. Additionally, to interpret the vegetation cooling effect, this current research took advantage of a method that had been simplified on the basis of the works by Rahman et al. (2011) and Gromke & Ruck (2012), an assignment to volumetric cooling, with the potential of  $350 \text{ W/m}^3$  per LAD was made to perform the function of a source term of the energy equation. Leaf Area Density (LAD), can be explained as the leaf area at a very large volume of vegetation. The diversity of species and spatial uncertainty of the vegetation make it challenging to model different

vegetation on a case-by-case basis, it can be modelled the geometry abiding by (Bitog et al., 2011), with a constant LAD of  $2.3 \text{ m}^2/\text{m}^3$ . For the definition of the effects exerted by vegetation on airflow, the Ergun equation was employed to ensure the viscous resistance factor ( $1/\alpha$ ) and the inertial resistance factor ( $C_2$ ). The Fluent theory guide works as a provider of the following formulae (ANSYS, Inc., Fluent User's Guide 18.1, ANSYS, Inc., Canonsburg, Pennsylvania, United States, 2017., n.d.):

$$\alpha = \frac{d^2}{150} \frac{\phi^3}{(1 - \phi)^2} \quad (5.1)$$

$$C_2 = \frac{3.5}{d} \frac{(1 - \phi)}{\phi^3} \quad (5.2)$$

According to Sonnenwald et al. (2016), where  $d$  denotes the particle diameter,  $\phi$  is the void fraction, which represents the fraction of the volume of voids over the total volume, with typical values recommended as 0.02 for solid particles and 0.96 for highly porous materials.

## 5.2.2 CFD geometry

### 5.2.2.1 Courtyard and computational domain

Hall et al. (1999b) carried out small-scale wind tunnel experiments to investigate the dispersion of pollutants emitted from the bottom of courtyards and other enclosed spaces. In their experiments, different types of closed courtyards were chosen for the experiment, with ratios of depth to width from 5 to 0.1. In this research, the closed courtyard model (ratio of depth to width is 1) was selected as the validation model and changed to the full-size model, for investigating the indoor thermal performance and ventilation conditions, some windows were added to the validation model. For the baseline courtyard model, a standard courtyard

model was modelled with the following dimensions: 20 m width, 20 m depth and 5 m height, there are two floors of the building, each floor with a height of 2.5 m. The courtyard is in the centre of the building, which is  $10 \times 10 \text{ m}^2$  (Figure 5.2).

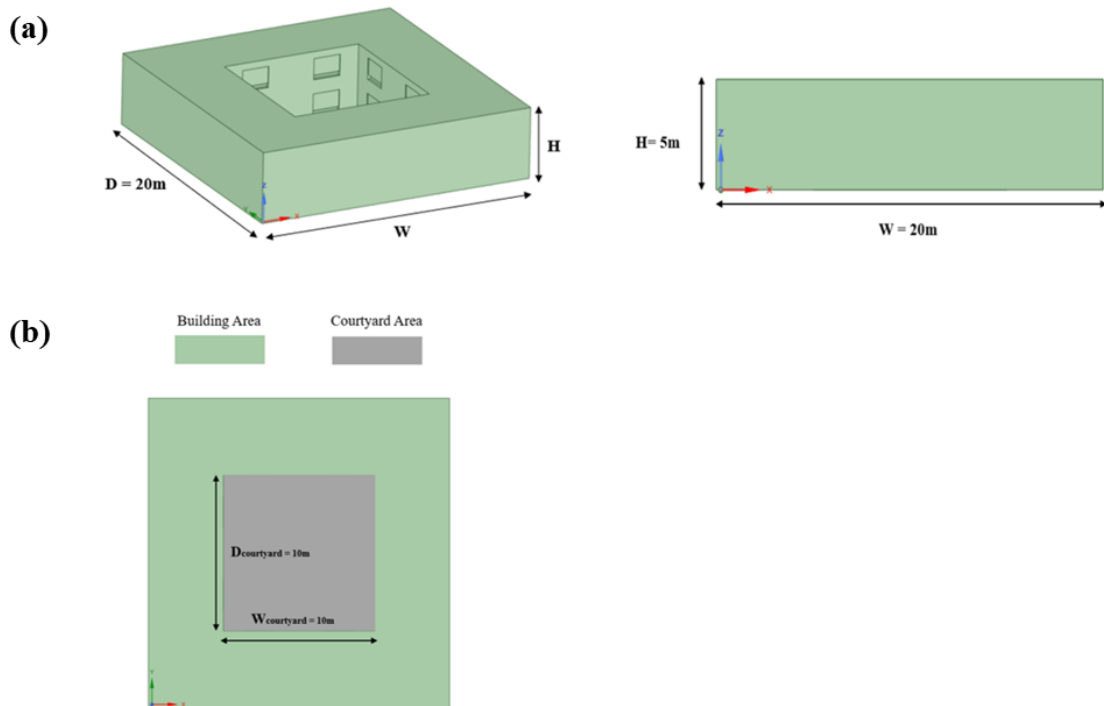


Figure 5.2 Courtyard model and geometry of the central courtyard. (a) Courtyard model (b) Geometry of the centre courtyard.

In order to study the indoor thermal performance and ventilation conditions, the building has laid out two storeys and 12 rooms on each storey, only 8 rooms facing the courtyard are used for simulation, the layout of the rooms on each floor is shown in Figure 5.3. The dimension of each room is 5 m width  $\times$  5 m depth  $\times$  2.5m height, the wall thickness is 0.24 m (ASTM C67 Standard, 2014), and the internal dimensions of each test room are 4.76m  $\times$  4.76m  $\times$  2.26m, which is shown in Figure 5.4 and the layout of each room facing the courtyard has a window. The courtyard model was scaled up from (Hall et al., 1999b). However, the original wind tunnel courtyard model did not include windows. Therefore, the

size of the window was assumed in this study, and its position was set in the centre of the wall. According to (ASHRAE-90.1-2013, 2013), the optimal window-to-wall ratio is recommended to be between 0.24 and 0.30. In this study, a window-to-wall ratio of 0.24 was chosen, resulting in window dimensions of 2 m x 1.5 m. The thickness of the window is 0.1m, with only 20% of the window opening area given the practical considerations (Figure 5.5).



Figure 5.3 The layout of the rooms on each floor (R - Room, N - North, W - West, S-South, E -East, G - Ground floor, F – First floor).

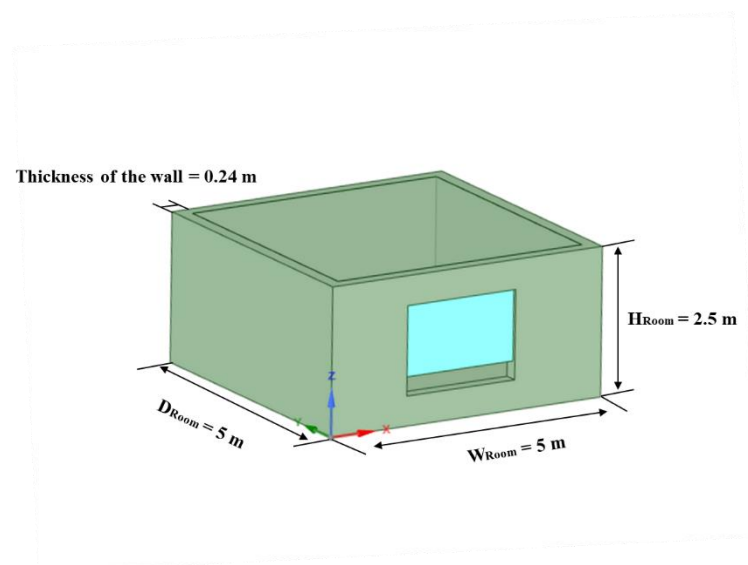


Figure 5.4 The dimensions of each room.

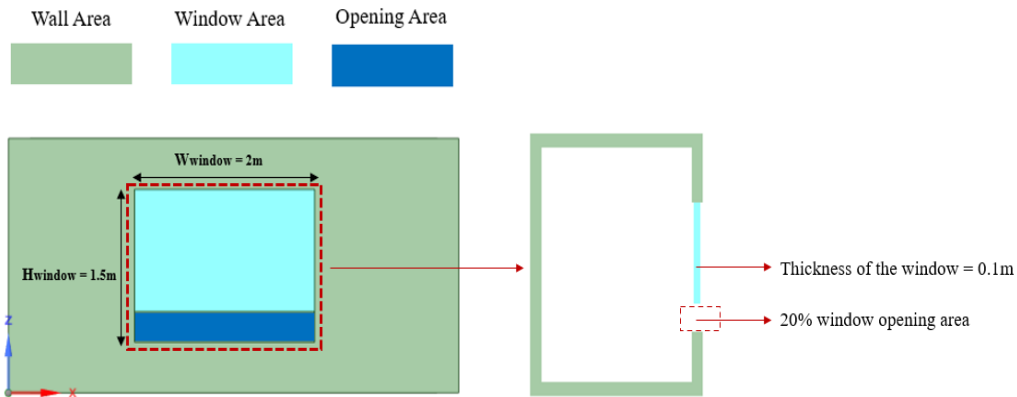


Figure 5.5 The dimensions of each window and schematic showing dimensions.

The domain of the courtyard is shown in Figure 5.6, which was obtained by equally scaling the domain of the validation model (Hall et al., 1999b). Two sides and top walls are set to symmetry walls, and the distance between the courtyard and two side symmetry walls was set to  $5H$ , which was  $25\text{ m}$ .  $5H$  and  $20H$  were selected for the distance between the courtyard, inlet and outlet, respectively, to provide sufficient space for airflow circulation. The distance between the courtyard and the top lane of the domain was set up to  $7H$ , which was  $35\text{ m}$ , the rationale for this setting is derived from the wind velocity profile (Hall et al., 1999b). The wind comes from the inlet, in the positive direction along the  $x$  axis.

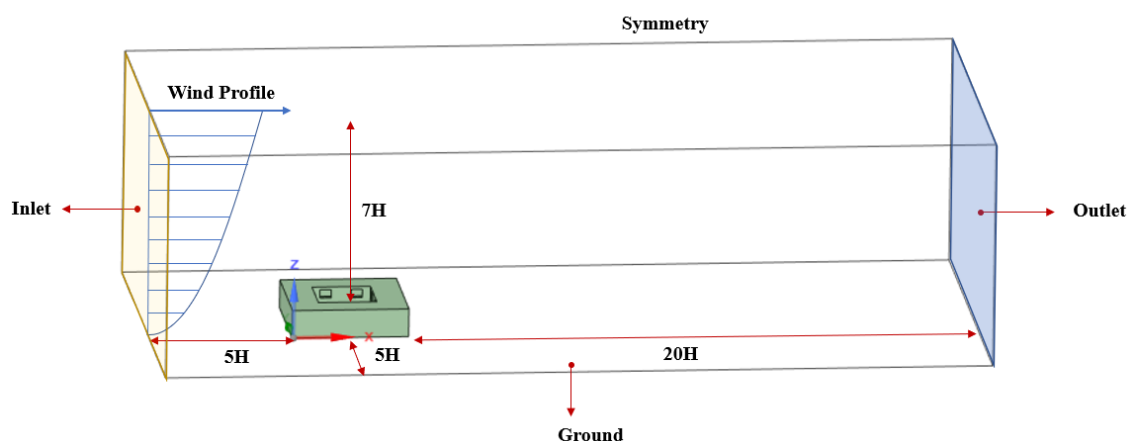


Figure 5.6 The dimension of the domain and the direction of the wind.

### 5.2.2.2 Vegetation

Vegetation in the form of cuboidal volumes is modelled as porous zones representing hedges. The model is an extension of the work by Manickathan et al. (2018b), wherein the vegetation zone was modelled as a 2D porous square. In the current case, the courtyard is divided into four sections, with a large hedge in the centre of each. The hedges extend 2.4 m in either direction, while two different heights (1.5 m and 2 m) of hedges are modelled for comparison. They are placed at a distance of 1.2 m away from the building with inter hedge distance of 2.8 m (Figure 5.7). The example of the simulated vegetation is shown in Figure 5.8.

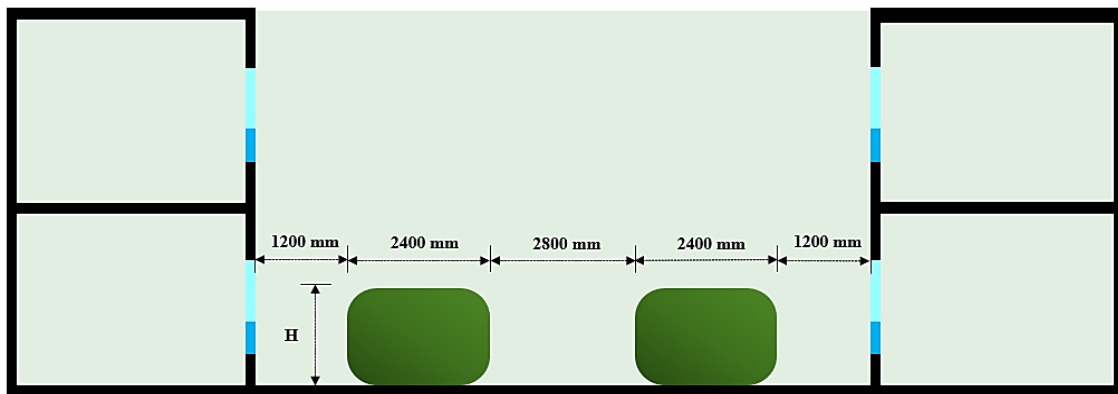


Figure 5.7 The dimension of the vegetation inside the courtyard.



Figure 5.8 Commercial example of cuboidal hedges and relationship of vegetation to occupants. (a) Commercial example of hedges trimmed to form a cuboidal shape ('New Leaf

Topiary-Quality Garden Plants <https://www.Newleaftopiary.Co.Uk/> [Accessed: 7-March-2021]’, n.d.), (b) Relationship of vegetation w.r.t occupants.

### 5.2.3 CFD mesh design and verification

The size and quality of the mesh influence the accuracy of the simulation, the finer mesh arrangement will provide more accurate simulation results. In this study, the computational domain was meshed using unstructured mesh. The mesh of the courtyard and surrounding buildings is refined to ensure that the flow field is accurately captured in the simulation. For airy areas around buildings, choosing a larger element size reduces calculation time and has a minor effect on the quality of the grid, such as skewness. Choosing finer meshes for the building facades as well as for the interior of buildings and courtyards provides more accurate results of the fluid flow around the building. In this study, there are some small components, such as the thickness of windows being 0.2 m, so a finer mesh is needed to pounce on them during the meshing process. The baseline courtyard model was meshed under the conditions in Table 5.2. As a result, for the baseline model, there are 5,067,770 elements and 989,698 nodes. The meshed courtyard and its surrounding environment are shown in Figure 5.9.

Mesh setup conditions		
Physics Preference: CFD	Solver Preference: Fluent	
Overall Sizing	Sizing Function: Adaptive	Relevance Centre: Fine
	Transition: Slow	Span Angle Centre: Fine
	Element Size: 1.5m	Minimum Edge Length: 0.05m
Inflation	Inflation Option: Smooth Uniform Transition	
Face Sizing: Building	Geometry: Building Area	Element Size: 0.1m

Table 5.2 Mesh setup condition.

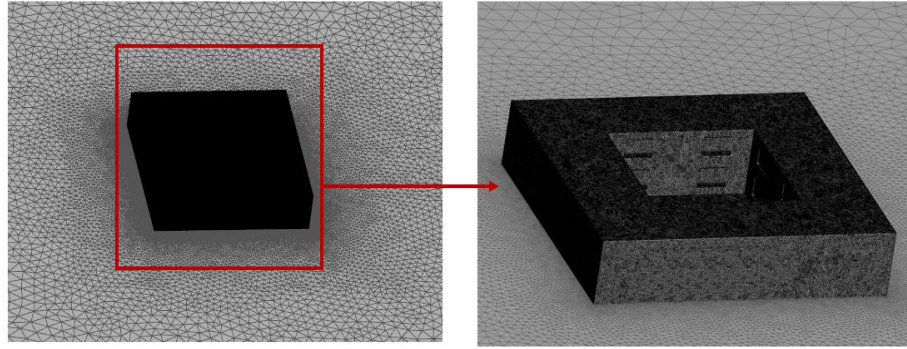


Figure 5.9 Meshed courtyard and its surrounding microclimate.

The sensitivity analysis was carried out to validate the model and to ensure that the results were independent of the size of the mesh. Sensitivity analysis requires validation of results using the same model under different mesh sizes. Four groups of meshes of different sizes have been selected for analysis, as shown in Table 5.3. In order to obtain more accurate validation results, a passive cooling strategy was incorporated into the courtyard, and the validation model used for the mesh sensitivity analysis was the courtyard model with four trees. To ensure the accuracy of the results, three different mesh sizes were selected for analysis: a coarse mesh with 3 million cells, a medium mesh with 5 million cells, and a fine mesh with 7 million cells. Figure 5.10 presents the analysis results of the temperature profile across the indoor area and the courtyard, comparing these three mesh sizes.

The greater cooling effect on the left side of the tree is primarily due to the cooling effect of the vegetation. The clockwise vortex in the courtyard first contacts the vegetation on the right, where the higher cooling effect and contact time slow down the airflow, resulting in a more pronounced cooling effect around the vegetation on the left.

The results indicate that the temperature difference between the coarse and medium mesh arrangements along the horizontal line was minimal, only 1.51%, while the difference



between the medium and fine mesh was 1.13%. These findings suggest that different mesh sizes do not affect the results. Consequently, the medium mesh size was selected for further calculations in this study.

Mesh Size	Mesh Settings	Number of	
	Building Vicinity Sizing (mm)	Elements	Nodes
Coarse	130	3,161,904	632,788
Medium	100	5,323,281	1,063,550
High	84	7,432,665	1,483,888

Table 5.3 Mesh setup for sensitivity analysis (courtyard with small trees).

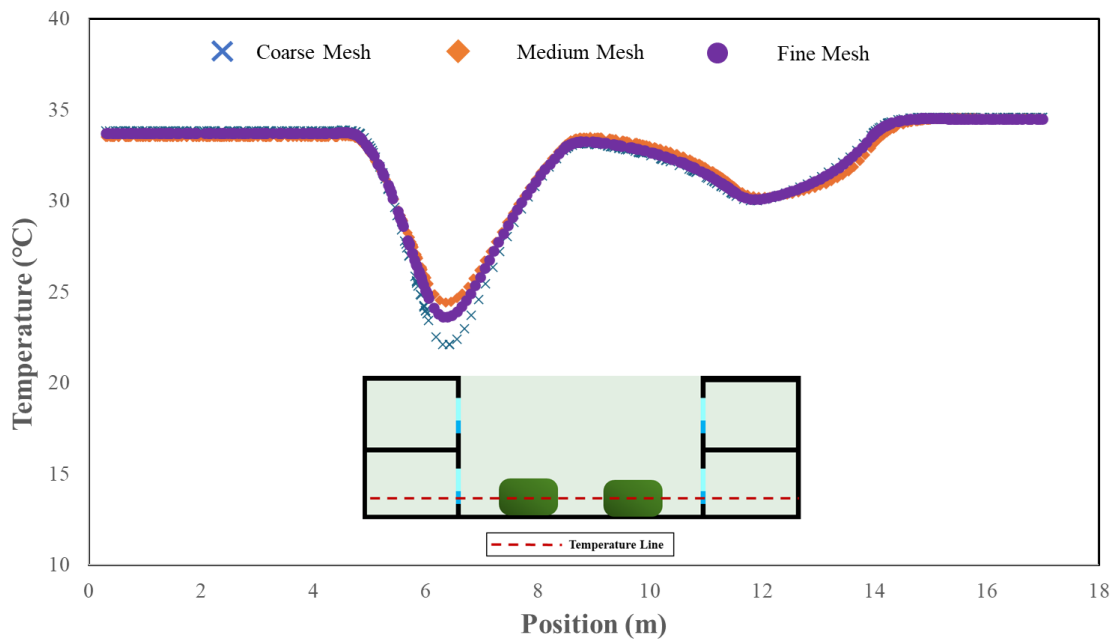


Figure 5.10 Simulated results of temperature along a horizontal centre line of the courtyard model with small trees at a height of 0.7 m for the grid sensitivity analysis.

#### 5.2.4 Boundary conditions for the simulation study

The fluid domain was created as an enclosure, which allows for the simulation of airflow around the courtyard model. In Figure 6, one side set as the velocity inlet, the wind velocity and longitudinal profile from the wind tunnel experiment of Hall et al. (1999b) was used to define the inlet boundary conditions, the other side set as the pressure outlet to be 0 Pa. To investigate the influence of passive cooling strategies on the courtyard and indoor areas in the hot climate, the air temperature for the inlet and outlet are constantly set to 309K (35.85°C). The CFD simulation considers the influence of buoyancy factors and the gravity in the simulation area to be set at  $-9.8 \text{ m/s}^2$ . Symmetry for the top and two sidewalls and ground boundaries are specified as no-slip boundary conditions. For the settings of materials in the courtyard model, the ground and symmetry boundary used ash-solid and bricks.

### 5.3 Results

#### 5.3.1 Validation of the courtyard model

In this study, a validation of the closed courtyard in CFD simulations was investigated based on wind tunnel experiments of the courtyard by (Hall et al., 1999b). In their experiments, different aspect ratios of courtyards have been selected to test the dispersion of pollutants in the courtyard. One of the aspect ratios ( $A = 0.1$ ,  $A$  is the aspect ratio of the courtyard, which is equal to  $H/W$ ) of the courtyard has been chosen to validate in this project. They tested the courtyards in the wind tunnel working section, which is 22 m long by 4.3 m wide and 1.5 m high, in order to get more accurate validation results, the similar size of the domain has been set in the Fluent 18.1, which was shown in Figure 5.11, the dimension of the validation courtyard is 0.6 m width  $\times$  0.6 m depth  $\times$  0.02 m height.

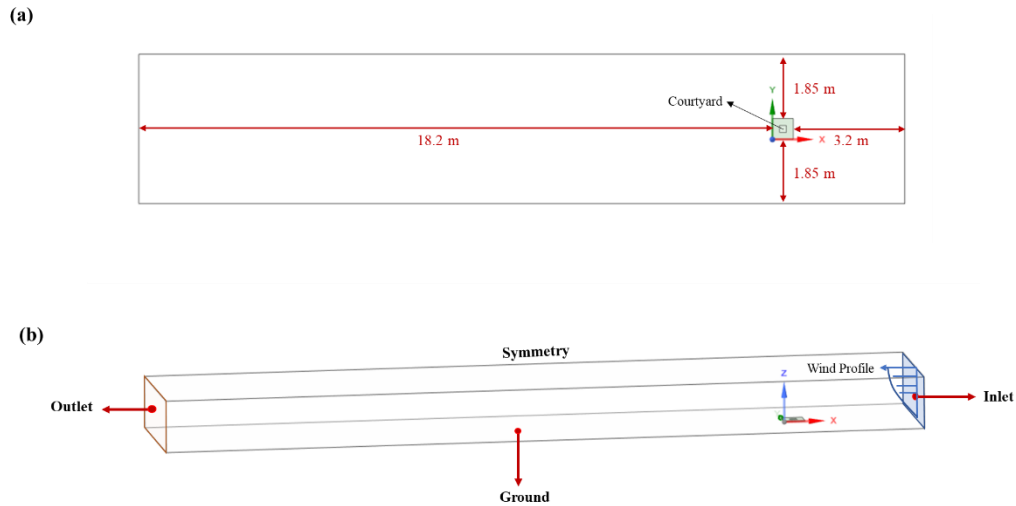


Figure 5.11 Simulation domain and dimensions of the validation model. (a) Simulation domain of the validation model (b)The dimension of the validation.

The velocity turbulence intensity profile through centre of the courtyard has been tested by the wind tunnel experiment by Hall et al. (1999b); for validating the wind velocity of the courtyard in the CFD, a wind velocity line perpendicular to the ground was set in the centre of the courtyard to collect data for comparison. The comparison results, as shown in Figure 5.12, CFD simulation results are slightly higher than the measured values from wind tunnel tests, and the average discrepancy between the two results was 3.2%, there are small errors between the two results, which is likely to be explained by factors including k- $\epsilon$  turbulence model limitations in the CFD simulation and experimental uncertainties. Overall, the results of the CFD simulations are in high agreement with the experimental results of (Hall et al., 1999b).

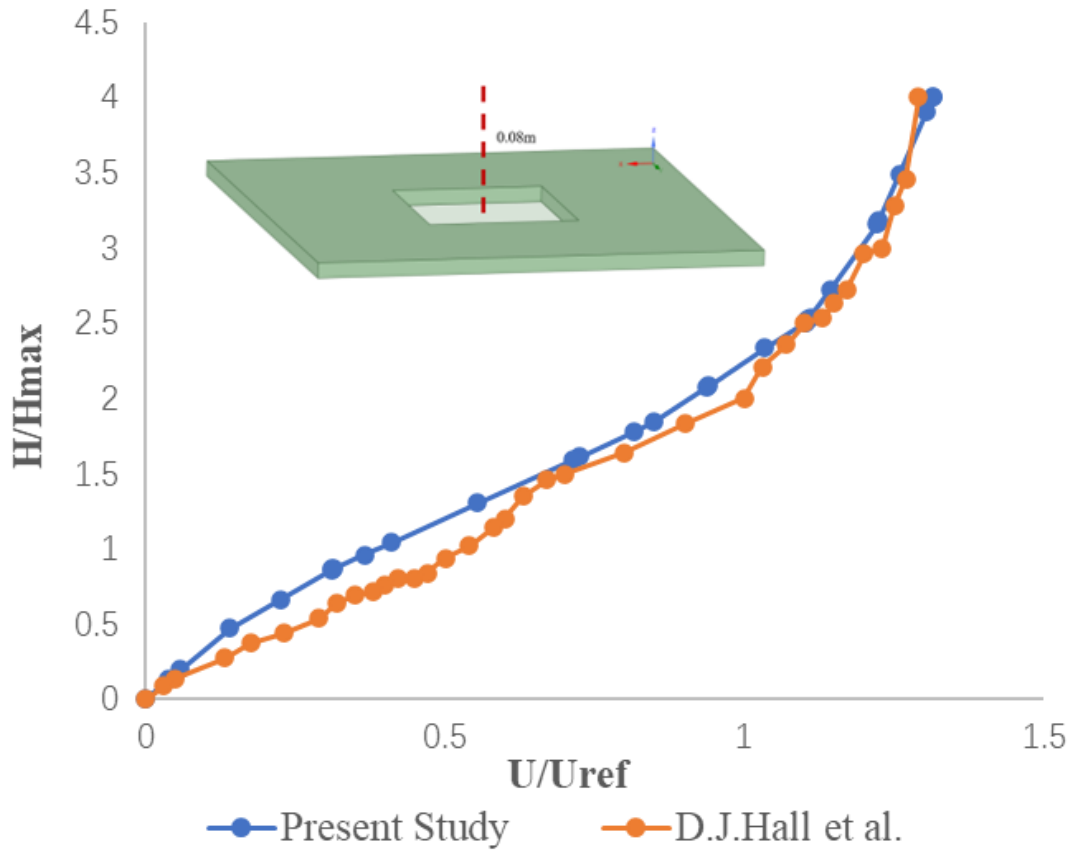


Figure 5.12 Comparison of dimensionless wind velocity along the analysis line. (H: height above the ground, Hmax: reference height for the wind velocity, U: wind velocity, Uref: wind velocity at the height of Hmax ((Hall et al., 1999b).

### 5.3.2 Validation of the vegetation

The validation of the vegetation model was based on Manickathan et al. (2018b), in which the domain size of the reference case had a length of 35 m and a height of 11.5 m (Figure 13). In the 2D field, vegetation was illustrated by a one-meter square in place of 8.5 m based on the inlet and 0.5 m on the ground. Inlet velocity was constructed with Richards & Norris (2015), in which the von Karman number and roughness height were individually placed to 0.41 and 0.0217 m. The inlet air temperature was imposed to the setting to 32 °C.

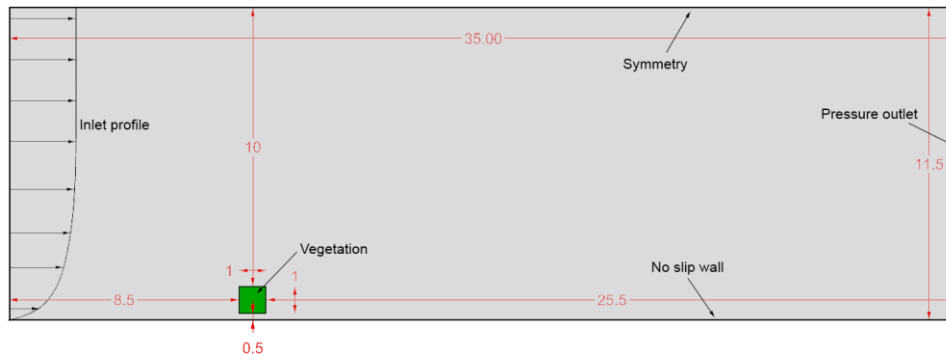


Figure 5.13 Simulation field of the validation model, based on the porous vegetation according to the indication of the green square and centred on the x-axis.

Figure 5.14 presents the velocity and temperature distribution featured by the area around the vegetation ( $-2 < X < 6$ ;  $0 < \text{Height} < 3$ ). The vegetation zone presents resistance toward the flow of air, on the basis of the decreased speeds following the zone. The velocity distribution shows fine conformity to the reference research (Manickathan et al., 2018b). A plot of velocity along the analysis line (with the marks in the figure running through the centre of the vegetation patch) can be revealed in Figure 5.15. The presentation of vegetation is achieved via the green patch in the extension range of  $-0.5 - 0.5$  on the x-axis. The trend committed a close following to the numerical model of (Manickathan et al., 2018b). The condition of a slight underprediction for the back of is the vegetation patch. An observation of nearly  $0.04 \text{ m/s}^2$  deviation is conducted to the far end. The model works rather well amidst the low modelling complexity featured by the vegetation zone. A temperature reduction of approximately  $1 \text{ }^\circ\text{C}$  can be observed in the wake of the vegetation, which is analogous to the reduction under estimation in the reference case.

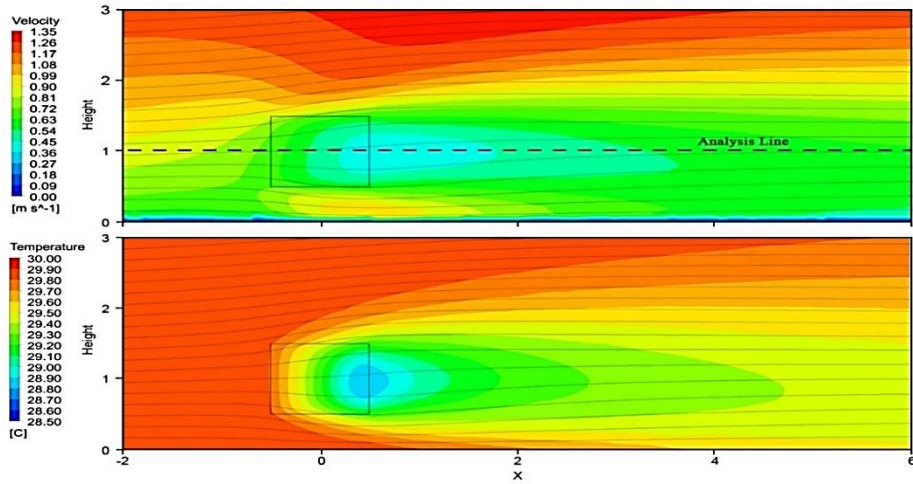


Figure 5.14 Contours of velocity and temperature near the vegetation (black square) based on the validation model.

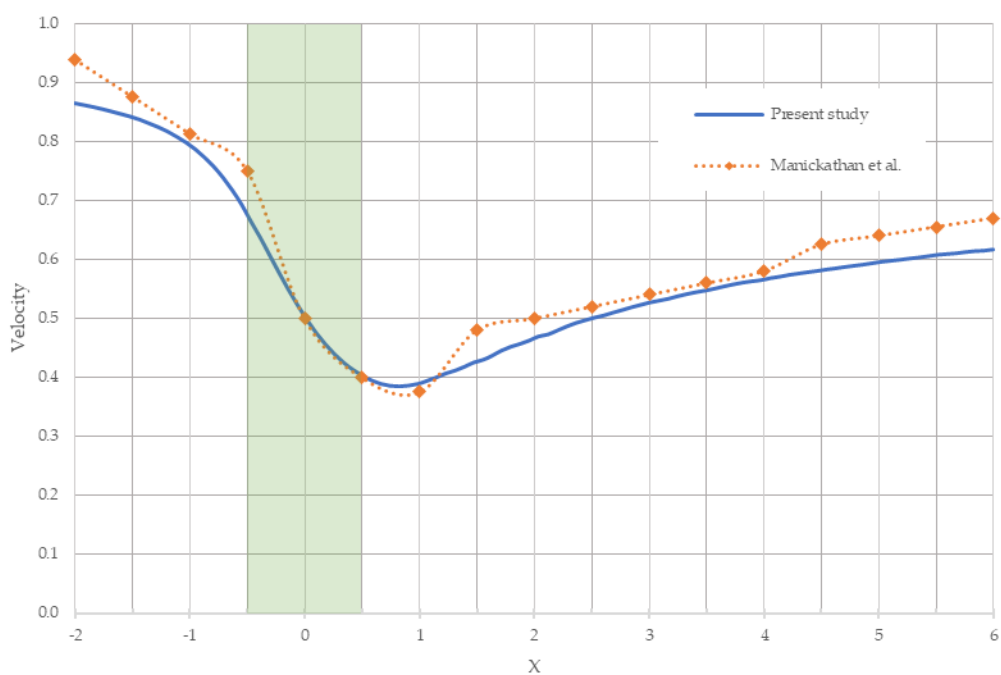


Figure 5.15 Comparison of wind speed on the analysis line, in addition to the vegetation zone under the in-dictation of the green patch in the range of  $-0.5$  to  $0.5$  on the x -axis.

Slight variations in temperature and velocity can occur due to the complex approach under the handle (Manickathan et al., 2018b). The author's source/sink terms for expounding modifications in such aspects as air humidity, temperature, momentum, and turbulence.

Nevertheless, as for this existing case, a simplified vegetation model was accepted here, considering no detailed energy fluxes at the leaf surface. Beyond that, the numerical simulation was implemented in ANSYS, just like being contrary to OpenFOAM, and they are employed in the reference case. In consideration of the target of the present research oriented with the determination of the attenuation affects which vegetation in a courtyard coupled with the seen wind pattern exerts upon the building platform, the deviations have been regarded to be of small scale; besides, the observed contour took on sufficient accuracy oriented with the further in-depth analysis.

### 5.3.3 Case 1: Baseline courtyard model

In this study, a baseline courtyard was set, and a fluid simulation of the courtyard was performed in Fluent 18.1 to verify the courtyard as one of the effective passive cooling techniques. Simulation results of velocity magnitude of the overall courtyard building. For the presence of the building, the airflow was altered, causing the air to move upwards. On the windward side, the wind speed was lower than 1m/s. On the leeward side, as impacted by the obstruction of the building, the wind speed was nearly consistent with the surface of the building, and a backflow phenomenon could be observed.

The aim of the present study was to investigate the effects of the combination of courtyard and other passive cooling technologies on the indoor thermal performance and natural ventilation conditions of buildings. To analyse the indoor thermal performance and natural ventilation conditions in the baseline courtyard model, two parameters, the indoor air-dry bulb temperature and the wind speed magnitude, were simulated and compared with the subsequent cases' results. Figure 5.16 presents the average wind speed magnitude in each room, the average wind speed and temperature in each room were calculated by setting up

nine test points in each room, collecting the wind speed and temperature at the mentioned nine points and determining their average value. The height of all test points was 0.6 m, based on the height of a normal person sitting on the chair. Figure 5.17 presents the simulation results of the wind speed in each room for the baseline courtyard model. According to the figure, the wind speed in the rooms was extremely low, with an average wind speed on the ground floor of around 0.0075 m/s in each room and that on the first floor around 0.02 m/s in each room. Since the courtyard was a closed space, it could also be observed that on the ground floor, the average indoor wind speed above 0.01m/s was recorded in the two rooms, i.e., REG2 and RSG1, with REG2 reaching 0.0144 m/s, whereas the lowest wind speed on this floor was in RWG1 on the west side at 0.0029m/s. On the first floor, the highest wind speeds were identified in the two rooms, i.e., REF1 and REF2, on the east side, which were significantly higher than the other rooms tested, with the wind speeds of 0.0447 m/s and 0.0357 m/s, respectively, while the lowest wind speed remained in REG1 on the west side (0.0051 m/s). In general, as suggested from the comparison of the wind speeds in the two rooms on different floors in identical directions, most of the wind speeds in the rooms on the first floor were higher than those in the rooms on the ground floor. In the Fluent18.1, specific to the baseline courtyard model, the air temperature for the inlet and the outlet was set to 309 K (35.85 °C) constantly, so the average temperature in each room was 35.85 °C.



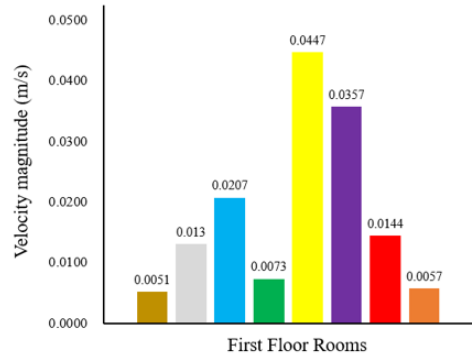
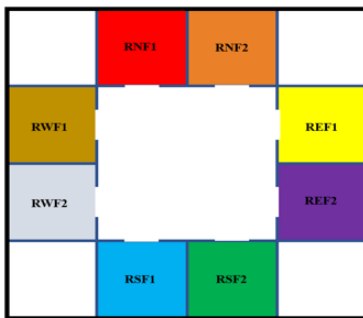
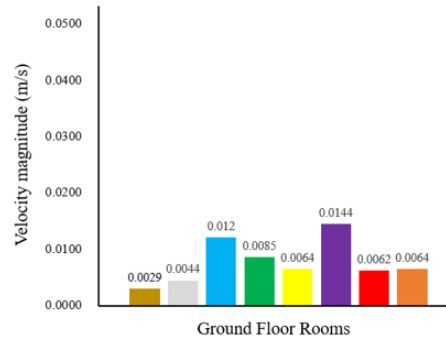


Figure 5.16 Average wind speed magnitude (m/s) in each room for the baseline courtyard model.

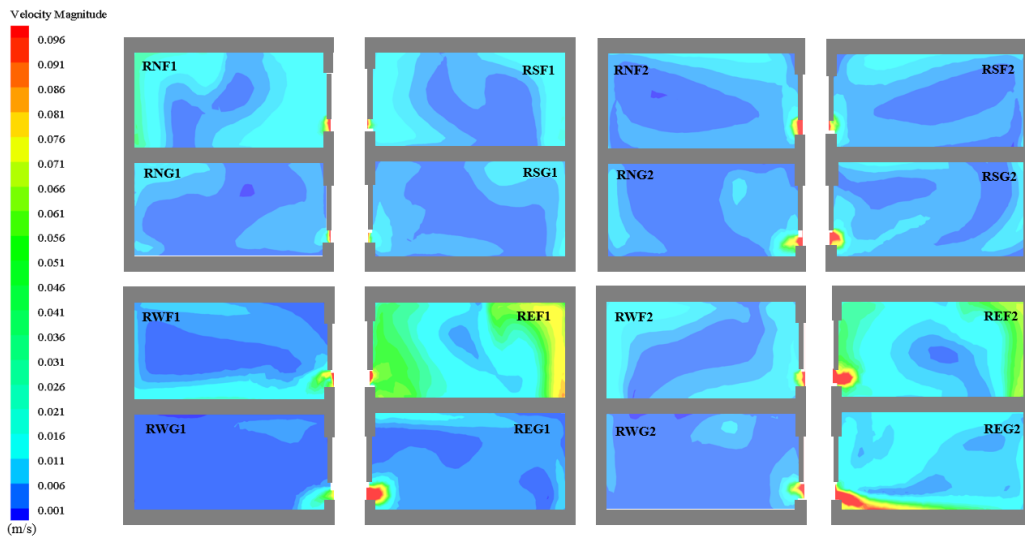


Figure 5.17 Contours of the wind speed in each room for the baseline courtyard model.

### 5.3.4 Case 2: Baseline courtyard model with four small trees

Vegetation in the courtyard could effectively improve the microclimate of the courtyard for its evaporative cooling effect and shading, which could improve the thermal comfort of the courtyard by reducing the temperature around it. In this section, four 1.5m height hedges were placed at the corners of a closed courtyard to determine the effect of small size vegetation on the indoor thermal performance and ventilation conditions of the building.

In the baseline courtyard model, the temperature was set to 35.85 °C, and it was kept constant. Figure 5.18 illustrates the air temperature in each room. Figure 5.19 illustrates the simulated results of the air temperature contour with isotherm in each room. According to the figure, the temperature in each room decreased after the configuration of vegetation in the courtyard, whereas the decrease was of a different magnitude. Among the 16 rooms tested on the two floors, the four rooms on the east side were reported to be warmer than the rooms in the other directions, which achieved average temperatures over 34 °C. The four rooms (RNG1, RNF1, RSG1 and RSF1) on the north and south sides close to the inlet were cooler, especially RSG1 and RSF1 on the south side, which were the lowest temperature rooms on the respective floor. The highest temperature of all the rooms tested was referred to as REF2 (34.77 °C), and the lowest temperature was RSF1 at 30.52 °C. In the eight test rooms on the ground floor, the average indoor temperature was 33.39 °C; on the second floor, it was 32.79 °C. Compared with the baseline courtyard model, the indoor temperatures dropped by 7.4% and 9.3%, respectively, which demonstrated that planting vegetation in the courtyard cooled the interior.

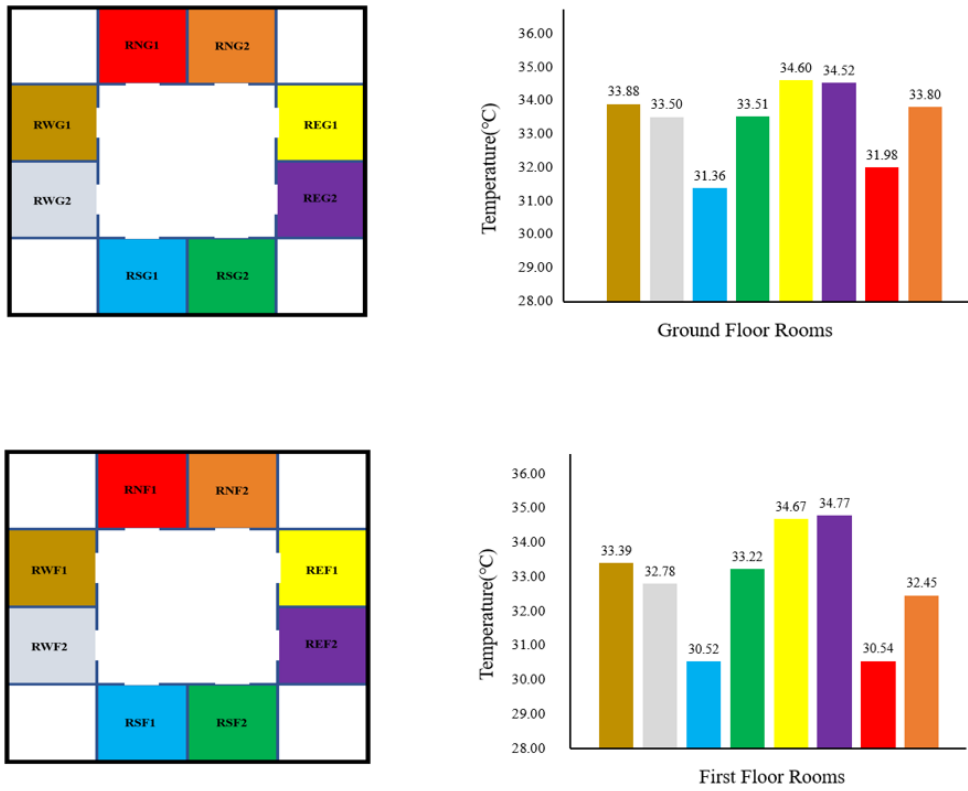


Figure 5.18 Average air temperature in each room for the baseline courtyard model with four small trees.

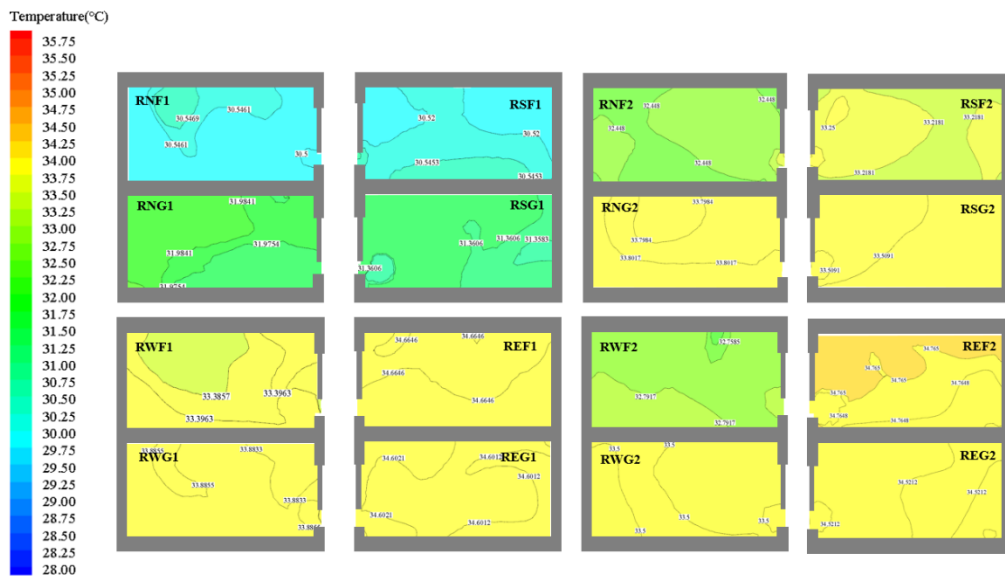


Figure 5.19 Simulated results of the air temperature contour with isotherm in each room for the baseline courtyard model with four small trees.

In Figure 5.20, the air temperature in each room for Case 1 and Case 2 was compared, and the relevant temperature difference was also shown. It was therefore indicated that the vegetation significantly cooled the interior of the courtyard building. According to the comparison of the temperatures of the rooms in the identical location, the temperatures of the first-floor rooms were lower than those of the ground-floor rooms. The most significant temperature reduction was in the two rooms on the first floor facing north and south (i.e., RNF1 and RSF1), the temperature declined by 5.31 °C and 5.33 °C, respectively. Besides, the temperature of RNG1 with a drop of 3.87 °C and RNS1 with a drop of 4.25 °C were in the next line. The rooms facing east and west had a minimal decrease in temperature, especially in the four rooms on the east side, in which the average room temperature only decreased by around 1.2 °C.

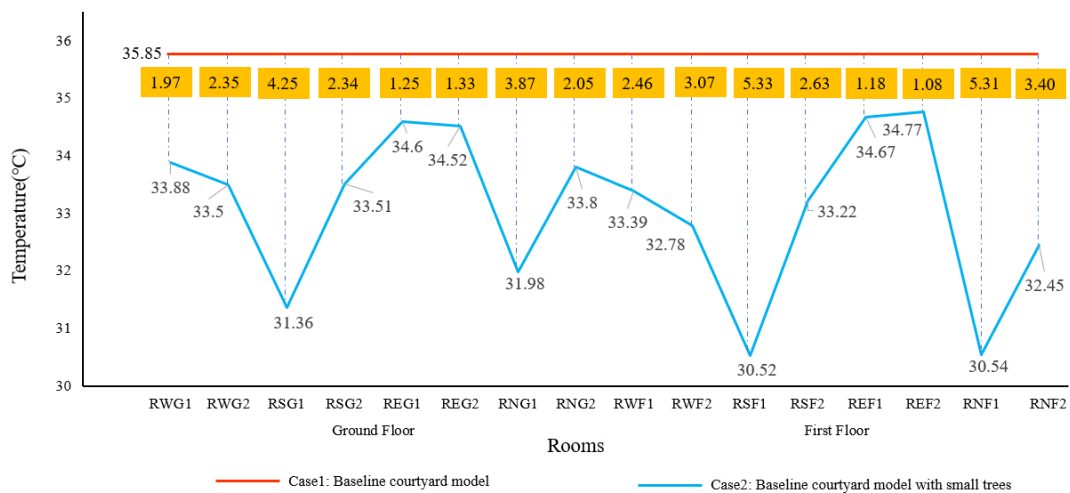


Figure 5.20 Comparison of air temperature for Case 1 and Case 2 in each room.

As indicated from the comparison of the mentioned results, in Case 2, the courtyard with four small trees cooled the interior of the building, whereas the extent of the cooling effect was determined by the specific location in each room. To be specific, the rooms facing north

and south exerted the best cooling effect, the rooms facing east achieved a limited cooling effect, and the rooms on the first floor had a better cooling performance than those on the first floor. The reason for this result was explained as the temperature reduction from vegetation was limited in scope.

Figure 5.21 presents the simulation results of the average wind speed magnitude in the respective room for the courtyard model with four small trees. According to the figure, the wind speeds on the ground floor were all smaller than 0.02 m/s, the two rooms with the highest and lowest wind speeds, at 0.0153 m/s and 0.0043 m/s, respectively, were both on the east side. The indoor wind speed in RNG1 and RNG2, both above 0.009 m/s, was higher than the average indoor wind speed of other rooms located on the ground floor. On the first floor, the indoor air speed in REF1 and REF2 on the east side was significantly higher than that in the other rooms, which was nearly four times higher than the other rooms. The contours of the wind speed in each room for the baseline courtyard model with four small trees are shown in Figure 5.22.

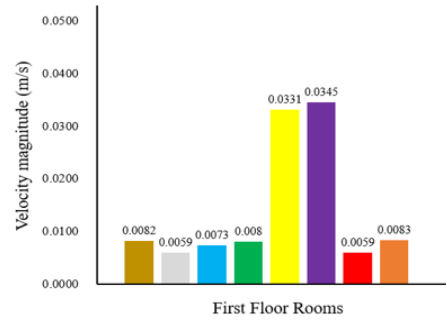
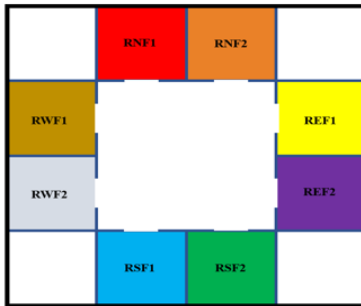
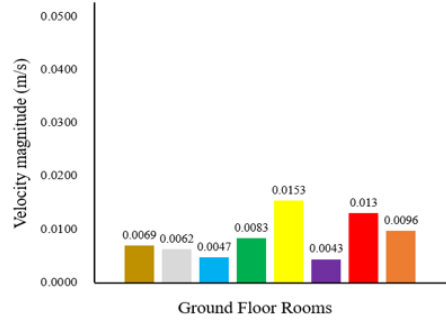
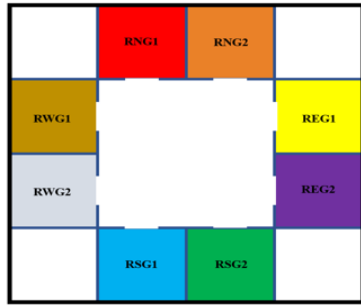


Figure 5.21 Average wind speed magnitude in each room for the baseline courtyard model with four small trees.

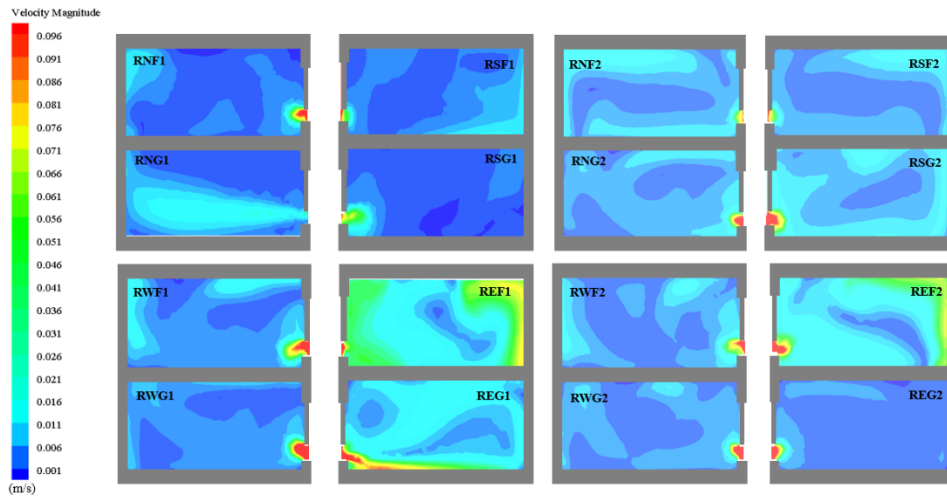


Figure 5.22 Contours of the wind speed in each room for the baseline courtyard model with four small trees.

Figure 5.23 shows the comparative results of the wind speed for the identical rooms in Case 1 and Case 2. According to the figure, the placement of four small trees in the closed courtyard impacted the ventilation of the building's interior. As indicated from the comparison of the simulation results, the effect of small trees on the indoor ventilation of rooms in different locations was not similar. On the ground floor, specific to the four rooms (i.e., RNG1, RNG2, RWG1 and RWG2) on the north and western sides, with the addition of small trees in the courtyard, the indoor wind speed significantly increased, especially the indoor wind speed of RWG1, increasing from 0.0029 m/s to 0.0069 m/s, nearly a 2.4 times improvement. As opposed to the mentioned, in the two rooms located to the south, RSG1 and RSG2, the indoor wind speed decreased due to the planting of small trees. The reduction in RSG1 was particularly pronounced, with a drop of 0.0073 m/s, while RSG2 only dropped by 0.0002m/s, which was nearly identical to the results for Case 1. However, on the east side, the trends in REG1 and REG2 were diametrically opposed, REG1 increased by 0.0089 m/s, while REG2 decreased by 0.0101 m/s. In the eight testing rooms on the ground floor, by arranging four small trees inside the courtyard, the greatest increase in indoor wind speed magnitude was identified in REG1, and the most significant decrease was reported in REG2. On the first floor, according to the comparison of the simulation results, the wind speed increased in three rooms, RNF2, RWF1 and RSF2, with the most significant increase in RWF1, where the wind speed magnitude increased by 0.0031 m/s. RSF2 (increase of 0.0007 m/s) and REF2 (decrease of 0.0012 m/s) achieved the minimum increase and the minimum decrease, respectively.

As suggested from the comparative results, the arrangement of four small trees in the courtyard impacted the indoor wind environment in surrounding buildings. Some rooms showed an increase in wind speed size, while some showed a decrease. A number of factors

could be responsible for this (e.g., the transpiration of the vegetation), which changed the temperature and pressure of the surrounding air, thereby indirectly impacting the wind environment in the courtyard or the vegetation. As a result, the wind might be blocked, and the direction of the wind flow might be changed, thereby regulating the wind speed in the courtyard and the interior.

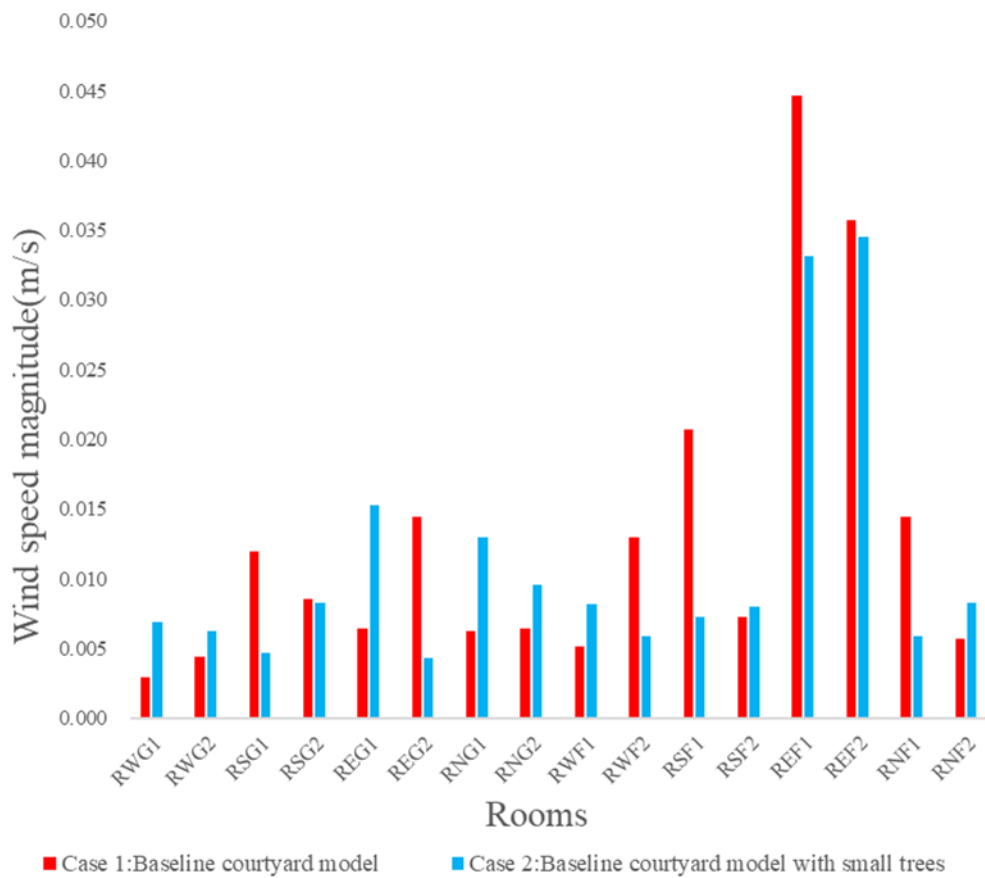


Figure 5.23 Comparison of wind speed magnitude for Case 1 and Case 2 in each room.

### 5.3.5 Case 3: Baseline courtyard model with four large trees

To investigate the effect of different sizes of vegetation in the courtyard on the indoor thermal and wind environment, four trees with a height of 1.5 m were placed in the courtyard in Case 2. In this section, the height of the original vegetation was regulated, and the height



of each tree increased to 2 m. The simulation results were employed to determine the effect of large trees on the indoor air temperature and natural ventilation.

Figure 5.24 illustrates the average air temperature in 16 separate rooms with four large trees within the courtyard. A large temperature range could be found between different rooms on the identical floor, as well as a slight temperature difference between two rooms on the identical vertical line. On the ground floor, RNG1 and RSG1 were the two rooms with the lowest temperatures, which achieved indoor air temperatures at 30.83 °C and 30.79 °C, respectively. Adjacent to the two rooms mentioned above, the air temperatures in RNG2 and RSG2 reached over 33 °C. However, the warmest rooms were REG1 (34.24 °C) and REG2 (34.21 °C) on the east side, with a maximum indoor temperature difference of 3.45 °C in the eight rooms tested on the ground floor. Compared with the average room temperature (32.94 °C) on the ground floor, the temperature in the first-floor room was reduced to 32.11°C. Consistent with the indoor thermal conditions on the ground floor, RNF1 and RSF1 were the two rooms on the first floor with the lowest temperatures at 29.27 °C and 29.39 °C respectively, while REF1 and REF2 were the rooms with the highest temperatures. According to the simulation results, among the 16 examined rooms in Case 3, the largest temperature differences were identified in REF1 and RSF1 on the first floor, with a difference of 5.1°C. The temperature difference between two rooms on different floors located in the identical vertical direction was smaller, and the indoor temperature on the first floor would be lower than that on the ground floor, except for REF1 and REF2, where the room temperatures were 0.13 °C and 0.08 °C higher than those of REG1 and REG2, respectively. Simulated results of the air temperature contour with isotherm in each room for the baseline courtyard model with four large trees are shown in Figure 5.25.

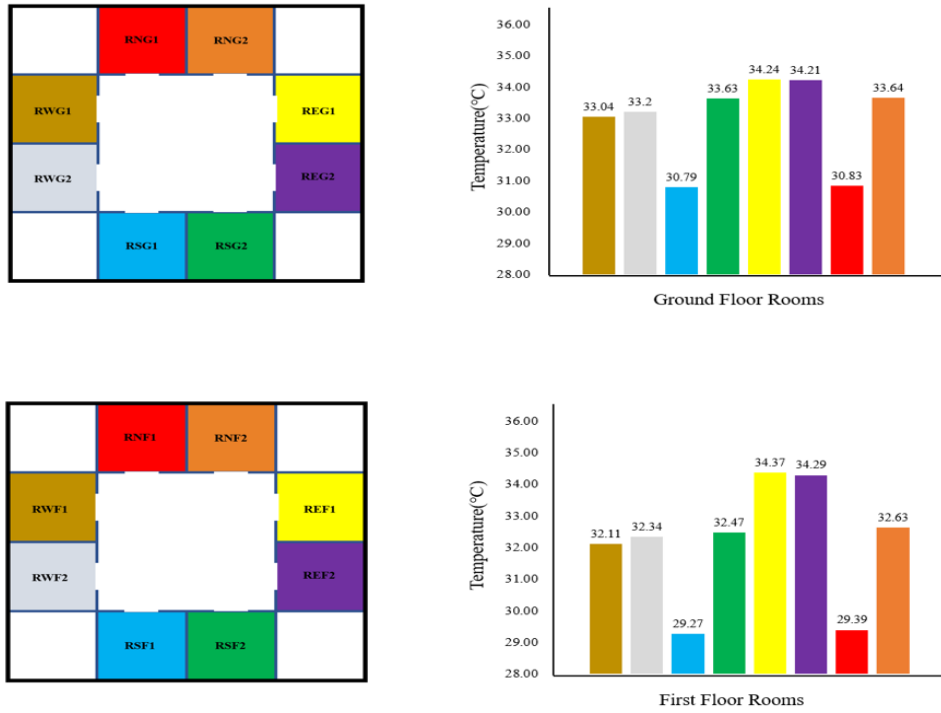


Figure 5.24 Average air temperature in each room for the baseline courtyard model with four large trees.

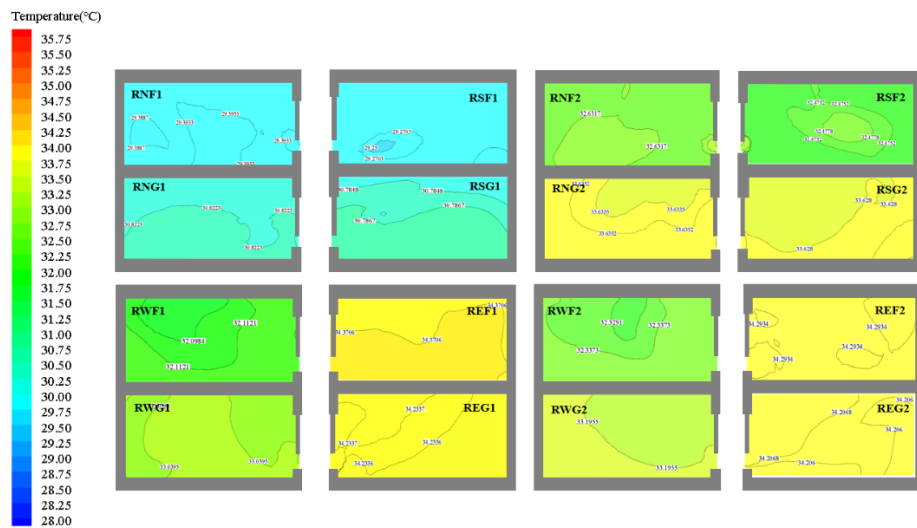


Figure 5.25 Simulated results of the air temperature contour with isotherm in each room for the baseline courtyard model with four large trees.

Figure 5.26 presents a comparative result of the temperature in each room of Case 1 and Case 3, which indicates the effect of the large trees in the courtyard on the indoor thermal environment and the difference in the thermal condition of the rooms in different locations. In the baseline model, the temperature was kept constant. Thus, in Case 1, the air temperature in each room was 35.85 °C. In Figure 29, the temperature in each room decreased, proving that placing large trees in the courtyard helped improve the indoor thermal environment. On the ground floor, the average indoor temperature decreased by 2.91 °C, and RSG1 and RNG1 were the two rooms with a temperature reduction of more than 5 °C. The minimum temperature reduction was in the two rooms on the east side, in which the temperature only dropped by 4.49% in REG1 and 4.57% in REG2, while the rest underwent a 2 °C to 3 °C temperature decrease. On the first floor, the most significant temperature decrease was identified in RSF1, which experienced a 6.58 °C reduction; RNF1 ranked behind RSF1, located on the north side, with a drop of 6.46 °C. Overall, the best cooling performance was achieved in the four rooms located on the north and south sides near the inlet, and the worst cooling effect was achieved in the four rooms on the east side.



Figure 5.26 Comparison of air temperature for Case 1 and Case 3 in each room.

In Figure 5.27, the average temperature in each room from Case 2 and Case 3 is presented to compare the improvement of the indoor thermal environment with different sizes of vegetation in the courtyard. As indicated from the comparative results, the average indoor temperature in Case 3 was generally lower than that in Case 2, with only two rooms (RSG2 and RNF2) slightly higher than those in Case 2. The largest temperature drop was in RWF1 with a drop of 1.28 °C, and the smallest drop was only 0.3 °C in RWG2 and REF1 and the largest temperature difference was found in RSF1, reaching 1.25 °C.



Figure 5.27 Comparison of air temperature for Case 2 and Case 3 in each room.

Figure 5.28 presents the simulation results of the average wind speed magnitude in each room for the courtyard model with four large trees. As indicated from the figure, on the ground floor, the room with the highest indoor wind speed was RSG2, located in the south, with a wind speed of 0.0132 m/s, the lowest indoor air speed was in RWG1, which was located at the west side with only 0.0059 m/s. It could be observed that the magnitude of the indoor air speed in the two rooms located in opposite positions was significantly close to each other. For instance, RNG2 and RSG2 were two rooms located on the north and south sides of the room. They were in opposite positions, with indoor air speeds above 0.01 m/s in both

rooms, and the air speed magnitude was relatively close. On the first floor, the highest indoor wind speeds were found in the two eastern side rooms (REF1 and REF2), measured as 0.0256 m/s and 0.0263 m/s, respectively. The two rooms on the west side had the lowest wind speed, both less than 0.008 m/s. As suggested from the comparison of the simulation results, on the first floor, the indoor air speed in the two rooms on the same side was closer. Contours of the wind speed in each room for the baseline courtyard model with four small trees are shown in Figure 5.29.

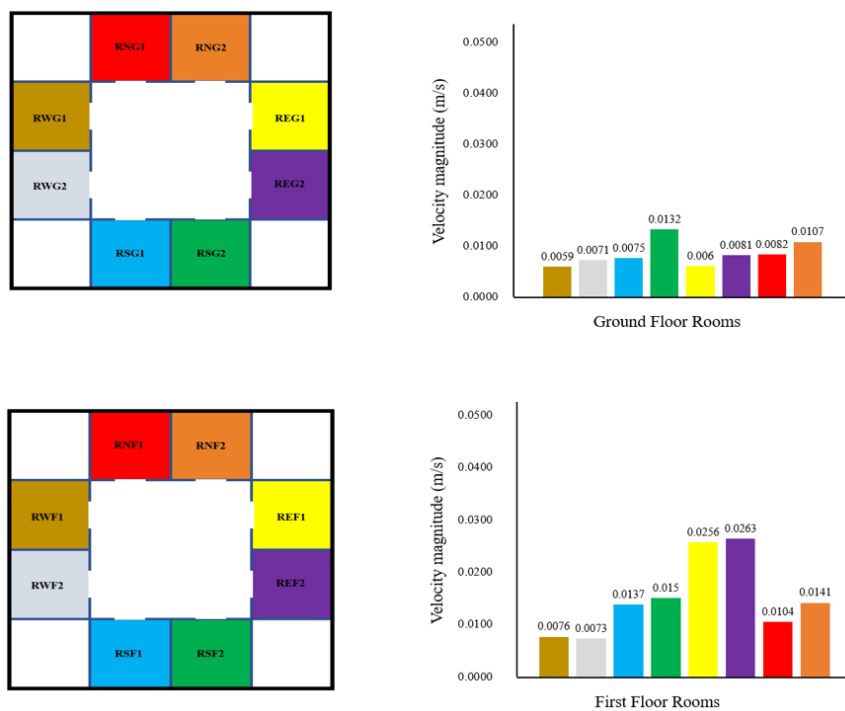


Figure 5.28 Average wind speed magnitude in each room for the baseline courtyard model with four large trees.

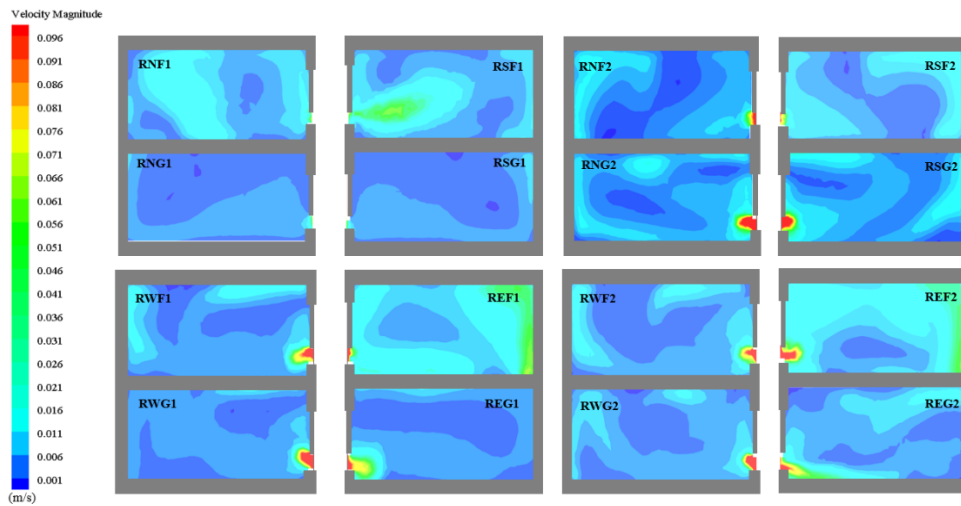


Figure 5.29 Contours of the wind speed in each room for the baseline courtyard model with four small trees.

Figure 5.30 compares the indoor air speeds in each room for three different scenarios. As indicated by the simulation results, the arrangement of different sizes of vegetation in the courtyard impacted the indoor ventilation of rooms with different orientations. By comparing the results of Case 1 and Case 3, the change in indoor wind speed produced by planting large trees in the courtyard could be observed. On the ground floor, four large trees in the courtyard increased the indoor wind speed in a total of five rooms, i.e., four rooms on the north and west sides and RSG2 on the south side. The largest increase was achieved in RSG2 where the wind speed increased by 0.0047 m/s, and in the other three rooms, the wind speed declined, with the most significant decline in REG2 (a decrease of 0.0063 m/s). On the first floor, only three rooms showed an increase in wind speed (i.e., RWF1, RSF2 and RNF2), marking an increase of 0.0025 m/s, 0.0077 m/s and 0.0084 m/s, respectively. The other five rooms underwent varying reductions in wind speed magnitude, with the largest drop happening in REF1 at 0.0191 m/s.

By comparing the effect of planting small and large trees in the courtyard on the indoor wind environment, the indoor wind speed magnitude was suggested to increase in 10 of the 16 individual rooms on the two floors due to the existence of large trees, with the most significant increase of 0.007 m/s in RSF2 located in the south side of the first floor. However, the wind speed in the remaining six rooms decreased, with the highest reduction observed in REG1 (0.0093 m/s).

As revealed from the comparison of the wind environment of each individual room in different scenarios, the indoor wind speed conditions were different in each room. There was no guarantee that planting vegetation in a courtyard would improve the indoor wind environment in surrounding buildings, and it was also not indicated that the larger size of the vegetation installed in the courtyard would improve the indoor wind environment. For instance, on the ground floor, Case 2 exhibited the highest average indoor wind speed (0.00854 m/s) for the eight rooms as compared with the other two cases. Furthermore, on the first floor, the highest average indoor wind speed was reported in Case 1 (0.0183 m/s).

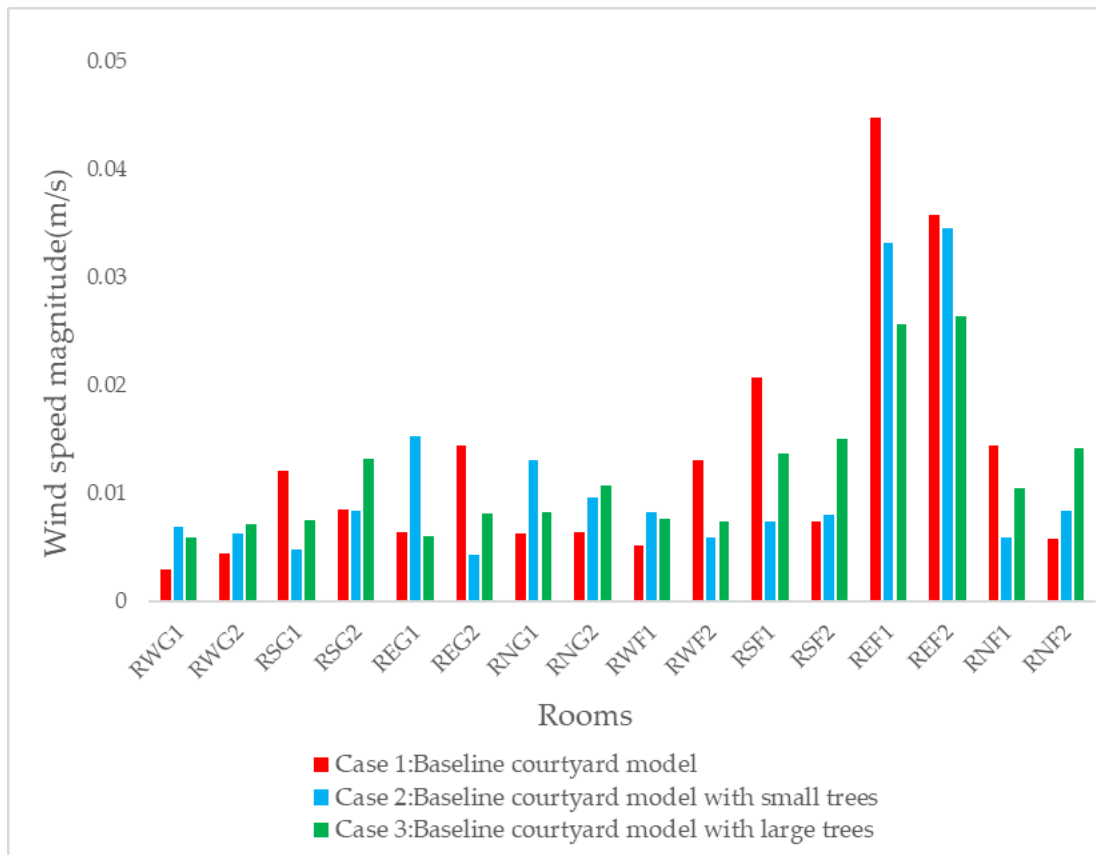


Figure 5.30 Comparison of wind speed magnitude for Case 1, Case 2 and Case 3 in each room.

### 5.3.6 Ventilation and temperature conditions inside the courtyard

In the present project, the vegetation of different sizes was set up in the courtyard. The study primarily aimed to determine the effect of the mentioned elements on the indoor thermal and wind environment, whereas the courtyard acted as a microclimate regulator, and adding vegetation into the courtyard could impact the microclimate of the courtyard. One slice (S1: X = 7500 mm) was selected to study the ventilation and temperature conditions within the courtyard impacted by different sizes of trees. Figure 5.31 illustrates the locations of the slices in the courtyard layout plan.





Figure 5.31 Position of the slice in the courtyard layout diagram.

Figure 5.32 presents the wind speed and temperature conditions for three different cases in terms of the S1. For the courtyard in Case 1, no passive cooling technology was installed in such a courtyard, so the airflow in the courtyard was relatively constant. Besides, the wind velocity decreased from top to bottom, nearly 0.3 m/s in the parts close to the building, accounting for the low air velocity in the indoor areas. However, the wind environment within the courtyard changed with the addition of different sizes of vegetation, with a reduction in wind speed around the vegetation, which was primarily attributed to the sheltering effect of the vegetation on the wind. The height of the small trees in Case 2 was 1.5 m, and the height of the large trees in Case 3 reached 2 m, which clearly indicated that the height of the vegetation could impact the overall wind environment of the courtyard. Besides,

the thermal environment of the whole courtyard was significantly improved by the vegetation. It could be found that the air temperature around the trees dropped significantly, the temperature at the bottom of the 1.5 m small trees in Case 2 reached approximately 27.5 °C, and the temperature at the bottom of the 2m large trees in Case 3 was only 26 °C. Moreover, the larger the vegetation, the more pronounced the effect of transpiration on the surrounding environment would be. Furthermore, the temperatures in the center of the courtyard were inconsistent with Case 2 and Case 3, at 34 °C and 33.5 °C, respectively, which also proved that different sizes of vegetation could exert different cooling effects on the interior of the courtyard.

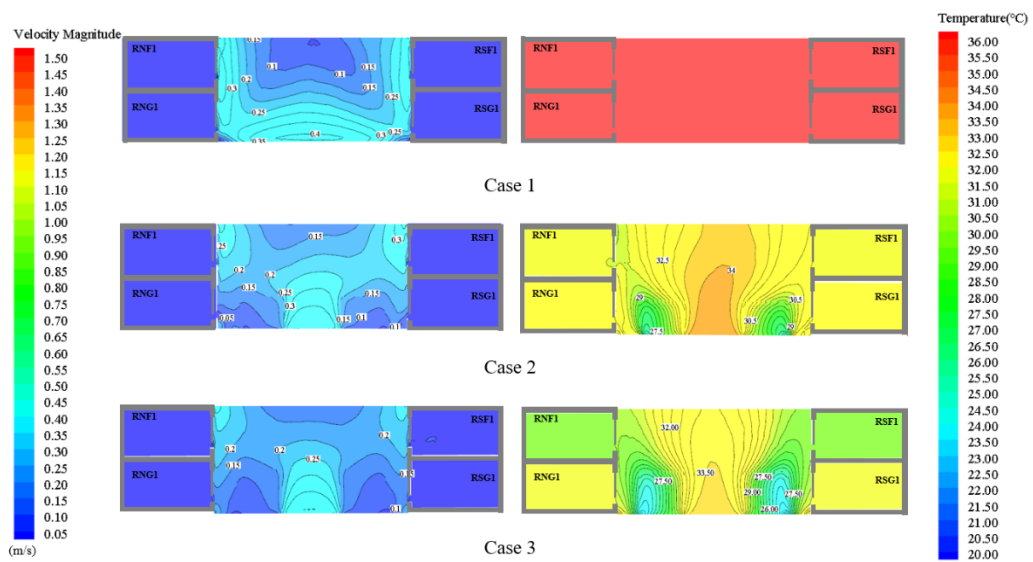


Figure 5.32 Contours for the wind speed magnitude and temperature within the courtyard with small trees and large trees (S1: X=7500mm).

## 5.4 Conclusion

In this study, an investigation was conducted on the effects of installing different heights of vegetation in a closed courtyard on the indoor wind and thermal environment of the surrounding buildings. In the present project, three different sets of cases were simulated in CFD Fluent 18.1. In Case 1, the wind and thermal conditions in the baseline courtyard model were simulated. Besides, in Case 2 and Case 3, four trees with heights of 1.5m and 2m were set up in the courtyard, respectively, as a major attempt to explore the effect of different sizes of vegetation on the courtyard and on the indoor wind and thermal environment. Throughout the study, the parameters selected for the thermal and wind environments consisted of wind speed magnitude (m/s) and temperature (°C). In addition, the effect of vegetation on indoor thermal comfort and natural ventilation was determined by comparing the changes in wind speed and temperature in the respective rooms of the different cases. The courtyard building was set up on two floors, each with eight rooms in different orientations, and the windows were set at 20% of the opening size. Furthermore, when different passive cooling techniques were set up in the courtyard, differences were identified in the variation of air velocity and temperature in the rooms at a range of locations.

For the indoor wind environment in the courtyard building, the comparison of the results of three different cases indicated that the wind speed inside each room was significantly small, which was essentially explained by the small window openings that affected the natural ventilation in the rooms. When different sizes of vegetation were installed in the courtyard, the wind speed in different rooms changed, with some rooms experiencing an increased wind speed. The main reason for this phenomenon was that the addition of vegetation could change the overall direction of airflow in the courtyard and, due to the transpiration effect of the vegetation, decrease the temperature in the courtyard, thereby impacting the wind speed in

the room. As revealed from the comparison of the wind speed in the eight rooms on the ground floor with different tree sizes in the courtyard, the wind speed increased in five rooms with both small 1.5 m and large 2 m trees in the courtyard, and the wind speed in the rooms on the north and west sides increased. However, specific to the eight rooms on the first floor, the indoor wind speed increased only in three rooms as impacted by the vegetation in the courtyard. Both in the baseline courtyard model and the courtyard model with small trees or large trees, the room with the highest indoor wind speed was found on the east side of the first floor. According to the comparison of the indoor wind speeds in the respective room, adding vegetation could decrease the maximum indoor wind speed and increase the minimum indoor wind speed. After simulating the wind speed magnitude in each room in different cases, the overall average indoor air speed magnitude was calculated for different cases. For Case1, which was the baseline courtyard model with no passive cooling strategy, the average indoor wind speed for the 16 rooms was 0.013 m/s; for Case 2 and Case 3, with four small and large trees within the courtyard, respectively, the average indoor wind speed reached 0.0112 m/s and 0.0117 m/s, Different sizes of the vegetation in the courtyard exerted different effects on the indoor wind performance. The larger the trees, the more pronounced the transpiration effect will be, and the more it will increase the wind speed in the room.

After the analysis of the indoor temperature of different rooms by installing a range of passive cooling strategies within the courtyard, the temperature of the baseline courtyard was kept constant (35.85 °C). With vegetation added into the courtyard, the temperature in each room dropped, but by different amounts. It could be suggested that when the vegetation was installed in the courtyard, a significant cooling effect was exerted on the surrounding area due to transpiration, which impacted the temperature of the rooms, especially on the first floor. However, it was noticed that the rooms in Case 2 and Case 3 with the highest temperatures

were located on the east side of the first floor, as impacted by the higher wind speed in these two rooms. The rooms with the most significant cooling effect were those located on the north and south sides close to the inlet. As revealed from the comparison of the temperatures of the different rooms in three cases, Case 3, where there were four large trees in the courtyard, had the lowest average indoor temperature, which demonstrated that planting large trees in the courtyard could exert a significant cooling effect on the indoor temperature. The most significant drop in temperature was 6.58 °C in the RSF1.

It is important to clarify that the vegetation and courtyard buildings in this chapter are based on a hypothetical model, which differs from real-world conditions. Regarding vegetation, this study does not fully simulate all properties of real vegetation. Instead, it simulates some characteristics of vegetation, such as the ability to absorb heat from the surrounding environment, acting as a heat sink. The model assumes the presence of real trees, but accurately simulating trees and vegetation in CFD poses challenges. Therefore, the trees and vegetation in this study are simplified assumptions and also, overly large vegetation that limits space for social activities. This limitation highlights a direction for future research, which will aim to simulate more specific vegetation characteristics within courtyard buildings to provide more accurate results.

Subsequent research should continuously find different passive cooling techniques to optimize the indoor wind and thermal environment of courtyard buildings. The optimal solution to enhance indoor thermal comfort will be determined by investigating the application of different passive cooling technologies in courtyard buildings. First, in this study, only 20% of the window openings were provided. To improve the natural ventilation within the room, different window opening sizes can be tested subsequently to determine the

most suitable window opening sizes. Second, in this study, different sizes of vegetation were set up in the courtyard, whereas the vegetation was set up on the four corners of the courtyard. Moreover, the vegetation can be further set up in different locations and be simulated. Lastly, a combination of several passive cooling techniques can be employed in the courtyard (e.g., by placing both vegetation and water jets in the courtyard) to explore the improvement in indoor thermal performance.

## Chapter 6 Pollutant Cross-transmission within Courtyards

### 6.1 Introduction

Courtyards are crucial for facilitating social interaction, contributing to community bonding, and improving the quality of urban life (Zheng, 2015; Gunasagaran et al., 2022). They offer environmental benefits by enhancing natural lighting, supporting ventilation, and aiding in passive cooling in residential areas (Aldawoud, 2008; Yang et al., 2014). However, the aspect of pollutant accumulation and dispersion within these spaces remains underexplored (Leng et al., 2020). Courtyard buildings, through their unique structural design, create distinct airflow patterns that can inadvertently transport indoor pollutants across rooms via the courtyard (Li et al., 2022; Rajapaksha et al., 2003; Sharples & Bensalem, 2001; Zamani et al., 2018).

In considering the dynamic relationship between architectural form and environmental flow in these semi-enclosed spaces, it becomes apparent that courtyards play a more active role than previously understood. Unlike isolated structures, the design of courtyards creates a unique microclimate. Here, air movement is primarily dictated by the courtyard's geometry, rather than merely reacting to external wind conditions (Jamei et al., 2016). This complex interaction between architecture and airflow is often underappreciated, yet crucial in understanding how it may amplify or mitigate pollutant levels in these types of environments.

To contextualize the discussion, consider a practical scenario: an individual cooking on the windward side of a courtyard. The process not only releases culinary aromas but also potentially hazardous cooking emissions. These are not confined to the immediate vicinity; rather, they are likely to be carried across the courtyard by prevailing winds, infiltrating

neighbouring living spaces (see Figure 6.1). This situation leads us to ask some important questions: When it comes to the design of courtyards, which side—the side sheltered from the wind (leeward), or the side exposed to it (windward)—is less likely to facilitate the transfer of pollutants from one unit to another through the courtyard? And conversely, which side is more prone to unintentional pollutant exchange? Additionally, how does the height of rooms within the courtyard affect the dispersion of pollutants? Which floors are most impacted by such pollutant transfer? Gaining insight into the answers to these questions is crucial for resolving the complexities of how pollutants disperse within architectural layouts like courtyards. Furthermore, this understanding can guide design strategies aimed at reducing the health risks that can inadvertently arise from an architectural style intended to improve urban living conditions.

This study employs an idealized model to simulate the courtyard geometry and environmental conditions. While the model provides a controlled framework to investigate pollutant dispersion, it does not encompass all real-world complexities, such as simultaneous pollutant-generating activities. Nevertheless, this analysis underscores the intricate dynamics of pollutant dispersion in courtyard buildings and highlights the necessity of such studies for practical applications.



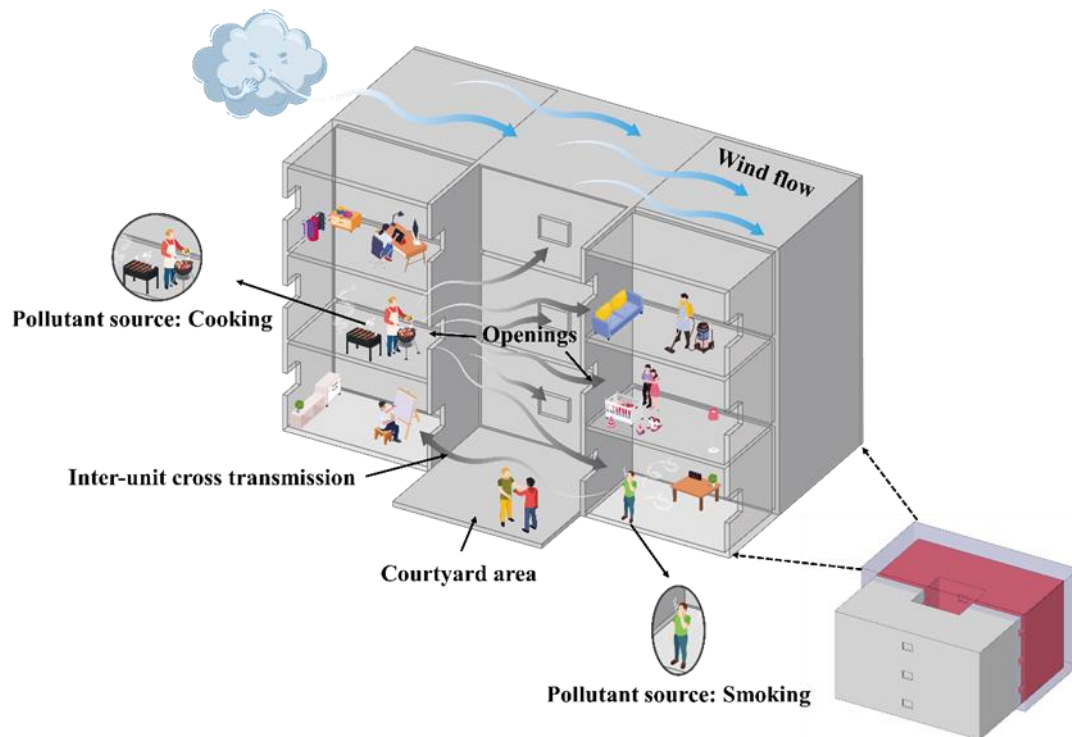


Figure 6.1 Cross-transmission of pollutants between naturally ventilated courtyard units.

The objective of this research is to evaluate the courtyard design, aiming to mitigate pollutant dissemination and enhance environmental health within urban habitats. This study seeks to fill gaps in existing research by exploring how wind influences pollutant movement in courtyard structures, utilizing a blend of wind tunnel testing and CFD simulations. Section 6.2 describes the wind tunnel experiment, while Section 6.3 presents the CFD approaches, including the evaluation of different turbulence models, mesh refinement study, and validation of the selected model. Section 6.4 presents the numerical simulation outcomes for diverse pollutant sources under varying wind speeds and directions. Finally, Sections 6.5 and 6.6 discuss the study's results and limitations, provide a conclusion, and outline potential future work.

## 6.2 Experimental method

### 6.2.1 Physical model and wind tunnel experimental setup

The experimental study employed a courtyard model at a 1:50 scale. This model was constructed from acrylic panels with a thickness of 3mm. As presented in Figure 6.2 (b), the dimensions were 300 mm x 300 mm x 180 mm (L x W x H). The model comprises 4 three-story buildings that face the courtyard, each measuring 100 mm x 100 mm x 60 mm. These buildings are interconnected by peripheral walls, creating a closed courtyard structure. Each room within these buildings features two windows measuring 20 mm x 15 mm to facilitate crossflow ventilation, shown in Figure 6.2 (c) and Figure 6.2 (d).

As depicted in Figure 6.2 (a), the experiments were conducted in the ABL wind tunnel laboratory within the Department of Civil Engineering at the University of Nottingham. The test section of this wind tunnel has dimensions of 3.1 m in length, 2.4 m in width, and 1.9 m in height. Preceding the 2 m diameter circular turntable is an 11.5 m long fetch. The wind direction can be modified by rotating this turntable. Given the dimensions of the 1:50 model and the wind tunnel section, the blockage ratio attributed to the scaled-down courtyard model in the wind tunnel is 1.18%. No adjustments were made to the measurements derived from these configurations as recommended by (Mercker, 1986).

In my wind tunnel experiments, similarity criteria are essential to ensure that our scaled model accurately represents full scale conditions, particularly fluid dynamics. A key aspect of these criteria is the establishment of dynamic similarity. In this study, we did not match the Reynolds number because of the wind tunnel speed limitations, although we did exceed the threshold highlighted by previous works. For our experiments, reference wind speeds were

measured at the height of the building. Two different values were used:  $U_{\text{ref}} = 5 \text{ m/s}$  and  $U_{\text{ref}} = 10 \text{ m/s}$ . At these speeds, the Reynolds numbers calculated using a characteristic length (the height of the courtyard model) of 180 mm were  $5.49 \times 10^4$  and  $1.08 \times 10^5$ , respectively. These values exceeded the threshold (Reynolds number =  $3.3 \times 10^4$ ) indicated by (Cui et al., 2014) for achieving Reynolds number independence in similar studies.

This independence from the Reynolds number suggests that the flow characteristics around the model are comparable to those in the actual environment, thus satisfying the criteria for dynamic similarity. Cui et al. (2022) highlight the importance of Reynolds number independence in indoor flow and pollutant dispersion studies. This research supports our approach by showing that flow characteristics remain consistent within a specific Reynolds number range, confirming our model's reliability. By achieving and verifying these Reynolds numbers, our model under both wind conditions accurately represents full-scale scenarios, adhering to the essential similarity criteria for modeling and analysis.

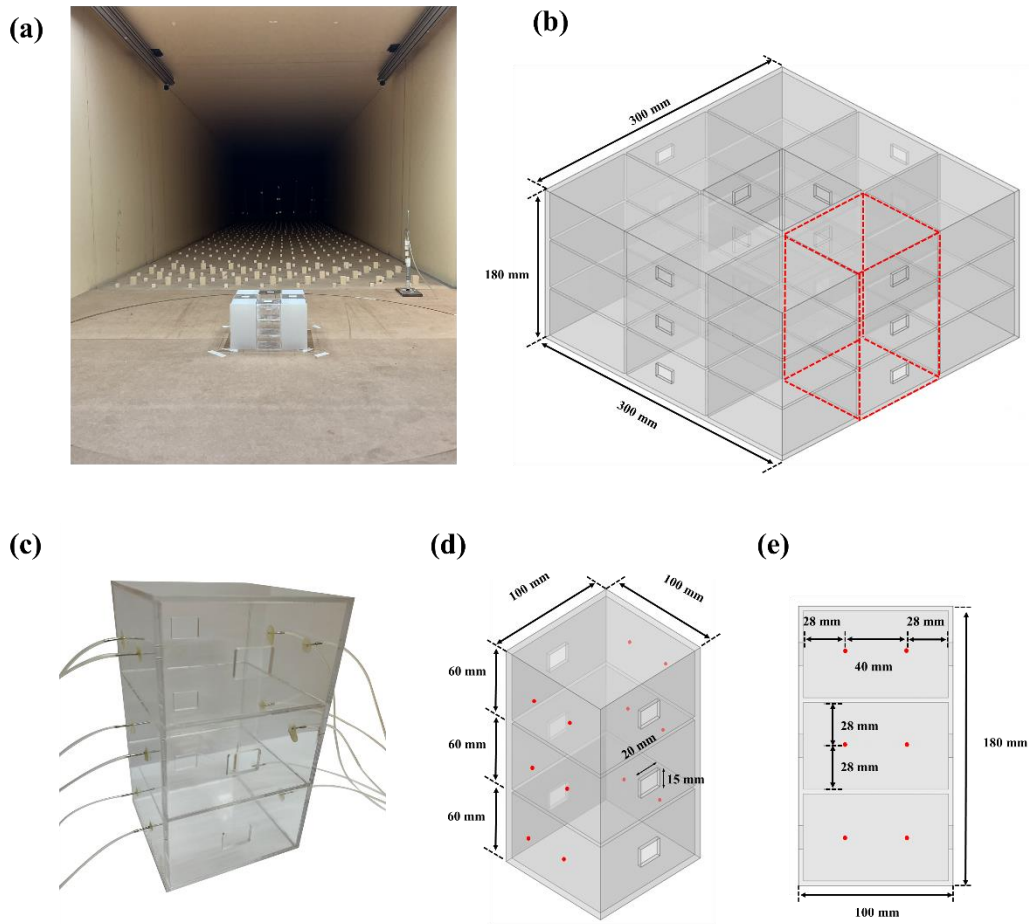


Figure 6.2 Courtyard model in wind tunnel, overall dimensions, pressure tube connections, window dimensions, and pressure measurement points. (a) The courtyard model positioned on the turntable within the ABL wind tunnel. (b) Overall dimensions of the courtyard building model. (c) Single building model and connection of pressure tubes. (d) Dimensions of a single building and windows. (e) Arrangement of pressure measurement points on the side wall within the indoor domain.

An ABL velocity profile was established utilizing a combination of spires and surface roughness elements. Average velocity and turbulence intensity were precisely measured using the Testo 450i thermal anemometer. The instrument has a measuring range from 0 to 30 m/s, coupled with a high-resolution capability of 0.01 m/s; It ensures accuracy of  $\pm (0.1 \text{ m/s} + 5\% \text{ of mv})$  for speeds up to 2 m/s and  $\pm (0.3 \text{ m/s} + 5\% \text{ of mv})$  for speeds up to 15 m/s. The

profiles of inlet velocity and turbulence intensity at the centre of the turntable in the absence of the building models are shown in Figure 6.3 and Table 6.1 respectively. For the measurement, the reference height is  $Z = 0.18\text{m}$ .

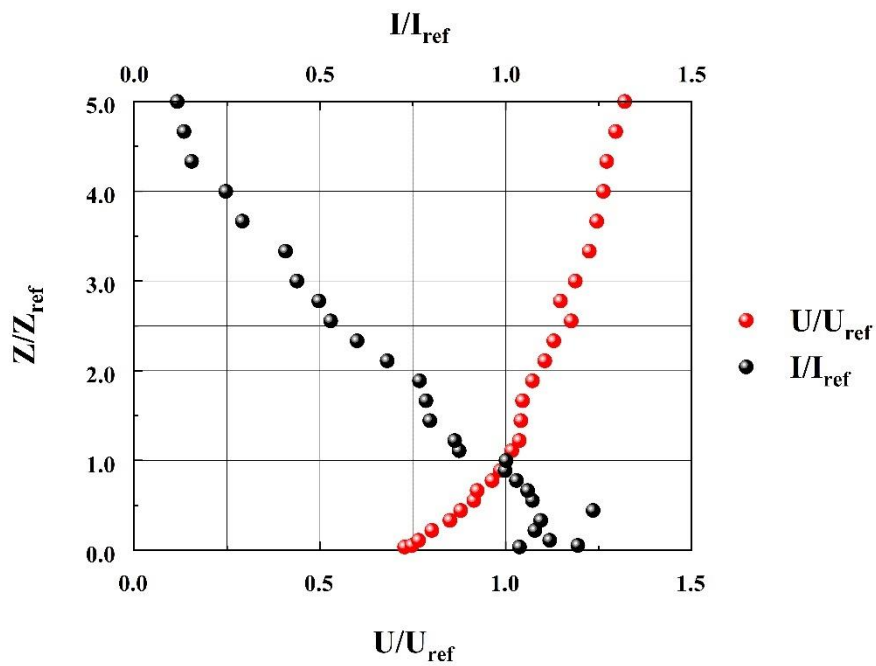


Figure 6.3 Relationship between  $Z/Z_{ref}$  ,  $U/U_{ref}$  and  $I/I_{ref}$ .

<b>Z (m)</b>	<b>Z/Zref</b>	<b>U (m/s)</b>	<b>U/Uref</b>	<b>I</b>	<b>I/Iref</b>
0.007	0.039	3.28	0.877	6.20%	1.036
0.01	0.056	3.37	0.901	7.13%	1.193
0.02	0.111	3.45	0.922	6.68%	1.118
0.04	0.222	3.61	0.965	6.44%	1.078
0.06	0.333	3.83	1.024	6.54%	1.093
0.08	0.444	3.96	1.059	7.38%	1.234
0.1	0.556	4.12	1.102	6.40%	1.071

0.12	0.667	4.16	1.112	6.33%	1.058
0.14	0.778	4.34	1.160	6.15%	1.028
0.16	0.889	4.44	1.187	5.96%	0.998
0.18	1.000	4.51	1.206	5.98%	1.000
0.2	1.111	4.58	1.225	5.22%	0.874
0.22	1.222	4.67	1.249	5.15%	0.862
0.26	1.444	4.69	1.254	4.76%	0.795
0.3	1.667	4.71	1.259	4.69%	0.785
0.34	1.889	4.83	1.291	4.59%	0.767
0.38	2.111	4.98	1.332	4.07%	0.680
0.42	2.333	5.09	1.361	3.58%	0.599
0.46	2.556	5.3	1.417	3.16%	0.528
0.5	2.778	5.17	1.382	2.97%	0.497
0.54	3.000	5.35	1.430	2.62%	0.438
0.6	3.333	5.52	1.476	2.43%	0.407
0.66	3.667	5.61	1.500	1.74%	0.291
0.72	4.000	5.69	1.521	1.47%	0.247
0.78	4.333	5.73	1.532	0.92%	0.155
0.84	4.667	5.84	1.561	0.80%	0.134
0.9	5.000	5.95	1.591	0.69%	0.116

Table 6. 1 Measured average velocity and turbulence intensity of the wind profile for different heights.

### 6.2.2 Wind tunnel experimental setup for the pressure measurement

To assess the pressure distribution within the courtyard building, 2 pressure taps were located inside each of the rooms, as illustrated in Figure 6.2 (e). In total 48 pressure taps were employed, which were designed to measure the indoor pressure coefficients. Pressure taps were connected to a 64-channel Scanivalve MPS4264 digital pressure transducer using vinyl tubing with an external diameter of 0.001 m and a length of 1.2 m. The digital sensor array has a full-scale measurement range of 995.4 Pa with an accuracy of  $\pm 0.06\%$ FS. The backing pressure was taken from the static port of a Pitot-static tube positioned at the reference height of 180mm in line with the front of the model. The Pitot-static tube was also used to measure the mean wind speed. Pressure data were collected for a duration of 200 seconds at a sampling rate of 50 Hz.

### 6.2.3 Wind tunnel experimental setup for the CO<sub>2</sub> measurement

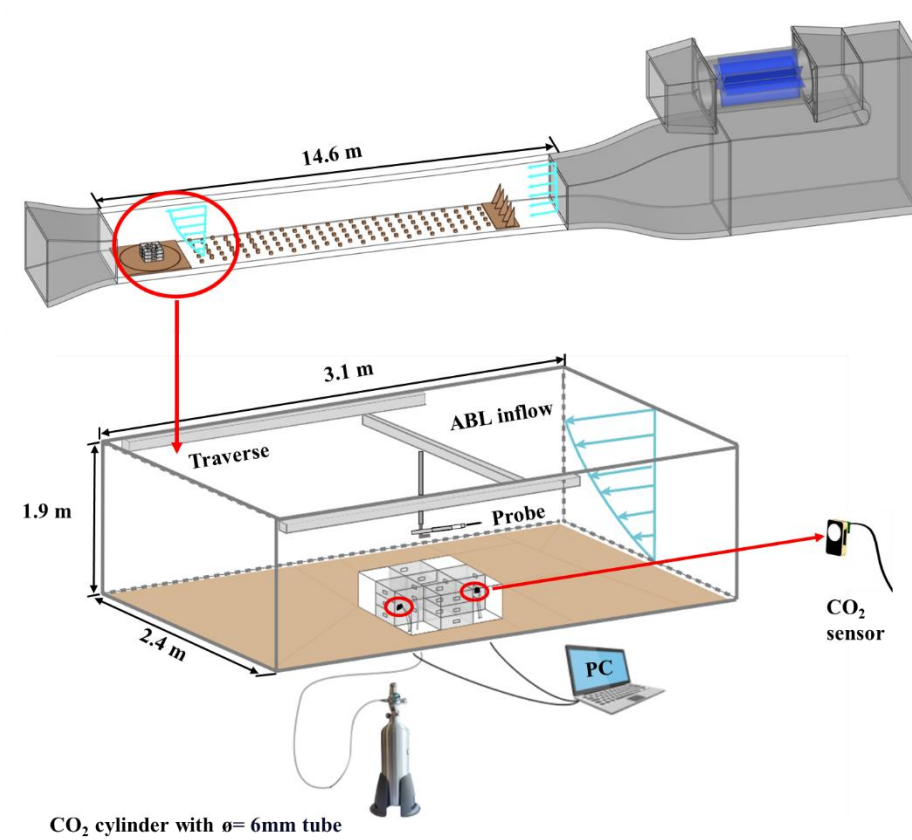
The study was not limited to the pressure measurements but also included CO<sub>2</sub> measurements at the specified four test scenarios: the model was oriented at 0° with a wind speed of 5 m/s; with the same orientation, the wind speed was increased to 10 m/s; when the model was positioned at 45°, the wind speed was set at 5 m/s; and finally, with the model still at 45°, the wind speed was adjusted to 10 m/s.

To simulate the dispersion of an indoor source of gaseous pollutants, the tracer gas CO<sub>2</sub> was released from the CO<sub>2</sub> cylinder. As shown in Figure 6.4 (a) and Figure 6.4 (b), CO<sub>2</sub> concentration sensors were placed on the second floor of both the windward and leeward sides of the model building. The CozIR®-LP CO<sub>2</sub> sensor, which employs NDIR solid-state LED optics and has a measurement precision of 30 ppm, was employed to measure the CO<sub>2</sub>

concentration. These sensors can monitor CO<sub>2</sub> concentrations up to 5000 ppm and feature an automatic calibration mechanism. A polyurethane tube, 6mm in outer diameter, was positioned on the same floor of the windward building, and it was connected to a 1 L aluminum CO<sub>2</sub> cylinder under the wind tunnel. This cylinder was equipped with a control valve to ensure a consistent release of CO<sub>2</sub>. Throughout the experiment, varying CO<sub>2</sub> emission rates were established based on wind speeds and model orientations to guarantee accurate readings by both sensors. Specifically, with the model at 0°, a steady release rate of 2.8 ml/s was maintained for both 5 m/s and 10 m/s wind speeds. Conversely, when the model was at 45°, the release rates were set at 0.45 ml/s and 0.8 ml/s for wind speeds of 5 m/s and 10 m/s, respectively. Given that one of the CO<sub>2</sub> sensors and the emission source were situated in the same room, it was imperative to ensure that the emission rate was not excessively high. The monitored concentration within the room should not exceed 5,000 ppm. Following the sensors' calibration, a consistent CO<sub>2</sub> release was initiated, and data recording ceased once readings from both sensors stabilized.



(a)



(b)

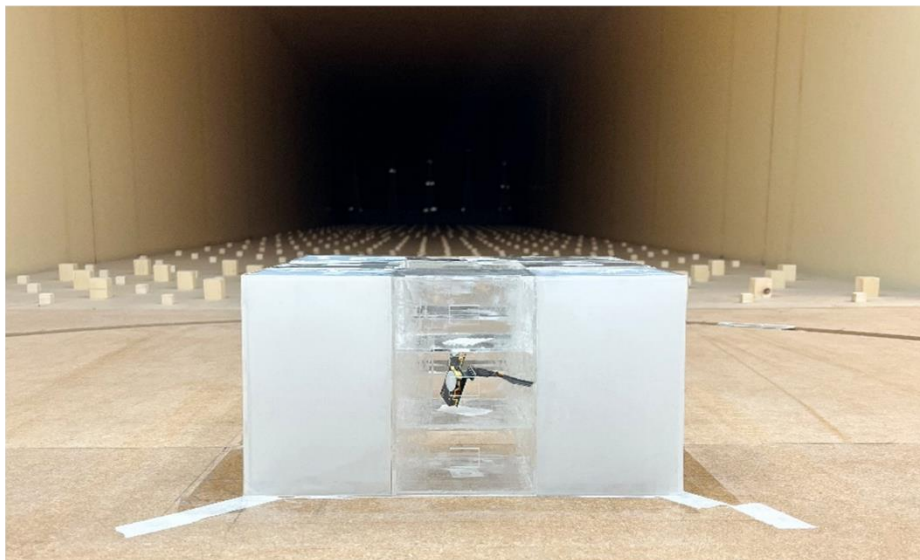


Figure 6.4 Wind tunnel CO<sub>2</sub> dispersion measurement setup and courtyard model with CO<sub>2</sub> sensors. (a) Wind tunnel CO<sub>2</sub> dispersion measurement setup. (b) The courtyard model with CO<sub>2</sub> sensors in the wind tunnel.

## 6.3 CFD Method

### 6.3.1 Numerical methods and solver settings

This research employs the control volume method, using the software ANSYS FLUENT 18.1, to conduct steady-state RANS calculations for flow and mass fraction equations. 3D CFD simulations were run, assuming a fully turbulent and incompressible flow. The RANS equations are closed using the *k*-epsilon Realizable model. The employed CFD program adopts the Finite Volume Method (FVM) with a semi-implicit velocity-pressure coupling algorithm (SIMPLE) for the second order windward discrete pressure correlation equations. Solution convergence is established when the residuals for the mass, momentum, and species transport equations are reduced to a threshold below  $10^{-6}$ .

This study evaluates the predictive capabilities of three turbulence models: the *k*-epsilon standard model (Launder & Spalding, 1974), the *k*-epsilon RNG model (Yakhot et al., 1992), and the *k*-epsilon Realizable model (Shih et al., 1995) for pressure distribution and CO<sub>2</sub> dispersion in wind tunnels. Based on the results (refer to Figure 6.9), the *k*-epsilon Realizable model was chosen for further in-depth analysis. The turbulent Schmidt number ( $S_{ct}$ ) is pivotal in dispersion simulation. For all cases, an  $S_{ct}$  value of 0.7 was adopted. Tominaga & Stathopoulos (2007) found this value to align well with experimental results when comparing experiments and simulations for air pollution dispersion around a building. This selection is further supported by Spalding (1971), based on the comparison between wind tunnel and CFD results. The governing equations, as defined by the (Ansys Fluent Theory Guide 2021R2 [Online], 2021), are as follows:

Equation of continuity:

$$\frac{\partial U_i}{\partial x_i} = 0 \quad (6.1)$$

Equation of momentum:

$$\frac{\partial(\rho \bar{u}_i \bar{u}_j)}{\partial x_j} = -\frac{\partial \bar{p}}{\partial x_i} + \frac{\partial}{\partial x_j} \left( \mu \frac{\partial \bar{u}_i}{\partial x_j} \right) + \frac{\partial}{\partial x_j} \left( \mu_t \frac{\partial \bar{u}_i}{\partial x_j} \right) - \frac{2}{3} \frac{\partial(\rho k)}{\partial x_i} \quad (6.2)$$

In the equations provided, the variables  $U_i$  represent the velocity components in the Cartesian directions and represent the mean speed of the fluid flow. The continuity equation establishes that the velocity field is divergence-free, indicating incompressibility. The momentum equation takes into account changes in momentum over time and space, encompassing both mean flow and turbulence effects. Where  $\rho$  denotes the fluid density,  $\bar{u}_i, \bar{u}_j$  are mean velocities, and  $\bar{p}$  is the mean pressure.  $\mu$  is the molecular viscosity, and the  $\mu_t$  represents the turbulent viscosity,  $k$ , is turbulent kinetic energy. Kronecker delta is  $\delta_{ij}$ .

Energy Equation:

$$\frac{\partial}{\partial u_i} \cdot (\bar{u}_i (\rho E + p)) = \frac{\partial}{\partial u_i} \cdot \left( \kappa_{\text{eff}} \cdot \frac{\partial T}{\partial u_i} \right) + S_h \quad (6.3)$$

Where  $E$  is the total energy,  $\kappa_{\text{eff}}$  is the effective thermal conductivity,  $T$  is temperature, and  $S_h$  is the heat source term.

Transport equation for the turbulent kinetic energy  $k$ :

$$\frac{\partial}{\partial x_j} (\rho k u_j) = \frac{\partial}{\partial x_j} \left[ \left( \mu + \frac{\mu_t}{\sigma_k} \right) \frac{\partial k}{\partial x_j} \right] + G_k + G_b - \rho \varepsilon - Y_M + S_k \quad (6.4)$$

$$\frac{\partial}{\partial x_j}(\rho \varepsilon u_j) = \frac{\partial}{\partial x_j} \left[ \left( \mu + \frac{\mu_t}{\sigma_\varepsilon} \right) \frac{\partial \varepsilon}{\partial x_j} \right] + \rho C_1 S \varepsilon - \rho C_2 \frac{\varepsilon^2}{k + \sqrt{v \varepsilon}} + C_{1\varepsilon} \frac{\varepsilon}{k} C_{3\varepsilon} G_b + S_\varepsilon \quad (6.5)$$

$$\mu_t = \rho C_\mu \frac{k^2}{\varepsilon} \quad (6.6)$$

$$C_1 = \max \left[ 0.43, \frac{\eta}{\eta + 5} \right], \eta = S \frac{k}{\varepsilon}, S = \sqrt{2 S_{ij} S_{ij}} \quad (6.7)$$

$$C_{1\varepsilon} = 1.44, C_2 = 1.9, \sigma_k = 1.0, \sigma_\varepsilon = 1.2$$

The turbulent kinetic energy equation parameters define the dynamics of turbulence in a fluid flow:  $\varepsilon$  its isotropic dissipation, and  $G_k$  and  $G_b$  represent turbulence production from mean velocity gradients and buoyancy, respectively, and the contribution of the fluctuating dilatation in compressible turbulence to the overall dissipation rate is  $Y_M$ . The turbulent Prandtl numbers  $\sigma_k$  and  $\sigma_\varepsilon$  adjust the dispersion of  $k$  and  $\varepsilon$ . Model constants  $C_{1\varepsilon} = 1.44, C_2 = 1.9, \sigma_k = 1.0$ , along with  $\mu_t$ , the turbulence viscosity, close the system, reflecting the balance between turbulence generation, transport, and dissipation.

Species transport equation:

$$\left[ \frac{\partial}{\partial t} (\rho u_x Y_i) + \frac{\partial}{\partial t} (\rho v_y Y_i) + \frac{\partial}{\partial t} (\rho w_z Y_i) \right] = - \left( \frac{\partial j_{ix}}{\partial x} + \frac{\partial j_{iy}}{\partial y} + \frac{\partial j_{iz}}{\partial z} \right) + R_i + S_i \quad (6.8)$$

In the species transport equation,  $Y_i$  is the mass fraction of species  $i$ , The velocity components  $u, v, w$  represent the flow in the  $x, y, z$  directions.  $j_{ix}, j_{iy}$  and  $j_{iz}$  are the

respective dispersion flux components for species  $i$ .  $R_i$  quantifies the net production rate of species  $i$  from reactions, and  $S_i$  includes additional source terms.

### 6.3.2 Courtyard geometry, computational domain, and boundary conditions

As demonstrated in Figure 6.5 (a), for both modelling and wind tunnel experiments, the dimensions of the courtyard building model and the computational fluid domain were replicated at a 1:1 scale. In the CFD context, the model's dimensions are 300 mm x 300 mm x 180 mm. Each floor comprises four test rooms, located in the east, west, north, and south corners. Rooms adjacent to the courtyard were distinctly labelled based on floor and orientation to facilitate the analysis across different rooms, as presented in Figure 6.5 (c). Figure 6.5 (b) illustrates that nine sampling points were strategically positioned at the mid-height of each test room, ensuring uniform distribution for the collection of CO<sub>2</sub> concentration data. Fig. 6. Shows the fluid domain's dimensions, which mirror those of the test section, measuring 2.4 m x 1.9 m x 3.1 m. In the computational domain, both side and top walls were designated as symmetry walls. The spacing between the courtyard and the two side symmetry walls was set at 1050 mm, while the distances from the courtyard to the velocity inlet and pressure outlet were 950 mm and 1850 mm, respectively. The gap between the courtyard and the domain's top wall was established at 1882 mm. In all CFD simulation scenarios, the release rate of CO<sub>2</sub> is consistently set at 2.8 ml/s. For both the inlet and outlet, the initial configurations are maintained with a CO<sub>2</sub> concentration of 400 ppm and a temperature of 300K.

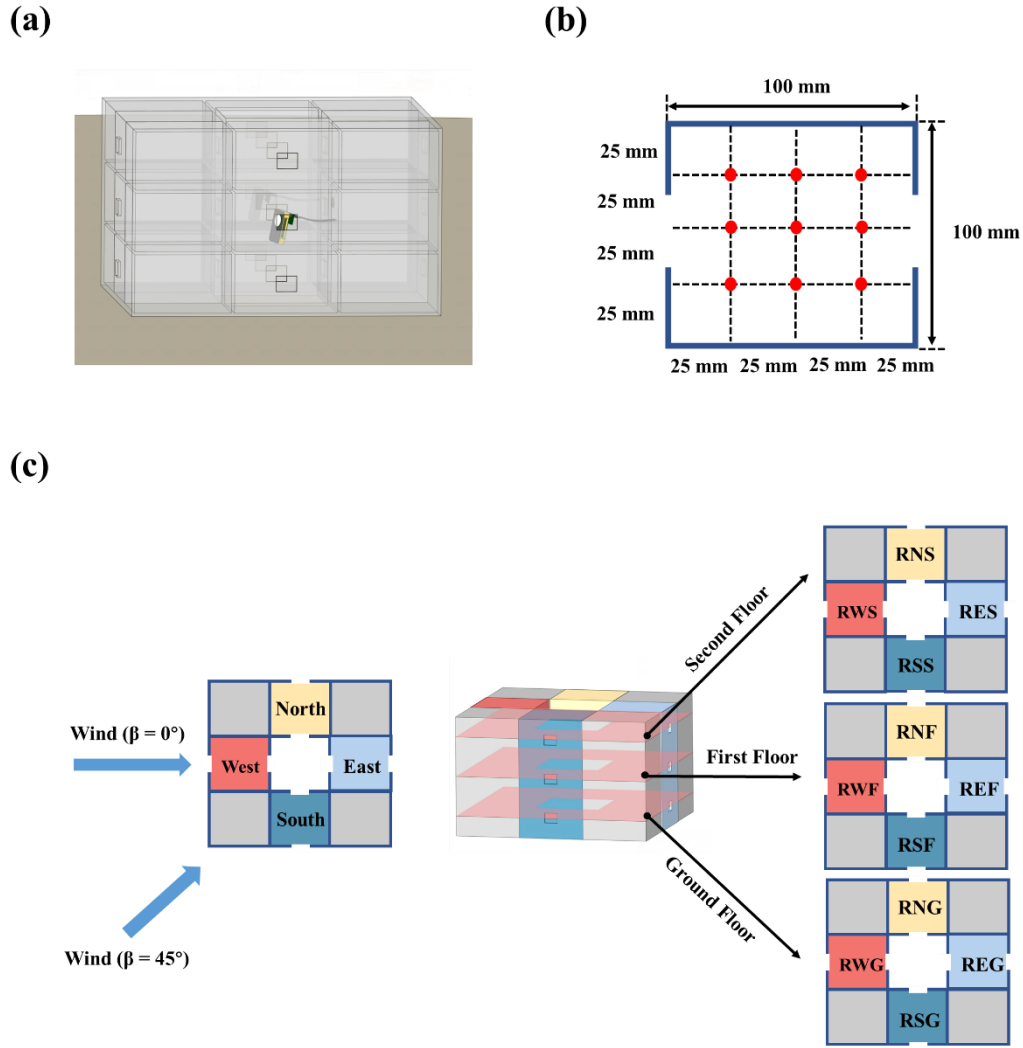


Figure 6.5 Courtyard building model for CFD modelling, distribution of monitoring points, and orientation and naming of test rooms. (a) The courtyard building model for the CFD modelling. (b) Distribution of nine monitoring points inside the test room. (c) Orientation and naming of each test room for analysis.

The inlet wind profile was consistent for all simulation scenarios. The average wind speed was derived using the power law formula, the formula is given by:

$$u(z) = u_{\text{ref}} \left( \frac{z}{z_{\text{ref}}} \right)^\alpha \quad (6.9)$$

where  $u(z)$  is the mean velocity at height  $z$  (m/s),  $\alpha$  is the power law exponent found by curve fitting the wind tunnel data,  $z_{\text{ref}} = 180$  mm is the reference height corresponding to the height of the courtyard model, the  $u_{\text{ref}}$  is the reference velocity at height  $H$  are 4.51 m/s (corresponding to the 5m/s scenario) and 8.86 m/s (for the 10 m/s scenario). Given these velocities, the Reynolds numbers were calculated to be approximately  $5.49 \times 10^4$  and  $1.08 \times 10^5$ , respectively.

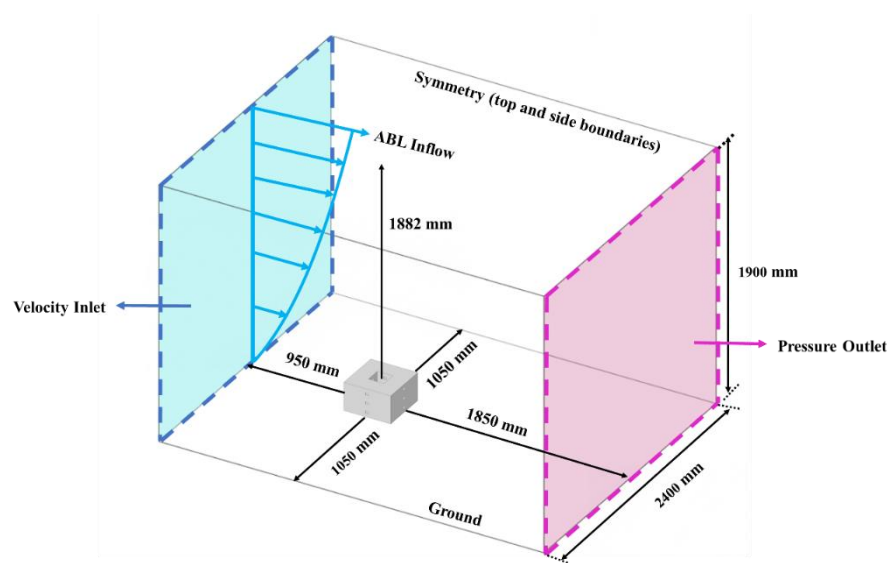


Figure 6.6 The dimensions and boundary conditions of the computational domain.

### 6.3.3 Grid and sensitivity analysis

The accuracy of the numerical simulation and computation time is significantly influenced by the quality of the mesh used in modelling. The mesh for the fluid domain was generated as a tetrahedral mesh in ANSYS Meshing. Near the courtyard building's walls, windows, and floors, a finer grid was employed, the mesh resolution for both window areas and the CO<sub>2</sub> source area were set to 1mm, and for building areas, it was set to 5mm. While a coarser grid (50 mm) was chosen further from these areas. The expansion ratio between two adjacent cells was kept below 1.2. To optimize computational efficiency and reduce

processing time, the tetrahedral mesh in the fluid domain was transformed into a more efficient polyhedral mesh within ANSYS Fluent. To ensure the accuracy of the numerical model, a mesh sensitivity analysis was conducted to assess the results' variation across different mesh sizes. The uncertainty arising from discretization was evaluated using the GCI method, which was introduced by Roache (1994). The specifics and parameters of the analysis are provided below:

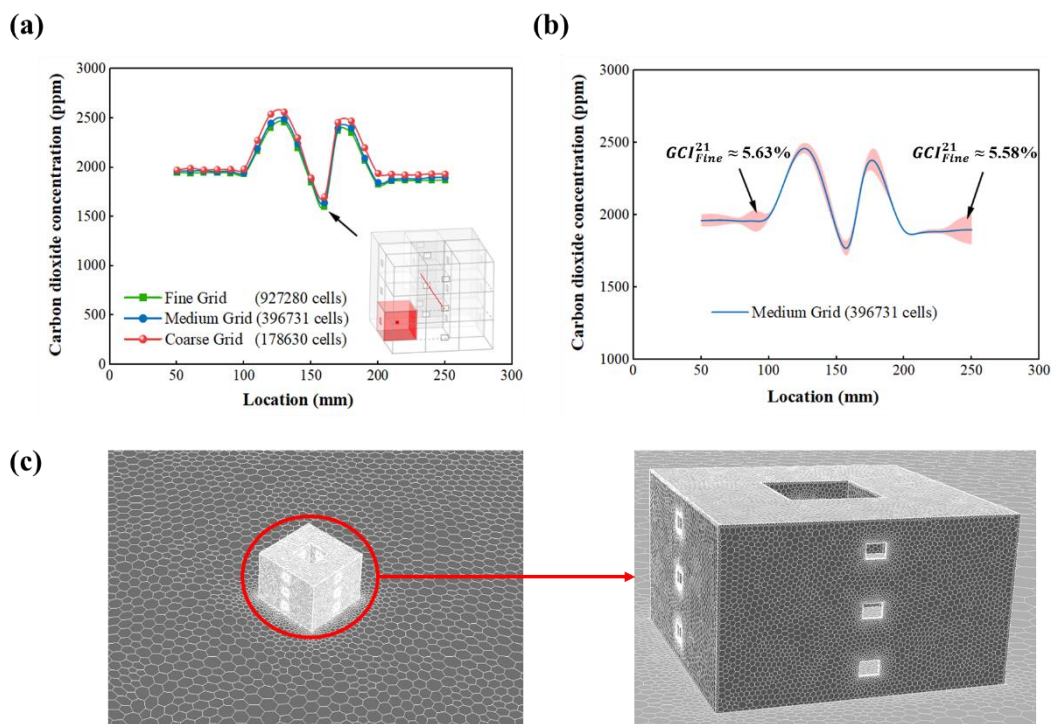


Figure 6.7 Simulated CO<sub>2</sub> concentration and grid sensitivity analysis with polyhedral mesh around courtyard surfaces. (a) Simulated CO<sub>2</sub> concentration results along a horizontal centre line of the courtyard model at the height of 90 mm for the grid sensitivity analysis. (b) The grid sensitivity analysis by using the GCI method. (c) The polyhedral mesh around the courtyard surfaces.

The calculation first needs to define the grid size  $h$ ,  $\Delta V_i$  is the volume,  $N$  is the total number of cells used for the computations.



$$h = \left[ \frac{1}{N} \sum_{i=1}^N (\Delta V_i) \right]^{1/3} \quad (6.10)$$

As shown in Figure 6.7 and Table 6.1, three distinct grid sizes—fine, medium, and coarse—were selected. Simulations were conducted to ascertain the values of pivotal variables  $(\phi_1, \phi_2, \phi_3)$  pertinent to the study's objective. It is recommended that the grid refinement factor, denoted as  $r = h_{\text{coarse}}/h_{\text{fine}}$  exceeds 1.3 (Roache, 1994). Given the conditions  $h_1 < h_2 < h_3$ , the ratios are defined as  $r_{21} = h_2/h_1$ ,  $r_{32} = h_3/h_2$ . Consequently, the grid sizes were N1 (927,280), N2 (396,713), and N3 (178,630), resulting in  $r$  values of 1.327 and 1.305. The method's apparent order,  $p$ , can be derived using expressions from Eq. (6.11) to Eq. (6.17), where  $\varepsilon_{32} = \phi_3 - \phi_2$ ,  $\varepsilon_{21} = \phi_2 - \phi_1$ .

$$p = \frac{1}{\ln(r_{21})} |\ln |\varepsilon_{32}/\varepsilon_{21}| + q(p)| \quad (6.11)$$

$$q(p) = \ln \left( \frac{r_{21}^p - s}{r_{32}^p - s} \right) \quad (6.12)$$

$$s = 1 \cdot \text{sgn} (\varepsilon_{32}/\varepsilon_{21}) \quad (6.13)$$

The extrapolated values based on Eq. (6.13):

$$\phi_{\text{ext}}^{21} = (r_{21}^p \phi_1 - \phi_2) / (r_{21}^p - 1) \quad (6.14)$$

The approximate relative error, denoted as  $e_a^{21}$ , the extrapolated relative error,  $e_{\text{ext}}^{21}$ , the extrapolated relative error,  $\text{GCI}_{\text{fine}}^{21}$ , can be determined using Eq. (6.15) to Eq. (6.17).

$$e_a^{21} = \left| \frac{\phi_1 - \phi_2}{\phi_1} \right| \quad (6.15)$$

$$e_{\text{ext}}^{21} = \left| \frac{\phi_{\text{ext}}^{12} - \phi_1}{\phi_{\text{ext}}^{12}} \right| \quad (6.16)$$

$$\text{GCI}_{\text{fine}}^{21} = \frac{1.25e_a^{21}}{r_{21}^p - 1} \quad (6.17)$$

	CO <sub>2</sub> Concentration (ppm) at Y = 60 mm	CO <sub>2</sub> Concentration (ppm) at Y = 120 mm	CO <sub>2</sub> Concentration (ppm) at Y = 180 mm
N1	927,280	927,280	927,280
N2	396,713	396,713	396,713
N3	178,630	178,630	178,630
$r_{21}$	1.327	1.327	1.327
$r_{32}$	1.305	1.305	1.305
$\phi_1$	1945.207	2405.236	2348.362
$\phi_2$	1964.026	2448.301	2399.195
$\phi_3$	1990.212	2540.542	2469.876
$p$	1.433	3.014	1.430
$\phi_{\text{ext}}^{21}$	1907.567	2737.260	2246.481
$e_a^{21}$	0.967%	1.790%	2.165%
$e_{\text{ext}}^{21}$	1.973%	1.347%	4.535%
$\text{GCI}_{\text{fine}}^{21}$	2.419%	1.662%	5.423%

Table 6.2 Sample discretization error calculation using GCI method.

In this study, grid sensitivity was examined by selecting the first floor with coordinates X=150 mm, Z=90 mm, and Y ranging from 50 mm to 250 mm. A total of 21 points were chosen to observe the CO<sub>2</sub> concentration (ppm) under three different grid sizes, as depicted in Figure 6.7 (a). Data presented in Table 6.2 specifically highlights Y = 60 mm, Y = 120 mm, and Y = 180 mm. The grid convergence index for these points is 2.419%, 1.662%, and 5.423%, respectively. The medium mesh size was ultimately selected for this study, as its results exhibited minimal error compared to the fine mesh size, and significant computational cost savings were observed. Figure 6.7 (b) illustrates the medium grid convergence index and discretization error bars for all 21 points, with the maximum  $\text{GCI}_{\text{fine}}^{21}$  being 5.63% and the

average  $GCI_{\text{fine}}^{21}$  across the 21 points, being 2.210%. Hence, the medium mesh size is well-suited for subsequent simulations.

### 6.3.4 Validation of the numerical model

This section compares wind tunnel experimental data with CFD simulations, focusing on two key areas: the internal air pressure distribution and CO<sub>2</sub> dispersion in courtyard buildings. This comparison is crucial for verifying the precision and reliability of the computational models used.

#### 6.3.4.1 Validation of internal room pressure distribution

The outcomes of the wind tunnel test and CFD simulations have been evaluated with a focus on the pressure coefficient ( $C_p$ ), as defined by Eq. (6.18). In this context, ' $P$ ' denotes the observed pressure, while ' $P_{\text{ref}}$ ' and ' $U_{\text{ref}}$ ' represent the reference pressure and velocity, respectively. Additionally, ' $\rho$ ' signifies the air density.

$$C_p = \frac{P - P_{\text{ref}}}{0.5\rho U_{\text{ref}}^2} \quad (6.18)$$

In the wind tunnel experiments, the MPS4264 Scanivalve digital pressure transducer was employed to gather data on the pressure coefficient ( $C_p$ ) at 48 monitoring points located inside courtyard buildings. This data was then compared and validated against the results from CFD simulations. As indicated in Table 6.2, the study utilized two different wind speeds (5 m/s and 10 m/s) and two wind directions ( $\beta = 0$  and  $\beta = 45$ ). Five commonly used RANS models were selected for this research:  $k$ -epsilon standard,  $k$ -epsilon RNG,  $k$ -epsilon

Realizable,  $k$ -Omega standard, and  $k$ -Omega SST. Three validation metrics were applied: the normalized mean squared error (NMSE), the fractional bias (FB), and the fraction of predictions within a factor of two of the observations (FAC2). These metrics were employed to conduct a comprehensive and quantitative evaluation of the performance of all five RANS turbulence models, using Eq. (6.19) to Eq. (6.21).

$$FB = \frac{[O]-[P]}{0.5([O]+[P])} \quad (6.19)$$

$$NMSE = \frac{[(O_i - P_i)^2]}{[O_i][P_i]} \quad (6.20)$$

$$FAC2 = \frac{1}{N} \sum_{i=1}^N n_i \text{ with } n_i = \begin{cases} 1 & \text{for } 0.5 \leq \frac{P_i}{O_i} \leq 2 \\ 0 & \text{else} \end{cases} \quad (6.21)$$

<b>Model</b>		<b>NMSE</b>	<b>FB</b>	<b>FAC2</b>
Wind direction $\beta$ = 0, Wind velocity = 5 m/s	$k$ -epsilon standard	1.543	0.305	0.75
	$k$ -epsilon RNG	1.529	0.099	0.750
	$k$ -epsilon Realizable	1.031	0.130	0.750
	$k$ -omega standard	1.573	0.073	0.750
	$k$ -omega SST	1.946	0.135	0.750
Wind direction $\beta$ = 0, Wind velocity = 10 m/s	$k$ -epsilon standard	1.008	0.111	0.750
	$k$ -epsilon RNG	1.766	-0.009	0.750
	$k$ -epsilon Realizable	1.255	-0.063	0.750
	$k$ -omega standard	2.074	-0.138	0.750
	$k$ -omega SST	1.774	-0.035	0.750
Wind direction $\beta$ = 45, Wind velocity = 5 m/s	$k$ -epsilon standard	0.280	0.002	0.854
	$k$ -epsilon RNG	0.358	0.260	0.521
	$k$ -epsilon Realizable	0.292	0.068	0.813
	$k$ -omega standard	0.643	0.242	0.542
	$k$ -omega SST	0.351	0.153	0.542
Wind direction $\beta$ = 45, Wind velocity = 10 m/s	$k$ -epsilon standard	0.256	0.049	0.875
	$k$ -epsilon RNG	0.413	0.274	0.500
	$k$ -epsilon Realizable	0.218	0.177	0.625
	$k$ -omega standard	0.796	0.414	0.500
	$k$ -omega SST	0.519	0.321	0.500
Target, Acceptance criteria		0, <1.5	0, [-0.3, 0.3]	1, >0.3

Table 6.3 Validation metrics for the internal pressure coefficient.

According to the results presented in Table 6.3, the RANS models demonstrate effective predictive capabilities for the flow characteristics around buildings, particularly in accounting for the influence of wind direction and speed on wind pressure distribution. The performance of various turbulence models varies with wind directions at 0 and 45 degrees. Under 0-degree wind direction, the *k*-epsilon Realizable model exhibits lower NMSE values (1.031 and 1.255 for wind speeds of 5 m/s and 10 m/s, respectively), acceptable FB values (0.13 and -0.063 respectively), and satisfactory FAC2 values (both 0.75). This indicates its accuracy in capturing pressure variations on the windward (west) and leeward (east) sides. In the case of a 45-degree wind direction, the *k*-epsilon Realizable model particularly stands out. At a wind speed of 5 m/s, it achieves an NMSE value of 0.292, an FB value of 0.068, and a FAC2 value of 0.813; at 10 m/s, these values are 0.218, 0.177, and 0.625, respectively, significantly outperforming other models like *k*-epsilon standard and *k*-Omega SST. These findings suggest that the RANS models, especially the *k*-epsilon Realizable variant, are highly effective in predicting wind pressure distribution around courtyard buildings. They provide accurate predictions under various wind directions and speeds. Therefore, due to its superiority across all key evaluation metrics, the *k*-epsilon Realizable model has been chosen for subsequent CFD simulations.

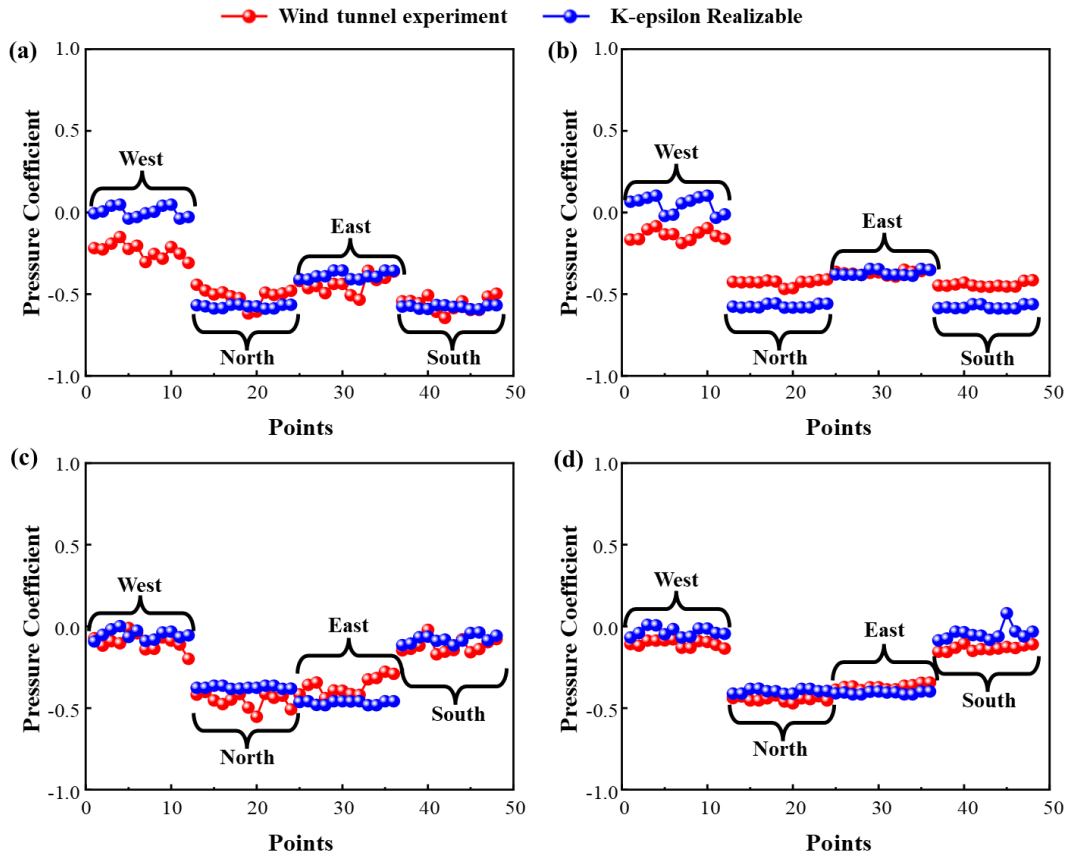


Figure 6.8 Comparison of pressure coefficient values between the experiment and CFD simulations. (a) Wind direction at 0 degrees and wind speed at 5 m/s. (b) Wind direction at 0 degrees and wind speed at 10m/s. (c) Wind direction at 45 degrees and wind speed at 5 m/s. (d) Wind direction at 45 degrees and wind speed at 10 m/s.

Figure 6.8 shows the distribution of pressure coefficients at various measurement points within a courtyard building, with experimental data (red dots) compared with the predictions from the k-epsilon Realizable model (blue dots). These points cover the building's east, west, north, and south orientations, under wind conditions of 0 and 45 degrees and wind speeds of 5 m/s and 10 m/s. The comparison of the red and blue dots for each scenario allows an evaluation of the model's alignment with the experimental data. The k-epsilon Realizable model results generally follow the experimental data well, particularly in capturing the wind pressure trends on both windward (e.g., west side at 0 degrees wind direction) and leeward

(e.g., east side at 0 degrees) aspects. It also shows commendable predictive accuracy for crosswind conditions (e.g., north, and south sides at 45 degrees). The discrepancies between wind tunnel data and CFD predictions, notably on the west building's windward side at 0 degrees, could be influenced by factors like local turbulence at internal test points near openings and the inherent differences in turbulence model approaches. These factors can impact the precision of pressure coefficient measurements and the accuracy of simulation results. The fixed boundary conditions in CFD simulations also play a role, as they represent an averaged state of flow under specific wind conditions, contrasting with the more variable and transient nature of actual wind fields. Despite these nuances, the k-epsilon Realizable model proves effective in predicting the pressure coefficient in courtyard building interiors under varying wind conditions.

#### 6.3.4.2 Validation of CO<sub>2</sub> dispersion in the courtyard buildings

In this study, CO<sub>2</sub> is used as the pollutant in wind tunnel testing to investigate the cross-transmission of pollutants in the courtyard building through crossflow natural ventilation. The choice of CO<sub>2</sub> is driven by its availability and cost-effectiveness, along with its suitable sensitivity range, which makes it ideal for this study. Additionally, the safety profile of CO<sub>2</sub>, particularly its non-toxic nature at concentrations under 5000 ppm (Azuma et al., 2018), makes it a viable option for our controlled experimental studies. Although it doesn't mimic the heavier molecular weight of SF<sub>6</sub> or the reactivity of C<sub>2</sub>H<sub>4</sub>, CO<sub>2</sub>'s properties closely resemble those of many indoor pollutants (Graham et al., 2004; Zhang et al., 2017), making it relevant for studying airflow in buildings (Bartzanas et al., 2007; Van & Blocken, 2013; Zhang et al., 2015). Despite the limitations of not encompassing all pollutants' properties, this

research will maintain methodological through frequent calibration and multiple test runs, ensuring the reliability of findings.

Figure 6.9 shows a comparison between CO<sub>2</sub> dispersion predictions from wind tunnel experiments and those from CFD simulations. This figure illustrates the dynamic evolution of CO<sub>2</sub> concentration in two test rooms, REF and RWF, as recorded by sensors. The observation period encompasses the entire duration from the initial release of CO<sub>2</sub> to its eventual stabilization. It's important to note that the experimental measurements were concluded only once the CO<sub>2</sub> concentration in these rooms reached a stable state. The data derived from three distinct turbulence models—*k*-epsilon standard model, *k*-epsilon RNG model, and *k*-epsilon Realizable model—are evaluated against the experimental measurements. Notably, the simulation parameters were aligned with the wind tunnel experimental setup. In the RWF room, both a CO<sub>2</sub> release source and a sensor were installed, whereas the REF room was equipped with a similar sensor. The results for the courtyard model at 0° wind speeds of 5m/s and 10m/s are detailed in Figure 6.9 (a) and Figure 6.9 (b), respectively, while Figure 6.9 (c) and Figure 6.9 (d) present findings at a 45°. As anticipated, the CO<sub>2</sub> concentration in the room diminishes with increasing wind speed, demonstrating the capability of natural ventilation to remove pollutants from indoor spaces.

The CFD simulations closely matched the experimental data, confirming a decrease in indoor CO<sub>2</sub> concentration as wind speeds increased, which was in line with general expectations. In terms of accuracy, while all turbulence models provided reliable predictions for the REF room, the *k*-epsilon Realizable model stood out for its precision in the RWF room. The *k*-epsilon standard model, despite slight deviations, remained largely accurate. However, the *k*-epsilon RNG model, especially at 45° and 10m/s, showed notable divergence,



even though its other predictions were consistent. This aligns with previous research that often favoured the  $k$ -epsilon Realizable model and  $k$ -epsilon RNG models for pollutant dispersion predictions. In these four tested scenarios, the  $k$ -epsilon Realizable model, the  $k$ -epsilon Standard model, and the  $k$ -epsilon RNG model demonstrated impressive accuracies of approximately 93.51%, 88.99%, and 92.27%, respectively, in predicting CO<sub>2</sub> concentrations within the two rooms of the experiment. Overall, the numerical model accurately simulated CO<sub>2</sub> dispersion within the courtyard building.

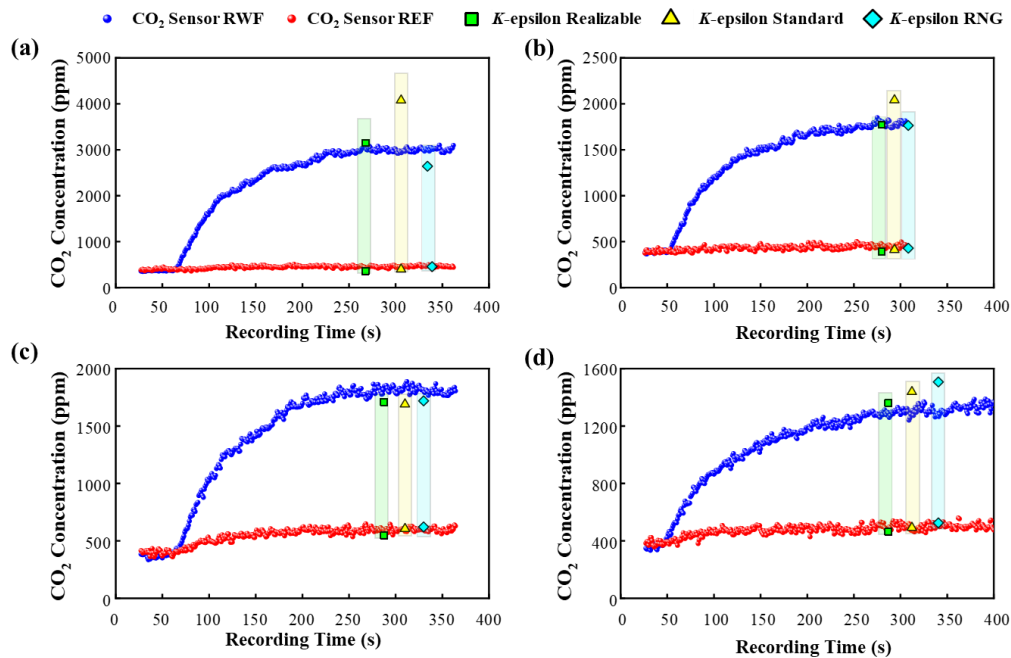


Figure 6.9 Comparison of CO<sub>2</sub> concentration between the experiment and CFD simulations with three turbulence models. (a) Wind direction at 0 degrees and wind speed at 5 m/s. (b) Wind direction at 0 degrees and wind speed at 10 m/s. (c) Wind direction at 45 degrees and wind speed at 5 m/s. (d) Wind direction at 45 degrees and wind speed at 10m/s.

## 6.4 Results of this chapter

In line with the wind tunnel experiments, CFD simulations were carried out to model pollutant dispersion from various rooms under different wind directions and speeds. The two column heights represent wind speeds of 5 m/s and 10 m/s. A total of 48 scenarios are presented, as shown in Figure 6.10. Cases 1-24 correspond to a wind direction of 0°, while Cases 25-48 are set at 45°. It is worth noting that in all simulation scenarios, the release rate of CO<sub>2</sub> is maintained at 2.8 m/l.

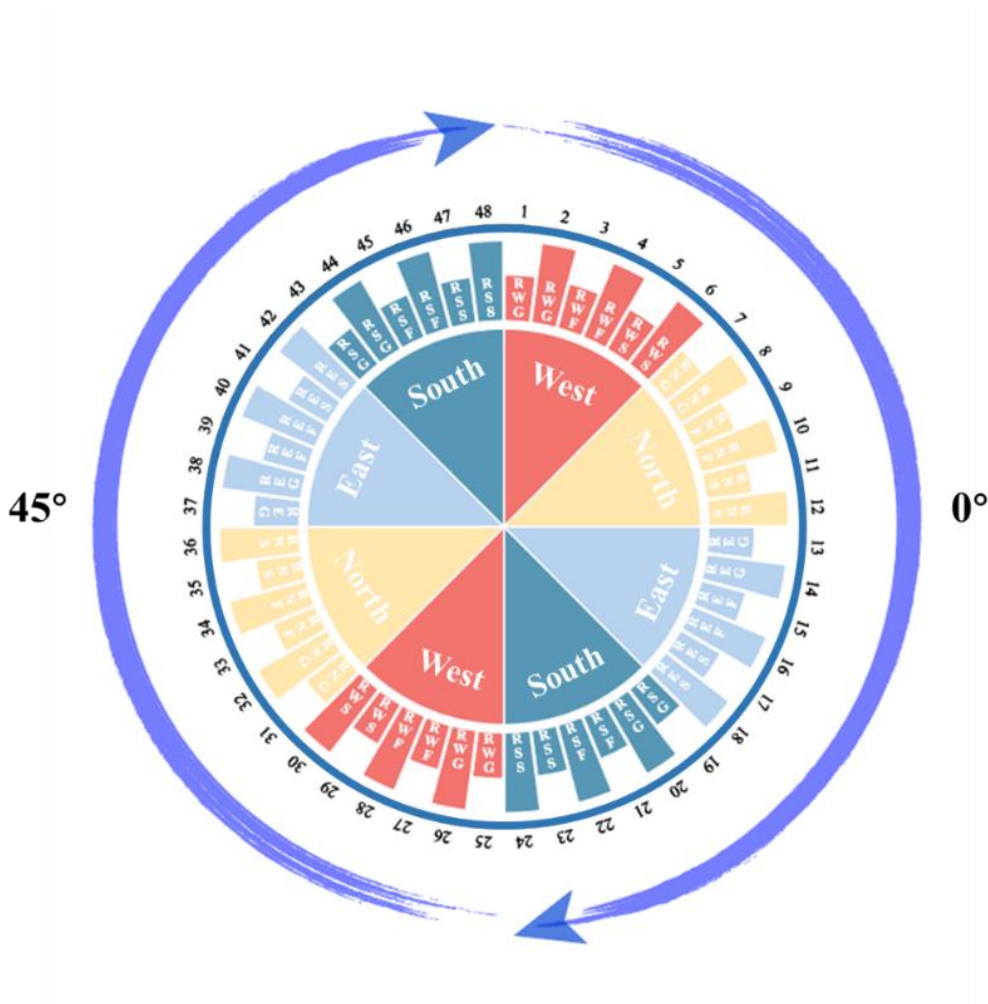


Figure 6.10 48 CFD simulation scenarios for evaluating the impact of different pollutant sources, wind speeds and directions.

## 6.4.1 Airflow movement and pollutant dispersion at 0° wind direction

### 6.4.1.1 Air flow velocity and pressure distribution

Figure 6.11 (a) depicts the airflow patterns within the courtyard building based on average results from CFD simulations. The wind approaches from the inlet, impacting the windward side and causing turbulence at the leeward side. These patterns demonstrate the flow from the west side rooms into the courtyard and then into the north and south side rooms, with the east-facing rooms receiving wind from the leeward side. The airflow patterns are consistent at both 5 m/s and 10 m/s wind speeds when aligned at 0°.

Figure 6.11 (b) to (e) presents the velocity and pressure distribution in the vertical and horizontal sections. As can be seen clearly from Figure 6.11 (c) and Figure 6.11 (e), positive pressure develops in the rooms located on the windward side of the courtyard with cross airflow. In contrast, negative pressure forms in the rooms on the leeward side and both lateral sides of the building. Figure 6.11 (b) shows airflow jets from the windward facade to the interior rooms, inclined due to pressure differences. Figure 6.11 (b) and Figure 6.11 (c) further reveal jets moving from these rooms into the courtyard. Similarly, smaller jets are observed from the leeward rooms to the courtyard, all influenced by varying pressure gradients.

Conversely, negative pressure arises in the rooms on the leeward side and both lateral sides of the building. The airflow from the windward rooms is directed into the courtyard. Additionally, a portion of the incoming wind from the inlet, which does not enter the windward rooms, generates a noticeable vortex on the leeward side as it traverses the courtyard. This vortex redirects a portion of the airflow back towards the courtyard on the leeward side. Figure 6.11 (e) indicates a low-pressure zone in the courtyard, with the pressure

reaching an average of  $-4.23$  Pa in the lower region. As observed in Figure 6.11 (b) and Figure 6.11 (d), the wind speed within the courtyard is higher ( $0.75$  m/s in the lower region and  $0.96$  m/s in the upper region) compared to the rooms. This is because the wind from the windward direction and that in the leeward direction converge within the courtyard. However, due to the lower pressure in the RN and RS rooms, the air in the courtyard flows towards them. The airflow speed in the ground-floor rooms of both RNG and RSG averages a modest  $0.01$  m/s, compared to the RWG and REG rooms, where the wind speeds are notably higher at  $0.31$  m/s and  $0.49$  m/s, respectively.

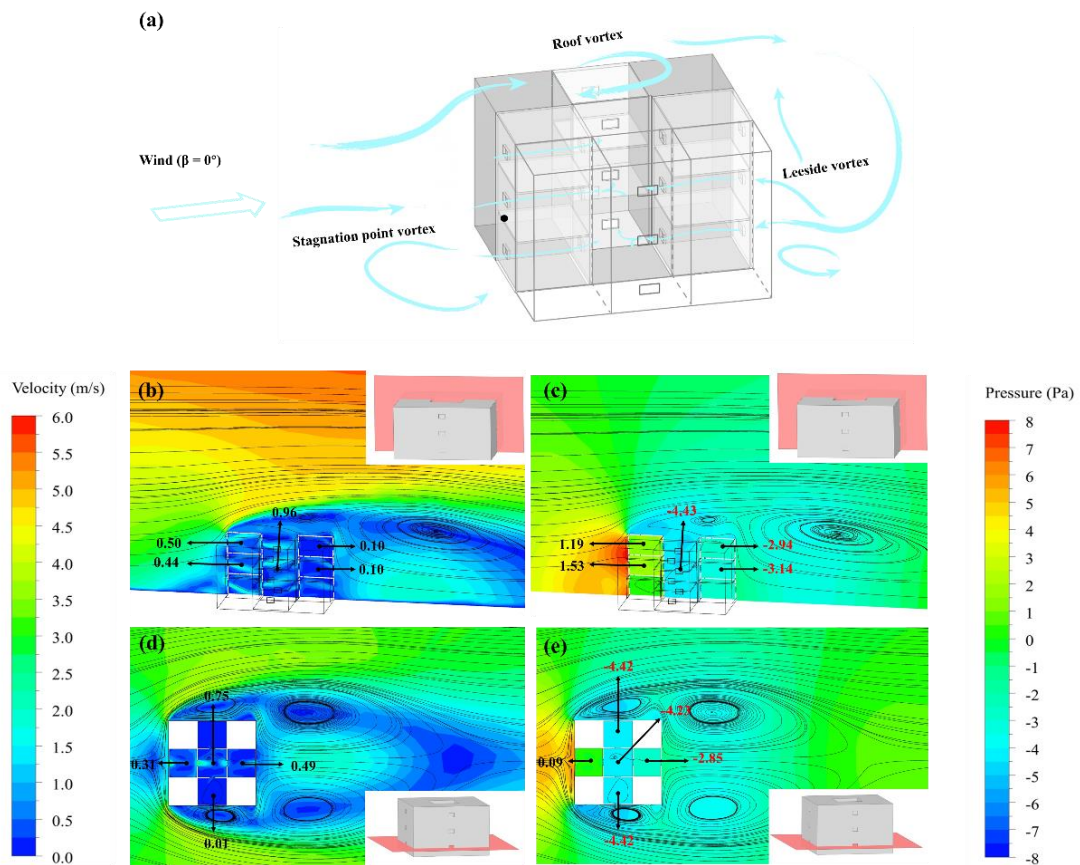


Figure 6.11 Observed airflow patterns, wind velocity, and pressure distribution around the courtyard building in vertical and horizontal orientations. (a) Observed airflow patterns in and around the courtyard building at 0 degrees wind. (b) Cross-sectional contours of wind velocity in vertical orientation around the courtyard building. (c) Pressure distribution in

vertical orientation around the courtyard building. (d) Wind velocity in horizontal orientation around the courtyard building. (e) Pressure distribution in horizontal orientation around the courtyard building.

#### 6.4.1.2 CO<sub>2</sub> concentration and dispersion for the courtyard at 0 degrees wind

Figure 6.12 presents the predicted average concentrations of CO<sub>2</sub> in different rooms under two wind speeds, with a constant release rate of 2.8 m/l from different rooms or sources. It is evident that as wind speed increases, the rooms become less effective at retaining CO<sub>2</sub>, but the observed trend remains similar under both wind speeds. When the source of pollution is located on either the windward (west rooms) or leeward (east rooms) side rooms, in particular the ground and first floor, there is noticeable cross-transmission of CO<sub>2</sub> into the adjacent side rooms (RN and RS), aligning with the distribution of airflow in the courtyard as depicted in Figure 11. For instance, at a wind speed of 5 m/s, the highest concentration is observed in the south-facing room RSG (2797 ppm) when pollutants are released on the windward ground floor RWG, where the indoor wind speed averages 0.1 m/s. The slower indoor wind speed leads to greater CO<sub>2</sub> retention within the space. The second-highest concentration is found in the north-facing room RNG on the same floor, reaching 2575 ppm. Furthermore, pollutants that diffuse from the RWG room on the ground floor to the courtyard also migrate to higher floors. As the elevation increases, the concentration of pollutants in the rooms progressively decreases.

However, when the source of pollutants originates from the side rooms (RN and RS), there is limited to almost no concentration of pollutants detected in any of the rooms. This aligns with the observed airflow patterns, which indicate that air flows from the courtyard into the side rooms and then exits outdoors. Consequently, the pollutants are effectively

exhausted into the outdoor environment. When the source of the pollutant is on the second floor, cross-transmission of pollutants was mainly observed when the source was the windward side room (RWS). This resulted in CO<sub>2</sub> concentrations of 942 ppm and 1064 ppm being detected in adjacent side rooms on the same floor. Notably, the pollutants released from the second-floor rooms did not disperse towards the lower floors. Additionally, when the source was the leeward side room (RES), the pollutant almost did not disperse towards the side rooms, in contrast to what was observed for the ground and first-floor rooms as sources. Pollutant concentrations are higher in some side rooms from releases in the leeward room due to the courtyard's airflow. The results suggest a downwash effect on the leeward side, causing pollutants to remain in the courtyard longer than those from windward rooms. Comparing values in Figure 6.12 with airflow in Figure 6.11 (b) reveals a clear difference: airflow from windward rooms moves up, while from leeward rooms, it moves down, which matches the seen pollutant behaviour in the courtyard.

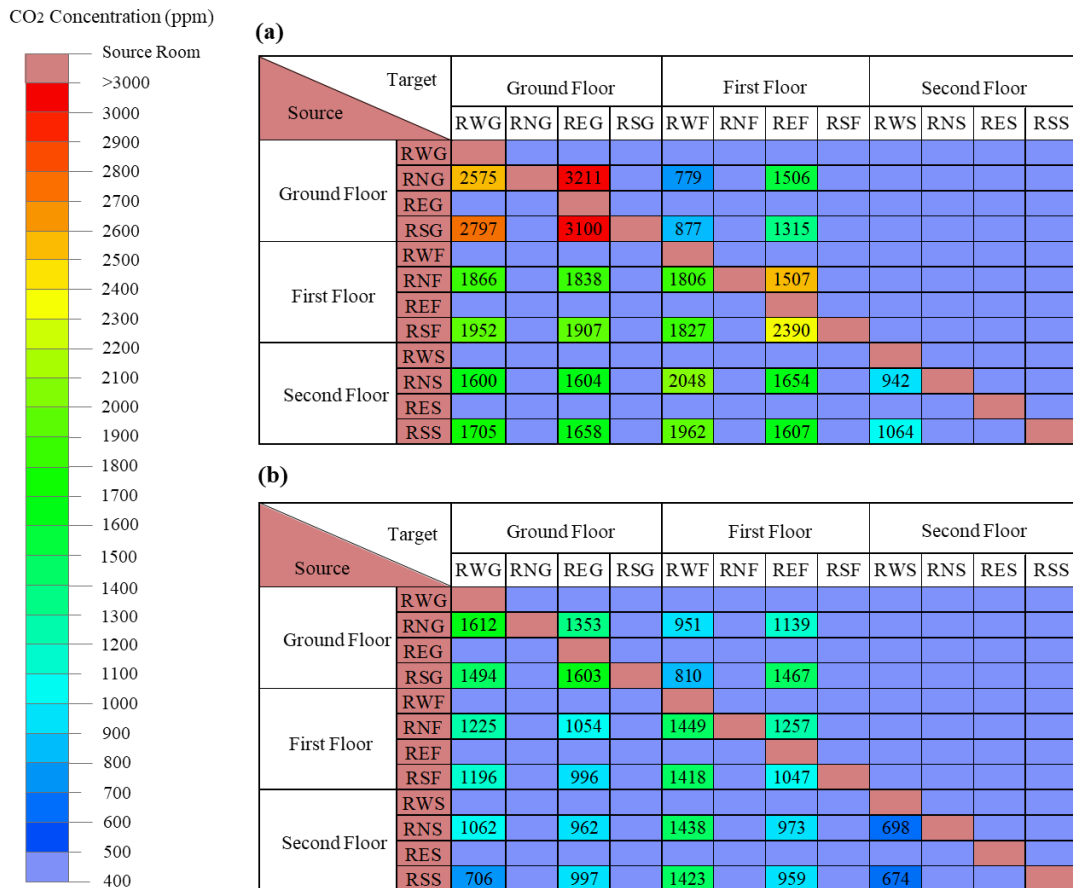


Figure 6.12 Average CO<sub>2</sub> concentrations in different rooms at wind speeds of 5 m/s and 10 m/s, based on different source locations. (a) 5 m/s and (b) 10 m/s.

In Figure 6.13 (a), the red lines indicate the pathway of dispersion for CO<sub>2</sub> on the windward side of the ground floor at a wind speed of 5m/s for Case 1. To better illustrate the pathway of dispersion and the concentrations in the adjoining rooms, an enlarged view of the courtyard is presented in Figure 6.13 (b), in which the average CO<sub>2</sub> concentration in each room is detailed. Evidently, the primary pathway of dispersion is on the immediate adjacent sides when the source of pollution is on the windward side. Notably, there is no dispersion at the other two levels on the same windward side and no dispersion into the rooms on the leeward side. As demonstrated in Figure 6.13 (c) and Figure 6.13 (d), the pathway of dispersion changes when pollutants originate from the leeward side of the ground floor under the same wind conditions. The pollutants diffuse into adjacent rooms on both sides and exist



in the rooms on the leeward side of both the first and second floors. Notably, as the number of floors rises, pollutant concentration is significantly reduced. This decrease is attributed to a rise in wind speed observed at higher floors, which reduces the indoor retention of pollutants.

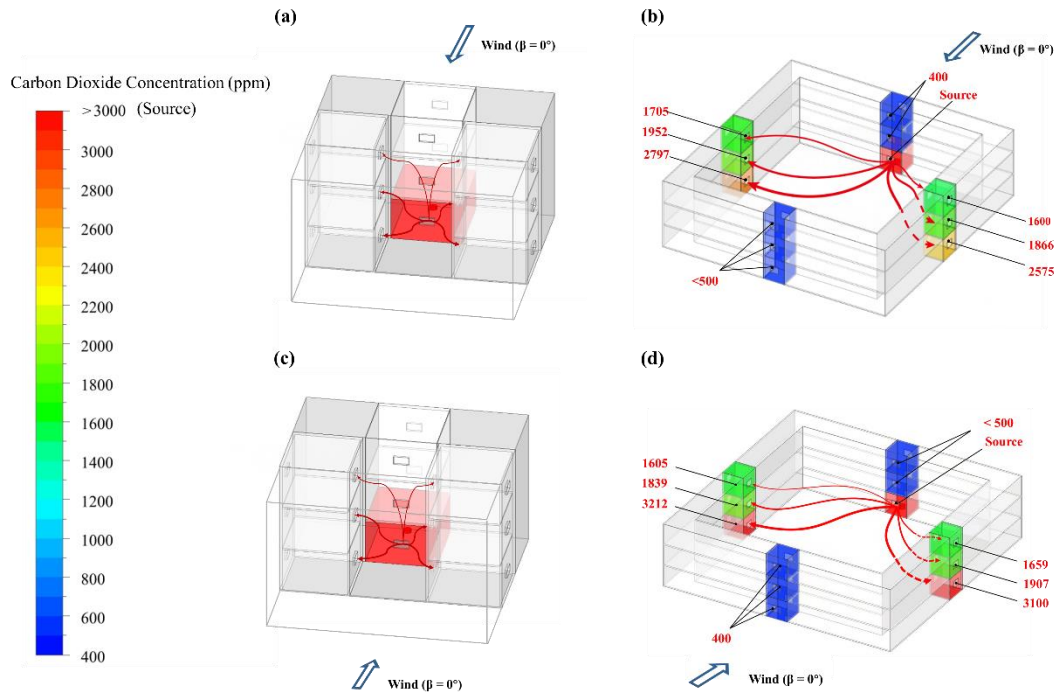


Figure 6.13 CO<sub>2</sub> dispersion pathways and indoor concentration levels from the windward side for Case 1 and Case 13. (a) Dispersion pathways for Case 1. (b) Enlarged view of the dispersion pathways and indoor concentration levels for Case 1. (c) Dispersion pathways of Case 13. (d) Enlarged view of the dispersion pathways and indoor concentration levels for Case 13.

## 6.4.2 Airflow movement and pollutant dispersion at 45° wind direction

### 6.4.2.1 Air flow velocity and pressure distribution

Figure 6.14 (a) illustrates the dynamics of airflow around the modelled courtyard with a 45° angle. The model indicates that the prevailing wind that blows from the inlet is split into two parts. One brings the airflow towards the periphery of the model, and the other directs the



airflow through the interior. In the rooms located on the RW and RS (windward) side, a large volume of incoming air subsequently flows into the central courtyard. Due to the pressure gradient, most of the air flows into the rooms on the leeward side (RE, RN), thus creating a system of "windward-courtyard-leeward" flow.

As shown in Figure 6.14 (b), the velocity distribution reveals that the average wind speed is 0.59 m/s in the rooms on the windward side, while the average wind speed is 0.86 m/s in one room on the leeward side. The average wind speed in the courtyard is 0.51 m/s. Figure 6.14 (c) shows the pattern of pressure distribution. In the windward rooms, the pressure is positive, while it is negative in the leeward rooms, reaching -3.73 pa and -2.38 pa. In the courtyard, there is a low-pressure zone where the pressure is approximately -1.48 pa. This pressure gradient plays a major role in directing the airflow from the courtyard towards the room RNG with a pressure of -3.73 pa. Conversely, the secondary airflow is directed to the room REG with a pressure of -2.38 pa.

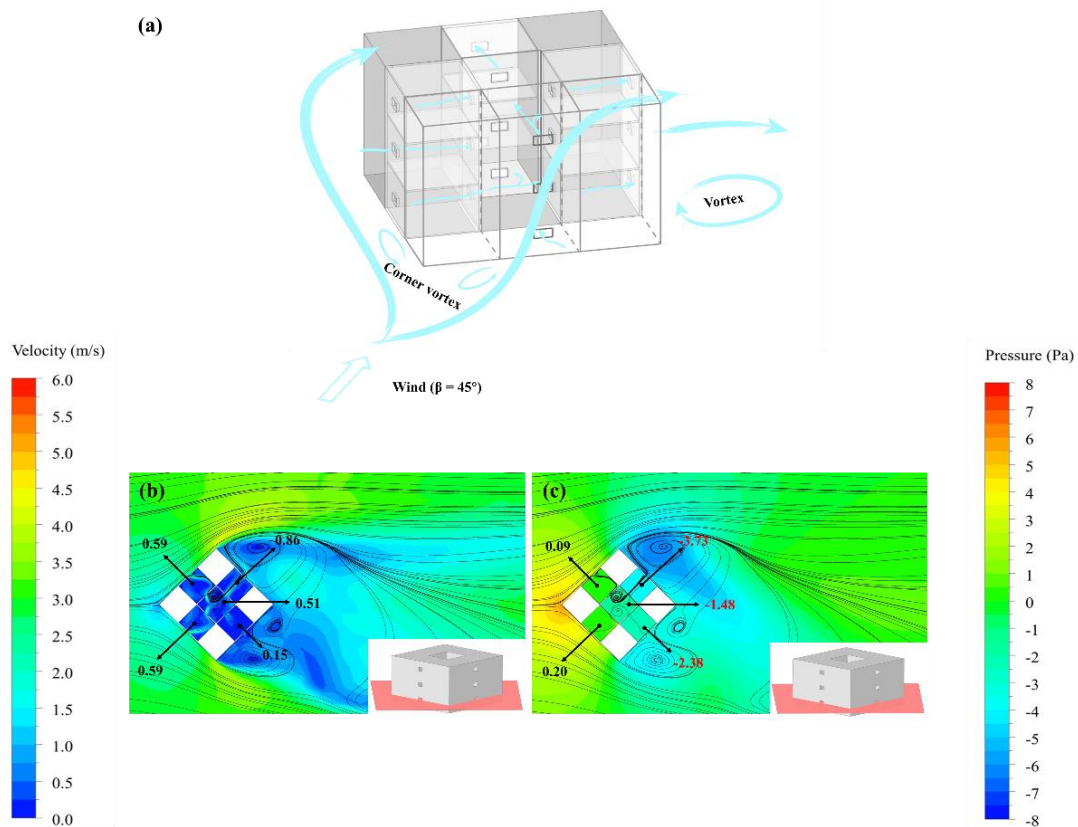


Figure 6.14 Airflow patterns, wind velocity, and pressure distribution around the courtyard building at 45 degrees wind. (a) Observed airflow pattern in and around the courtyard building at 45 degrees wind. (b) Cross-sectional contours of wind velocity in horizontal orientation around the courtyard building. (c) Pressure distribution in horizontal orientation around the courtyard building.

#### 6.4.2.2 CO<sub>2</sub> concentration and dispersion for the courtyard at 45 degrees wind

Figure 6.15 demonstrates the average concentrations of CO<sub>2</sub> in different rooms when the wind blows at a 45-degree angle towards the building, with the release rate maintained at 2.8 ml/s. Comparing Figure 6.15 (a) and (b), which present the results for wind speeds of 5 m/s and 10 m/s respectively, an increase in wind speed reduces CO<sub>2</sub> retention within the rooms. It can be observed that the pollutants on the windward side diffuse to the rooms on the leeward side. For instance, when CO<sub>2</sub> is present in the RWG room on the windward side, the CO<sub>2</sub>

dispersing from the RWG room is detected only in the rooms on the leeward side. The concentration of CO<sub>2</sub> is higher on the same floor as its source, diminishing with elevation. Moreover, when the release source is in the rooms with a greater elevation, there is a decreasing trend shown by the peak concentration in any room. For example, at a wind speed of 5 m/s, the concentration of CO<sub>2</sub> originating from the RSG room peaks at 2264 ppm in the RNG room. However, when the source of pollution is in the RSF and RSS rooms, the highest concentrations detected in the monitored rooms are 1579 ppm and 1290 ppm, respectively. In contrast to the scenario with a wind direction of 0 degrees, when the source of pollutants is the leeward side rooms, there is limited to almost no cross-transmission of pollutants to the other rooms. This aligns with the airflow and pressure results, where the air in these rooms is expelled towards the outdoor environment.

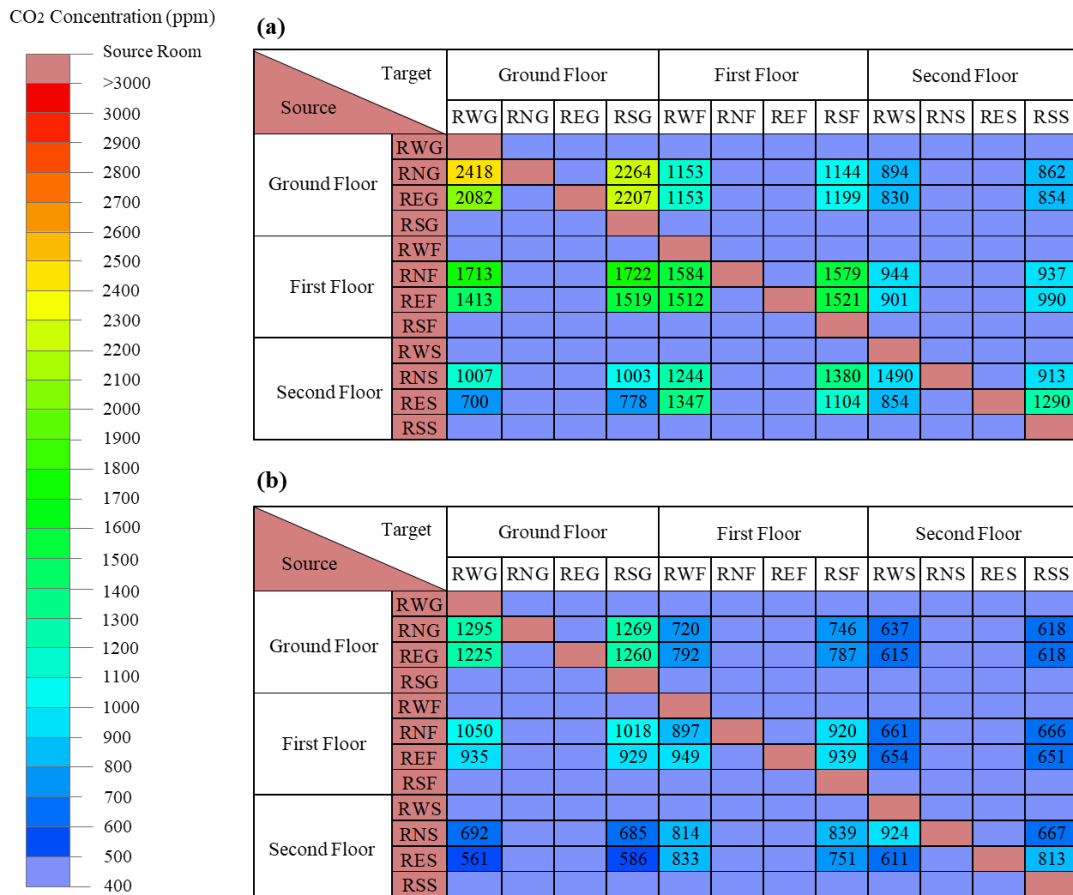


Figure 6.15 Average CO<sub>2</sub> concentrations in different rooms at wind speeds of 5 m/s and 10 m/s, based on different source locations. (a) 5 m/s and (b) 10 m/s.

Figure 6.16 (a) and Figure 6.16 (b) depict the dispersion of CO<sub>2</sub> in the RWG room on the windward side when the wind speed is 5 m/s, which is denoted as Case 25. The right panel in the figure shows an enlarged view of the courtyard, detailing the pathway of dispersion and the level of concentrations in nearby rooms. Notably, when the source of pollution is on one of the windward sides, the pollutants diffuse mainly into the two buildings on the leeward side, with no clear sign of dispersion into both windward facades. As the difference in pressure becomes more significant between the courtyard and the northern room, the airflow becomes faster in the north-facing room than in its east counterpart. In this case, there are more pollutants flowing from the courtyard to the northern room. Consequently, the

indoor concentration of pollutants in the north-facing RNG room reaches 2481 ppm, indicating a difference of approximately 400 ppm compared to the east-facing REG room.

As illustrated in Figure 6.16 (c) and Figure 6.16 (d), the pattern of dispersion when the source of pollution is on the southern side, which is opposite to the windward direction. The pollutants flow to the courtyard and then to the rooms on the leeward side. When the concentration of pollutants remains higher in the north-facing room than in the east-facing room, the overall trend of dispersion remains unchanged. This is consistent with Case 43 when the wind speed is 5 m/s. A similar trend has been observed at a wind speed of 10 m/s.

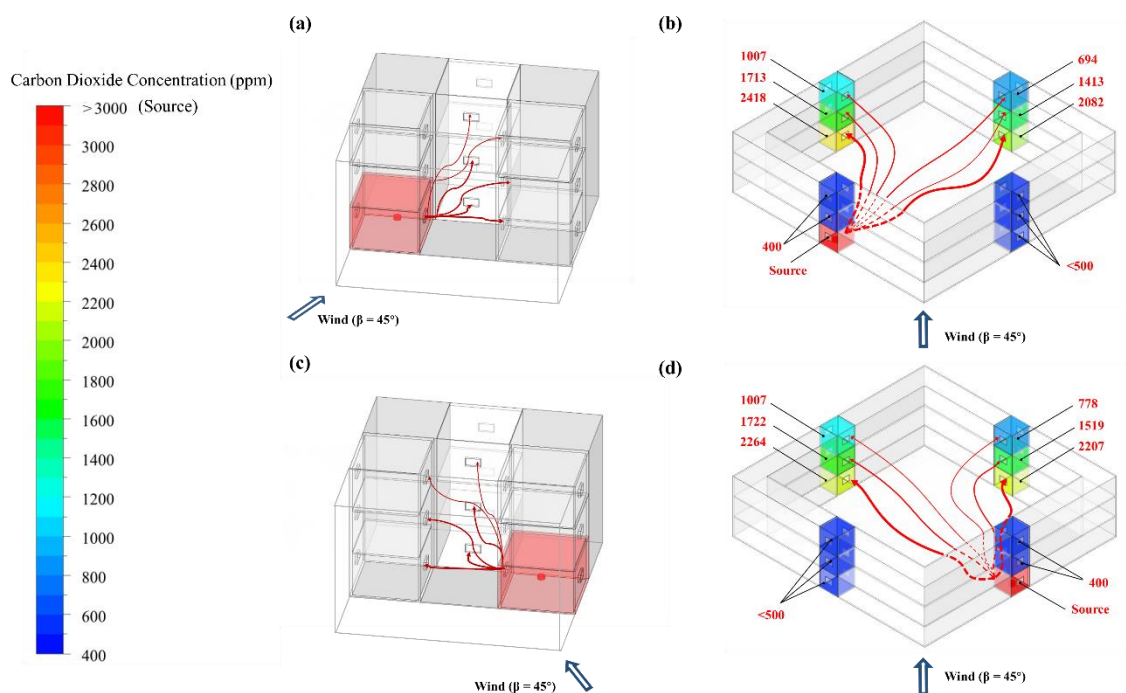


Figure 6.16 CO<sub>2</sub> dispersion pathways and indoor concentration levels from the windward side for Case 25 and Case 43. (a) Dispersion pathways for Case 25. (b) Enlarged view of the dispersion pathways and indoor concentration levels for Case 25. (c) Dispersion pathways of Case 43. (d) Enlarged view of the dispersion pathways and indoor concentration levels for Case 43.

## 6.5 Discussion

This section provides an analysis of the optimal and least favourable scenarios among the simulated 48 pollutant dispersion scenarios. Additionally, it will compare the results of wind tunnel experiments and CFD simulations with previous related studies, further identifying potential areas for improvement in this research.

### 6.5.1 Comparative analysis of optimal and adverse scenarios

As shown in Table 6.4, at a wind direction of  $0^\circ$ , the dispersion of pollutants in the first 24 scenarios is analysed at a wind speed of 5 m/s and 10 m/s, respectively. Then, the most and least favourable conditions are determined. At a wind speed of 5 m/s or 10 m/s, the optimal conditions of dispersion are met when the source of pollution is in the rooms facing north or south. Table 6.3 provides a detailed view of Cases 9, 10, 23, and 24, offering in-depth insights into RNF and RSG metrics. However, pollutants remain confined in any room on the non-windward or leeward side of all floors. This is attributed to the lower pressure in those rooms on these sides compared to the courtyard, which impedes the airflow from the courtyard into the room as the source of pollution. Thus, the dispersion of pollutants to other rooms is limited. Such confinement is considered optimal, as the aim is to minimize the widespread dispersion of pollutants across multiple rooms. Regarding the least favourable scenarios, the pollutants first diffuse from the room as the source of pollution to the courtyard and then to the other rooms, which increases the concentrations of  $\text{CO}_2$ .

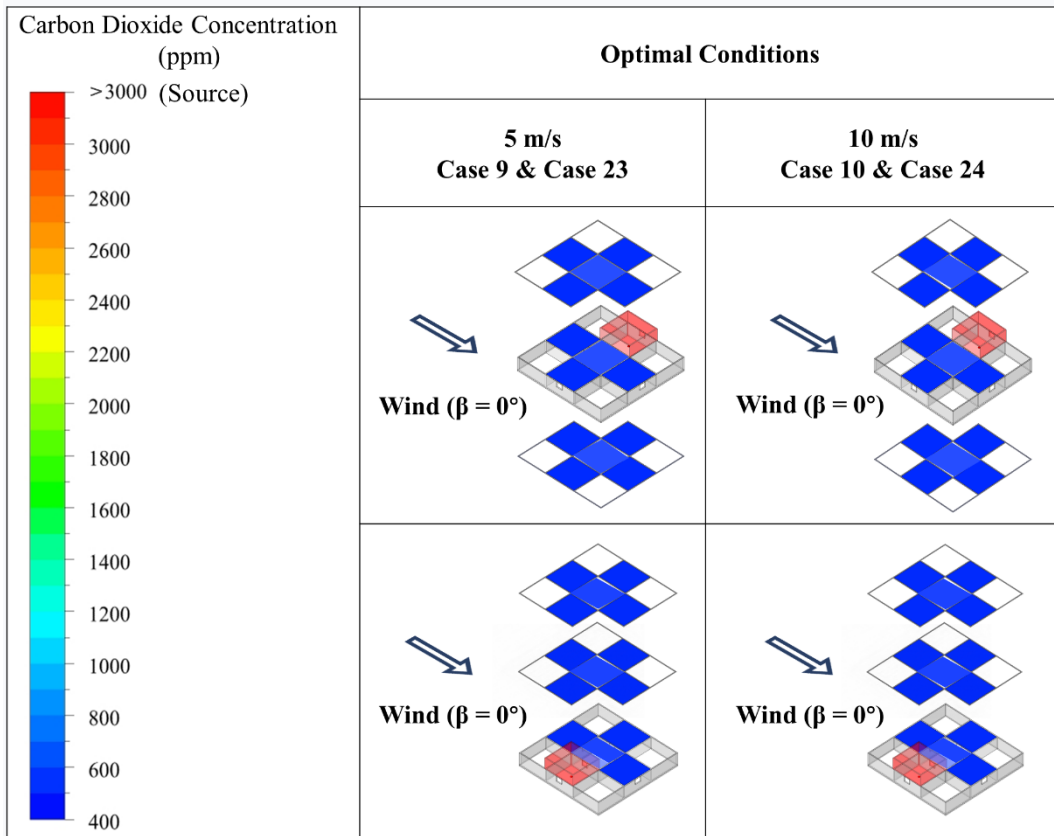


Table 6.4 Comparative analysis of optimal conditions across the first 24 scenarios under a wind direction of 0 degrees.

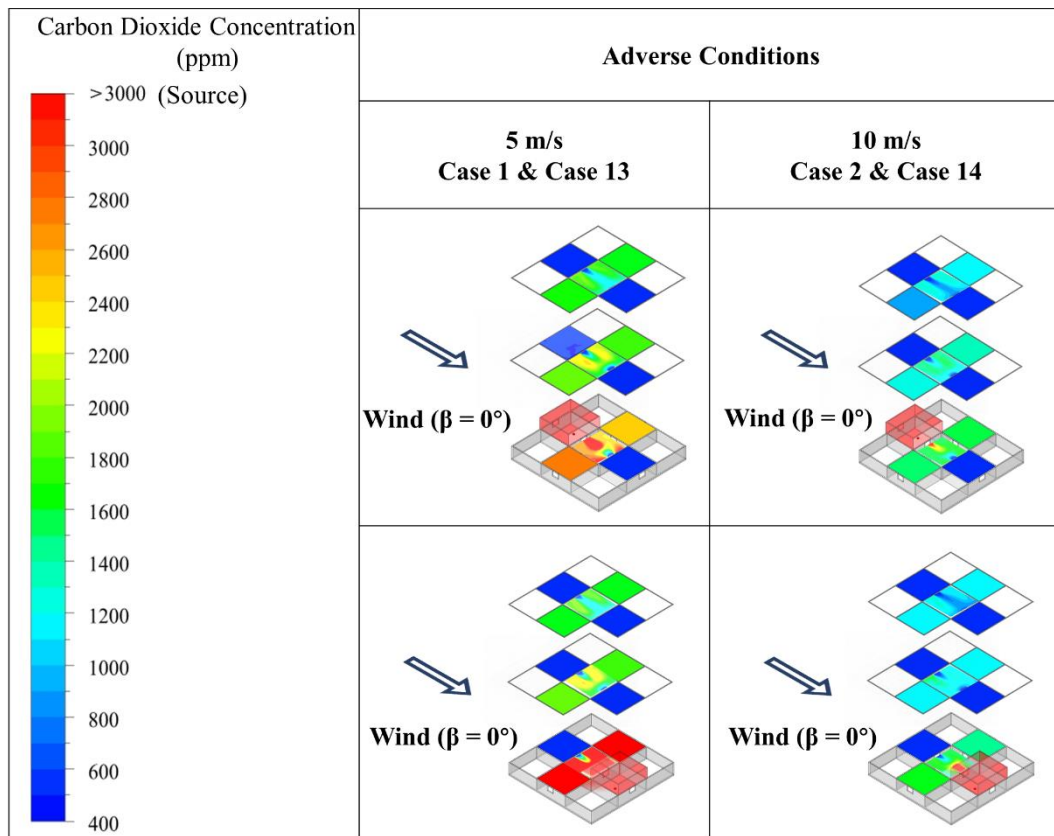


Table 6.5 Comparative analysis of adverse conditions across the first 24 scenarios under a wind direction of 0 degrees.

Table 6.5 illustrates four distinct scenarios at two different wind speeds. One is that the release source is on the windward side (Case 1 and Case 2) and the other is that it's on the leeward side (Case 13 and Case 14). It is evident that the pollutants disperse into adjacent rooms when the source of pollution is in the rooms either in or opposite the wind direction, especially the rooms facing north or south on the same floor. Additionally, the vertical dispersion into those rooms not directly facing or opposing the wind occurs, despite a decline in height. At a wind speed of 5 m/s, the highest CO<sub>2</sub> concentrations are measured to be 3212 ppm (with the source on the leeward side in REG) and 2797 ppm (with the source on the windward side in RWG). When the wind speed reaches 10 m/s, CO<sub>2</sub> concentration exceeds 1600 ppm in some monitored rooms. Judging from Table 3 and Table 4, the optimal scenario



is that the source of pollution is located in the rooms facing the north or the south (neither on the windward nor leeward sides), whereas the least favourable condition is that the source is in the rooms facing the east or the west, corresponding to the windward or leeward side, respectively.

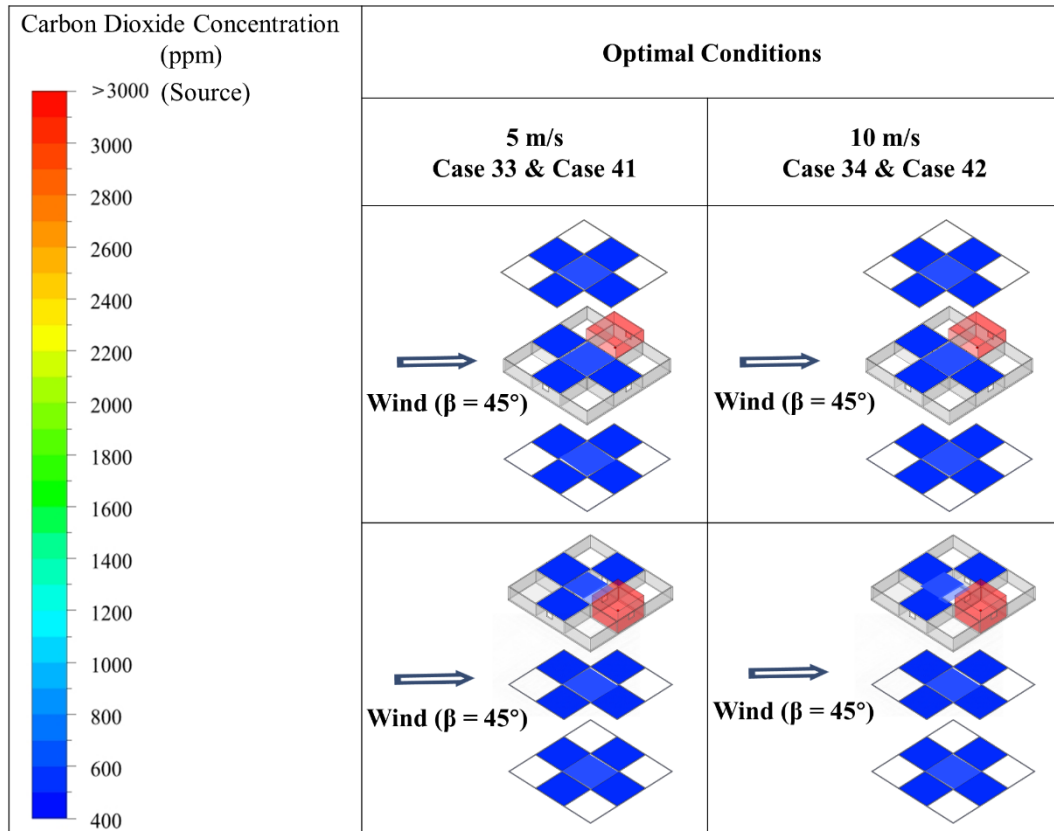


Table 6.6 Comparative analysis of optimal conditions across the later 24 scenarios under a wind direction of 45 degrees.

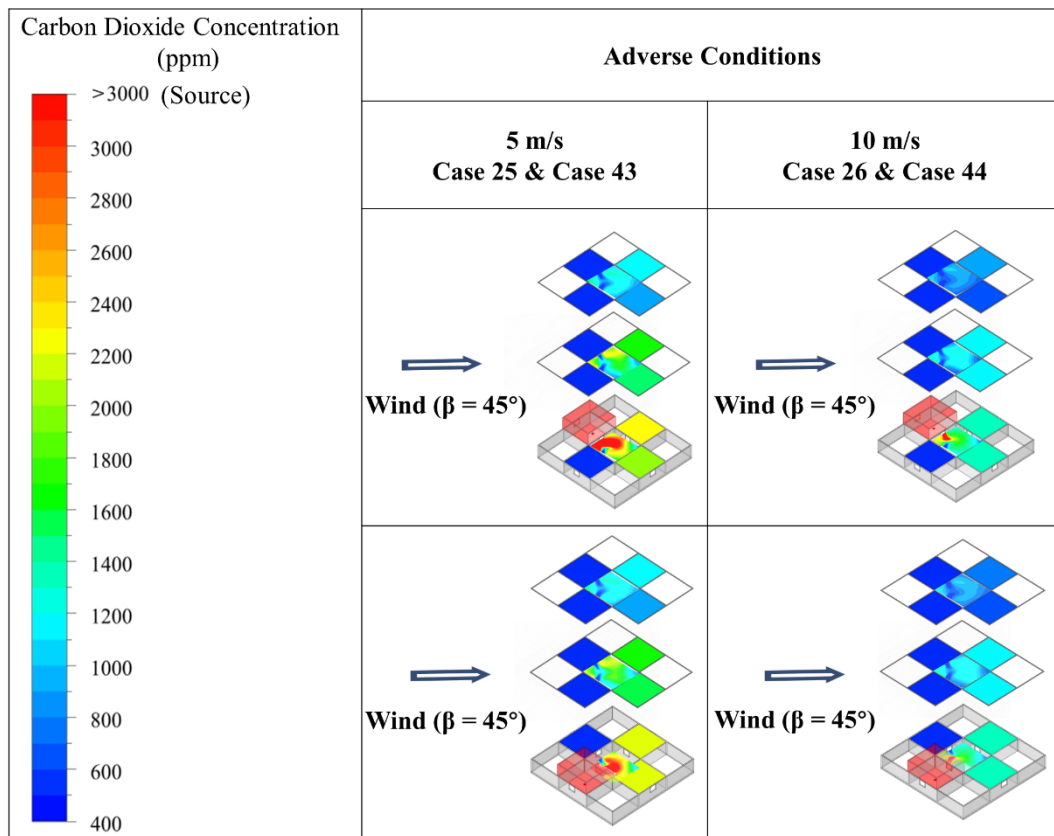


Table 6.7 Comparative analysis of adverse conditions across the later 24 scenarios under a wind direction of 45 degrees.

As shown in Table 6.6 and Table 6.7, at a wind direction of 45°, the patterns of dispersion of pollutants are evaluated at two different wind speeds under 24 different scenarios: 5 m/s and 10 m/s. According to the results, the best and the worst conditions for the dispersion of pollutants are identified. When the wind speed is 5 m/s or 10 m/s, the most conducive dispersion is observed when the pollutants originate from the rooms located on the north or east, suggesting the leeward side in the context of the wind direction. The pollutants tend to be trapped within the rooms on the leeward side without extensive dispersion to the courtyard or adjacent rooms. To a large extent, this is because the rooms on the leeward side show a decline in pressure relative to the courtyard, restricting airflow. Consequently, the pollutants flow to the nearby rooms. Such behaviour is deemed optimal as it is aligned with

the objective of limiting the dispersion of pollutants across different rooms. In contrast, the least favourable dispersion is characterized by the pollutants diffusing to the courtyard and then to other rooms, which increases the concentration of CO<sub>2</sub>. In Table 6.6, this is evident when the release source is on the windward side (Cases 25 and 26) and in the rooms directly facing the wind (Cases 43 and 44). The trend suggests a more pronounced dispersion of pollutants into the courtyard and subsequently into leeward rooms, with a noticeable decrease in concentration at higher elevations. At a wind speed of 5 m/s, the peak CO<sub>2</sub> concentrations reach 2418 ppm and 2264 ppm when the source of pollution is in the west and south on the windward side, respectively. At a wind speed of 10m/s, the concentrations exceed 1200 ppm in some rooms. It is underscored that the most effective dispersion occurs when the pollutants enter the northeast ward rooms on the leeward side, whereas the most adverse dispersion and the highest pollutant concentrations are observed when the source of pollution is in the northwest-facing rooms, which is aligned with the wind direction.

### 6.5.2 Comparison with other studies

In 48 different pollutant dispersion simulation scenarios, the dispersion of pollutants within crossflow ventilated courtyard buildings is related to the location of the pollution source and the changes in airflow patterns caused by wind direction. When the wind blows perpendicularly towards the courtyard building, if the pollution source is on the windward or leeward side room, pollutants will disperse to the adjacent buildings on both sides. However, when the pollution source is in a room that is neither windward nor leeward, the pollutants mainly concentrate in the room where they are released. The dispersion path of pollutants generally follows the trajectory of air movement within the courtyard. Even when the wind is at an oblique angle, the trajectory of pollutant movement still follows the airflow paths within the courtyard. This dispersion characteristic is unique to courtyard architecture, as its special

architectural form results in different directions and trajectories of airflow movement. In the study by Cui et al. (2021), they found that different pollution source locations and wind directions significantly affect the dispersion characteristics of pollutants. Compared to courtyard buildings, the pollutant dispersion in building complexes is characterized by concentration in street canyons and downstream dispersion when the wind is perpendicular, and a more extensive polluted area when the wind is at an oblique angle (Cui et al., 2021). When the wind blows perpendicularly towards the cross ventilated courtyard building, the reason pollutants do not disperse downstream is due to the formation of vortices on the leeward side of the building, leading to a significant influx of wind into the leeward rooms and subsequent dispersion to the courtyard and surrounding rooms.

As the location of the pollution source changes, this study has found that regardless of wind direction or speed, pollutants primarily disperse to surrounding rooms on the same floor. Changes in floor levels mean that the impact of pollution on floors farther from the source diminishes with distance. Moreover, pollutants primarily diffuse to adjacent floors, with other rooms in the same building being less affected. This finding is consistent with a study by Liu et al. (2010) on indoor air pollution dispersion in high-rise buildings in Hong Kong, which noted the potential risk of cross-contamination between adjacent apartments and possible inter-unit spread of pollutants. Similarly, Wang et al. (2020) found that when the pollution source is located on a central floor, the floors closest to the source have the highest risk of contamination. The innovation of this study lies in its examination of pollution sources located indoors. Through wind tunnel experiments and CFD simulations, I found that natural ventilation can remove some indoor particulate pollutants, but it may also introduce outdoor pollutants indoors, thereby affecting indoor air quality. This is in line with the findings of the

study by Chu & Yang (2022), which investigated how outdoor particulate matter affects indoor air quality through natural ventilation.

### 6.5.3 Limitations and recommendations for future works

This study is based on an idealized model designed to investigate pollutant dispersion in courtyard buildings, and while it provides foundational insights, it does not encompass all real-world complexities such as simultaneous indoor pollutant-generating activities and the influence of surrounding structures. Firstly, one limitation of this study is the need to vary CO<sub>2</sub> release rates based on wind angles and speeds to avoid exceeding the sensor's maximum detection limit. Future research could address this by using sensors with higher detection limits or by employing additional methods to normalize emission rates across different scenarios. Additionally, further studies should consider more complex pollutant generation scenarios, including simultaneous activities and full scaled model analyses, to better reflect real-world conditions and enhance the applicability of the findings to practical architectural design. It should be noted that this study focuses on the dispersion of pollutants within courtyard architecture and solely considers cross ventilation as the ventilation strategy. However, there are significant differences in the wind environment of courtyards under single-sided ventilation compared to cross ventilation, which this paper does not investigate. Additionally, in this study, the size of window openings was set uniformly, without considering the potential impact of their variation on pollutant dispersion. For future research directions, exploring pollutant dispersion in courtyard architecture under single-sided ventilation conditions, as well as examining the impact of different opening sizes and orientations on pollutant dispersion, will be of significant value. This will not only provide more comprehensive guidance for ventilation strategies in courtyard architecture but also contribute to a deeper understanding of the impact of architectural design on indoor air

quality. Furthermore, while this study mainly focuses on the exploration of pollutant concentrations and dispersion paths, future research on factors such as air change rate in different rooms will also be extremely valuable, further promoting understanding and innovation in controlling and improving air quality within buildings. The use of exhaust hoods has a significant effect on eliminating pollutants generated by cooking. Studying the transmission path from the exhaust outlet to the indoor environment is also an important direction for future research. Investigating the transmission of pollutants from the exhaust outlet to indoors can design more effective ventilation systems that reduce the spread of pollutants at the source.

For the validation and simulation of CFD, I selected the commonly used RANS models for comparison and application. RANS models are chosen for their ability to successfully predict airflow movement and pollutant dispersion in courtyard architecture, as well as their relatively lower computational cost. In this study, the *K*-epsilon Realizable model was selected based on the validation of wind tunnel experiments. Nevertheless, the study did not adopt LES models, based on considerations of computational resources and time efficiency. However, LES models are renowned for their high-precision description of complex flows, making them an important direction for future research. Therefore, in future work, comparing the differences and advantages of RANS and LES models in predicting pollutant dispersion in courtyard architecture will be an important research area. This will not only help us gain a deeper understanding of the applicability and accuracy of different models in specific architectural environments but also promote the development of more efficient and precise methods for simulating pollutant dispersion, providing stronger scientific support for courtyard architecture design.

## 6.6 Conclusion

This chapter conducts an in-depth investigation of the characteristics of pollutant dispersion in a crossflow ventilated courtyard architecture, employing a systematic approach through the integration of wind tunnel experiments and CFD simulations. Compared to previous studies, this research for the first time provides a detailed analysis of the dynamic process by which pollutants are transferred from indoors to outdoors and then recirculated back to other indoor areas through natural ventilation, filling a research gap in this field.

Through wind tunnel experiments, this study conducted detailed measurements of the wind environment within courtyard buildings, particularly assessing wind pressure distribution by measuring the pressure coefficient ( $C_p$ ). Additionally, CO<sub>2</sub> concentrations in the source room and other rooms were monitored using CO<sub>2</sub> sensors. Two different wind speeds (5 m/s and 10 m/s) and directions (0° and 45°) were selected for the experiments. The results of the wind tunnel experiments were validated using CFD simulations, comparing three different RANS models with the K-epsilon Realizable model, which was ultimately chosen as the turbulence model for subsequent research.

In the CFD model, 48 different scenarios of pollutant dispersion with varying wind speeds and directions were set up to analyse the dispersion effects when pollutants are placed in different rooms. The study found that:

(1) Cross ventilation in the courtyard building significantly influences the dispersion of indoor pollutants to the outside, especially as the unique structural form of courtyard buildings causes airflow movement to differ from other buildings. For instance, when the wind direction is 0°, pollutants disperse from windward or leeward side rooms to adjacent

side rooms; while at a 45° wind direction, they disperse to the opposite rooms at the windward corner.

(2) Changes in wind speed primarily affect the concentration of indoor pollutants, with high wind speeds aiding in reducing accumulation and low wind speeds leading to more, but not altering the direction of pollutant dispersion.

(3) The circulation of pollutants from indoors to the courtyard and back indoors caused by natural ventilation has a significant impact on rooms on the same floor, while as the floors change, the impact gradually diminishes on floors further away from the pollution source.

This study, through the combination of wind tunnel experiments and CFD modelling, has revealed the patterns of pollutant dispersion in courtyard architecture and identified the optimal scenarios where pollutants do not disperse to the courtyard and surrounding rooms, as well as the worst scenarios where pollutants extensively disperse to other rooms through natural ventilation. These findings not only deepen the understanding of natural ventilation patterns in courtyard architecture and the resultant pollutant dispersion but also provide valuable guidance to architects aiming to create safer and more comfortable living environments.



## Chapter 7 Conclusions and Future works

### 7.1 Conclusions

This research primarily investigates the interactions between courtyards and their adjacent indoor spaces. It focuses on the impact of various passive technologies such as different roof designs, vegetation, and water sprayers on the aerothermal conditions and pollutant dispersion within courtyard buildings. Previous studies mainly concentrated on the microclimate within the courtyards themselves. To fill this research gap, I utilized CFD simulations to explore natural ventilation, temperature control, and pollutant dispersion in courtyard buildings. I validated various courtyard models derived from wind tunnel experiments, comparing different turbulence models, especially the RANS models to ensure robust CFD model validation. This study examined the effects of ten different roof designs on natural ventilation and passive cooling in courtyard buildings. The results showed that dome roofs, compared to flat roofs, enhanced ventilation, increasing indoor wind speed by 80% and reducing temperature by up to 2.1°C. The arrangement of vegetation in the courtyard, particularly large trees, significantly improved the indoor thermal comfort of surrounding buildings. Additionally, water misting in single-sided ventilated courtyards improved indoor thermal conditions, reducing temperature by 2.06°C and increasing humidity by 4.29%. Pollutant dispersion analysis indicated that structure, orientation, and external wind patterns significantly influence pollutant spread, primarily affecting adjacent rooms on the same floor. This multidimensional analysis focuses on courtyard design features and their impact on indoor environments, evaluating roof designs and common natural elements in courtyards as passive technologies to regulate the microclimate and improve the indoor wind and thermal environment of surrounding buildings. It provides insights into design choices and air quality,

promoting sustainable building practices to address climate change and create healthier urban living spaces.

The study achieved its set objectives as defined in Chapter 1 (see Section 1.2 for details) through the comprehensive use of numerical analysis and experimental research methods. The main findings are summarized as follows:

1. The courtyard's shape significantly impacts the ventilation and passive cooling. The results showed that the streamlined design of the dome roof courtyard facilitates closer airflow along the roof surface, significantly enhancing natural ventilation compared to other styles. Specifically, the average indoor wind speed under a dome roof was found to be 80% higher than that of the baseline model (flat roof), and the finding suggests a linear relationship between indoor wind speed and passive cooling, higher wind speeds result in greater heat dissipation. Notably, courtyards with dome-shaped roofs achieved the lowest indoor temperature, 2.1 °C lower than that of the baseline model. In contrast, the parapet roof exhibits the least effective ventilation, with the highest average indoor temperature of 26.4°C and the lowest average wind speed.
2. The application of evaporative cooling systems in courtyards has been found to significantly impact the wind and thermal environment within courtyard buildings and the surrounding indoor spaces, capable of effectively reducing temperatures and increasing relative humidity. Deploying water sprayers in single-side ventilated courtyard buildings markedly transformed the indoor wind patterns, largely by blocking the inflow of wind and altering airflow directions due to shifts in

temperature and humidity. The introduction of sprayers led to a pronounced cooling effect, with the ground-floor rooms on the west side experiencing the most substantial decrease in temperature, up to 8.25 °C, and a humidity rise of 20.27%. Across the 16 evaluated rooms, there was an average temperature drop of 2.06 °C and a 4.29% increase in humidity. This cooling effect was most evident in rooms facing west and lessened with higher floor levels. Additionally, the study investigated how varying water flow rates, from 0.5 l/min, 1/min to 12 l/min, influenced thermal regulation indoors in these courtyard buildings. A distinct reduction in room temperature became noticeable as the water flow rate was adjusted from 5 l/min to 6 l/min, with further increases in flow rate reaching a point beyond which no additional cooling benefits were observed.

3. In this study on the impact of vegetation arrangement in courtyards on the indoor wind and thermal environment of surrounding buildings, I found that introducing vegetation of various sizes into the courtyard significantly altered the wind speed within rooms, with a noticeable increase in some rooms. This change is primarily attributed to the vegetation's adjustment of airflow direction and its transpiration effect, which lowers the temperature in the courtyard, thereby affecting indoor wind conditions. Notably, whether it was small trees of 1.5 m or large trees of 2 m, their presence increased the wind speed in five rooms, especially on the north and west sides of the courtyard. Moreover, the addition of vegetation not only effectively reduced the highest indoor wind speeds but also increased the lowest wind speed levels. Regarding indoor temperature, the introduction of vegetation into the courtyard led to a noticeable cooling effect, and the size of the vegetation had a significant impact: the larger the trees, the more substantial their contribution to

cooling the courtyard and the indoor environment of surrounding buildings. Particularly, in courtyards with large trees, the maximum cooling effect observed in one of the indoor rooms reached up to 6.58°C.

4. This study investigates the characteristics of pollutant dispersion within cross-ventilated courtyard buildings. Wind tunnel experiments were conducted to thoroughly examine the wind environment inside courtyard buildings, with CO<sub>2</sub> concentrations in the source room and other rooms monitored using carbon dioxide sensors. The experiments considered two different wind speeds (5 m/s and 10 m/s) and directions (0° and 45°), with CFD simulation employed to validate the results of the wind tunnel experiments. Among three different RANS models compared, the k-epsilon Realized model accurately simulated the pressure distribution and pollutant dispersion within the courtyard building. In the CFD model, scenarios of pollutant dispersion were set up for 48 different wind speeds and directions to analyze the dispersion effects when pollutants were placed in various rooms. The research revealed that cross-ventilation in courtyard buildings significantly impacts the dispersion of indoor pollutants to the outdoors, especially as the unique structural form of courtyard buildings leads to different airflow movement patterns compared to other buildings. For instance, at a 0° wind direction, pollutants could spread from windward or leeward side rooms to adjacent rooms; at a 45° wind direction, pollutants dispersed to rooms at the windward corner. Variations in wind speed mainly affected the concentration of indoor pollutants, with higher wind speeds helping to reduce the accumulation of pollutants, while lower speeds increased indoor pollutant concentrations but did not change the direction of pollutant dispersion. The pollutants moving from indoors to the courtyard and back indoors

due to natural ventilation significantly affected rooms on the same floor, but the impact gradually decreased with distance from the pollution source and with higher floor levels. Under adverse conditions, a notable propagation of pollutants to non-source rooms was observed, with a particularly unfavourable scenario identified where a room, not the initial source of pollutants, experienced an increase in pollutant concentration from a baseline of 400 ppm to 3,211 ppm.

5. Common ventilation modes in courtyard architecture primarily include single-sided and cross-ventilation. Compared to courtyard buildings with cross-ventilation, those utilizing single-sided ventilation more effectively demonstrate the courtyard's role in regulating the indoor wind and thermal environment, significantly reducing the impact of external disturbances. Particularly, when deploying various passive control technologies within the courtyard, single-sided ventilation, as opposed to cross-ventilation, can more significantly utilize methods such as vegetation and water sprayers to improve the courtyard's wind and thermal environment, thereby affecting the indoor wind and thermal environment of surrounding buildings. For instance, by installing evaporative cooling systems in the courtyard, it can be observed that in courtyard buildings with cross-ventilation, the impact of water sprayers on the indoor thermal environment is relatively limited, only causing minor changes in the indoor wind environment and cooling-humidifying effects. The single-sided ventilation strategy particularly highlights how changes in courtyard design can improve the microclimate of the courtyard, thus affecting the indoor environment of adjacent buildings.

## 7.2 Contribution to knowledge

This study applies simulation and experimental methodologies outlined in the literature review to bridge the research gap detailed in Chapter 2. Specifically, it enhances the understanding of how various passive technologies affect the microclimate of courtyards, with a focus on the indoor wind and thermal environment of courtyard buildings and the dispersion of pollutants within these settings. Herein, the contributions made to the field of courtyard buildings are summarized:

1. Extensive numerical simulation data have been provided on the application of various passive techniques and courtyard design to the study of the indoor aerothermal performance of courtyards, as well as experimental data from wind tunnel experiments on courtyard buildings.
2. Numerical studies have demonstrated the impact of different roof styles on the wind environment within courtyards and the indoor wind environment of surrounding buildings, as well as the effect of natural ventilation on cooling indoor spaces of courtyard architecture. Furthermore, the primary factors affecting the indoor wind environment of courtyard buildings are discussed (Chapter 3).
3. CFD numerical studies have indicated the impact of water sprayers on the wind speed, temperature, and relative humidity inside courtyard buildings with single-sided and cross-ventilation. Additionally, the effect of different water flow rates on indoor cooling efficiency is analysed (Chapter 4).

4. Numerical studies have explored the impact of arranging vegetation of different sizes within courtyards on the wind and thermal environment of both the courtyard and the indoor spaces of surrounding buildings, examining the effect of vegetation size on the microclimate of courtyard architecture (Chapter 5).
5. Research involving wind tunnel experiments and CFD simulations has revealed patterns of pollutant dispersion in courtyard architecture, presenting results under various wind speeds and directions. Additionally, CFD has validated the indoor airflow and CO<sub>2</sub> dispersion conditions observed in wind tunnel experiments of courtyard buildings (Chapter 6).

### 7.3 Limitations of the thesis

1. One of the limitations of this thesis is the use of three different courtyard building models. These models are derived from two separate wind tunnel studies of courtyard buildings, scaled and adapted for use in different chapters. Additionally, I conducted my own wind tunnel experiments using a specific courtyard building model. This resulted in the presence of three distinct courtyard models throughout the thesis. While this approach allowed for a comprehensive analysis of various aspects of courtyard design, it also introduced variability that could affect the consistency of the results. Furthermore, there were inconsistencies in the size and height of the buildings, as well as the location and size of the windows, such as openings facing the internal courtyard or both the internal courtyard and external facing. These variations impact the direct comparison of the passive strategies explored in the research.

2. Another limitation of this thesis is the use of different turbulence models in various chapters. The selection of turbulence models was primarily based on two key factors: the simulation results of wind tunnel experiments and the turbulence models commonly used in previous related research. This approach, while necessary, introduces variability that could affect the consistency of the results. Chapter 3 focuses on the airflow patterns within courtyard buildings with various roof styles. The  $k - \omega$  standard model was chosen based on validated CFD results from prior wind tunnel experiments using a similar courtyard model. This model is known for its accuracy in capturing detailed flow structures in such configurations. Chapter 4, which studies courtyard buildings with evaporative cooling systems (spray devices), and Chapter 5, which examines courtyard buildings with vegetation, used the  $k-\epsilon$  realizable model and the  $k-\epsilon$  standard model, respectively. These models were chosen because most previous studies on spray devices and vegetation utilized these turbulence models. In Chapter 6, the  $k-\epsilon$  realizable model was used to simulate pollutant dispersion in courtyard buildings. This choice was based on wind tunnel experiments and subsequent CFD validation, which demonstrated that the  $k-\epsilon$  realizable model more accurately reflects the experimental results for both the courtyard building and pollutant dispersion.
3. In the case of courtyard buildings with single-sided ventilation, the airflow primarily circulates within the courtyard, resulting in very low wind speeds indoors. Additionally, when windows are only 20% open, it further exacerbates the situation. This leads to the turbulence model being unable to accurately simulate the indoor conditions, as the airflow patterns indoors become highly complex. Therefore, it is crucial to use a laminar model for low wind speed conditions



indoors, in contrast to the turbulence model used for outdoor simulations. This distinction is necessary to accurately capture the differing airflow dynamics between the indoor and outdoor environments. Future research can address this issue by establishing separate fluid domains for indoor and outdoor areas, allowing for more accurate simulations of both environments.

4. Several settings related to courtyard buildings and certain passive technologies are based on hypothetical models, which differ from real-world conditions. For instance, the vegetation is modelled to act as a heat sink, absorbing surrounding heat, which is a simplification that cannot fully capture the complexities of actual vegetation. Similarly, various other elements, such as water spraying devices, roof styles, and pollutant dispersion models, involve idealized assumptions. These assumptions lead to discrepancies between the simulation results and real-life scenarios, such as unrealistic cooling effects of vegetation and very low indoor wind speeds. These limitations highlight the need for future research to incorporate more realistic settings and models to enhance the reliability and applicability of the findings.

## 7.4 Recommendations for further work

The following areas that require further investigation have been identified:

1. Future research should aim to use a standardized courtyard building model and a consistent turbulence model across all studies. This approach would minimize variability and enhance the comparability of results, providing a more cohesive understanding of the effects being studied. By standardizing these aspects,

researchers can ensure that their findings are more robust and universally applicable.

2. Future research on different roof designs for the courtyard has overlooked the specific impact of roof height and slope on airflow. Some suggest that increasing the roof slope could enhance wind speed at windows and roof openings, with airflow behaviour and characteristics largely influenced by the roof slope. These findings indicate a significant direction for future research. Moreover, the research set wind direction to 0°, neglecting the impact of other wind directions, which also marks an area for improvement in future studies.
3. Future work on the integration of water sprayers with courtyards will include adjusting the position, height, and water temperature of the sprayers to further investigate their impact on the indoor thermal environment. Moreover, my previous research indicated that evaporative cooling technologies in single-sided ventilated courtyard buildings have a significant impact only on specific areas. In contrast, courtyard buildings with cross-ventilation did not improve the indoor thermal and humidity conditions in all rooms. Future studies aim to extend these cooling and humidifying effects to a broader range of rooms.
4. In the current research, vegetation of different sizes is placed within courtyards, and the vegetation is positioned at the four corners of the courtyard. Future studies could explore the impact of vegetation located in different positions and even combine this with research on green roofs. Additionally, the effect of different types of vegetation on the indoor wind and thermal environment of courtyard

buildings could also be examined. Furthermore, future research on courtyard architecture could involve comparing different passive technologies in combination and contrasting their effects under specific climate conditions to provide recommendations for future courtyard building design.

5. In future research on pollutant dispersion in courtyard architecture, it would be valuable to explore pollutant dispersion under single-sided ventilation conditions, as well as to examine the effects of different opening sizes and directions on pollutant dispersion. Furthermore, although this study primarily focused on exploring pollutant concentrations and dispersion paths, future research on factors such as ventilation rates in different rooms will also be very valuable, further advancing the understanding and innovation in controlling and improving indoor air quality in buildings.
  
6. To validate and simulate using CFD, I chose to compare and apply the commonly used RANS models. The selection of RANS models was based on their ability to successfully predict vegetation, water sprayers, natural ventilation, airflow movement, and pollutant dispersion in courtyard architecture while also being relatively low in computational cost. However, due to considerations of computational resources and time efficiency, this study did not employ LES models. Nonetheless, LES models are renowned for their high-precision descriptions of complex flows, making them an important direction for future research. Therefore, comparing the differences and advantages of RANS and LES models in predicting pollutant dispersion in courtyard architecture will be an important research area in future work.

## References

- Abohela, I., Hamza, N., & Dudek, S. (2013). Effect of roof shape, wind direction, building height and urban configuration on the energy yield and positioning of roof mounted wind turbines. *Renewable Energy*, 50, 1106–1118. <https://doi.org/10.1016/j.renene.2012.08.068>
- Abu-Zidan, Y., Mendis, P., & Gunawardena, T. (2021). Optimising the computational domain size in CFD simulations of tall buildings. *Heliyon*, 7(4), e06723. <https://doi.org/10.1016/j.heliyon.2021.e06723>
- Akbari, H., Cherati, S. M., Monazam, N. H., & Noguchi, M. (2021). Effect of courtyards' geometrical parameters on climate adaptability and shading performance in hot-arid climate of Yazd (Iran). *Sustainable Energy Technologies and Assessments*, 48, 101594. <https://doi.org/10.1016/j.seta.2021.101594>
- Aldawoud, A. (2008). Thermal performance of courtyard buildings. *Energy and Buildings*, 40(5), 906–910. <https://doi.org/10.1016/j.enbuild.2007.07.007>
- Al-Hafith, O., B K, S., Bradbury, S., & de Wilde, P. (2017). The Impact of courtyard parameters on its shading level an experimental study in Baghdad, Iraq. *Sustainability in Energy and Buildings 2017: Proceedings of the Ninth KES International Conference, Chania, Greece, 5-7 July 2017*, 134, 99–109. <https://doi.org/10.1016/j.egypro.2017.09.539>
- Al-Masri, N., & Abu-Hijleh, B. (2012). Courtyard housing in midrise buildings: An environmental assessment in hot-arid climate. *Renewable and Sustainable Energy Reviews*, 16(4), 1892–1898. <https://doi.org/10.1016/j.rser.2012.01.008>
- Amaripadath, D., Rahif, R., Zuo, W., Velickovic, M., Voglaire, C., & Attia, S. (2023). Climate change sensitive sizing and design for nearly zero-energy office

building systems in Brussels. *Energy and Buildings*, 286, 112971.  
<https://doi.org/10.1016/j.enbuild.2023.112971>

Andreou, E. (2013). Thermal comfort in outdoor spaces and urban canyon microclimate. *Renewable Energy*, 55, 182–188.  
<https://doi.org/10.1016/j.renene.2012.12.040>

Andreou, E. (2014). The effect of urban layout, street geometry and orientation on shading conditions in urban canyons in the Mediterranean. *Renewable Energy*, 63, 587–596. <https://doi.org/10.1016/j.renene.2013.09.051>

*Ansys Fluent Theory Guide 2021R2 [online]*. (2021). Ansys Inc.  
<https://www.ansys.com/>

*ANSYS, Inc., Fluent User's Guide 18.1, ANSYS, Inc., Canonsburg, Pennsylvania, United States, 2017*. (n.d.).

Asfour, O. S. (2020). A comparison between the daylighting and energy performance of courtyard and atrium buildings considering the hot climate of Saudi Arabia. *Journal of Building Engineering*, 30, 101299.  
<https://doi.org/10.1016/j.jobe.2020.101299>

Asfour, O. S., & Gadi, M. B. (2008). Using CFD to investigate ventilation characteristics of vaults as wind-inducing devices in buildings. *Applied Energy*, 85(12), 1126–1140. <https://doi.org/10.1016/j.apenergy.2007.10.015>

*ASHRAE-90.1-2013*. (2013). <https://www.ashrae.org/>

ASTM C67 Standard. (2014). Standard test methods for sampling and testing brick and structural clay tile. *West Conshohocken, PA.: ASTM C67-14*.

Azuma, K., Kagi, N., Yanagi, U., & Osawa, H. (2018). Effects of low-level inhalation exposure to carbon dioxide in indoor environments: A short review on

human health and psychomotor performance. *Environment International*, 121, 51–56.  
<https://doi.org/10.1016/j.envint.2018.08.059>

Baboli, F. B. M., Ibrahim, N., & Sharif, D. M. (2015). Design Characteristics and Adaptive Role of the Traditional Courtyard Houses in the Moderate Climate of Iran. *AcE-Bs 2015 Tehran (6th Asian Conference on Environment-Behaviour Studies)*, Iran University of Science & Technology, Tehran, Iran, 20 - 22 February 2015, 201, 213–223. <https://doi.org/10.1016/j.sbspro.2015.08.170>

Bagasi, A. A., & Calautit, J. K. (2020). Experimental field study of the integration of passive and evaporative cooling techniques with Mashrabiya in hot climates. *Energy and Buildings*, 225, 110325.  
<https://doi.org/10.1016/j.enbuild.2020.110325>

Bartzanas, T., Kittas, C., Sapounas, A. A., & Nikita-Martzopoulou, Ch. (2007). Analysis of airflow through experimental rural buildings: Sensitivity to turbulence models. *Biosystems Engineering*, 97(2), 229–239.  
<https://doi.org/10.1016/j.biosystemseng.2007.02.009>

Bazdidi-Tehrani, F., Masoumi-Verki, S., & Gholamalipour, P. (2020). Impact of opening shape on airflow and pollutant dispersion in a wind-driven cross-ventilated model building: Large eddy simulation. *Sustainable Cities and Society*, 61, 102196.  
<https://doi.org/10.1016/j.scs.2020.102196>

Bensalem, R. (1991). *Wind-driven natural ventilation in courtyard and atrium-type buildings* [PhD thesis, University of Sheffield].  
<https://api.semanticscholar.org/CorpusID:106528234>

Bitog, J. P., Lee, I.-B., Hwang, H.-S., Shin, M.-H., Hong, S.-W., Seo, I.-H., Mostafa, E., & Pang, Z. (2011). A wind tunnel study on aerodynamic porosity and

windbreak drag. *Forest Science and Technology*, 7(1), 8–16.  
<https://doi.org/10.1080/21580103.2011.559939>

Blocken, B. (2015). Computational Fluid Dynamics for urban physics: Importance, scales, possibilities, limitations and ten tips and tricks towards accurate and reliable simulations. *Building and Environment*, 91, 219–245.  
<https://doi.org/10.1016/j.buildenv.2015.02.015>

Blocken, B., Stathopoulos, T., Saathoff, P., & Wang, X. (2008). Numerical evaluation of pollutant dispersion in the built environment: Comparisons between models and experiments. *Journal of Wind Engineering and Industrial Aerodynamics*, 96(10–11), 1817–1831. <https://doi.org/10.1016/j.jweia.2008.02.049>

Brian, E., Magda, S., Mohamad, H., & Peter, L. (2005). *Courtyard Housing: Past, Present and Future (1st ed.)*. Taylor & Francis.  
<https://doi.org/10.4324/9780203646724>

Cantón, M. A., Ganem, C., Barea, G., & Llano, J. F. (2014). Courtyards as a passive strategy in semi dry areas. Assessment of summer energy and thermal conditions in a refurbished school building. *Renewable Energy*, 69, 437–446.  
<https://doi.org/10.1016/j.renene.2014.03.065>

Cao, X., Dai, X., & Liu, J. (2016). Building energy-consumption status worldwide and the state-of-the-art technologies for zero-energy buildings during the past decade. *Energy and Buildings*, 128, 198–213.  
<https://doi.org/10.1016/j.enbuild.2016.06.089>

Carpentieri, M., Hayden, P., & Robins, A. G. (2012). Wind tunnel measurements of pollutant turbulent fluxes in urban intersections. *Atmospheric Environment*, 46, 669–674. <https://doi.org/10.1016/j.atmosenv.2011.09.083>

Castro, I. P., & Robins, A. G. (1977). The flow around a surface-mounted cube in uniform and turbulent streams. *Journal of Fluid Mechanics*, 79(2), 307–335. <https://doi.org/10.1017/S0022112077000172>

Chatzidimitriou, A., & Yannas, S. (2017). Street canyon design and improvement potential for urban open spaces; the influence of canyon aspect ratio and orientation on microclimate and outdoor comfort. *Sustainable Cities and Society*, 33, 85–101. <https://doi.org/10.1016/j.scs.2017.05.019>

Chu, C.-R., & Wu, S.-L. (2018). A transient transport model for gaseous pollutants in naturally-ventilated partitioned buildings. *Building Simulation*, 11(2), 305–313. <https://doi.org/10.1007/s12273-017-0390-z>

Chu, C.-R., & Yang, K.-J. (2022). Transport process of outdoor particulate matter into naturally ventilated buildings. *Building and Environment*, 207, 108424. <https://doi.org/10.1016/j.buildenv.2021.108424>

Cui, P.-Y., Chen, W.-Q., Wang, J.-Q., Zhang, J.-H., Huang, Y.-D., & Tao, W.-Q. (2022). Numerical studies on issues of Re-independence for indoor airflow and pollutant dispersion within an isolated building. *Building Simulation*, 15(7), 1259–1276. <https://doi.org/10.1007/s12273-021-0846-z>

Cui, P.-Y., Li, Z., & Tao, W.-Q. (2014). Investigation of Re -independence of turbulent flow and pollutant dispersion in urban street canyon using numerical wind tunnel (NWT) models. *International Journal of Heat and Mass Transfer*, 79, 176–188. <https://doi.org/10.1016/j.ijheatmasstransfer.2014.07.096>

Cui, P.-Y., Li, Z., & Tao, W.-Q. (2016). Wind-tunnel measurements for thermal effects on the air flow and pollutant dispersion through different scale urban areas. *Building and Environment*, 97, 137–151. <https://doi.org/10.1016/j.buildenv.2015.12.010>



Cui, P.-Y., Zhang, Y., Chen, W.-Q., Zhang, J.-H., Luo, Y., & Huang, Y.-D. (2021). Wind-tunnel studies on the characteristics of indoor/outdoor airflow and pollutant exchange in a building cluster. *Journal of Wind Engineering and Industrial Aerodynamics*, 214, 104645. <https://doi.org/10.1016/j.jweia.2021.104645>

Darvish, A., Eghbali, G., & Eghbali, S. R. (2021). Tree-configuration and species effects on the indoor and outdoor thermal condition and energy performance of courtyard buildings. *Urban Climate*, 37, 100861. <https://doi.org/10.1016/j.uclim.2021.100861>

Ding, S., Huang, Y., Cui, P., Wu, J., Li, M., & Liu, D. (2019). Impact of viaduct on flow reversion and pollutant dispersion in 2D urban street canyon with different roof shapes—Numerical simulation and wind tunnel experiment. *Science of The Total Environment*, 671, 976–991. <https://doi.org/10.1016/j.scitotenv.2019.03.391>

Diz-Mellado, E., López-Cabeza, V. P., Rivera-Gómez, C., & Galán-Marín, C. (2023a). Performance evaluation and users' perception of courtyards role in indoor areas of mediterranean social housing. *Journal of Environmental Management*, 345, 118788. <https://doi.org/10.1016/j.jenvman.2023.118788>

Diz-Mellado, E., López-Cabeza, V. P., Rivera-Gómez, C., & Galán-Marín, C. (2023b). Seasonal analysis of thermal comfort in Mediterranean social courtyards: A comparative study. *Journal of Building Engineering*, 78, 107756. <https://doi.org/10.1016/j.job.2023.107756>

Diz-Mellado, E., Ruiz-Pardo, Á., Rivera-Gómez, C., Sanchez De La Flor, F. J., & Galán-Marín, C. (2023). Unravelling the impact of courtyard geometry on cooling energy consumption in buildings. *Building and Environment*, 237, 110349. <https://doi.org/10.1016/j.buildenv.2023.110349>

Esfeh, M. K., Sohankar, A., Shahsavari, A. R., Rastan, M. R., Ghodrat, M., & Nili, M. (2021). Experimental and numerical evaluation of wind-driven natural ventilation of a curved roof for various wind angles. *Building and Environment*, 205, 108275. <https://doi.org/10.1016/j.buildenv.2021.108275>

Forouzandeh, A. (2018). Numerical modeling validation for the microclimate thermal condition of semi-closed courtyard spaces between buildings. *Sustainable Cities and Society*, 36, 327–345. <https://doi.org/10.1016/j.scs.2017.07.025>

Forouzandeh, A., & Richter, T. (2019). Accurate prediction of heating energy demand of courtyard's surrounding envelopes using temperature correction factor. *Energy and Buildings*, 193, 49–68.

Franke, J., & A. Hellsten, K. Schlünzen, B. Carissimo. (2007). *Model evaluation guidance and protocol document: COST action 732 Quality assurance and improvement of microscale meteorological models*. Univ. of Hamburg, Meteorological Inst.

Gao, Y., Yao, R., Li, B., Turkbeyler, E., Luo, Q., & Short, A. (2012). Field studies on the effect of built forms on urban wind environments. *Renewable Energy*, 46, 148–154. <https://doi.org/10.1016/j.renene.2012.03.005>

Gough, H. L., Barlow, J. F., Luo, Z., King, M.-F., Halios, C. H., & Grimmond, C. S. B. (2020). Evaluating single-sided natural ventilation models against full-scale idealised measurements: Impact of wind direction and turbulence. *Building and Environment*, 170, 106556. <https://doi.org/10.1016/j.buildenv.2019.106556>

Graham, L. A., Noseworthy, L., Fugler, D., O'Leary, K., Karman, D., & Grande, C. (2004). Contribution of vehicle emissions from an attached garage to residential indoor air pollution levels. *Journal of the Air & Waste Management Association*, 54(5), 563–584.

Gromke, C., Blocken, B., Janssen, W., Merema, B., Van Hooff, T., & Timmermans, H. (2015). CFD analysis of transpirational cooling by vegetation: Case study for specific meteorological conditions during a heat wave in Arnhem, Netherlands. *Building and Environment*, 83, 11–26. <https://doi.org/10.1016/j.buildenv.2014.04.022>

Gromke, C., & Ruck, B. (2012). Pollutant Concentrations in Street Canyons of Different Aspect Ratio with Avenues of Trees for Various Wind Directions. *Boundary-Layer Meteorology*, 144(1), 41–64. <https://doi.org/10.1007/s10546-012-9703-z>

Gross, G. (2012). Effects of different vegetation on temperature in an urban building environment. Micro-scale numerical experiments. *Meteorologische Zeitschrift*, 21(4), 399–412. <https://doi.org/10.1127/0941-2948/2012/0363>

Gunasagaran, S., Shiowee, B. T., Mari, T., Srirangam, S., & Ng, V. F. P. (2022). Revisiting the courtyard as lived heritage and social space. *Journal of Engineering Science and Technology*, 17, 74–89.

Guo, D.-P., Zhao, P., Yao, R.-T., Li, Y.-P., Hu, J.-M., & Fan, D. (2019). Numerical and Wind Tunnel Simulation Studies of the Flow Field and Pollutant Diffusion around a Building under Neutral and Stable Atmospheric Stratifications. *Journal of Applied Meteorology and Climatology*, 58(11), 2405–2420. <https://doi.org/10.1175/JAMC-D-19-0045.1>

Guo, Yang, F., Shi, X., Li, Y., & Yao, R. (2021). Numerical simulation and wind tunnel experiments on the effect of a cubic building on the flow and pollutant diffusion under stable stratification. *Building and Environment*, 205, 108222. <https://doi.org/10.1016/j.buildenv.2021.108222>

Hall, D. J., Walker, S., & Spanton, A. M. (1999a). Dispersion from courtyards and other enclosed spaces. *Atmospheric Environment*, 33(8), 1187–1203. [https://doi.org/10.1016/S1352-2310\(98\)00284-2](https://doi.org/10.1016/S1352-2310(98)00284-2)

Hall, D. J., Walker, S., & Spanton, A. M. (1999b). Dispersion from courtyards and other enclosed spaces. *Atmospheric Environment*, 33(8), 1187–1203. [https://doi.org/10.1016/S1352-2310\(98\)00284-2](https://doi.org/10.1016/S1352-2310(98)00284-2)

Hamdy, M., Carlucci, S., Hoes, P.-J., & Hensen, J. L. M. (2017). The impact of climate change on the overheating risk in dwellings—A Dutch case study. *Building and Environment*, 122, 307–323. <https://doi.org/10.1016/j.buildenv.2017.06.031>

He, X., Gao, W., & Wang, R. (2021). Impact of urban morphology on the microclimate around elementary schools: A case study from Japan. *Building and Environment*, 206, 108383. <https://doi.org/10.1016/j.buildenv.2021.108383>

Huang, Y., Zeng, N., Liu, Z., Song, Y., & Xu, X. (2016). Wind tunnel simulation of pollutant dispersion inside street canyons with galleries and multi-level flat roofs. *Journal of Hydrodynamics*, 28(5), 801–810. [https://doi.org/10.1016/S1001-6058\(16\)60683-2](https://doi.org/10.1016/S1001-6058(16)60683-2)

Hunter, L. J., Johnson, G. T., & Watson, I. D. (1992). An investigation of three-dimensional characteristics of flow regimes within the urban canyon. *Atmospheric Environment. Part B. Urban Atmosphere*, 26(4), 425–432. [https://doi.org/10.1016/0957-1272\(92\)90049-X](https://doi.org/10.1016/0957-1272(92)90049-X)

Hunter, L. J., Watson, I. D., & Johnson, G. T. (1990). Modelling air flow regimes in urban canyons. *Energy and Buildings*, 15(3–4), 315–324. [https://doi.org/10.1016/0378-7788\(90\)90004-3](https://doi.org/10.1016/0378-7788(90)90004-3)

IPCC Core Writing Team. (2023). *IPCC, 2023: Climate Change 2023: Synthesis Report: Summary for Policymakers* (First). Intergovernmental Panel on Climate Change (IPCC). <https://doi.org/10.59327/IPCC/AR6-9789291691647>

Isaac, M., & van Vuuren, D. P. (2009). Modeling global residential sector energy demand for heating and air conditioning in the context of climate change. *Energy Policy*, *37*(2), 507–521. <https://doi.org/10.1016/j.enpol.2008.09.051>

Jamei, E., Rajagopalan, P., Seyedmahmoudian, M., & Jamei, Y. (2016). Review on the impact of urban geometry and pedestrian level greening on outdoor thermal comfort. *Renewable and Sustainable Energy Reviews*, *54*, 1002–1017. <https://doi.org/10.1016/j.rser.2015.10.104>

Jiao, M., Zhou, W., Zheng, Z., Wang, J., & Qian, Y. (2017). Patch size of trees affects its cooling effectiveness: A perspective from shading and transpiration processes. *Agricultural and Forest Meteorology*, *247*, 293–299. <https://doi.org/10.1016/j.agrformet.2017.08.013>

Jon, K. S., Huang, Y., Sin, C. H., Cui, P., & Luo, Y. (2022). Influence of wind direction on the ventilation and pollutant dispersion in different 3D street canyon configurations: Numerical simulation and wind-tunnel experiment. *Environmental Science and Pollution Research*, *30*(11), 31647–31675. <https://doi.org/10.1007/s11356-022-24212-0>

Katayama, T., Hayashi, T., Shiotsuki, Y., Kitayama, H., Ishii, A., Nishida, M., Tsutsumi, J.-I., & Oguro, M. (1991). Cooling effects of a river and sea breeze on the thermal environment in a built-up area. *Energy and Buildings*, *16*(3–4), 973–978. [https://doi.org/10.1016/0378-7788\(91\)90092-H](https://doi.org/10.1016/0378-7788(91)90092-H)

Koutsourakis, N., Bartzis, J. G., & Markatos, N. C. (2012). Evaluation of Reynolds stress, k- $\epsilon$  and RNG k- $\epsilon$  turbulence models in street canyon flows using

various experimental datasets. *Environmental Fluid Mechanics*, 12(4), 379–403.  
<https://doi.org/10.1007/s10652-012-9240-9>

Lateb, M., Masson, C., Stathopoulos, T., & Bédard, C. (2010). Numerical simulation of pollutant dispersion around a building complex. *Building and Environment*, 45(8), 1788–1798. <https://doi.org/10.1016/j.buildenv.2010.02.006>

Launder, B. E., & Spalding, D. B. (1974). The numerical computation of turbulent flows. *Computer Methods in Applied Mechanics and Engineering*, 3(2), 269–289. [https://doi.org/10.1016/0045-7825\(74\)90029-2](https://doi.org/10.1016/0045-7825(74)90029-2)

Leng, J., Wang, Q., & Liu, K. (2020). Sustainable design of courtyard environment: From the perspectives of airborne diseases control and human health. *Sustainable Cities and Society*, 62, 102405. <https://doi.org/10.1016/j.scs.2020.102405>

Li, M., Jin, Y., & Guo, J. (2022). Dynamic characteristics and adaptive design methods of enclosed courtyard: A case study of a single-story courtyard dwelling in China. *Building and Environment*, 223, 109445. <https://doi.org/10.1016/j.buildenv.2022.109445>

Li, W.-W., & Meroney, R. N. (1983). Gas dispersion near a cubical model building. Part I. Mean concentration measurements. *Journal of Wind Engineering and Industrial Aerodynamics*, 12(1), 15–33. [https://doi.org/10.1016/0167-6105\(83\)90078-8](https://doi.org/10.1016/0167-6105(83)90078-8)

Li, Y., & Stathopoulos, T. (1998). Computational evaluation of pollutant dispersion around buildings: Estimation of numerical errors. *Journal of Wind Engineering and Industrial Aerodynamics*, 77–78, 619–630. [https://doi.org/10.1016/S0167-6105\(98\)00177-9](https://doi.org/10.1016/S0167-6105(98)00177-9)

Liu, X. P., Niu, J. L., Kwok, K. C. S., Wang, J. H., & Li, B. Z. (2010). Investigation of indoor air pollutant dispersion and cross-contamination around a

typical high-rise residential building: Wind tunnel tests. *Building and Environment*, 45(8), 1769–1778. <https://doi.org/10.1016/j.buildenv.2010.02.003>

López-Cabeza, V. P., Rivera-Gómez, C., Roa-Fernández, J., Hernandez-Valencia, M., & Herrera-Limones, R. (2023). Effect of thermal inertia and natural ventilation on user comfort in courtyards under warm summer conditions. *Building and Environment*, 228, 109812. <https://doi.org/10.1016/j.buildenv.2022.109812>

Lozhkin, V., Lozhkina, O., & Dobromirov, V. (2018). A study of air pollution by exhaust gases from cars in well courtyards of Saint Petersburg. *Transportation Research Procedia*, 36, 453–458. <https://doi.org/10.1016/j.trpro.2018.12.124>

Ma, H., Zhou, X., Tominaga, Y., & Gu, M. (2022). CFD simulation of flow fields and pollutant dispersion around a cubic building considering the effect of plume buoyancies. *Building and Environment*, 208, 108640. <https://doi.org/10.1016/j.buildenv.2021.108640>

Mahdavinejad, M., & Javanroodi, K. (2016). Impact of roof shape on air pressure, wind flow and indoor temperature of residential buildings. *International Journal of Sustainable Building Technology and Urban Development*, 7(2), 87–103. <https://doi.org/10.1080/2093761X.2016.1167645>

Manickathan, L., Defraeye, T., Allegrini, J., Derome, D., & Carmeliet, J. (2018a). Parametric study of the influence of environmental factors and tree properties on the transpirative cooling effect of trees. *Agricultural and Forest Meteorology*, 248, 259–274. <https://doi.org/10.1016/j.agrformet.2017.10.014>

Manickathan, L., Defraeye, T., Allegrini, J., Derome, D., & Carmeliet, J. (2018b). Parametric study of the influence of environmental factors and tree properties on the transpirative cooling effect of trees. *Agricultural and Forest Meteorology*, 248, 259–274. <https://doi.org/10.1016/j.agrformet.2017.10.014>

Manioğlu, G., & Oral, G. K. (2015). Effect of courtyard shape factor on heating and cooling energy loads in hot-dry climatic zone. *Energy Procedia*, 78, 2100–2105.

Martinelli, L., & Matzarakis, A. (2017). Influence of height/width proportions on the thermal comfort of courtyard typology for Italian climate zones. *Sustainable Cities and Society*, 29, 97–106. <https://doi.org/10.1016/j.scs.2016.12.004>

Martins, T. A. de L., Adolphe, L., Bastos, L. E. G., & Martins, M. A. de L. (2016). Sensitivity analysis of urban morphology factors regarding solar energy potential of buildings in a Brazilian tropical context. *Solar Energy*, 137, 11–24. <https://doi.org/10.1016/j.solener.2016.07.053>

Meir, I. A., Pearlmutter, D., & Etzion, Y. (1995). On the microclimatic behavior of two semi-enclosed attached courtyards in a hot dry region. *Building and Environment*, 30(4), 563–572. [https://doi.org/10.1016/0360-1323\(95\)00018-2](https://doi.org/10.1016/0360-1323(95)00018-2)

Meng, H., Jiao, W., Hong, J., & Anna, L. (2016). Analysis on Wind Environment in Winter of Different Rural Courtyard Layout in the Northeast. *The 8th International Cold Climate HVAC Conference*, 146, 343–349. <https://doi.org/10.1016/j.proeng.2016.06.408>

Menter, F. R. (1994). Two-equation eddy-viscosity turbulence models for engineering applications. *AIAA Journal*, 32(8), 1598–1605. <https://doi.org/10.2514/3.12149>

Menter, F. R. (2009). Review of the shear-stress transport turbulence model experience from an industrial perspective. *International Journal of Computational Fluid Dynamics*, 23(4), 305–316. <https://doi.org/10.1080/10618560902773387>

Mercker, E. (1986). A blockage correction for automotive testing in a wind tunnel with closed test section. *Journal of Wind Engineering and Industrial Aerodynamics*, 22(2–3), 149–167. [https://doi.org/10.1016/0167-6105\(86\)90080-2](https://doi.org/10.1016/0167-6105(86)90080-2)



Moey, L. K., Kong, M. F., Tai, V. C., Go, T. F., & Adam, N. M. (2021). Effects of roof configuration on natural ventilation for an isolated building. *Journal of Mechanical Engineering and Sciences*, 15(3), 8379–8389. <https://doi.org/10.15282/jmes.15.3.2021.15.0659>

Moghimi, S., Azizpour, F., Mat, S., Lim, C. H., Salleh, E., & Sopian, K. (2014). Building energy index and end-use energy analysis in large-scale hospitals—Case study in Malaysia. *Energy Efficiency*, 7(2), 243–256. <https://doi.org/10.1007/s12053-013-9221-y>

Mohammadi, M., & Calautit, J. (2021). Impact of Ventilation Strategy on the Transmission of Outdoor Pollutants into Indoor Environment Using CFD. *Sustainability*, 13(18), 10343. <https://doi.org/10.3390/su131810343>

Mohammadi, M., Tien, P. W., & Kaiser Calautit, J. (2020). Influence of Wind Buffers on the Aero-Thermal Performance of Skygardens. *Fluids*, 5(3), 160. <https://doi.org/10.3390/fluids5030160>

Montazeri, H., Blocken, B., & Hensen, J. L. M. (2015a). CFD analysis of the impact of physical parameters on evaporative cooling by a mist spray system. *Applied Thermal Engineering*, 75, 608–622. <https://doi.org/10.1016/j.applthermaleng.2014.09.078>

Montazeri, H., Blocken, B., & Hensen, J. L. M. (2015b). Evaporative cooling by water spray systems: CFD simulation, experimental validation and sensitivity analysis. *Building and Environment*, 83, 129–141. <https://doi.org/10.1016/j.buildenv.2014.03.022>

Montazeri, H., Toparlak, Y., Blocken, B., & Hensen, J. L. M. (2017). Simulating the cooling effects of water spray systems in urban landscapes: A computational fluid

dynamics study in Rotterdam, The Netherlands. *Landscape and Urban Planning*, 159, 85–100. <https://doi.org/10.1016/j.landurbplan.2016.10.001>

Moonen, P., Dorer, V., & Carmeliet, J. (2011). Evaluation of the ventilation potential of courtyards and urban street canyons using RANS and LES. *Journal of Wind Engineering and Industrial Aerodynamics*, 99(4), 414–423. <https://doi.org/10.1016/j.jweia.2010.12.012>

Mughal, M. O., Kubilay, A., Fatichi, S., Meili, N., Carmeliet, J., Edwards, P., & Burlando, P. (2021). Detailed investigation of vegetation effects on microclimate by means of computational fluid dynamics (CFD) in a tropical urban environment. *Urban Climate*, 39, 100939. <https://doi.org/10.1016/j.uclim.2021.100939>

Muhaisen, A. S. (2006). Shading simulation of the courtyard form in different climatic regions. *Building and Environment*, 41(12), 1731–1741. <https://doi.org/10.1016/j.buildenv.2005.07.016>

Noordin, M. A. M. J., Nasir, N. C. M., Nasir, R. M., & Mustapa, D. (2021). New added values to the existing Chinese heritage shop-houses' courtyards towards occupant environment wellness: A case study at Kota Bharu, Kelantan, Malaysia. *IOP Conference Series: Earth and Environmental Science*, 738(1), 012055. <https://doi.org/10.1088/1755-1315/738/1/012055>

Nosek, Š., Kluková, Z., Jakubcová, M., & Jaňour, Z. (2022). The effect of courtyard buildings on the ventilation of street canyons: A wind-tunnel study. *Journal of Wind Engineering and Industrial Aerodynamics*, 220, 104885. <https://doi.org/10.1016/j.jweia.2021.104885>

Nottingham, England, United Kingdom Weather Conditions, *WeatherUnderground*. (n.d.). Retrieved 1 September 2021, from <https://www.wunderground.com/history/monthly/gb/derby/EGNX/date/2021-7>

Oke, T. R. (1988). Street design and urban canopy layer climate. *Energy and Buildings*, 11(1), 103–113. [https://doi.org/10.1016/0378-7788\(88\)90026-6](https://doi.org/10.1016/0378-7788(88)90026-6)

Perén, J. I., Van Hooff, T., Leite, B. C. C., & Blocken, B. (2015). CFD analysis of cross-ventilation of a generic isolated building with asymmetric opening positions: Impact of roof angle and opening location. *Building and Environment*, 85, 263–276. <https://doi.org/10.1016/j.buildenv.2014.12.007>

Peren, J. I., Van Hooff, T., Ramponi, R., Blocken, B., & Leite, B. C. C. (2015). Impact of roof geometry of an isolated leeward sawtooth roof building on cross-ventilation: Straight, concave, hybrid or convex? *Journal of Wind Engineering and Industrial Aerodynamics*, 145, 102–114. <https://doi.org/10.1016/j.jweia.2015.05.014>

Prakash, D. (2022). Ventilation performance analysis on low-rise courtyard building for various courtyard shape factors and roof topology. *International Journal of Ventilation*. <https://doi.org/10.1080/14733315.2022.2036477>

Prakash, D. (2023). Ventilation performance analysis on low-rise courtyard building for various courtyard shape factors and roof topology. *International Journal of Ventilation*, 22(1), 56–76. <https://doi.org/10.1080/14733315.2022.2036477>

Rahman, M. A., Smith, J. G., Stringer, P., & Ennos, A. R. (2011). Effect of rooting conditions on the growth and cooling ability of *Pyrus calleryana*. *Urban Forestry & Urban Greening*, 10(3), 185–192. <https://doi.org/10.1016/j.ufug.2011.05.003>

Rajapaksha, I., Nagai, H., & Okumiya, M. (2003). A ventilated courtyard as a passive cooling strategy in the warm humid tropics. *Renewable Energy*, 28(11), 1755–1778. [https://doi.org/10.1016/S0960-1481\(03\)00012-0](https://doi.org/10.1016/S0960-1481(03)00012-0)

Rapoport, A. (2007). The Nature of the Courtyard House: A Conceptual Analysis. *Traditional Dwellings and Settlements Review*, 18(2), 57–72.

Ratti, C., Raydan, D., & Steemers, K. (2003). Building form and environmental performance: Archetypes, analysis and an arid climate. *Special Issue on Urban Research*, 35(1), 49–59. [https://doi.org/10.1016/S0378-7788\(02\)00079-8](https://doi.org/10.1016/S0378-7788(02)00079-8)

Richards, P. J., & Norris, S. E. (2015). Appropriate boundary conditions for a pressure driven boundary layer. *Journal of Wind Engineering and Industrial Aerodynamics*, 142, 43–52. <https://doi.org/10.1016/j.jweia.2015.03.003>

Roache, P. J. (1994). Perspective: A Method for Uniform Reporting of Grid Refinement Studies. *Journal of Fluids Engineering-Transactions of The Asme*, 116, 405–413.

Rodríguez-Algeciras, J., Tablada, A., Chaos-Yeras, M., De La Paz, G., & Matzarakis, A. (2018). Influence of aspect ratio and orientation on large courtyard thermal conditions in the historical centre of Camagüey-Cuba. *Renewable Energy*, 125, 840–856. <https://doi.org/10.1016/j.renene.2018.01.082>

Rojas, J. M., Galán-Marín, C., & Fernández-Nieto, E. D. (2012). Parametric Study of Thermodynamics in the Mediterranean Courtyard as a Tool for the Design of Eco-Efficient Buildings. *Energies*, 5(7), 2381–2403. <https://doi.org/10.3390/en5072381>

Saadatjoo, P., Badamchizadeh, P., & Mahdavinejad, M. (2023). Towards the new generation of courtyard buildings as a healthy living concept for post-pandemic era. *Sustainable Cities and Society*, 97, 104726. <https://doi.org/10.1016/j.scs.2023.104726>

Sahebzadeh, S., Dalvand, Z., Sadeghfar, M., & Heidari, A. (2018). Vernacular architecture of Iran's hot regions; elements and strategies for a comfortable living environment. *Smart and Sustainable Built Environment*, 9(4), 573–593. <https://doi.org/10.1108/SASBE-11-2017-0065>

Salameh, M., & Taleb, H. (2017, April). *Courtyard as Passive Design Solution for School Buildings in Hot Area*. The 2nd World Congress on Civil, Structural, and Environmental Engineering. <https://doi.org/10.11159/awspt17.141>

Salata, F., Golasi, I., Vollaro, A. de L., & Vollaro, R. de L. (2015). How high albedo and traditional buildings' materials and vegetation affect the quality of urban microclimate. A case study. *Energy and Buildings*, 99, 32–49. <https://doi.org/10.1016/j.enbuild.2015.04.010>

Santamouris, M. (2016). Innovating to zero the building sector in Europe: Minimising the energy consumption, eradication of the energy poverty and mitigating the local climate change. *Solar Energy*, 128, 61–94. <https://doi.org/10.1016/j.solener.2016.01.021>

Santiago, J. L., Rivas, E., Buccolieri, R., Martilli, A., Vivanco, M. G., Borge, R., Carlo, O. S., & Martín, F. (2022). Indoor-outdoor pollutant concentration modelling: A comprehensive urban air quality and exposure assessment. *Air Quality, Atmosphere & Health*, 15(9), 1583–1608. <https://doi.org/10.1007/s11869-022-01204-0>

*Seville, Spain Weather History, Weather Underground*. (n.d.). Retrieved 7 August 2023, from <https://www.wunderground.com/history/daily/es/seville/LEZL/date/2023-7-17>

Sharples, S., & Bensalem, R. (2001). Airflow in courtyard and atrium buildings in the urban environment: A wind tunnel study. *Solar Energy*, 70(3), 237–244. [https://doi.org/10.1016/S0038-092X\(00\)00092-X](https://doi.org/10.1016/S0038-092X(00)00092-X)

Shashua-Bar, L., Pearlmutter, D., & Erell, E. (2009). The cooling efficiency of urban landscape strategies in a hot dry climate. *Landscape and Urban Planning*, 92(3–4), 179–186. <https://doi.org/10.1016/j.landurbplan.2009.04.005>

Shih, T.-H., Liou, W. W., Shabbir, A., Yang, Z., & Zhu, J. (1995). A new  $k-\epsilon$  eddy viscosity model for high reynolds number turbulent flows. *Computers & Fluids*, 24(3), 227–238. [https://doi.org/10.1016/0045-7930\(94\)00032-T](https://doi.org/10.1016/0045-7930(94)00032-T)

Sonnenwald, F., Stovin, V., & Guymer, I. (2016). Feasibility of the Porous Zone Approach to Modelling Vegetation in CFD. In P. Rowiński & A. Marion (Eds.), *Hydrodynamic and {Mass} {Transport} at {Freshwater} {Aquatic} {Interfaces}* (pp. 63–75). Springer International Publishing. [https://doi.org/10.1007/978-3-319-27750-9\\_6](https://doi.org/10.1007/978-3-319-27750-9_6)

Spalding, D. B. (1971). Concentration fluctuations in a round turbulent free jet. *Chemical Engineering Science*, 26(1), 95–107. [https://doi.org/10.1016/0009-2509\(71\)86083-9](https://doi.org/10.1016/0009-2509(71)86083-9)

Subhashini, S., & Thirumaran, K. (2020). CFD simulations for examining natural ventilation in the learning spaces of an educational building with courtyards in Madurai. *Building Services Engineering Research and Technology*, 41(4), 466–479. <https://doi.org/10.1177/0143624419878798>

Sun, H., Calautit, J. K., & Jimenez-Bescos, C. (2022). Examining the regulating impact of thermal mass on overheating, and the role of night ventilation, within different climates and future scenarios across China. *Cleaner Engineering and Technology*, 9, 100534. <https://doi.org/10.1016/j.clet.2022.100534>

Sun, H., Jimenez-Bescos, C., Mohammadi, M., Zhong, F., & Calautit, J. K. (2021). Numerical investigation of the influence of vegetation on the aero-thermal performance of buildings with courtyards in hot climates. *Energies*, 14(17), 5388. <https://doi.org/10.3390/en14175388>

Sureshkumar, R., Kale, S. R., & Dhar, P. L. (2008). Heat and mass transfer processes between a water spray and ambient air – I. Experimental data. *Applied*

<https://doi.org/10.1016/j.applthermaleng.2007.09.010>

Tablada, A., Blocken, B., Carmeliet, J., De Troyer, F., & Verschure, H. (2005). The influence of courtyard geometry on air flow and thermal comfort: CFD and thermal comfort simulations. *Proceedings of 22nd Conference on Passive and Low Energy Architecture, 1*, 75–80.

Takano, Y., & Moonen, P. (2013). On the influence of roof shape on flow and dispersion in an urban street canyon. *Journal of Wind Engineering and Industrial Aerodynamics*, 123, 107–120. <https://doi.org/10.1016/j.jweia.2013.10.006>

Taleghani, M., Kleerekoper, L., Tenpierik, M., & van den Dobbelen, A. (2015). Outdoor thermal comfort within five different urban forms in the Netherlands. *Special Issue: Climate Adaptation in Cities*, 83, 65–78. <https://doi.org/10.1016/j.buildenv.2014.03.014>

Taleghani, M., Tenpierik, M., & van den Dobbelen, A. (2012). Environmental impact of courtyards—A review and comparison of residential courtyard buildings in different climates. *Journal of Green Building*, 7(2), 113–136.

Taleghani, M., Tenpierik, M., & van den Dobbelen, A. (2014). Indoor thermal comfort in urban courtyard block dwellings in the Netherlands. *Building and Environment*, 82, 566–579. <https://doi.org/10.1016/j.buildenv.2014.09.028>

Teshnehdel, S., Mirnezami, S., Saber, A., Pourzangbar, A., & Olabi, A. G. (2020). Data-driven and numerical approaches to predict thermal comfort in traditional courtyards. *Sustainable Energy Technologies and Assessments*, 37, 100569. <https://doi.org/10.1016/j.seta.2019.100569>

Tominaga, Y., & Blocken, B. (2016). Wind tunnel analysis of flow and dispersion in cross-ventilated isolated buildings: Impact of opening positions. *Journal*

*of Wind Engineering and Industrial Aerodynamics*, 155, 74–88.  
<https://doi.org/10.1016/j.jweia.2016.05.007>

Tominaga, Y., Mochida, A., Yoshie, R., Kataoka, H., Nozu, T., Yoshikawa, M., & Shirasawa, T. (2008). AIJ guidelines for practical applications of CFD to pedestrian wind environment around buildings. *Journal of Wind Engineering and Industrial Aerodynamics*, 96(10–11), 1749–1761. <https://doi.org/10.1016/j.jweia.2008.02.058>

Tominaga, Y., Murakami, S., & Mochida, A. (1997). CFD prediction of gaseous diffusion around a cubic model using a dynamic mixed SGS model based on composite grid technique. *Journal of Wind Engineering and Industrial Aerodynamics*, 67–68, 827–841. [https://doi.org/10.1016/S0167-6105\(97\)00122-0](https://doi.org/10.1016/S0167-6105(97)00122-0)

Tominaga, Y., & Stathopoulos, T. (2007). Turbulent Schmidt numbers for CFD analysis with various types of flowfield. *Atmospheric Environment*, 41(37), 8091–8099. <https://doi.org/10.1016/j.atmosenv.2007.06.054>

Tominaga, Y., & Stathopoulos, T. (2009). Numerical simulation of dispersion around an isolated cubic building: Comparison of various types of k- $\epsilon$  models. *Atmospheric Environment*, 43(20), 3200–3210. <https://doi.org/10.1016/j.atmosenv.2009.03.038>

Tominaga, Y., & Stathopoulos, T. (2010). Numerical simulation of dispersion around an isolated cubic building: Model evaluation of RANS and LES. *Building and Environment*, 45(10), 2231–2239. <https://doi.org/10.1016/j.buildenv.2010.04.004>

Tominaga, Y., & Stathopoulos, T. (2011). CFD modeling of pollution dispersion in a street canyon: Comparison between LES and RANS. *Journal of Wind Engineering and Industrial Aerodynamics*, 99(4), 340–348. <https://doi.org/10.1016/j.jweia.2010.12.005>



Tominaga, Y., & Stathopoulos, T. (2013). CFD simulation of near-field pollutant dispersion in the urban environment: A review of current modeling techniques. *Atmospheric Environment*, *79*, 716–730. <https://doi.org/10.1016/j.atmosenv.2013.07.028>

Tominaga, Y., & Stathopoulos, T. (2017). Steady and unsteady RANS simulations of pollutant dispersion around isolated cubical buildings: Effect of large-scale fluctuations on the concentration field. *Journal of Wind Engineering and Industrial Aerodynamics*, *165*, 23–33. <https://doi.org/10.1016/j.jweia.2017.02.001>

Tominaga, Y., & Stathopoulos, T. (2018). CFD simulations of near-field pollutant dispersion with different plume buoyancies. *Building and Environment*, *131*, 128–139. <https://doi.org/10.1016/j.buildenv.2018.01.008>

Trindade Da Silva, F., Reis, N. C., Santos, J. M., Goulart, E. V., & Engel De Alvarez, C. (2021). The impact of urban block typology on pollutant dispersion. *Journal of Wind Engineering and Industrial Aerodynamics*, *210*, 104524. <https://doi.org/10.1016/j.jweia.2021.104524>

Van Hooff, T., & Blocken, B. (2013). CFD evaluation of natural ventilation of indoor environments by the concentration decay method: CO<sub>2</sub> gas dispersion from a semi-enclosed stadium. *Building and Environment*, *61*, 1–17. <https://doi.org/10.1016/j.buildenv.2012.11.021>

Van Hooff, T., Blocken, B., & Tominaga, Y. (2017). Investigation of indoor air pollutant dispersion and cross-contamination around a typical high-rise residential building: Wind tunnel tests. *Building and Environment*, *114*, 148–165. <https://doi.org/10.1016/j.buildenv.2016.12.019>

Vesilind, P. A. (1980). The Rosin-Rammler particle size distribution. *Resource Recovery and Conservation*, 5(3), 275–277. [https://doi.org/10.1016/0304-3967\(80\)90007-4](https://doi.org/10.1016/0304-3967(80)90007-4)

Wang, J., Huo, Q., Zhang, T., Wang, S., & Battaglia, F. (2020). Numerical investigation of gaseous pollutant cross-transmission for single-sided natural ventilation driven by buoyancy and wind. *Building and Environment*, 172, 106705. <https://doi.org/10.1016/j.buildenv.2020.106705>

Wang, X., & McNamara, K. F. (2006). Evaluation of CFD Simulation using RANS Turbulence Models for Building Effects on Pollutant Dispersion. *Environmental Fluid Mechanics*, 6(2), 181–202. <https://doi.org/10.1007/s10652-005-5656-9>

Wilcox, D. C. (2008). Formulation of the k-w Turbulence Model Revisited. *AIAA Journal*, 46(11), 2823–2838. <https://doi.org/10.2514/1.36541>

Xie, H., & Zhang, T. (2023). Impact of roof shape on indoor gaseous pollutant level for natural ventilation buildings in a street canyon: Numerical simulation. *Journal of Air Pollution and Health*. <https://doi.org/10.18502/japh.v8i3.13789>

Xiong, Y., Zhang, J., Yan, Y., Sun, S., Xu, X., & Higuera, E. (2022). Effect of the spatial form of Jiangnan traditional villages on microclimate and human comfort. *Sustainable Cities and Society*, 87, 104136. <https://doi.org/10.1016/j.scs.2022.104136>

Yakhot, V., Orszag, S. A., Thangam, S., Gatski, T. B., & Speziale, C. (1992). Development of turbulence models for shear flows by a double expansion technique. *Physics of Fluids A: Fluid Dynamics*, 4(7), 1510–1520.

Yakubu, P. W., & Alibaba, H. Z. (2018). *Performance of Courtyard Systems of Housing in Hot and Humid Climate (Bauchi, Nigeria)*. 6(2), 13.

Yang, F., Kang, Y., Gao, Y., & Zhong, K. (2015). Numerical simulations of the effect of outdoor pollutants on indoor air quality of buildings next to a street canyon. *Building and Environment*, 87, 10–22. <https://doi.org/10.1016/j.buildenv.2015.01.008>

Yang, L., Liu, X., Qian, F., & Niu, S. (2020). Research on the wind environment and air quality of parallel courtyards in a university campus. *Sustainable Cities and Society*, 56, 102019. <https://doi.org/10.1016/j.scs.2020.102019>

Yang, L., Ye, M., & He, B.-J. (2014). CFD simulation research on residential indoor air quality. *Science of The Total Environment*, 472, 1137–1144. <https://doi.org/10.1016/j.scitotenv.2013.11.118>

Yang, Li, Y., & Yang, L. (2012). Predicting and understanding temporal 3D exterior surface temperature distribution in an ideal courtyard. *Building and Environment*, 57, 38–48. <https://doi.org/10.1016/j.buildenv.2012.03.022>

Yaşar, E., & Ok, V. (2014). Evaluation of the effects of courtyard building shapes on solar heat gains and energy efficiency according to different climatic regions. *Energy and Buildings*, 73, 192–199. <https://doi.org/10.1016/j.enbuild.2013.12.042>

Yassin, M. F. (2011). Impact of height and shape of building roof on air quality in urban street canyons. *Atmospheric Environment*, 45(29), 5220–5229. <https://doi.org/10.1016/j.atmosenv.2011.05.060>

Yassin, M. F., Al-Rashidi, M., & Ohba, M. (2022). Experimental and numerical simulations of air quality in an urban canopy: Effects of roof shapes and atmospheric stability. *Atmospheric Pollution Research*, 13(12), 101618. <https://doi.org/10.1016/j.apr.2022.101618>

Yılmaz, Z. (2007). Evaluation of energy efficient design strategies for different climatic zones: Comparison of thermal performance of buildings in temperate-humid

and hot-dry climate. *Energy and Buildings*, 39(3), 306–316.  
<https://doi.org/10.1016/j.enbuild.2006.08.004>

You, J., Wang, M., Li, J., Xu, S., Cao, C., & Shao, S. (2022). Influence of cooking pollutant diffusion regularity by high-rise residential inner-courtyard forms in Wuhan. *Buildings*, 12(9), 1452. <https://doi.org/10.3390/buildings12091452>

Yu, C.-R., Guo, H.-S., Wang, Q.-C., & Chang, R.-D. (2020). Revealing the Impacts of Passive Cooling Techniques on Building Energy Performance: A Residential Case in Hong Kong. *Applied Sciences*, 10(12), 4188. <https://doi.org/10.3390/app10124188>

Zakaria, M. A., Kubota, T., & Toe, D. H. C. (2015). The Effects of Courtyards on Indoor Thermal Conditions of Chinese Shophouse in Malacca. *The 9th International Symposium on Heating, Ventilation and Air Conditioning (ISHVAC) Joint with the 3rd International Conference on Building Energy and Environment (COBEE), 12-15 July 2015, Tianjin, China*, 121, 468–476. <https://doi.org/10.1016/j.proeng.2015.08.1094>

Zamani, Z., Heidari, S., & Hanachi, P. (2018). Reviewing the thermal and microclimatic function of courtyards. *Renewable and Sustainable Energy Reviews*, 93, 580–595. <https://doi.org/10.1016/j.rser.2018.05.055>

Zango, M. S., Ossen, D. R., Toe, D. H. C., Nimlyat, P. S., & Luke, B. J. (2017). The Effect of Vegetation in Enhancing the Performance of Courtyard in Buildings of Tropical Climate. *Journal of Applied Sciences*, 10.

Zhang, W., Wang, L., Ji, Z., Ma, L., & Hui, Y. (2015). Test on ventilation rates of dormitories and offices in university by the CO<sub>2</sub> tracer gas method. *The 9th International Symposium on Heating, Ventilation and Air Conditioning (ISHVAC) Joint with the 3rd International Conference on Building Energy and Environment*

(COBEE), 12-15 July 2015, Tianjin, China, 121, 662–666.

<https://doi.org/10.1016/j.proeng.2015.08.1061>

Zhang, X., Wargocki, P., & Lian, Z. (2017). Physiological responses during exposure to carbon dioxide and bioeffluents at levels typically occurring indoors. *Indoor Air*, 27(1), 65–77.

Zhang, X., Weerasuriya, A. U., & Tse, K. T. (2020). CFD simulation of natural ventilation of a generic building in various incident wind directions: Comparison of turbulence modelling, evaluation methods, and ventilation mechanisms. *Energy and Buildings*, 229, 110516. <https://doi.org/10.1016/j.enbuild.2020.110516>

Zheng, H. W. (2015). A Review of ‘Courtyard housing and cultural sustainability: Theory, practice and product’, By Donia Zhang. *International Journal of Housing Policy*, 15(4), 509–511. <https://doi.org/10.1080/14616718.2015.1092794>

Zhong, Chaudhry, H. N., & Calautit, J. K. (2021). Effect of Roof Cooling and Air Curtain Gates on Thermal and Wind Conditions in Stadiums for Hot Climates. *Energies*, 14(13), 3941. <https://doi.org/10.3390/en14133941>

Zhong, H.-Y., Sun, Y., Shang, J., Qian, F.-P., Zhao, F.-Y., Kikumoto, H., Jimenez-Bescos, C., & Liu, X. (2022). Single-sided natural ventilation in buildings: A critical literature review. *Building and Environment*, 212, 108797. <https://doi.org/10.1016/j.buildenv.2022.108797>

Zhu, J., Feng, J., Lu, J., Chen, Y., Li, W., Lian, P., & Zhao, X. (2023). A review of the influence of courtyard geometry and orientation on microclimate. *Building and Environment*, 236, 110269. <https://doi.org/10.1016/j.buildenv.2023.110269>

Zobaied, A., Tai, V. C., Go, T. F., Chong, P. L., & Moey, L. K. (2022). Effect of gable roof with various roof pitches and obstacle heights on natural ventilation

performance for an isolated building. *Journal of Mechanical Engineering and Sciences*, 16(3), 9033–9042. <https://doi.org/10.15282/jmes.16.3.2022.06.0715>